MINISTÉRIO DA CIÊNCIA, TECNOLOGIA E INOVAÇÃO
INSTITUTO NACIONAL DE PESQUISAS ESPACIAIS

sid.inpe.br/mtc-m21d/2023/06.01.22.35-TDI

CHARACTERIZATION OF THE EQUATORIAL AND LOW-LATITUDE IONOSPHERE DURING THE DEEP SOLAR MINIMUM OF SOLAR CYCLE 24

Frank Simbarashe Chingarandi

Doctorate Thesis of the Graduate Course in Space Geophysics, guided by Drs. Fábio Becker Guedes, Cláudia Maria Nicoli Cândido, and Olusegun Folarin Jonah, approved in June 28, 2023.

URL of the original document:
<http://urlib.net/8JMKD3MGP3W34T/497SGP5>

INPE
São José dos Campos
2023

PUBLISHED BY:

Instituto Nacional de Pesquisas Espaciais - INPE
Coordenação de Ensino, Pesquisa e Extensão (COEPE)
Divisão de Biblioteca (DIBIB)
CEP 12.227-010
São José dos Campos - SP - Brasil
Tel.:(012) 3208-6923/7348
E-mail: pubtc@inpe.br

MINISTÉRIO DA CIÊNCIA, TECNOLOGIA E INOVAÇÃO
INSTITUTO NACIONAL DE PESQUISAS ESPACIAIS

sid.inpe.br/mtc-m21d/2023/06.01.22.35-TDI

CHARACTERIZATION OF THE EQUATORIAL AND LOW-LATITUDE IONOSPHERE DURING THE DEEP SOLAR MINIMUM OF SOLAR CYCLE 24

Frank Simbarashe Chingarandi

Doctorate Thesis of the Graduate Course in Space Geophysics, guided by Drs. Fábio Becker Guedes, Cláudia Maria Nicoli Cândido, and Olusegun Folarin Jonah, approved in June 28, 2023.

URL of the original document:
<http://urlib.net/8JMKD3MGP3W34T/497SGP5>

INPE
São José dos Campos
2023

Cataloging in Publication Data

Chingarandi, Frank Simbarashe.

C441c Characterization of the equatorial and low-latitude ionosphere during the deep solar minimum of solar cycle 24 / Frank Simbarashe Chingarandi. – São José dos Campos : INPE, 2023.

xxxiv + 199 p. ; (sid.inpe.br/mtc-m21d/2023/06.01.22.35-TDI)

Thesis (Doctorate in Space Geophysics) – Instituto Nacional de Pesquisas Espaciais, São José dos Campos, 2023.

Guiding : Drs. Fábio Becker Guedes, Cláudia Maria Nicoli Cândido, and Olusegun Folarin Jonah.

1. Deep solar minimum. 2. High-speed streams. 3. Co-rotating interaction regions. 4. Space weather. I.Title.

CDU 523.98

MINISTÉRIO DA CIÊNCIA, TECNOLOGIA E INOVAÇÃO

INSTITUTO NACIONAL DE PESQUISAS ESPACIAIS
Serviço de Pós-Graduação - SEPGR

DEFESA FINAL DE TESE DE FRANK SIMBARASHE CHINGARANDI
REG. 478440/2018, BANCA Nº 169/2023

No dia 28 de junho de 2023, de forma virtual, o(a) aluno(a) mencionado(a) acima defendeu seu trabalho final (apresentação oral seguida de arguição) perante uma Banca Examinadora, cujos membros estão listados abaixo. O(A) aluno(a) foi APROVADO(A) pela Banca Examinadora, por unanimidade, em cumprimento ao requisito exigido para obtenção do Título de Doutor em Geofísica Espacial/Ciências do Ambiente Solar-Terrestre, com a exigência de que o trabalho final a ser publicado deverá incorporar as correções sugeridas pela Banca Examinadora, com revisão pelo(s) orientador(es).

Título: Characterization of the Equatorial and Low-Latitude Ionosphere during the Deep Solar minimum of Solar Cycle 24

Membros da banca:

Dra. Maria Paulete Pereira Martins – Presidente – INPE
Dr. Fábio Becker Guedes – Orientador – INPE
Dra. Cláudia Maria Nicoli Cândido – Orientadora – UNIVAP
Dr. Olusegun Folarin Jonah – Orientador – SRI International
Dra. Emilia Correia – Membro Interno – INPE
Dr. Hisao Takahashi – Membro Interno – INPE
Dra. Virginia Klausner de Oliveira – Membro externo – UNIVAP
Dra. Linda Habash Krause – Membro externo – NASA

Declarações de aprovação do Orientador Dr. Olusegun Folarin Jonah e da Dra. Linda Habash Krausea anexas ao processo.

Documento assinado eletronicamente por **Fábio Becker Guedes**, **Pesquisador**, em 28/08/2023, às 14:35 (horário oficial de Brasília), com fundamento no § 3º do art. 4º do Decreto nº 10.543, de 13 de novembro de 2020.

Documento assinado eletronicamente por **Emilia Correia**, **Pesquisadora**, em 28/08/2023, às 14:44 (horário oficial de Brasília), com fundamento no § 3º do art. 4º do Decreto nº 10.543, de 13 de novembro de 2020.

Documento assinado eletronicamente por **Maria Paulete Pereira Martins**, **Pesquisadora**, em 28/08/2023, às 14:45 (horário oficial de Brasília), com fundamento no § 3º do art. 4º do Decreto nº 10.543, de 13 de novembro de 2020.

Documento assinado eletronicamente por **Virginia Klausner de Oliveira (E)**, **Usuário Externo**, em 28/08/2023, às 15:07 (horário oficial de Brasília), com fundamento no § 3º do art. 4º do Decreto nº 10.543, de 13 de novembro de 2020.

Documento assinado eletronicamente por **hisao takahashi (E)**, **Usuário Externo**, em 28/08/2023, às 15:30 (horário oficial de Brasília), com fundamento no § 3º do art. 4º do Decreto nº 10.543, de 13 de novembro de 2020.

Documento assinado eletronicamente por **CLAUDIA MARIA NICOLI CANDIDO (E)**, **Usuário Externo**, em 31/08/2023, às 10:56 (horário oficial de Brasília), com fundamento no § 3º do art. 4º do Decreto nº 10.543, de 13 de novembro de 2020.

A autenticidade deste documento pode ser conferida no site https://sei.mcti.gov.br/verifica.html, informando o código verificador **11325591** e o código CRC **8FEA9C7E**.

Referência: Processo nº 01340.007131/2023-24 SEI nº 11325591

"... and of Christ, in whom are hidden all the treasures of wisdom and knowledge."

Colossians 2:2-3

To my parents Alista and Sakhile Chingarandi, my sisters Lorraine and Shamiso, and my little brother Alistair Jr. I would also like to dedicate this to all the youth from my nation Zimbabwe and my many African brothers and sisters, those who will come after me. I hope this work will inspire you to excel beyond what I did. NaJesu zvinogoneka.

ACKNOWLEDGEMENTS

First and foremost, I thank my Lord and Savior who made me what I am today and granted me the grace to finish this course. He has carried me through the highs and the lows and sustained me.

I am grateful to my supervisors Dr. Cláudia Candido, Dr. Fábio Becker and Dr. Olusegun Folarin Jonah who guided me throughout my journey at INPE. Their vast knowledge and experience contributed immensely to my work and scientific discoveries without them, I would not be the person I am today.

I would also like to thank my colleagues and postgraduate students from the Space Physics division, my office mates Sául Sanchez and Stella Santos, my colleagues Taiwo Osanyin, Prosper Kwamla Nyassor, Dorcas Dupe, Oluwasegun Adebayo for their unwavering support, generosity, and encouragement. I also would like to thank Dr. Alisson Dal Algo who was always there to provide invaluable advice. I am also grateful to my sisters, Vera Brown and Tosin for their love and prayers, without them none of this would have been possible. I never lacked any help anytime I needed it. I also like to make a special mention to my brother back in Zimbabwe Pastor Godwin Mashira who always stood by me in prayers and always had a word from the Lord. Thank you for helping me grow spiritually and for keeping my light burning in the darkness.

This study would not have been possible without the funding from Coordenação de Aperfeiçoamento de Pessoal de Nível Superior (CAPES) organization for which I am truly grateful for sponsoring my studies.

ABSTRACT

The aim of this work is to characterize the equatorial and low-latitude ionosphere and the influence of high-speed solar wind streams (HSSWSs) over Brazil during the deep solar minimum of solar cycle 24 (SC24). Multiple ground-based and space-based instruments namely; ground-based GNSS receivers, magnetometers as well as NASA Global-scale Observations of Limb and Disk (GOLD) and SWARM satellites were employed for the first time. Total electron content (TEC) obtained from GNSS receivers was used to derive multiple ionospheric parameters namely: (1) percentage deviation from quiet time (δTEC); (2) the rate of TEC (ROT) ; (3) the rate of TEC index (ROTI) and (4) spatial gradients (∇TEC). This was done to characterize gradients associated with irregularities and to quantify ionospheric response to geomagnetic storms. GOLD OI 135-6 nm disk measurements brought new insights into the structure of plasma bubbles and the post-sunset EIA over South America while ROTI facilitated the continuous monitoring of irregularities at a high temporal resolution. Analysis of the solar wind and interplanetary space showed that during the deep solar minimum, solar activity was weak, with low solar flux, solar flares and fewer intense geomagnetic storms. Coronal holes were the main source of recurring, long-duration, weak-moderate geomagnetic storms that periodically impacted solar wind and the thermosphere-ionosphere over South America. Long-duration CIR-driven storms (days) had remarkable effects on the thermosphere composition as well as plasma density while shorter-duration CIRs (hours) also produced unexpected changes in the thermosphere-ionosphere system. Our results showed that the minor CIR/HSS-driven storms caused positive ionospheric storms of over 20 TECU (+300%) and negative storms of –20 TECU (–80%) over the South crest of the equatorial ionization anomaly (EIA). Thus, weaker HSS/CIR-driven storms have a larger impact than intense, CME-driven storms. In addition, the amplitude of ionospheric storms and irregularities was maximum in the recovery phase. Ionospheric storms revealed seasonal differences in response due to changes in the thermosphere background conditions. The amplitude of ionospheric irregularities and spatial gradients in TEC showed a strong correlation with the magnitude of TEC. For the first time, GOLD 135.6 nm images, GNSS TEC and ROTI maps reveal periodic separation of EPBs and small-scale irregularities during very low solar activity. Geomagnetic activity during solar minimum is significant and can no longer be ignored. Understanding Sun-Earth interactions and monitoring of the thermosphere-ionosphere is of great interest for Space Weather forecasting and GNSS applications.

Keywords: Deep solar minimum. High-speed streams. Co-rotating Interaction Regions. Space Weather.

CARACTERIZAÇÃO DA EQUATORIAL E IONOSFERA DE BAIXA LATITUDE DURANTE O SOLAR PROFUNDO MÍNIMO DE CICLO SOLAR 24

RESUMO

O objetivo do trabalho foi caracterizar a ionosfera equatorial e de baixa latitude sobre o Brasil e a influência das correntes de vento solar de alta velocidade (HSSWSs) do mínimo solar profundo do ciclo solar 24 (SC24). Varias instrumentos foram utilizados, incluindo receptores GNSS terrestres, magnetômetros, satélites; o GOLD da NASA e o SWARM. O conteúdo total de elétrons (TEC) obtido dos receptores GNSS foi usado para derivar múltiplos parâmetros ionosféricos, a saber: (1) desvio percentual do tempo calma (δTEC); (2) a taxa de TEC (ROT); (3) a taxa do índice TEC (ROTI) e (4) gradientes espaciais em TEC (∇TEC). Isso foi feito para caracterizar gradientes associados a irregularidades e quantificar a resposta ionosférica a tempestades geomagnéticas. As observações do GOLD OI 135-6 nm trouxeram novos conhecimentos sobre a estrutura das bolhas de plasma e a anomalia equatorial. O ROTI tornou possível o monitoramento contínuo de irregularidades em alta resolução temporal. A análise do vento solar e do espaço interplanetário mostrou que a atividade solar era fraca, com baixo fluxo solar, erupções solares e menos tempestades geomagnéticas intensas. Os buracos coronais (CHs) foram a principal fonte de tempestades geomagnéticas fracas a moderadas recorrentes e de longa duração que impactaram periodicamente o vento solar e a termosfera-ionosfera sobre a América do Sul. A magnitude das tempestades geomagnéticas impulsionadas pelo HSSWS era semelhante. Um total de 28 tempestades geomagnéticas fracas a moderadas (–30< Sym–H < –60nT), incluindo uma intensa tempestade geomagnética (Sym–H = 205nT) foram examinadas. Os tempestades induzidas por CIR de longa duração (dias) tiveram efeitos notáveis, enquanto CIRs de curta duração (horas) também produziram mudanças inesperadas no TI. Os resultados mostraram que as tempestades menores causadas por CIR/HSS causaram tempestades ionosféricas positivas de mais de 20 TECU em magnitude (+300%) e tempestades negativas de –20 TECU (–80%) sobre a crista sul da anomalia equatorial de ionização (EIA). Além disso, a amplitude das tempestades e irregularidades ionosféricas foi máxima na fase de recuperação. As tempestades ionosféricas revelaram diferenças sazonais em resposta devido a mudanças nas condições de fundo da termosfera. Grandes variações diurnas no EIA e irregularidades foram observadas sob a influência de campos elétricos de penetração imediata (PPEF) e ventos perturbadores. A amplitude das irregularidades e gradientes apresentaram um forte correlação com o TEC. Pela primeira vez, os mapas de ROTI revela uma separação periódica de irregularidades durante a baixa atividade solar. Tempestades geomagnéticas fracas podem causar distúrbios ionosféricos mais significativos do que tempestades intensas e, portanto, não podem mais ser ignoradas.

Palavras-chave: profundo mínimo solar. fluxos de vento solar de alta velocidade. Regiões de interação corotantes. Clíma Espacial.

LIST OF FIGURES

Page

LIST OF TABLES

Page

LIST OF ABBREVIATIONS

AE	–	Auroral electrojet index
AIA	–	Atmospheric Imaging Assembly
ASI	–	All-Sky Imager
Ap	–	Planetary activity index
CCD	–	Charge-coupled Device
CEJ	–	Counter-electrojet
CH	–	Coronal Hole
CIR	–	Co-rotating Interaction Region
CME	–	Coronal mass ejection
CWT	–	Continuous Wavelet Transform
DDEF	–	Disturbance dynamo electric field
Dst	–	Disturbance Storm Time
EEJ	–	Equatorial electrojet
EIA	–	Equatorial ionization anomaly
EMBRACE	–	Estudo e Monitoramento BRAsileiro de Clima Espacial
EPB	–	Equatorial plasma bubble
FOV	–	Field of view
FUV	–	Far ultra-violet
GBAS	–	Ground-based Augmentation System
GEC	–	Global Electron Content
GLONASS	–	Globalnaya Navigatsionnaya Sputnikovaya Sistema
GNSS	–	Global Navigation Satellite Systems
GOLD	–	Global Observations of Limb and Disk
GPS	–	Global Positioning System
GSM	–	Geocentric Solar Magnetospheric system
HILDCAA	–	High-Intensity Long-Duration Continuous Auroral Activity
HMI	–	Helioseismic and Magnetic Imager
HSA	–	High Solar Activity
HSS	–	High-speed stream
IBGE	–	Instituto Brasileiro de Geografia e Estatística
IEF	–	Interplanetary electric field
IGRF	–	International Geomagnetic Reference Field
IMF	–	Interplanetary magnetic field
INTERMAGNET	–	International Real-time Magnetic Observatory Network
IPP	–	Ionospheric Piercing Point
ITM	–	Ionosphere-Thermosphere-Mesosphere
LASCO	–	Large Angle and Spectrometric Coronagraph
LEO	–	low-Earth Orbit
LISN	–	Low-Latitude Ionospheric network
LSA	–	Low Solar Activity
LSTID	–	Large-scale Travelling Ionospheric Disturbance
MSA	–	Moderate Solar Activity
MSTID	–	Medium-scale Travelling Ionospheric Disturbance

NH	–	Northern Hemisphere
NS	–	Negative ionospheric storm
PPEF	–	Prompt penetration field
PRE	–	Prereversal enhancement
PRN	–	Pseudo-random noise
PS	–	Positive ionospheric storm
RBMC	–	Rede Brasileira de Monitoramento Contínuo dos Sistemas GNSS
ROT	–	Rate of TEC
ROTI	–	Rate of REC index
RTI	–	Rayleigh-Taylor instability
SAO	–	Standard Archiving Output
SC	–	Solar Cycle Number
SDO	–	Solar Dynamics Observatory
SFU	–	Solar flux Units
SH	–	Southern Hemisphere
SSN	–	Sunspot number
SSWS	–	Slow-Solar Wind Stream
SUPIM	–	Sheffield University Plasmasphere Ionosphere Model
TEC	–	Total Electron Content
TI	–	Thermosphere–Ionosphere
TIMED	–	Thermosphere Ionosphere Mesosphere Energy and Dynamics
VHF	–	Very High Frequency
WAAS	–	Wide Area Augmentation System
WHI	–	Whole Heliosphere Interval
WHPI	–	Whole Heliosphere and Planetary Interactions

CONTENTS

Page

1 INTRODUCTION TO DEEP SOLAR MINIMUM

Solar activity follows an 11-year cycle which begins with a minimum, followed by the ascending phase ($\sim$ 3 years long), reaches a maximum ($\sim$ 2 years duration), and then descends ($\sim$ 4 years) into another minimum as a new cycle begins (HATHAWAY, 2015). In general, solar activity has been progressively declining over the past 4 solar cycles (KRAINEV, 2012; HADY, 2013; JIANG et al., 2015) reaching the deepest levels in almost 100 years at the end of solar cycle 23 (SC23) (RUSSELL et al., 2010; GIBSON et al., 2011; HADY, 2013). This period referred to as *deep solar minimum*, was marked by unprecedented levels of low solar activity in the Space Age, and has become synonymous with solar cycles 23 and 24 (RUSSELL et al., 2010; CHEN; WANG, 2015; AA et al., 2021; DERGHAZARIAN et al., 2021). Interestingly, it has been likened to the Maunder Minimum of 1645–1715, a period of extremely low activity (RUSSELL et al., 2010; HADY, 2013; LAPENTA, 2020). SC23 began in 1996 and ended in 2008 and reached maximum solar activity in 2014. It was unusual in many respects in comparison with previous solar cycles (ECHER et al., 2011; KRAINEV, 2012; HADY, 2013; HATHAWAY, 2015). For instance, it had a duration of $\sim$ 13.5 years (HADY, 2013), 2 years above the median and the longest in over 23 solar cycles (ECHER et al., 2011; BASU, 2013; HATHAWAY, 2015). The descending phase also lasted for much longer than previous cycles, leading to an extended deep solar minimum (RUSSELL et al., 2010; ECHER et al., 2011; HADY, 2013) which was associated with a delayed flux emergence (GIBSON et al., 2011; BASU, 2013). For perspective, solar cycles 20, 21 and 22 were 11.7, 10.3 and 9.7 years long, respectively (ECHER et al., 2011). This peculiar minimum prompted several initiatives to better understand deep solar minimum which brought many insights. One such initiative was the *The Whole Sun Month*, WSM, an international campaign which covered the minimum of SC22, from August 8 to September 10, 1996 (GALVIN; KOHL, 1999). The objective was to explore features such as the equatorial helmet streamers and Coronal Holes that impact the interconnected Sun-Earth system for prolonged intervals (GIBSON et al., 2011). A follow-up on this initiative was the *Whole Heliosphere Interval*, WHI, which focused on the SC23 minimum of 2008 to 2009 which was reported by Gibson et al. (2011), Emery et al. (2011), Nitta (2011) and the references therein. A more recent campaign, the *Whole Heliosphere and Planetary Interactions*, WHPI, established a new focus, *"to broaden the emphasis further to include planetary magnetospheres and atmospheres"*, in a more holistic approach, and in particular, planetary space weather (CANDIDO et al., 2022). These efforts aimed to understand the features of deep solar minimum such as its duration, solar flux levels, solar wind and the interplanetary magnetic field

(GIBSON et al., 2011; HADY, 2013; ABRAMENKO et al., 2010; RUSSELL et al., 2010). All this influences the interconnected solar wind magnetosphere-ionosphere-thermosphere.

The thermosphere–ionosphere (TI) is very important to our understanding of space weather (LIU, 2016). TI variability can be disruptive to radio communication and Global Navigation Satellite Systems (GNSS) (CAI et al., 2020b; LIU, 2016; SARRIS, 2019). During quiet time, the TI is influenced from below principally by tides, planetary waves, and gravity waves (LIU, 2016; EASTES et al., 2017; CAI et al., 2021). Verkhoglyadova et al. (2011), Jonah et al. (2015), Abreu et al. (2017) found strong 13.5, 16 and 27-day oscillation in the TEC within low latitudes. The larger 16,27 and 32 which correspond to the F10.7 are related to the influence of tides and semi-diurnal tides respectively (JONAH et al., 2015; ABREU et al., 2017). Jonah et al. (2015), Abreu et al. (2017) also observed shorter 1-5 and 8-10-day oscillations in TEC attributed to the propagation of planetary waves. In addition, gravity waves originate from tropospheric sources (AJITH et al., 2020; JONAH et al., 2016; HINES, 1960), causing perturbations in the ionosphere called Travelling ionospheric Disturbances (TIDs) (VADAS, 2007). TIDs are known to play an important role in the initiation of equatorial plasma bubbles, EPBs, at the F layer bottomside (AA et al., 2020; ABDU et al., 2009; AJITH et al., 2020; FIGUEIREDO et al., 2018). The ionosphere over Brazilian low latitudes is uniquely influenced by complex electrodynamics processes which are driven by the disturbance of electric fields and winds. During the daytime, the fountain effect is responsible for the formation of the equatorial ionization anomaly (EIA). At sunset, the pre-reversal enhancement (PRE) (KELLEY, 2009) creates favorable conditions for the growth of Rayleigh-Taylor instability, RTI at the F layer bottomside (ABDU et al., 1981). The high declination angle of the magnetic field over Brazil explains the peculiar behavior of plasma irregularities over this region. (ABDU et al., 1981) The alignment between the magnetic meridian and the solar terminator results in a larger PRE in the zonal electric field which controls the formation of plasma irregularities (KELLEY, 2009). In addition, the strengthening (weakening) of the daytime EIA is driven by enhancement (suppression) of the equatorial electrojet (EEJ) over low latitudes under the action of penetration electric fields and disturbance winds (FAGUNDES et al., 2016; LIU et al., 2012). The effect of these electric fields on the low-latitude electrodynamic processes depends on the local time of the storm (FAGUNDES et al., 2016; ABREU et al., 2010; FEJER, 2011) resulting in the triggering or suppressing the RTI (AA et al., 2021; ABDU, 2001; MORO et al., 2021). However, the TI is also occasionally influenced by energy input from the magnetosphere through

charged particles, electric currents, and penetration electric fields during geomagnetic storms (EASTES et al., 2017; ASTAFYEVA et al., 2015). Burns et al. (2004) studied the thermosphere temperature and composition responses to moderate geomagnetic storms and found that the effects of moderate geomagnetic storms were greater during solar minimum than in solar maximum. Recent studies have shown large variations in the TI during deep solar minimum under weak geomagnetic activity (GAN et al., 2020; AA et al., 2021; CAI et al., 2020b; CAI et al., 2020a). Disturbance winds cause long-lasting changes in the thermospheric composition, O/N2 ratio(CAI et al., 2020b; ASTAFYEVA et al., 2020). The F region electron density is modulated by the O/N2 ratio (DANILOV; MOROZOVA, 1985; MORO et al., 2021; TITHERIDGE, 1974) which is an important parameter in quantifying thermospheric composition response (BURNS et al., 2014; LIU et al., 2020; CAI et al., 2020a). Under weak background conditions (CHEN; WANG, 2015), the thermosphere response is highly sensitive to geomagnetic disturbances (BURNS et al., 2014). Apart from solar activity, the seasonal variations in the background thermosphere also influence TI response (BURNS et al., 2004; LEKSHMI et al., 2011). This is important at low latitudes where the greatest temperature and composition changes occur (LIU, 2016). Knowledge of pre-storm background conditions of the TI determines the accuracy of Space Weather forecasts (LIU, 2016).

1.1 A brief review of deep solar minimum

As shown in Figure 1.1, the historic solar activity presents maxima and minima with a clear progressive decrease for the past four cycles. Solar Cycle 23 as mentioned was deeper than previous minima.

Figure 1.1 - Sunspot number showing Solar cycles 21 to 25.

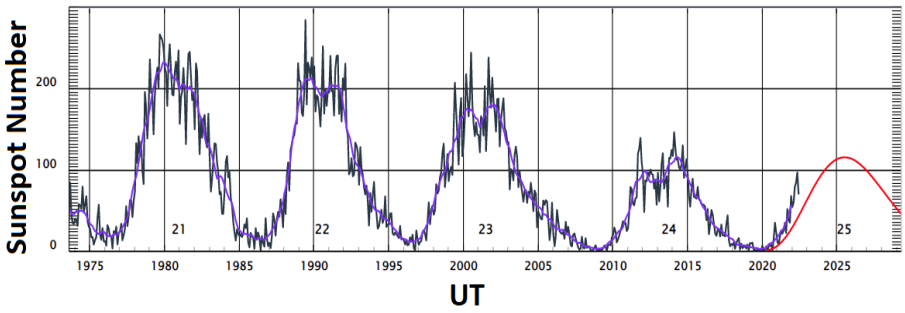

Progression of solar activity from solar cycle 21 to 24. The prediction of solar cycle 25 is shown in red.

It had several unique characteristics (ECHER et al., 2011) which are arranged in order from the Sun, solar wind and IMF as follows:

a) SC23 had very low levels of solar activity (GIBSON et al., 2011). During 2008 the sunspot number reached a yearly mean of only 3 sunspots (ABREU et al., 2017) compared to 110 during SC23 maximum (HADY, 2013; RUSSELL et al., 2010). It also had the highest number of spotless days, $\sim$ 268 in total according to <https://spaceweather.com/>, which corresponds to 73% of the days of the year (RUSSELL et al., 2010). The level of solar irradiance, solar flux, F10.7 ($\sim 69SFU$) was also below previous solar cycles of(GIBSON et al., 2011; EMMERT et al., 2010). Solar flares were so rare (NITTA, 2011) that the yearly flare index was only 0.03 during 2008 (HADY, 2013).

b) The solar wind speed ($v_{sw} < 350km/s$) measured by the **ACE** and **WIND** spacecraft was less than during SC22 (BASU, 2013; RUSSELL et al., 2010), among the lowest ever recorded in history (EMERY et al., 2011). Consequently, the radiation belt flux also dropped significantly because it is energized by High-speed Streams (RUSSELL et al., 2010).

c) In general, the magnetic field strength at the poles, which is a proxy for solar activity, was low (GIBSON et al., 2011; GRANDIN et al., 2019; RUSSELL et al., 2010; WATARI, 2017).

d) The interplanetary magnetic field (IMF) magnitude of 3nT was weaker compared to $\geq 5nT$ during previous cycles (ECHER et al., 2011) and the Southward component of Bz, solar wind dynamic pressure and proton density were also lower (RUSSELL et al., 2010). This was caused by a weakening in the flux emergence. As a result of weaker IMF magnitude, Bz and solar wind speed (RUSSELL et al., 2010), less energy was transferred from the solar wind to the magnetosphere (RUSSELL et al., 2010; ECHER et al., 2011; CHEN; WANG, 2015).

e) The historical lows in the properties of Geospace meant maximum galactic cosmic ray flux (protons, electrons, ionized species) in the absence of CMEs (RUSSELL et al., 2010) and a weaker Interplanetary Magnetic Field and low solar wind dynamic pressure(GIBSON et al., 2011; HADY, 2013).

f) The thermospheric neutral density, according to satellite drag measurements (EMMERT et al., 2010), fell by 30% from 1996 while peak plasma

density dropped by 20% (SOLOMON et al., 2018). Model simulations showed a significant decrease in the Global mean Total Electron Content. This was attributed to the decrease in EUV radiance (LIU et al., 2012; CHEN; WANG, 2015; SOLOMON et al., 2018).

Despite the low solar activity, large, low-latitude, and long-lasting Coronal Holes (CHs) were still present on the sun (ABRAMENKO et al., 2010; GIBSON et al., 2011). As a result, recurring high-speed streams (HSSs) periodically impacted the Earth's magnetosphere and upper atmosphere. The weaker, recurrent geomagnetic disturbances during deep minimum caused significant variability of the ionosphere (CHEN; WANG, 2015). In addition, the response of the daily mean in the Global Electron Content (GEC) showed a strong positive correlation with the planetary activity index, Ap, (CHEN; WANG, 2015). SC23 was succeeded by a similar weak cycle, SC 24 which is reviewed in the next section.

1.2 Solar cycle 24

Figure 1.1 shows a downward progression in the sunspot number(SSN) showing a larger decline from SC23 to SC24. Solar Cycle 24, began in December 2008 and ended in November 2019, lasting for a typical 11 years unlike SC23 (PESNELL, 2008). At solar maximum, the SSN during SC24 was 166.4 compared to 180 during SC23 (WATARI, 2017), indicating a significantly weaker cycle. In many ways, SC24 shared similarities with its predecessor in terms of peculiarity (BASU, 2013). For instance, its ascension into high solar activity was slower compared to the previous three cycles (BASU, 2013; RICHARDSON et al., 2017; RAO et al., 2019). The minimum of SC24 in 2018–2020 was also characterized by extremely low solar activity, also among the weakest in history (WATARI, 2017; DERGHAZARIAN et al., 2021; AA et al., 2021). Cycle 24 minimum was characterized by an unusually weak magnetic field (BASU, 2013; GOPALSWAMY et al., 2011), attributed to weaker polar fields. The solar wind speed and IMF magnitude were lower than in the same period of SC23. Consequently, the geoeffectiveness of HSS was lower (GRANDIN et al., 2019) because of lesser energy input from solar wind into the magnetosphere-ionosphere (RUSSELL et al., 2010) as previously mentioned.

SC24 was also characterized by weak geomagnetic activity with fewer intense geomagnetic storms (min $Dst < -100nT$) which are usually caused by halo CMEs (GRANDIN et al., 2019). CME rates in 2013 and 2014 (2%) were lower than during SC23 (6%) associated with a drop in the sunspot number. The total number

of ICMEs (12) in SC24 was also lower than at the same stage during SC23 (32) (GRANDIN et al., 2019). During 2018–2019, only weak B and C-class solar flares were detected according to <https://spaceweather.com/>. Despite being quiet, several low-to-moderate geomagnetic storms impacted the thermosphere-ionosphere in SC24 minimum. An unexpected intense storm (Sym-H ~ -207 nT) occurred on 24 August 2018 caused by a CME associated with a solar flare eruption which is unusual for low solar activity(IMTIAZ et al., 2021).

1.3 High-speed streams and the low-latitude ionosphere

During solar minimum, HSSs from CHs interact with forward Slow-Solar Wind Streams, SSWSs, generating Co-rotating Interaction Regions (CIRs) that drive weak to moderate geomagnetic storms (TSURUTANI et al., 1995). Coronal holes can appear for several solar rotations, which is the source of recurrent, periodic geomagnetic disturbances. HSS are drivers of weak to moderate geomagnetic activity which is known to cause significant changes in the thermosphere-ionosphere during solar minimum (CHEN; WANG, 2015; CAI et al., 2020a; MORO et al., 2021). Weak-to-moderate, long-duration geomagnetic storms during solar minimum can trigger a long-lasting modification in the ionosphere (VERKHOGLYADOVA et al., 2011; LIU et al., 2012). There have been numerous studies of ionospheric response to long-duration HSSWS/CIR during deep solar minimum. In particular, Candido et al. (2018), Verkhoglyadova et al. (2011), Liu et al. (2012) investigated the response of the low-latitude ionosphere over Brazilian low-latitude to recurrent HSSWS/CIRs during deep minimum and found significant changes in plasma density. For instance Candido et al. (2018) found large ionospheric storms in TEC of amplitude 120 % over quiet time average, a magnitude that is comparable to those caused by CME-driven storms. One important feature that distinguishes CIR storms is large fluctuations in the IMF B_z during extended recovery phases caused by nonlinear Alfvén waves (RAGHAV et al., 2019) which may lead to several episodes of prompt penetration fields (PPEFs) that are responsible for significant ionospheric perturbations during long recovery phases (LIU et al., 2012; KELLEY et al., 2003). The negative B_z in the HSSs causes High-Intensity Long-Duration Continuous Auroral Activity (HILDCAA) events (TSURUTANI et al., 1995; SILVA et al., 2017) which can last up to a full solar rotation, during which there is the continuous injection of energy into the magnetosphere during substorms (TSURUTANI et al., 2006). The Alfévenic fluctuations during substorms play an important role in causing positive ionospheric storms (PS) during the recovery phase (LIU et al., 2012; MORO et al., 2021). During geomagnetic storms, harmful radiation can impact astronauts in space, and destroy

satellite circuitry. On the other hand, thermospheric expansion can increase orbital drag leading to the loss of satellites. Of note was the February 2022 case, a moderate solar flux interval, during which 38 Starlink low-Earth Orbit (LEO) satellites burned up on re-entry soon after launch as a result of prolonged, minor geomagnetic storm conditions that led to increased orbital drag (FANG et al., 2022). This shows that minor storms do have a significant but yet unexplored impact on Space Weather. Interestingly, the series of storms had similar characteristics to geomagnetic storms observed during the deep solar minimum of SC24 such as maximum (Kp ~ 5), solar wind speed of $\sim 600 km/s$, and a minimum $B_z \sim 20nT$.

1.4 Motivation

Although the effects of CME-driven storms are well-known, the influence of CIR-HSS-driven storms is still poorly characterized. Further, few studies have focused on the impact of HSSWS/CIR-driven storms during the deep minimum of cycle 24 over South America hence the influence of solar HSSWS on the heliosphere is not well known. The high frequency of occurrence during solar minimum of HSSWS/CIR-driven storms warrants more detailed research on solar wind, interplanetary magnetic field, magnetosphere and the thermosphere-ionosphere (GIBSON et al., 2011). The period of deep Solar Minimum also offers an opportune window to investigate the nominal behavior of the ionosphere and the interaction with the heliosphere under relatively low solar flux conditions, and in the absence of continuous geomagnetic disturbances which are more common in periods of High-Solar Activity, (HSA) (RUSSELL et al., 2010; VERKHOGLYADOVA et al., 2011; CANDIDO et al., 2018). This baseline can also then be used as a reference for model tuning and improving space weather forecasts.

Furthermore, few attempts have been made to investigate the similarities and differences in how CME and CIR-driven geomagnetic storms influence the ionosphere during solar cycle 24 (SS24) since the occurrence of CMEs during this period is rare. The recently launched Global Observations of Limb and Disk (GOLD) mission into geostationary orbit shall be fully utilized to bring new perspectives on the low latitude ionosphere over South America and together with ground-based observations to study geomagnetic storms during solar minimum. Deep Solar Minimum offers an opportune window to investigate the nominal behavior of solar wind, IMF, magnetosphere and the thermosphere-ionosphere in the absence of strong geomagnetic disturbances which are more common in periods of High-Solar Activity, (HSA) (RUSSELL et al., 2010; CANDIDO et al., 2018).

1.5 Objectives

The general objective is to use the parameters of Geospace and geomagnetic indices to improve the understanding of the Deep Solar Minimum. To achieve this, multiple solar wind, IMF parameters and Geomagnetic indices were analyzed to study the behavior of the equatorial and low-latitude ionosphere during quiet and disturbed periods. Furthermore, correlations between these ionospheric indices were explored.

- Identify the main drivers of the ionosphere during deep solar minimum;
- Investigate how geomagnetic storms driven by HSSWS/CIR influence the thermospheric composition and ionospheric, plasma density and post-sunset irregularities;
- Calculate multiple ionospheric indices and parameters from ground-based GNSS TEC;
- Characterize the occurrence of EPB/ irregularities and estimate ionospheric gradients from TEC;
- Establish a correlation between TEC and TEC-derived indices, as well as with ground-based ionospheric parameters, such as F-layer virtual height, $h'F$, peak height h_mF_2 and critical frequency, f_oF_2, vertical $E \times B$ drifts, equatorial electrojet indices, EEJ and others;
- Calculate the magnitude of ionospheric storms using the deviation of TEC from average quiet time.

2 THE SUN, SOLAR WIND AND CORONAL HOLES

In this chapter, a theoretical background of the sun, solar wind, geomagnetic storms, and subsequent ionospheric response is presented.

2.1 The Sun

The sun is the largest star in the solar system and is the main source of radiation and charged particles. It emits electromagnetic radiation over a wide spectral range, a continuous stream of plasma, and bursts of energetic particles. The visible surface, the photosphere, approximates a black body at 6400°K (HARGREAVES, 1992). It is made up of gas at extremely high temperatures which allows the atoms and electrons to move freely creating a unique state of matter called plasma. It is mainly made up of Hydrogen and Helium gas as well as other minor constituents. The source of energy is the nuclear fusion of the light Helium and Hydrogen nuclei, forming heavier nuclei releasing vast amounts of energy and at its core reaching temperatures of up to millions of degrees Kelvin (HARGREAVES, 1992). It has a differential rotation period of 25.4 days at the equator and 36 days at the poles. This is thought to be responsible for the twisting of magnetic field lines which leads to reconnection processes in the photosphere. The solar atmosphere is made up of the photosphere, chromosphere, and corona. Most of the visible light is emitted in the photosphere citelapenta2020space. Figure 2.1 shows the structure of the sun and the main processes in each layer. The density and temperature of the gas change drastically from the center to the corona.

Figure 2.1 - Illustraction of solar structure and the different processes.

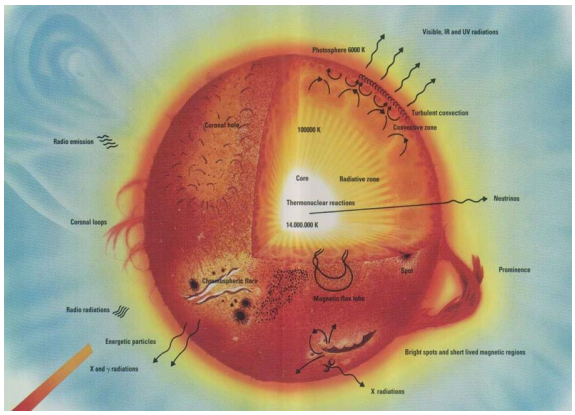

SOURCE: Hamilton (2020).

Within the Sun there is the radiative zone where energy moves slowly outward, taking more than 170,000 years to radiate through this layer. In the Convection Zone, energy continues to move toward the surface through the convection currents of the heated and cooled gas. The solar atmosphere is made up of the Photosphere: 300 km thick, temperature decreases with a height of $\sim 10,000$ K up to ~ 5000 K (HARGREAVES, 1992). The Chromosphere is a thin layerfrom which prominences are formed that extend into the corona. Solar material is ejected from the Sun at times during spectacular events. The temperature increases rapidly from the minimum temperature of 5800 K to about 10000 K near the base of the outer atmosphere. The corona is the outermost layer which contains extremely hot ionized plasma upwards of a million $^{\circ}K$ that typically extends several sun radii from the core. There is an extremely sharp increase in temperature from the photosphere into the corona, an anomaly named, the *Coronal Heating Problem*, which has been a long-standing topic of research for many decades.

2.1.1 Sunspots

On the sun's photosphere are dark spots called sunspots. An example of a sunspot is shown in Figure 2.2 (a) while (b) shows a polar coronal hole together with a solar flare eruption. Sunspots are characterized by an intense magnetic field and significantly lower temperatures, about 2000K cooler, compared to the surrounding photosphere (HARGREAVES, 1992). The central region is called the umbra (T $\sim$ 4000 K and B

Figure 2.2 - (a) Helioseismic and Magnetic Imager (HMI) at 6173 Å on 6 September 2017 showing sunspots. (b) Atmospheric Imaging Assembly(AIA) at 193 Å. A solar flare is observed above the sunspots. Credit: NASA.

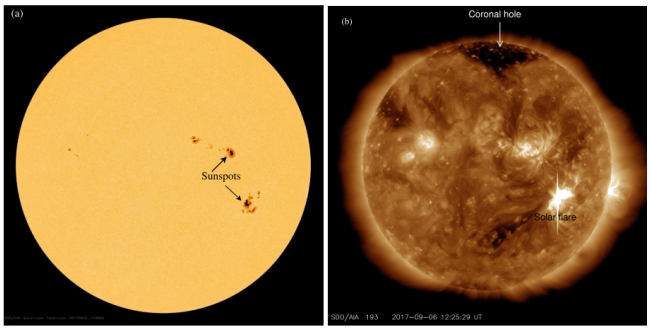

SOURCE: Matamba (2017).

$\sim$ 0.3 T) from which perpendicular field lines emerge while the region with a radial structure of dark and light filaments from which more horizontal field lines emerge is the penumbra. Sunspots usually emerge in groups on either hemisphere and can last up to 2 solar rotations (HATHAWAY, 2015). The polarity of sunspots in opposite hemispheres reverses every 22 years though the mechanism for this is not yet well known (HARGREAVES, 1992). The number of sunspots has been used to measure solar activity by taking into account the individual number of sunspots as well as their groups. At the beginning of each cycle, sunspots occur at about 40° of the solar equator and then gradually migrate toward the equator at solar maximum. This is illustrated in the famous "butterfly diagram" shown in Figure 2.3 which shows the sunspot area variation with latitude and year.

Figure 2.3 - The top panel shows the latitude distribution of sunspots on the sun as a function of time. The lower panel shows, for the same epoch, the area of the solar disk occupied by sunspots. Sunspots migrate to low latitudes as the solar cycle progresses.

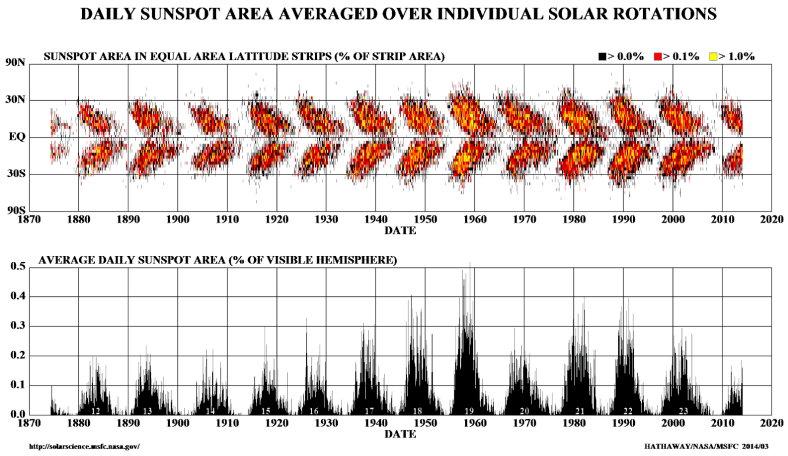

SOURCE: Hathaway (2015).

Figure 2.4 shows the clear difference between the quiet sun during deep minimum and solar maximum. Several prominences (loops) and active regions can be seen during solar maximum while at solar minimum polar coronal holes are indicated by the dark emissions.

Figure 2.4 - 193 Å X-ray emissions observed by NASA Solar Dynamics Observatory (SDO) comparing on the Left: Solar maximum on April 2014 and on the Right: Solar minimum of December 2019 at the start of Solar Cycle 25. A clear contrast is observed between the quiet and active sun.

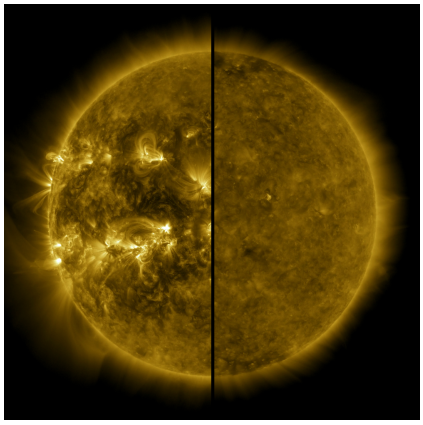

2.1.2 Solar flares

A Solar flare is a sudden brightening of the solar atmosphere near active regions (HARGREAVES, 1992). These bursts expel large quantities of radiation usually X-rays and EUV and charged particles called Solar Energetic Particles SEPs (HATHAWAY, 2015). The radiation bursts can drastically impact the upper atmosphere. Figure 2.2 (b) shows an example of an X9.3 solar flare eruption observed near an active region during high solar activity. Such magnitude of solar flares cause radio blackouts and can damage satellites. Solar flares occur near sunspots or active regions and are sometimes observed together with CMEs (HARGREAVES, 1992). The principal cause of flares is magnetic re-connection, which releases large amounts of energy (GeV) stored in twisted field lines. X-class flares are the most intense explosions in the solar system which form loops tens of times the size of Earth. The sporadic nature of occurrence poses a great challenge to space weather predictions.

2.1.3 Coronal mass ejections

Coronal holes are expulsions of large solar material and magnetic field which can be as large as 1/4 the size of interplanetary space associated with active regions (GONZALEZ; PARKER, 2016). CMEs together with solar flares are prevalent during solar maximum (TSURUTANI et al., 2006; GONZALEZ et al., 1994; BOROVSKY; DENTON, 2006) and can reach very high velocities of up to 1000 km/s. Coronal

mass ejections (CMEs) and their associated phenomena are the key drivers of major Space Weather on Earth and throughout the heliosphere associated with closed field lines in the active regions. If a CME is large enough and has a velocity greater than the solar wind ahead of it can generate a forward shock compressing the earth's magnetosphere on the dayside and extending to the nightside (GONZALEZ et al., 1994). This shock is accompanied by a surge in the magnetic field, plasma velocity, density, and temperature. The intense magnetic field within the CME often produces a large Southward IMF Bz component, which causes strong effects on the Earth's magnetosphere (GONZALEZ et al., 1994) resulting in particle precipitation at the polar region. CMEs pose great risks to space-based technological systems, and communication, the extreme radiation can burn electrical circuits on board satellites and extreme doses of radiation is a biohazard to astronauts in space, sudden increase in radiation is known to cause radio blackouts, an increase in satellite drag and electrical power grid failures (MCDONALD et al., 2008). The ability to predict the arrival time and possible magnitude of impact is therefore, of crucial importance. An example of a CME observed in 2001 is shown in Figure 2.5.

However, only Earth-directed CMEs that are located close to the equator (GOPALSWAMY et al., 2009) are geoeffective while those originating at higher latitudes in general have a weaker impact. The propagation of CMEs to Earth is not straightforward. For instance, CMEs have been known to deflect after collision with each other (GOPALSWAMY et al., 2009). Furthermore, under certain conditions, the path of a CME can deviate nearer or further from the Sun-Earth line depending on the nature of collision with a fast wind stream (GOPALSWAMY et al., 2009). This is of great significance during low solar activity since CIRs are a common occurrence.

Figure 2.5 - NASA Large Angle and Spectrometric Coronagraph, LASCO, images showing a coronal mass ejection observed on 6 November 2001 during solar cycle 23 maximum. Bright emissions can be observed.

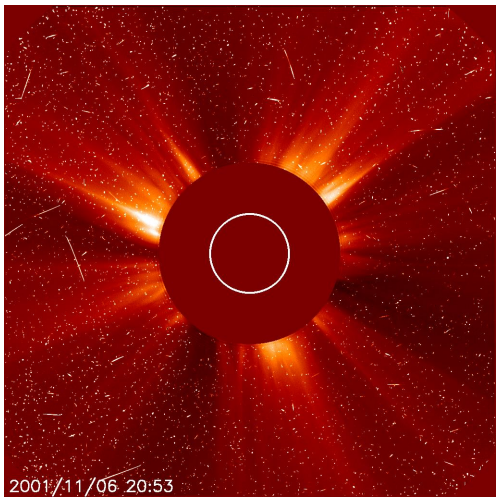

2.1.4 Solar wind

Solar wind is a steady stream of charged particles which is made up of He^{2+} ions, protons, and electrons which flows steadily from the sun (HARGREAVES, 1992). The heliosphere is the region in space within the influence of the solar magnetic field. The solar wind carries with it a weak magnetic field "frozen in" to the plasma (HARGREAVES, 1992). This constant flux of particles is deflected by the Earth's magnetic field forming a bow shock at the front end of the dayside as the magnetosphere is compressed. The slow-moving solar wind speed is typically below $400km/s$ (TSURUTANI et al., 2006). During geomagnetically disturbed periods the solar wind speed can exceed $1000km/s$. It takes 3 to 4 days for the slow-moving solar wind to reach the Earth (DAVIES, 1990). The solar wind is very important during deep solar minimum since it has the main influence on the magnetosphere during the descending phase or solar minimum in the absence of active regions (TSURUTANI et al., 2006).

2.1.5 Coronal holes

Coronal Holes (CHs) are dark regions of open magnetic field lines and lower plasma temperature and density. CHs are more prevalent at the poles of the Sun during high solar activity but expand and move to lower latitudes as solar activity decreases. The

structure of CHs varies in terms of size and shape. First, there are polar CHs, which are located at the solar poles and have a lifetime comparable to that of the solar cycle (ABRAMENKO et al., 2010). Included in this category are CH extensions, such as the "elephant trunk" CH observed in 1996 August (ABRAMENKO et al., 2010). The second type is isolated CHs, which are mostly limited to the low and middle latitudes and are not connected to the polar CHs. CHs are very important structures that dominate the photosphere during the descending phase and can be as large as 50% of the solar surface. CHs can develop at any location and time and can extend to low latitudes where they become more geo-effective. During solar minimum, it has been shown that CH can be long-lasting on the solar surface up to 7–27 solar rotations resulting in the recurrence of high-speed streams and geomagnetic disturbances (ABRAMENKO et al., 2010).

Figure 2.6 shows an example of a low latitude CH observed by the STEREO-B spacecraft EUVI emission and MHD simulation on 9 July 2008 during deep solar minimum. The CH boundaries, magnetic field lines, and emissions are shown. The open field regions in the model which are the dark black areas agree quite well with the STEREO observations.

Figure 2.6 - Left panel: CH boundaries and magnetic field lines from an MHD model of the solar corona prior to the 2008 August 1 solar eclipse. The black regions shown on the surface are open-field regions computed from the model; the grey areas are regions of closed magnetic field lines. Closed magnetic field lines are colored blue and open field lines are red. Middle panel: simulated STEREO EUVI 195 Å emission from the MHD model and observed EUV 195 Å emission from the STEREO-B spacecraft on 2008 July 9 (right panel). CHs are characterized by open field lines.

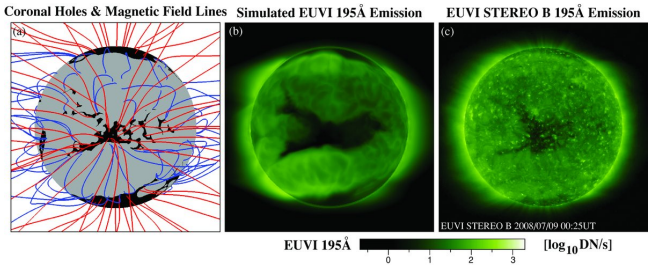

SOURCE: Abramenko et al. (2010).

2.1.6 Corotating interaction regions

The open configuration of the magnetic field in CHs allows the solar wind to escape (KRIEGER et al., 1973), referred to as a high-speed solar wind stream (HSSWS) with solar wind speed, $v_{sw} > 400kms$. They can interact with the slow-moving solar wind creating a compression region that rotates with the sun called a Corotating Interaction Region (TSURUTANI et al., 2006), periodically impacting the Geospace despite extremely quiet conditions in solar activity (ABRAMENKO et al., 2010). The fast-moving solar wind from coronal holes has periodicity constituting the sub-harmonics of the solar rotation period (5, 7, 9 and 13.5-day) (EMERY et al., 2011). A CIR is characterized by an increase in the IMF magnitude and proton density created by increased ram pressure on the magnetosphere detected as an increase in the horizontal component of ground magnetometers (TSURUTANI et al., 2006) during the initial phase (IP) (HARGREAVES, 1992). CIRs can cause recurring moderate (–100nT $\leq$ Dst $\leq$ –50nT) to weak (–50nT $\leq$ Dst $\leq$ –25nT) storms (TSURUTANI et al., 2006; CORREIA et al., 2018).

Figure 2.7 - The formation of a CIR. Interaction of a steady, localized stream of high-speed plasma with the slower ambient solar wind. (b) High-speed plasma from a solar flare driving an interplanetary shock. The ejected plasma contains an ordered magnetic field, but the magnetic field is turbulent between the shock and the ejecta.

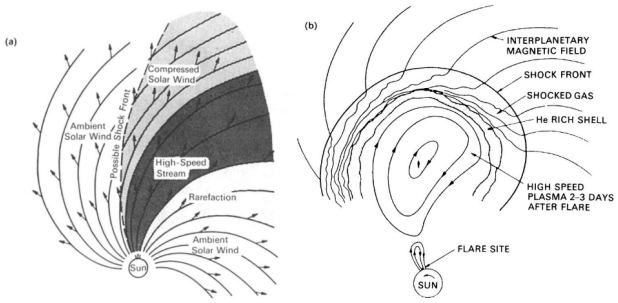

SOURCE: Hargreaves (1992).

Figure 2.7(a) illustrates the formation of a CIR when fast-moving solar wind encounters slow-moving solar wind, causing compression in the magnetic field and plasma (HARGREAVES, 1992) and Figure 2.7(b) illustrates the structure of flare eruption.

Most CIR storms are weak to moderate in magnitude due to the highly oscillatory nature of IMF Bz (TSURUTANI et al., 1995; SOBRAL et al., 2001). HSSs emanating from long-lived CHs can cause geomagnetic disturbances that last from several days up to a full solar rotation period ($\sim$ 27 days) (TSURUTANI et al., 1995).

Geomagnetic storms are more frequent during periods of high solar activity as compared to low solar activity (GRANDIN et al., 2019). These storms are usually due to Coronal Mass Ejections (CMEs) associated with solar flares which emanate from active regions on the solar chromosphere and produce more intense storms. At solar maximum, 50% of the geomagnetic storms are caused by CMEs compared to only 30% during solar minimum (RICHARDSON et al., 2000). CIRs on the other hand account for $\sim$ 70 % of the geomagnetic activity storms outside solar maximum(TSURUTANI et al., 2006). Figure 2.8 shows the annual number of detected CIR/HSS events with a maximum velocity of solar wind $V_{sw} \geq 500 km/s$. The sunspot number is overlayed on top to show the solar activity from the descending phase of Cycle 23 to 24 (GRANDIN et al., 2019). The curves indicate the rising phase (red), solar maximum (green), early declining phase (blue), and late declining phase (black). It is evident that most CIRs occur during the descending phase. Thus CIRs cause the majority of geomagnetic storms during the descending phase and solar minimum (GONZALEZ et al., 1994; TSURUTANI et al., 2006; GRANDIN et al., 2019).

Figure 2.8 - Yearly distribution of HSS events detected with the method using the criterion $V_{max} \geq 500$ km/s. Line plot: Monthly sunspot number. The colors indicate the ascending phase (red), solar maximum (green), early declining phase (blue) and late declining phase (black) of solar cycles. The line plot shows the monthly sunspot number.

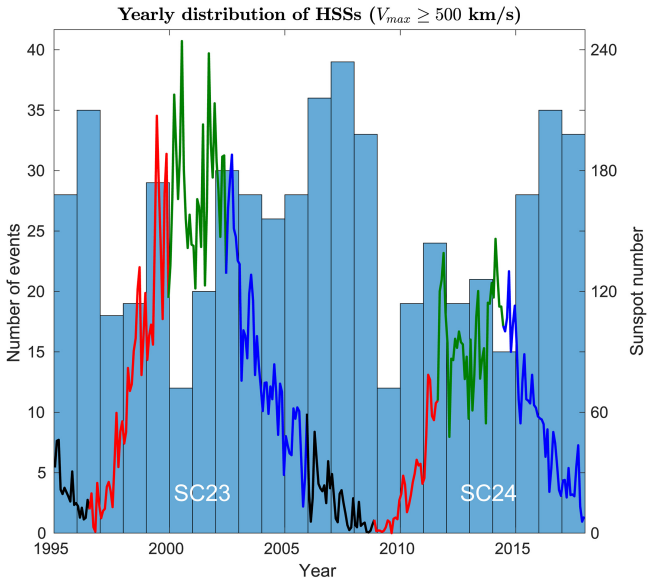

SOURCE: Grandin et al. (2019).

There are also several key differences between geomagnetic storms caused by CMEs and by CIRs. Figure 2.9 illustrates the typical features of each according to the Dst index. In general, CMEs are characterized by a sudden impulse (SIs) shown by a positive peak in the Dst due to an increase in the near-equatorial magnetic field. The abrupt jumps are caused by sudden enhancement of ram pressure impinging upon the magnetosphere (TSURUTANI et al., 2006) on the other hand typically do not have a SI (ASTAFYEVA et al., 2020). During the main phase CIR-driven there are oscillations in the Dst (TSURUTANI et al., 2006). It can be seen that CIR-driven storms have longer recovery phase than CMEs, lasting for up to several days (TSURUTANI et al., 2006).

Further, ionospheric variability during the descending phase and solar minimum is strongly influenced by HSS/CIRs (VERKHOGLYADOVA et al., 2011; CANDIDO et al., 2018). Candido et al. (2018) studied the response of TEC in the Brazilian equatorial and low latitude sector to HSS during SC23 minimum. Using wavelet spectral analysis, they found periodicity in TEC which are sub-harmonics of solar

Figure 2.9 - An example of (a) a CME-driven storm during 17–20 March 2015 and (b) a CIR-driven storm from 02–12 January 2008 measured by Dst index. Both storms are characterized by initial(IP), main(MP) and recovery phases (RP).

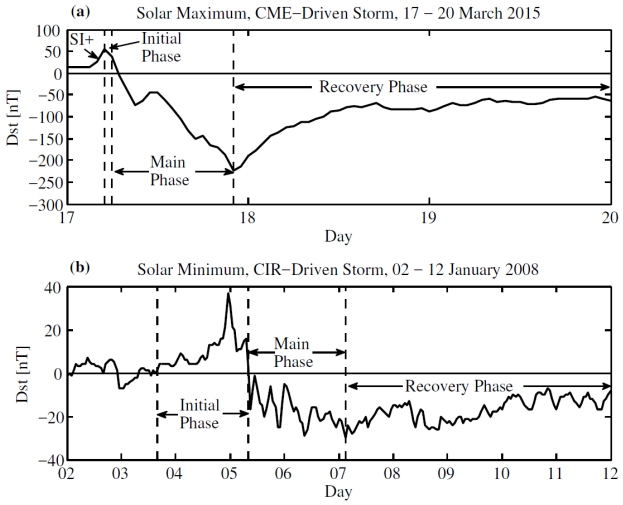

SOURCE: Matamba (2017).

rotation (27, 16, 13.5, 9, 7 and 5 days) which were related to that of solar wind parameters v_{sw} and IMF B_z. This demonstrates the effect of PPEFs during HSS/CIR events, which are also responsible for variations in TEC (VERKHOGLYADOVA et al., 2011; LIU et al., 2012; CANDIDO et al., 2018). Lei et al. (2008) reported similar periodicity in TEC while Liu et al. (2012) reported complex, 9-day periodicity in the h_mF_2 and f_oF_2 over South America during SC23 minimum. Since the periods are also sub-harmonics of solar rotation, there is a clear influence of HSS on the ionosphere through the injection of energy into the magnetosphere (LEI et al., 2008; LIU et al., 2012; CANDIDO et al., 2018).

2.2 Sun-Earth interactions

Sun-Earth interactions can drastically affect the magnetosphere-ionosphere-thermosphere system causing a variety of physical phenomena, including geomagnetic storms and ionospheric storms for example (ABREU et al., 2017). The interaction is driven by several processes originating from the sun mainly through CMEs and HSSWS/CIR. X-rays from solar flares as well as visible have the shortest arrival times reaching the Earth from the Sun in only 8 minutes. Magnetic clouds or CMEs travel more slowly reaching Earth in 3 to 4 days similar to the ambient solar wind.

Figure 2.10 - Ionosphere-Thermosphere-Mesosphere coupling processes.

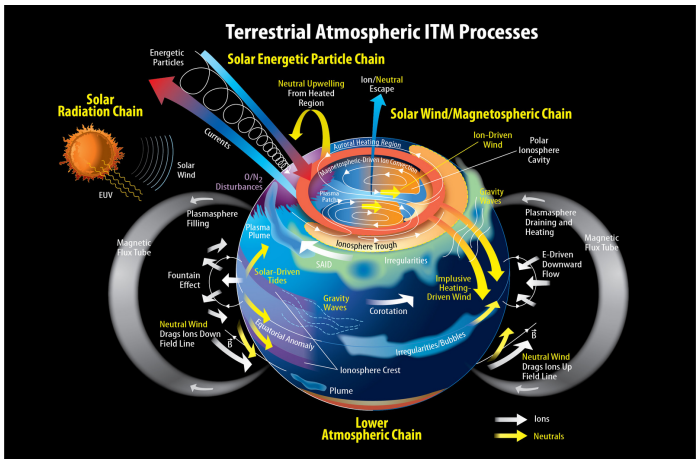

SOURCE: NASA (2021b).

The Sun-Earth system is a complex one that involves coupling between the Solar wind, magnetosphere, ionosphere, and thermosphere. Figure 2.10 summarizes the main physical processes in the MIT. The three main chains of interrelated processes that occur at low, mid, and high latitudes are shown. During quiet time, the physical processes at each latitude sector are separate from the others. However, under geomagnetically disturbed periods there is the coupling of the TI from high to low latitude resulting in the injection of energy from the solar wind into the magnetosphere (ASTAFYEVA et al., 2015). This occurs through particle penetration, and disturbed winds caused by auroral heating (ASTAFYEVA et al., 2015). Equatorward winds cause changes in the thermospheric composition ratio [O]/[N2] that result in ionospheric storms at low-mid latitudes. Currents flow from the magnetosphere into the ionosphere while ions can escape from high latitudes. The Interplanetary Electric Field can penetrate to equatorial and low latitudes causing ionospheric storms. The Disturbance Dynamo Electric Fields are formed by the disturbance winds formed at high latitudes (BLANC; RICHMOND, 1980; FEJER, 2011). Upwelling due to the expansion of the thermosphere due to heating can cause negative ionospheric storms. Gravity waves caused by auroral heating cause the transfer of energy and momentum in the MLT region. Large- and Medium scale Travelling Ionospheric Disturbances (LSTIDs & MSTIDs) caused by enhanced convection propagate from high (middle) latitude and are detected as oscillations in the F layer height (JONAH et al., 2016). It also was observed that the main phases of geomagnetic storms trigger post-sunset

equatorial plasma bubbles while the recovery phases of geomagnetic storms have the suppression effect of storms on equatorial plasma bubble irregularities (PAULA et al., 2019a). This space weather forecasting is even more complex making it difficult to model ionospheric response.

3 IONOSPHERE FORMATION AND COMPOSITION

The Earth's ionosphere is a region of the upper atmosphere which is sufficiently ionized to interact with electromagnetic waves (RISHBETH, 1971). The ionosphere is formed primarily by the absorption of radiation by the neutral atmosphere (BANKS; KOCKARTS, 1973). Figure 3.1 shows the atmospheric temperature and plasma density profile for mid-latitudes.

Figure 3.1 - Typical profile of ionospheric temperature and electron density at mid-latitudes.

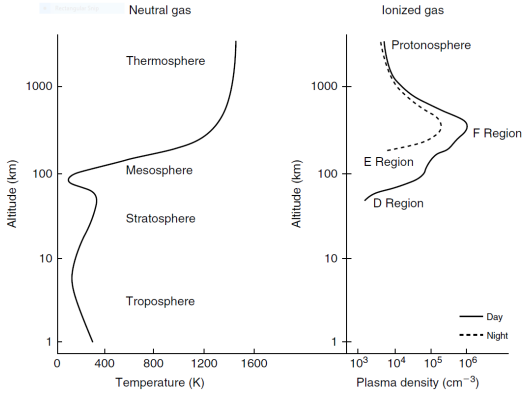

SOURCE: Kelley (2009).

3.1 D region

The D region is located approximately 50 km–90 km above the Earth's surface. The density of the atmosphere is very high in the lower atmosphere hence recombination processes dominate over transport and diffusion. The collision frequency between ions and neutrals is much higher than the gyrofrequency which means the effect of the magnetic field is negligible in this region. The concentration of plasma is determined by local production and loss processes because the lifetimes of transport processes are much longer than the rate of recombination (BANKS; KOCKARTS, 1973). The D layer also has the least density and disappears rapidly after sunset due to recombination processes as compared to the F layer which is present after sunset (HANSON; PATTERSON, 1964; BANKS; KOCKARTS, 1973).

3.2 E region

The E region is located approximately 90–150 km in altitude. The rate of recombination is less than that of the D region. In the E region, the plasma can drift across the field lines leading to the formation of electric fields (BANKS; KOCKARTS, 1973). The E region has the highest conductivity and is responsible for the majority of the E and F region dynamo during daytime (FORBES, 1981). At the magnetic equator, an intense current called the *Equatorial Electrojet* flows during daytime forming two bands North and South of the magnetic equator due to the enhancement in the Cowling Conductivity (FORBES, 1981).

3.3 F region

The F layer is divided into F1 and F2 layers. The peak of the ionosphere density occurs in the F2 layer at an altitude of approximately 250–350 km (RISHBETH; EDWARDS, 1989). However, the F layer peak height changes depending on local conditions such as thermospheric winds and electric fields (ABDU et al., 2009). In the F layer transport processes and diffusion are dominant because their lifetimes are much longer than that of local production and recombination. The gyrofrequency is much greater than the collision frequency and hence the magnetic field has more influence on the motion of the ions through drift (KELLEY, 2009). The F layer can be present at nighttime due to the effect of meridional winds which push up the F layer upward along the magnetic field lines to higher altitudes where the rate of recombination is lower (HANSON; PATTERSON, 1964). An additional layer, the F3 layer, appears at an altitude above the F2 layer and has similar characteristics to that of the F1 and F2 layers during daytime (BALAN et al., 1997). It has higher peak electron density than the F2 layer and occurs during both geomagnetically disturbed and quiet periods because of a sharp increase in the fountain effect which causes F2 layer uplift to higher altitudes (PAZNUKHOV et al., 2007). Thermospheric winds that flow towards the equator can also cause the formation of the F3 layer (BALAN et al., 1997).

3.4 The equatorial ionosphere

The objective of this section is to review the electrodynamic processes of the equatorial ionosphere that affect transionospheric propagation as well as their variation with solar cycle and geomagnetic activity. Lastly, the variation of these processes with the solar cycle and the effect of geomagnetic storms is discussed. The equatorial ionosphere is located $\pm 15°$ from the magnetic equator within the low latitude region.

The behavior of the equatorial ionosphere is quite peculiar because of the horizontal inclination of the magnetic field (ABDU, 1997). As a result, several phenomena occur some of which interfere with the propagation of electromagnetic waves. These include among others the Equatorial Electrojet, Equatorial Ionization Anomaly, and Plasma Bubbles.

3.4.1 The E Region dynamo and equatorial electrojet

The E region dynamo is driven by atmospheric tides (KELLEY, 2009). Solar tides are caused by the differential solar heating of the atmosphere which creates pressure gradients. The tides have a diurnal and semi-diurnal period related to the Earth's rotation. Lunar tides are caused by the gravitational action of the moon. The mechanism of formation of the E region dynamo is shown in Figure 3.2. (KELLEY, 2009).

Figure 3.2 - The equatorial electrojet in slab geometry.

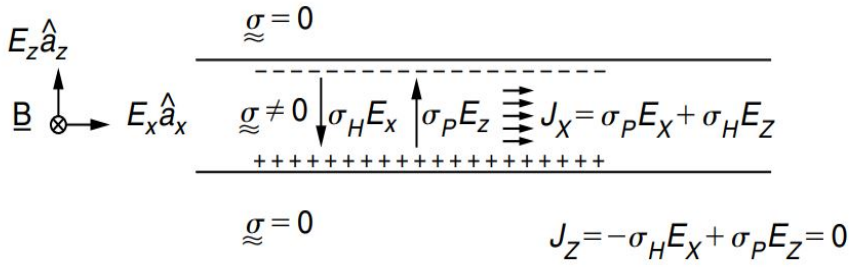

The figure shows an eastward zonal current J_x, the sum of the zonal Pedersen and Hall currents with the respective Pedersen and Hall conductivities. There is charge accumulation at the boundaries due to regions of low conductivity $\sigma = o$ hence $J_z = 0$.

SOURCE: Kelley (2009).

Considering a thin slab geometry of the E layer with a uniform magnetic field **B** acting normal to the surface, and assuming that the conductivity above and below the layer is negligible. The presence of an Eastward wind causes the separation of heavier ions from the lighter electrons which induces an Eastward electric field E_x. This electric field drives a Pedersen current. A current begins to flow vertically downwards due to the eastward electric field and the magnetic field, called the

Hall current. The current continues to flow until the charges accumulate at the boundary due to zero conductivity (RISHBETH; GARRIOTT, 1969). This creates a polarization electric field E_z which points in the direction of the $\hat{a_z}$ unit vector (KELLEY, 2009).

The current in the vertical direction is given by ;

$$J_z = \sigma_p E_z - \sigma_H E_x = 0, \tag{3.1}$$

where ;

$$E_z = \frac{\sigma_H}{\sigma_p} E_x \tag{3.2}$$

The zonal current is given by the vector sum of all the currents;

$$J_x = \sigma_p E_x + \sigma_H E_z, \tag{3.3}$$

From Equation 3.2 the zonal current can be re-written as

$$J_x = \sigma_p E_x + \sigma_H \frac{\sigma_H}{\sigma_p} E_x, \tag{3.4}$$

$$J_x = \sigma_p E_x \Big[1 + \Big(\frac{\sigma_H}{\sigma_p}\Big)^2\Big], \tag{3.5}$$

$$J_x = \sigma_c E_x, \tag{3.6}$$

Where σ_c is the *Cowling conductivity*. It is clear that there is an intensification in the zonal conductivity by a large factor (KELLEY, 2009). This results in the flow of large currents near the magnetic equator during the day known as the *Equatorial Electrojet*. The equatorial electrojet is part of a system of solar quiet, *Sq*, currents (MATSUSHITA, 1969). This system of currents has a diurnal variation and with a daily peak at noon which is located at 90 and 120 km in altitude according to Matsushita (1969). These currents can be detected by ground magnetometers since horizontal currents induce vertical magnetic fields. The global system of Sq currents is shown in Figure 3.3. It can be observed that the magnitude of the currents is highest at the equator and decreases with latitude.

Figure 3.3 - Average contours of the vertical magnetic field in nT due to the Sq system measured during the International Geophysical Year.

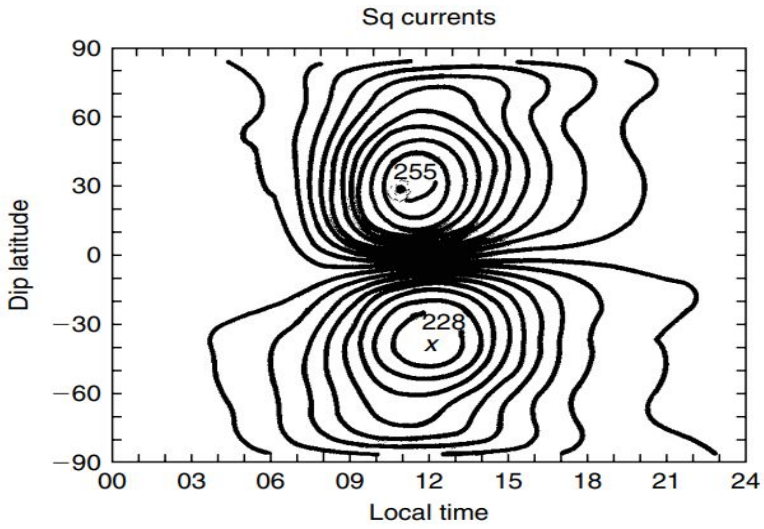

SOURCE: Matsushita (1969).

The intensity of the Sq also varies with the season of the year and solar activity. The magnitude is higher in the summer hemisphere than in the winter hemisphere (MATSUSHITA, 1969). The intensity of Sq currents is also minimum in the June solstice (winter) due to a lower electron density owing to reduced solar flux (PARK et al., 2010). It is fairly even between the hemispheres during equinox as shown in Figure 3.4. It was also shown by Sharma et al. (2011) and Takahashi et al. (2016) that the equatorial electrojet can be enhanced during periods of magnetically disturbed conditions and consequently an uplift of the F-layer and promoting the development of the EIA.

Figure 3.4 - Seasonal external Sq current systems. Clockwise from left; December solstice, equinox, yearly average and the June solstice during the International Geophysical Year (1958).

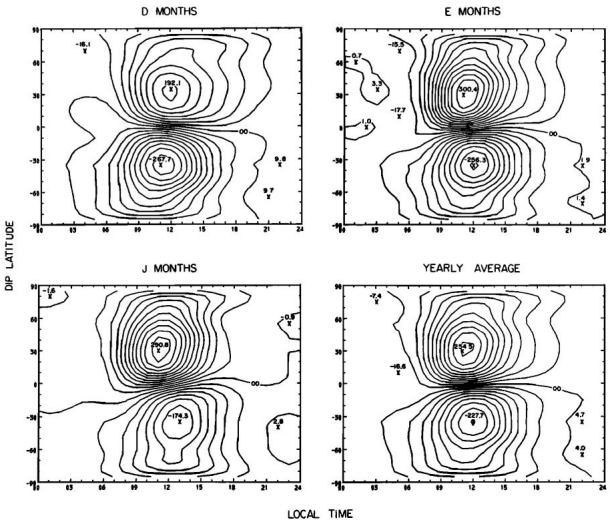

The current intensity between two consecutive lines is the numbers near the cross marks indicate the total current intensities of vortices in units of 10^3 Ampere.

SOURCE: Matsushita (1969).

3.4.2 F region dynamo

The F region dynamo is driven by eastward neutral winds in the thermosphere. The winds are caused by the absorption of solar radiation by the neutral atmosphere and are called thermospheric winds. The wind direction is Eastward during the day (KELLEY, 2009). Figure 3.5 illustrates the formation of the F region dynamo in slab geometry. Assuming that the F layer is a thin conductive layer with no conductivity in the regions outside the layer and a uniform magnetic field acting normal to the equatorial plane as shown (KELLEY, 2009).

Figure 3.5 - Electrodynamics of the equatorial F region in which the density and conductivity profiles are modeled using slab geometry, subject to a constant zonal eastward neutral wind.

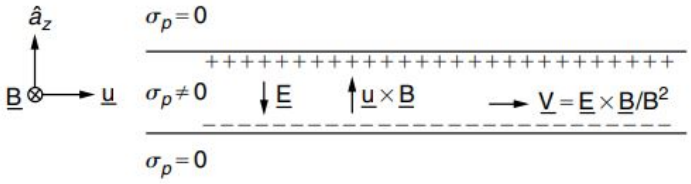

SOURCE: Kelley (2009).

The action of the $U \times B$ drift caused by the wind and the magnetic field causes separation between the ions and electrons and a current begins to flow upwards in the direction of the unit vector $\hat{a_z}$. Since the divergence of the current is zero a polarisation electric field E begins to develop inside the F layer. An $E \times B$ drift created by the electric field and the magnetic causes the plasma to drift zonally along with the wind (KELLEY, 2009). The drift velocity of the plasma is given by;

$$v = \frac{\vec{E} \times \vec{B}}{B^2}, \tag{3.7}$$

Where v is the drift velocity;
E is the Electric field;
B is the Earth's Magnetic Field. The E region conductivity is mapped to the F region along the field lines. This causes the F region dynamo to be only present after sunset because during the day it is short-circuited by the E region conductivity (KELLEY, 2009).

3.4.3 The prereversal enhancement

The post-sunset prereversal (PRE) enhancement occurs when the zonal eastward electric field reaches a sharp peak sunset before reversing direction. This results in F region plasma being driven to higher altitudes where the rate of recombination is lower (KELLEY, 2009). This effect can be observed in the vertical drift velocity which is also enhanced due to the increase in the $E \times B$. The magnitude of the drift can be measured using the incoherent scatter radar, one of which is at the Jicamarca Radio Observatory close to the magnetic equator (KELLEY, 2009). The

vertical drift can also be inferred from ionosonde measurements of the rate of change of the F layer true heights (REINISCH, 1996) and F-layer peak height Abdu et al. (2009). Figure 3.6 shows a sharp increase in the vertical drift velocity. The vertical drift is upwards during the day and downward at night as illustrated in the figure while the zonal drift is westward during the day and eastward at night (KELLEY et al., 2003).

Figure 3.6 - Calculated vertical ion drift velocities for several driving wind components.

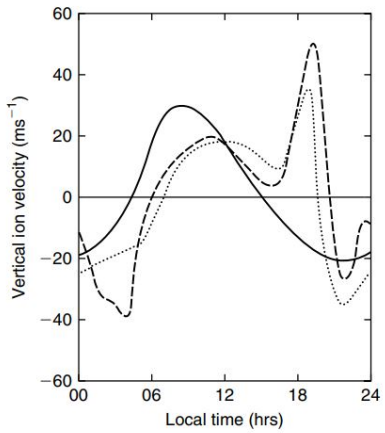

The solid line includes only the tidal-driven E region dynamo, while the dashed line includes the F-region dynamo as well. Typical measured vertical plasma drifts are indicated by the dotted line.

SOURCE: Kelley (2009).

Figure 3.7 shows a model of the E and F region with the dayside and nightside separated by the solar terminator. The vertical plane is the equatorial plane and the field line, **B** is shown. The F region dynamo is driven by an eastward wind,**U**. The vertical electric field E_Z formed by the F-region is downwards on both the dayside and the nightside as shown. However, the magnitude of the Electric field is greater on the night side than on the dayside because on the dayside it is shorted by the E region (KELLEY, 2009). This electric field is then mapped to the equator along the magnetic field lines to an electric field E_θ. This electric field drives a westward hall current but since there is no conductivity on the nightside there is charge accumulation at the terminator. An eastward polarization electric field, E_ϕ, is formed in order to cancel out this current. This electric field is large because of

high hall conductivity (KELLEY, 2009).

Figure 3.7 - Simplified model of the F-region prereversal enhancement driven by a uniform F-region wind, $\underline{\mathbf{U}}$.

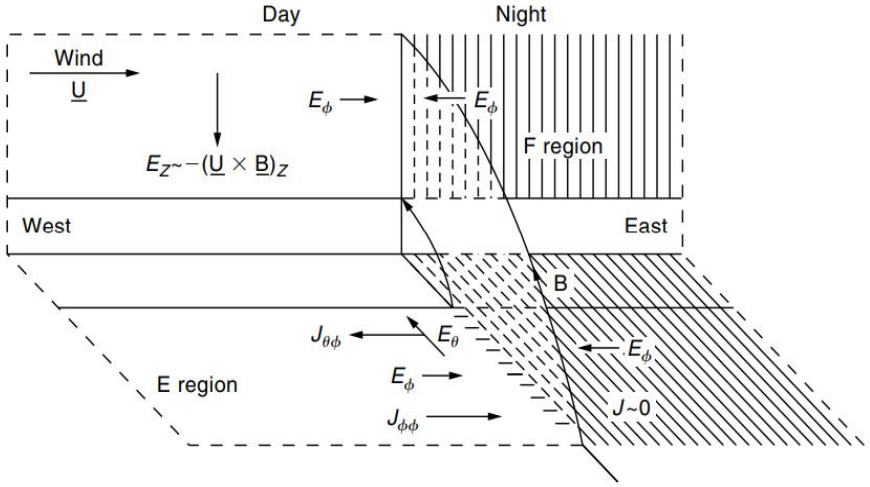

The electric field E_z is mapped to the equator as E_θ. A hall current $J_\theta\phi$ flows westward and is cancelled out by $J_\phi\phi$. No current flows on the nightside and hence $J = 0$.

SOURCE: Farley et al. (1986).

This electric field is mapped back to the F region from the equator along the magnetic field lines leading to an enhancement in the zonal electric field (FARLEY et al., 1986). The prereversal enhancement is an important factor in the formation of equatorial plasma bubbles (ABDU et al., 2009). The vertical drifts vary with solar activity and season of the year (ABDU et al., 1981)

3.4.4 Equatorial ionization anomaly

The equatorial ionization anomaly is formed by the fountain effect caused by the action of the electric field and the geomagnetic field which results in plasma drifting vertically upwards to higher altitudes where the rate of recombination is low (KELLEY, 2009). The plasma diffuses downwards along the field lines to low latitudes under the action of gravity and the pressure gradient force. This causes the ionisation at low latitudes to be higher than that at the equator even though there is more incident radiation (BANKS; KOCKARTS, 1973).

Figure 3.8 - The Equatorial Ionisation Anomaly.

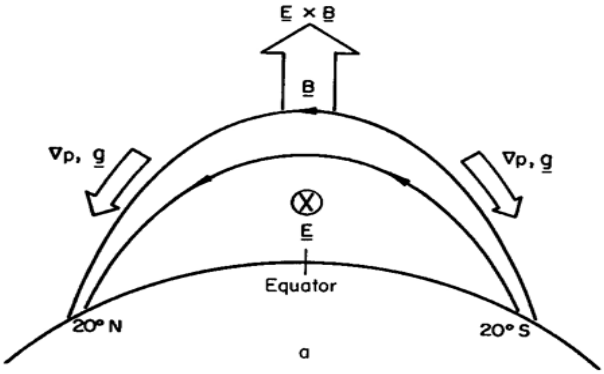

The $E \times B$ drift is vertically upwards while plasma diffuses downward due to gravity, $\underline{g}$ and the pressure gradient force, ∇p.

SOURCE: Rezende et al. (2007).

The mechanism for the formation of the EIA is shown in Figure 3.8. An example of the EIA using data from the Sheffield University Plasmasphere Ionosphere Model, (SUPIM) model is illustrated in Figure 3.9. The crests can be clearly observed on either side of the magnetic equator at a latitude of $\pm 20°$. In this case, the anomaly is symmetrical about the magnetic equator because there was no consideration of neutral winds which can create asymmetries between the two hemispheres (ABDU et al., 2009).

3.4.5 Equatorial plasma bubbles

The horizontal inclination of the magnetic field over the Brazilian equatorial ionosphere leads to several unique phenomena among them post-sunset irregularities. Equatorial plasma bubble irregularities are one of the major phenomena in Space Weather that have a high occurrence at equatorial and low latitudes. These are large-scale, field-aligned depletions in plasma density that develop at the magnetic equator after sunset (KELLEY, 2009). Plasma bubbles appear as dark bands which show regions of low plasma density. The large field of view of the All-sky imager allows for the observation of large-scale structures such as EPB (PIMENTA et al., 2001). Airglow images are important in the study of plasma bubbles because they show the temporal and spatial variation of the bubbles as they develop (SOBRAL et al., 2002). Figure 3.10 shows an example of plasma bubbles observed under three levels of solar activity; High Solar Activity (HSA), Moderate Solar Activity or descending

Figure 3.9 - Altitude-latitude map of electron density, $N_e(10^5 cm^{-3})$ at 13 : 00 LT modelled by SUPIM for magnetically quiet $Ap = 4$ conditions at high solar activity, Day 303, $F10.7 = 268$) in Jicamarca; longitude 283°E with $E \times B$ drift only around noon and no neutral wind. The positive latitude is north of the magnetic equator.

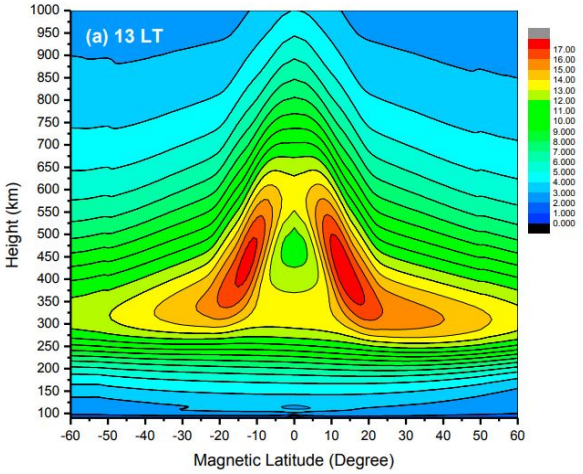

SOURCE: Balan et al. (2013).

phase (MSA) and Low Solar Activity (LSA) in a study by (AGYEI-YEBOAH et al., 2019). The images are for the OI 630 nm emission line due to atomic Oxygen O^+ which is produced at the F-layer bottom side at a peak of about $250 - 300$ km in altitude (PIMENTA et al., 2001). EPB occurrence rates are highest during HSA followed by MSA while LSA has the lowest frequency (SOBRAL et al., 2002; AGYEI-YEBOAH et al., 2019). Figure 3.11 shows another example of EPBs that were observed using a 30 MHz radar located at Gadanki, India. The EPBs reached a maximum height of over 700 km. The radar has scanning capability in a plane perpendicular to the geomagnetic field and an interferometry/imaging system to study drifts and spatial distribution of large- and small-scale irregularities. Observations of F region irregularities with this radar show bottom-type, bottom-side, and plume structures.

They are formed under the Rayleigh-Taylor (RT) instability as a result of large density gradients which occur near sunset (ABDU et al., 1981; ABDU, 2001). The pre-reversal enhancement in the zonal electric field enhances the $E \times B$ drift driving plasma up to higher altitudes which creates favorable conditions for the RT

Figure 3.10 - OI 630nm airglow images, recorded at Cariri, showing EPB events during high solar activity (HSA), medium solar activity (MSA) and low solar activity (LSA).

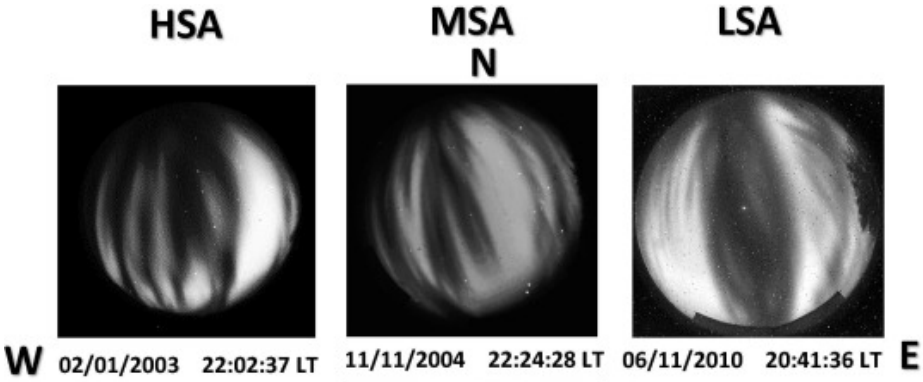

SOURCE: Agyei-Yeboah et al. (2019).

instability (ABDU, 2001). Figure 3.12 shows the mechanism in which the plasma irregularities or bubbles grow. Near sunset there are steep plasma density gradients (ABDU et al., 1981) which creates instability at the F layer bottomside (KELLEY, 2009). A uniform magnetic field, **B** acts normally to the equatorial plane perpendicular to the gravitational acceleration, **g**. Assuming that the rate of collisions within the plasma is negligible such that the magnetic field dominates the motion; and given a small initial perturbation at the bottomside, a net current begins to flow perpendicular to the gravity vector (KELLEY, 2009). The magnitude of the current depends on the plasma density, n, mass, gravity, and magnetic field given as;

$$|\hat{J}_x| = \frac{nMg}{B} \tag{3.8}$$

However, because the current cannot flow across the boundary charges begin to accumulate at the edges of the boundaries so that a small perturbation electric field is formed (KELLEY, 2009). The electric field is in both directions as shown in the figure. These electric fields cause $E \times B$ to upward for low-density plasma and negative $E \times B$ for high-density plasma. This causes the instability to grow in size (KELLEY, 2009). The bubbles first develop vertically upwards due to the drift until they reach the equatorial apex height. This is the maximum height to which a plasma can attain above the magnetic equator before diffusion along the field lines reaching low latitudes (ABDU et al., 1983). EPBs generally drift Eastward during geomagnetically quiet periods driven by vertical electric fields. However, the direction can be reversed during geomagnetic storms (MARTINIS et al., 2005).

Figure 3.11 - Examples of plasma bubbles observed by the Gadanki radar in India on 07 February 2005. RTI maps obtained from MST radar observations show that EPBs developed on the bottom side of the equatorial F region after sunset.

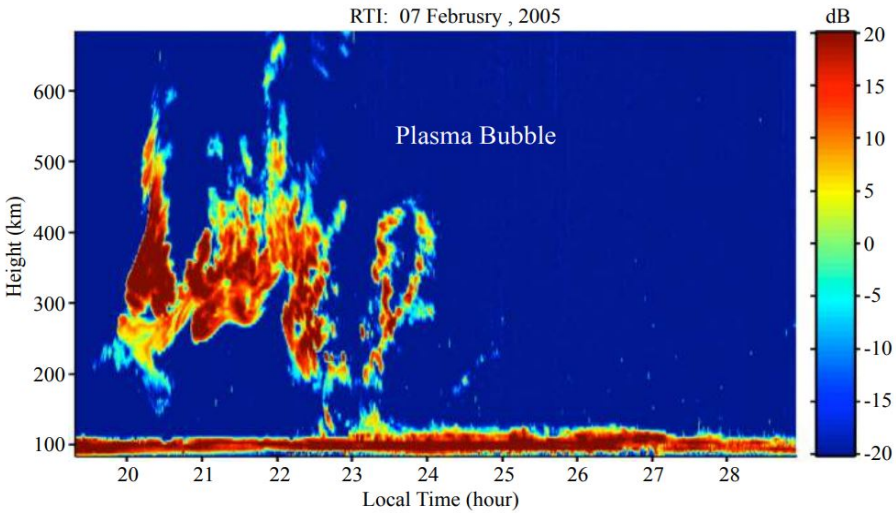

SOURCE: Balan et al. (2018).

To illustrate the importance of the PRE in the formation of EPBs, Figure 3.13 shows the vertical drift velocity for three stations; Campo Grande(CG), dip: $-22.19°$; Boa Vista (BV), dip: $22°$ and Cachimbo (CX), dip: $-4.15°$. It can be seen that the drift is highest near the magnetic equator and is fairly similar for the conjugate stations. In this study to ascertain the relationship between vertical drift and Spread F occurrence, the magnitude of the drift was plotted according to Spread F occurrence and non-occurrence together with the ΣK_p, the sum of the planetary index, Kp, values.

Figure 3.12 - Schematic diagram of the Rayleigh-Taylor instability in equatorial geometry.

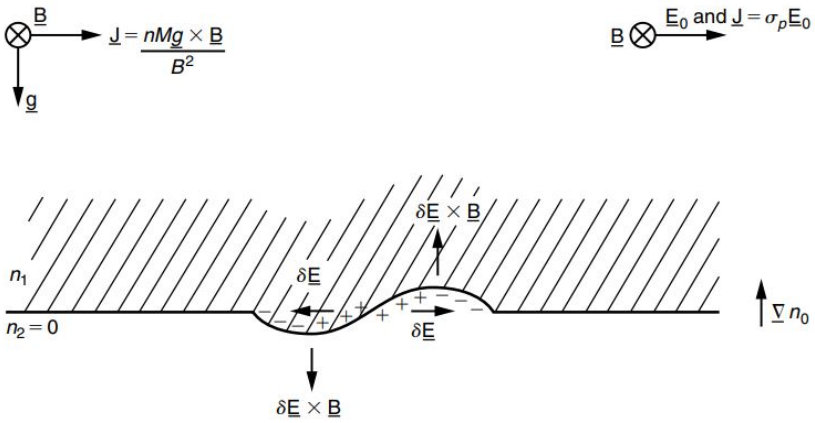

SOURCE: Kelley (2009).

Figure 3.13 - Mean vertical drift velocities over the three COPEX sites are plotted for different groups of days: (a) for the cases of early spread F occurrence (at or before 2000 LT) over Cachoeira Paulista; (b) for the group of days when SF occurred at and before 2200 LT over CP; (c) for the group of days when SF did not occur before midnight over Cachoeira Paulista; and (d) for the group of days when SF did not occur over Campo Grande and CP. (ΣKp is the daily sum of the 3-hourly Kp values representing its mean value for the days considered).

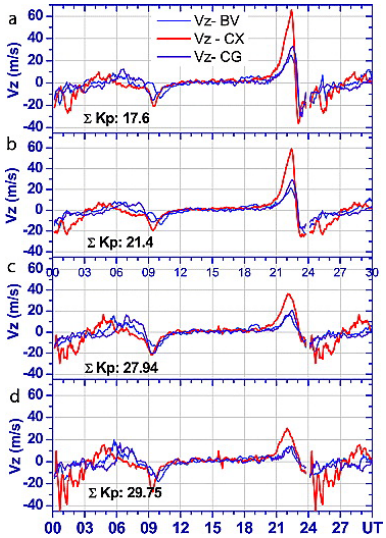

Station names are BV, Boa Vista; CX, Cachimbo; and CG, Campo Grande. In the horizontal axis, the LT exceeding 24 hr corresponds to a new day.

SOURCE: Abdu et al. (2009).

The magnitude of the drift depends on factors such as time of the day, solar cycle, season, and geomagnetic activity (FEJER, 2011). It was found that for peak vertical drifts below a certain threshold, no Spread F was observed (ABDU et al., 2009). However, for higher values of drift the Spread F not only occurred earlier as compared to days with lower drift, but it also reached lower latitudes as far as Cachoiera Paulista,–16° magnetic latitude (ABDU et al., 2009).

EPB formation is a complex non-linear process that depends on multiple factors such as the background plasma density, magnitude of $E \times B$ drift, magnetic declination, thermospheric winds, planetary waves, tides, and even geomagnetic storms (ABDU, 2001; ABDU et al., 2009; HUBA; LIU, 2020). Some factors play a more important role than others such as the $E \times B$ drift and seeding mechanism (ABDU et al., 2009; FEJER, 2011). As a result, EPB occurrence is marked by high day-to-day variability (EASTES et al., 2019; AJITH et al., 2020) and hence predicting the occurrence remains a challenge. The presence of an initial perturbation or a seeding mechanism at the F layer bottom side near sunset is essential for the development of the instability (ABDU et al., 2009; RETTERER; RODDY, 2014; TAKAHASHI et al., 2018). Several studies reported that periodic large-scale wave structure (LSWS) (SINGH et al., 1997; ABDU et al., 2009; TAKAHASHI et al., 2016; TAKAHASHI et al., 2018) and Traveling ionospheric disturbances precede EPBs (TIDs) (TAKAHASHI et al., 2018; AA et al., 2020; AJITH et al., 2020). Attempts have been made to associate the occurrence of EPBs and TIDs in particular the relationship between the horizontal wavelength of MSIDs and the inter-bubble distance derived from airglow observations (TAKAHASHI et al., 2009) although recent findings show that the two are not always correlated (TAKAHASHI et al., 2018).

More recently, physics-based models of the ionosphere have been used to simulate plasma bubbles by introducing initial seed perturbations in the pre-and post-sunset ionosphere (HUBA; JOYCE, 2010) which highlighted the importance of atmospheric gravity waves in the seeding of the RT instability (HUBA; LIU, 2020). In addition, the detailed structure and spatiotemporal evolution of the seeding mechanisms are not well known (TAKAHASHI et al., 2018; AA et al., 2020). Plasma bubbles can also lead to the formation of successively smaller irregularities, the extent to which depends on the density gradients. Higher density gradients lead to the formation of irregularities with varying scale size (HAERENDEL et al., 1992). These irregularities can cause scintillation in the post-sunset sector (KINTNER et al., 2001).

3.4.6 Impact of ionosphere on trans-ionospheric propagation

The ionosphere can have a significant negative impact on the operation of GNSS through range delay as well as scattering (KNEPP; HAUSMAN, 2007; DAS et al., 2014) particularly at equatorial and low latitudes due to the horizontal inclination of the magnetic field (ABDU, 1997; PAULA et al., 2003). Radio waves are refracted as they propagate to the ionized medium causing signal delay, called ionospheric delay. This delay is proportional to the integral of the electron density from the satellite to the receiver and is used to obtain an important parameter called the Total Electron Content (TEC). This ionospheric delay can be as high as 21 m (80 TECU) at the zenith during high solar activity (RISHBETH; GARRIOTT, 1969). During the day there is the presence of the equatorial ionization anomaly and high density of ionization at low latitudes. Large spatial gradients in TEC at the crest cause large ionospheric range delays in GNSS positioning systems. In addition to ionospheric delay, the presence of irregularities in particular at low latitudes also introduces significant errors in the GNSS range measurements.

Post-sunset ionospheric irregularities can also significantly undermine the operation of GNSS-based systems by diminishing the quality of the signals that traverse the ionosphere by degrading the received signal amplitude causing a loss of lock between the satellite and the receiver (KLOBUCHAR, 2002; DAS et al., 2014). When a signal passes through irregularities it suffers rapid fluctuations in amplitude and phase called amplitude and phase scintillation respectively (MUELLA et al., 2013). In the L Band, amplitude scintillation is caused by irregularities up to tens of kilometers in size (ABDU, 2001). Irregularities in general are more intense over the crests of the ionization anomaly where there are higher density gradients in the post-sunset hours (BASU et al., 1999; PAULA et al., 2019a). The scintillation can be reflected on an Ionogram as *Spread-F* (ABDU et al., 1983) as illustrated in Figure 3.14. Two conjugate stations; Campo Grande, dip latitude 22.3 ° S, and Boa Vista, dip latitude 22° N, were used to investigate the development conditions for Spread F occurrence. It can be seen that Spread F occurrence coincided with the presence of plasma bubbles as seen in the ionogram. The effects of irregularities are more significant over the Brazilian low latitude where irregularities have a higher frequency of occurrence due to the large magnetic declination angle (ABDU et al., 1981; ABDU, 1997; PAULA et al., 2003).

The occurrence of scintillation has a seasonal dependence with the highest frequency during the local summer for Brazil and low frequency during winter (SOBRAL et

Figure 3.14 - Ionograms over Boa Vista and Campo Grande and the simultaneous all-sky images on the night of 9 October 2002 showing the presence of Spread F.

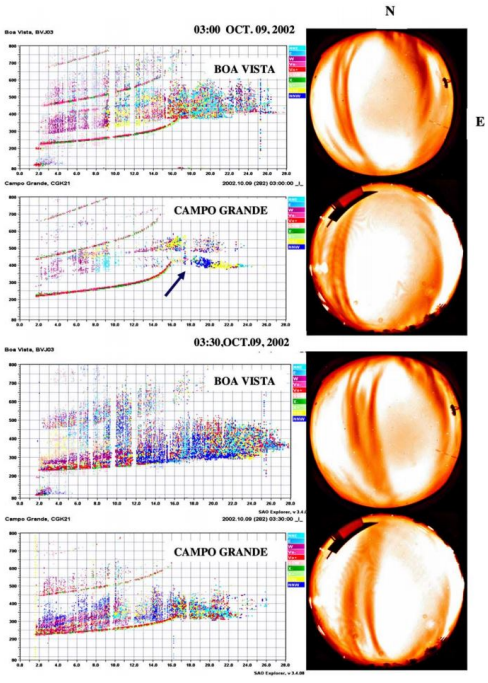

SOURCE: Abdu et al. (2009).

al., 2002; PAULA et al., 2003). In addition, there is a higher occurrence of scintillation during high solar activity compared to solar activity (SOBRAL et al., 2002; CORREIA et al., 2018). This is due to the increased solar flux that is responsible for the production of ionization (REZENDE et al., 2007). During higher solar activity there are high production rates due to increased solar flux (BANKS; KOCKARTS, 1973) such that the plasma density is higher compared to solar minimum (BANKS; KOCKARTS, 1973). The intensity of the scintillation at this station is usually higher than at equatorial stations since the station is located in the region of the EIA crest (PAULA et al., 2007).

Figure 3.15 shows the variation of scintillation for the period 1998–2014 a period over 2 solar cycles at Cachoeira Paulista: 22.7°S, 45° W a station located at the then southern crest of the anomaly. The mean monthly solar flux $F10.7$ was used to indicate solar activity. During quiet time, scintillation occurs from sunset to midnight after which they disappear but during solar maximum, the occurrence can extend to the post-sunrise sector (ABDU et al., 1983). The climatology of EPB/scintillation

has been studied by many researchers including Sobral et al. (2002), Paula et al. (2007), Correia et al. (2018). Figure 3.15 shows the percentage of occurrence of scintillation at São José dos Campos, dip latitude : 17.8°S. The climatology is controlled by the magnitude of the pre-reversal enhancement in the zonal electric field (ABDU et al., 1983).

Figure 3.15 - Scintillation percentage of occurrence from September 1997 to June 2002, at São José dos Campos, for 2 levels of scintillation indices as a function of local time and mean F10.7 cm solar flux index

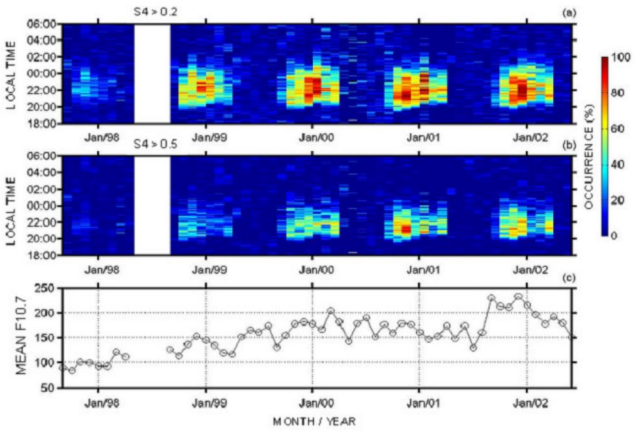

SOURCE: Paula et al. (2007).

Transequatorial winds are also responsible for the dynamics of the F region (BALAN et al., 2010). Winds have the effect of changing the F layer peak height by pushing plasma up along the field lines in the "upward" hemisphere while lowering it in the "downward" hemisphere (JYOTI et al., 2004; ABDU et al., 2009). This has the effect of promoting or suppressing the growth rate of plasma bubbles in either hemisphere. Abdu et al. (2009) showed that if the velocity of the wind is sufficiently high, it can inhibit plasma bubble development. The magnitude of the transequatorial wind has been determined by taking the difference in the h_mF_2 at conjugate locations (BITTENCOURT; SAHAI, 1978).

3.5 Travelling ionospheric disturbances

Travelling ionospheric disturbances (TIDs) are oscillations in the F layer plasma, with horizontal wavelengths ranging from hundreds of meters to thousands of kilo-

meters and velocity hundreds of meters per second (HINES, 1960; HUNSUCKER; HARGREAVES, 2002). TIDs are classified according to their wavelengths and periods. Medium-Scale traveling ionospheric disturbances, (MSTIDs) have wavelengths of 100-1000 km and periods in 15–60 minutes (HARGREAVES, 1992) and are generated by atmospheric processes (HINES, 1960) which lead to the formation of gravity waves such as tropospheric convection, windy climates, magnetosphere plasma precipitations in the polar ionosphere and many others (HARGREAVES, 1992). Gravity Waves with horizontal wavelengths of 400–600 km can propagate above 220 km before dissipating (VADAS, 2007). The propagation direction depends on the source region and the background winds in the lower atmosphere (HINES, 1960). MSTIDs are known to be associated with the occurrence of EPBs (TAKAHASHI et al., 2018). Over South America nighttime MSTIDs propagate to the northwest after sunset (FIGUEIREDO et al., 2018). A close relationship between the inter-bubble distance and the horizontal wavelength of MSTIDs was shown by Takahashi et al. (2009) while Takahashi et al. (2018) reported simultaneous observations of MSTIDs and EPBs during the March and September equinoxes.

3.6 Ionospheric response to geomagnetic storms

During geomagnetic storms, there are complex changes in the electrodynamics of the ionosphere through perturbation of electric fields and winds and cause large variations in the temporal and spatial response of the ionosphere (FEJER, 2011). A geomagnetic storm occurs when the Interplanetary Magnetic Field B_z component turns southward (GONZALEZ et al., 1994; PROLSS, 1995; LOEWE, 1997). The southward turning causes magnetic reconnection between the IMF and magnetosphere which results in the injection of vasts amounts of energy from the solar wind into the magnetosphere (HARGREAVES, 1992; PROLSS, 1995; FULLER-ROWELL et al., 1996). The coupling between the magnetosphere, and solar wind occurs through penetration of electric fields, charged particles and currents (PROLSS, 1995; GONZALEZ; PARKER, 2016).

A condition for the under-shielding PPEF is the sudden southward turning of IMF Bz (KELLEY et al., 2003). The PPEF is of eastward polarity during the day and reverses polarity after sunset whiles sudden northward turning is believed to result in an overshielding PPEF of opposite polarity to the undershielding PPEF (KELLEY et al., 1979). The PPEF is transient in nature, lasting from a few minutes to several hours (KELLEY et al., 1979) and appear instantaneously at mid to equatorial latitudes (KIKUCHI et al., 2000; SHARMA et al., 2011). At high lati-

tudes, there is Joule heating of the high-latitude atmosphere. This heating causes large pressure gradients which generate global winds that flow equatorward from the poles (BLANC; RICHMOND, 1980; PROLSS, 1995). The action of the wind and the Coriolis force forms the disturbance dynamo electric field (DDEF) (BLANC; RICHMOND, 1980) of westward polarity during the day. The disturbance dynamo is usually observed several hours to days after the storm onset (RICHMOND et al., 2003; FEJER, 2011). The$E \times B$ drift is largely responsible for the formation of the EIA during the day (KELLEY, 2009) while at sunset the PRE is a favorable condition for the formation of ionospheric irregularities (ABDU et al., 1981; SOBRAL et al., 2002). The response of the ionosphere to geomagnetic storms using TEC has been reported by many researchers including Becker-Guedes et al. (2007) ,Jonah et al. (2018),Candido et al. (2018), Takahashi et al. (2016), Balan et al. (2010), Astafyeva et al. (2015) and Abreu et al. (2010). TEC is an important parameter not only in GNSS applications but also in the study of the ionosphere (BIDAINE; WARNANT, 2009).

Further studies have also been made to investigate the effect of solar activity on the dynamics of the equatorial ionosphere during solar minimum such as Candido et al. (2018), Candido et al. (2011). An increase in the plasma density compared to quiet time is termed a *Positive ionospheric storm* (PS) (BALAN et al., 2010) on the other hand it may also decrease in what is termed a *Negative ionospheric storm* (DANILOV; MOROZOVA, 1985). Positive ionospheric storms have been attributed to undershielding PPEF associated with reconnection processes and auroral activity during the recovery phase of CIR-driven storms (CANDIDO et al., 2018; VERKHOGLYADOVA et al., 2011). The eastward Prompt-Penetration Electric Field (PPEF) greatly enhances the equatorial electric field causing positive storms at low latitude (KELLEY et al., 2003; BECKER-GUEDES et al., 2007; ABREU et al., 2010; MORO et al., 2021).

Fagundes et al. (2016) observed both positive and negative phases in the TEC over the Brazilian sector during a geomagnetic storm. The PPEF can enhance the nighttime ionization anomaly by increasing the magnitude of the $E \times B$ drift so that the vertical drift is enhanced which causes the poleward expansion to latitudes as far as $\pm 30^{\circ}$ from the magnetic equator (MANNUCCI et al., 2005; FEJER, 2011; VENKATESH et al., 2017; MORO et al., 2021). However, Yao et al. (2016), Balan et al. (2013), Balan et al. (2018) argued that the effect of the PPEF alone is not enough to cause such an intense positive storm effect and suggested that equatorward neutral winds are a more effective process than the PPEF. Figure 3.16 shows the

mechanism for the formation of the EIA due to the $E \times B$ drift.

Figure 3.16 - Sketches illustrating the effects of upward $E \times B$ drift on ionospheric plasma at the magnetic equator higher latitudes (b and c); the field line inclination is equal in b and c.

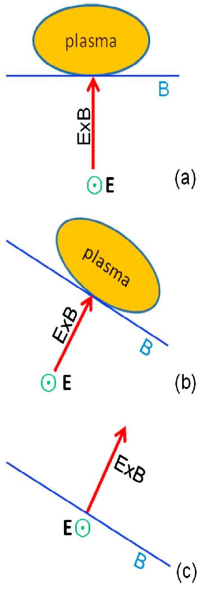

SOURCE: Balan et al. (2013).

Through this mechanism, the plasma is driven vertically upwards and eventually diffuses along the field lines to higher latitudes. However, at higher latitudes where the field lines have higher inclination, the drift is less effective because it has a higher downward component and as a result drives plasma down to lower altitudes through diffusion where the rate of recombination is higher. Transequatorial winds on the other hand inhibits the downward diffusion of plasma along the field and also drives plasma up to higher altitudes as far as 30° from the magnetic equator(BALAN et al., 2010; BALAN et al., 2013).

On the other hand, DDEF formed by high-latitude Joule heating (VERKHOGLYADOVA et al., 2011; LIU et al., 2012) inhibits the fountain effect by restricting the vertical drift of plasma and thus causing a decrease in the F-layer peak height weakening the EIA and causing NS at low latitudes (BLANC; RICHMOND, 1980; ASTAFYEVA et al., 2015). Rastogi and Klobuchar (1990), Sharma et al.

(2011) showed that the strength of ΔH is reduced when due to a counter-electrojet generated by a westward electric field which is observed through the weakening of the EIA compared to quiet time. Additionally, ionospheric storms are caused by changes in thermospheric neutral composition (DANILOV; MOROZOVA, 1985; BUONSANTO, 1999). Geomagnetic storms also cause disturbances in global circulation patterns and winds (DANILOV et al., 1994). The upwelling of the thermosphere causes the enhancement of Nitrogen concentration in the thermosphere (FULLER-ROWELL et al., 1996). This causes a reduction in the ratio of O/N2 concentration in the thermosphere causing the formation of negative storms (DANILOV et al., 1994; PROLSS, 1995; FULLER-ROWELL et al., 1996). Thus, positive (negative) storms are primarily explained by the increase (decrease) in the neutral composition ratio O/N2 leading to an enhancement (loss) in ionization (PROLSS, 1995; FULLER-ROWELL et al., 1996; MORO et al., 2021; CAI et al., 2021). Lastly, storm-induced equatorward neutral winds drive plasma up along the field lines to higher altitudes where the rate of recombination is lower causing positive storms (BALAN et al., 2010) while poleward winds can drive plasma to lower altitudes (ABDU et al., 2009), causing negative ionospheric storms (BUONSANTO, 1999; PROLSS, 1995). However, the effectiveness of geomagnetic storms depends on factors such as the dip latitude of the station, latitude and longitude, time of the day, the season of the year, and solar activity (ABDU, 1997; ABREU et al., 2010; FAGUNDES et al., 2016; JONAH et al., 2016).

TEC response over Brazil to the super geomagnetic storm of 15 May 2005 was investigated by Abreu et al. (2011). The stations were Belém (BELE), dip latitude (1.8°), which is close to the magnetic equator, Brasília (BRAZ), dip latitude (11.7°), which is a low-latitude station Presidente Prudente (UEPP), dip latitude (14.9°) and Porto Alegre (POAL), dip latitude (20.7°) close to the crest of the anomaly. The SSC began at 02:39 UT on 15 May after which the main phase began at 09:00UT. Figure 3.17 shows the geomagnetic indices, IMF, and solar wind parameters during the storm period.

Figure 3.17 - Variations of the solar wind, interplanetary magnetic field (IMF) parameters on 14-17 May 2005.

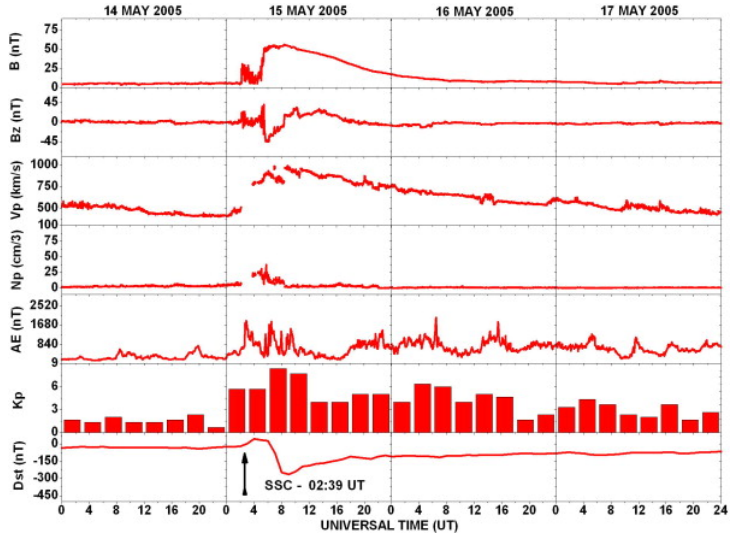

SOURCE: Abreu et al. (2011).

It can be seen that during the main phase, there was an increased auroral activity as seen by the increase in the AE index. The Kp index also reached a high of 8+ on 15 May. There was a rapid fluctuation of the Dst and AE indices during the storm main phase (ABREU et al., 2011).

Figure 3.18 shows the variation of the average VTEC for all 4 stations during the disturbed period. A quiet day, 14 May was also plotted for comparison with the disturbed days. Soon after the SSC a decline was observed at BELE whereas there were clear peaks at UEPP. This indicates the strengthening of the nighttime EIA which removed more plasma from the equator to low latitudes. This negative phase over the equator, BELE, lasted up to daytime which is evidence of a prompt penetration electric field. A large positive phase was also seen during the daytime at BRAZ, UEPP, and POAL during the recovery phase. On the following day, a positive phase was observed at the equatorial station BELE. This appeared to be related to an equatorward meridional wind which can cause a strong positive phase at low latitudes (ABREU et al., 2010; BALAN et al., 2013). Both low-latitude stations POAL and UEPP showed a much higher increase in TEC (PROLSS, 1995; ABREU et al., 2011).

Figure 3.18 - Variations of the average vertical total electron content from GPS observations at 4 receiving stations during the period 14—17 May 2005. The black vertical arrow indicates the sudden storm commencement (SSC).

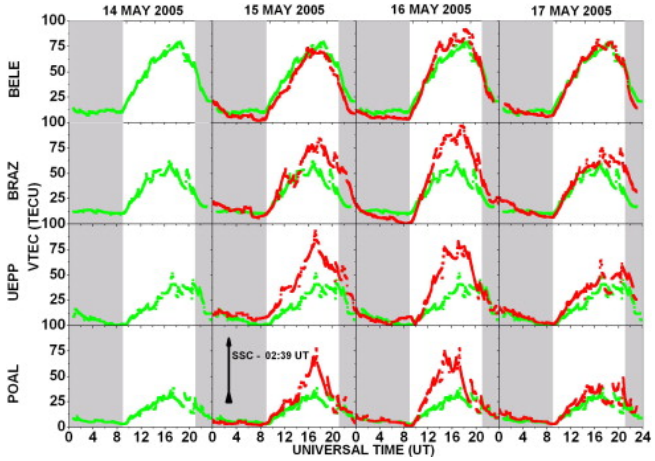

SOURCE: Abreu et al. (2011).

Takahashi et al. (2016) reported an enhancement of the EIA during a geomagnetic storm that occurred on 14 July 2013. The variation of the ΔH component of the magnetic field at Euzebio station which is located at low latitude, the Dst index and AE index on 14–16 July 2013 is shown in Figure 3.19. The main phase of the storm occurred at around 21:00 UT, with a minimum Dst of $-75nT$ while the AE index varied from $700 - 1200nT$ during the main phase. The ΔH component increased dramatically during the storm main phase leading to a strong enhancement in the TEC compared to the quiet time average. Figure 3.20 shows the temporal variation of TEC in the South American region on; **(A)** the quiet day before the storm, **(B)** during the main phase and **(C)** in the recovery phase. On 14 July the crest of the anomaly moved to higher latitudes from the magnetic equator as compared to the day before the storm. This was possibly due to an increase in the $E \times B$ drift that was due to a prompt penetration electric field as was also reported by Takahashi et al. (2016), Abreu et al. (2010).

Figure 3.19 - a) Magnetometer H component at Euzebio (38.4° W, 3.8° S), (b) Dst index, and (c) AE index during the period of 14–16 July 2013.

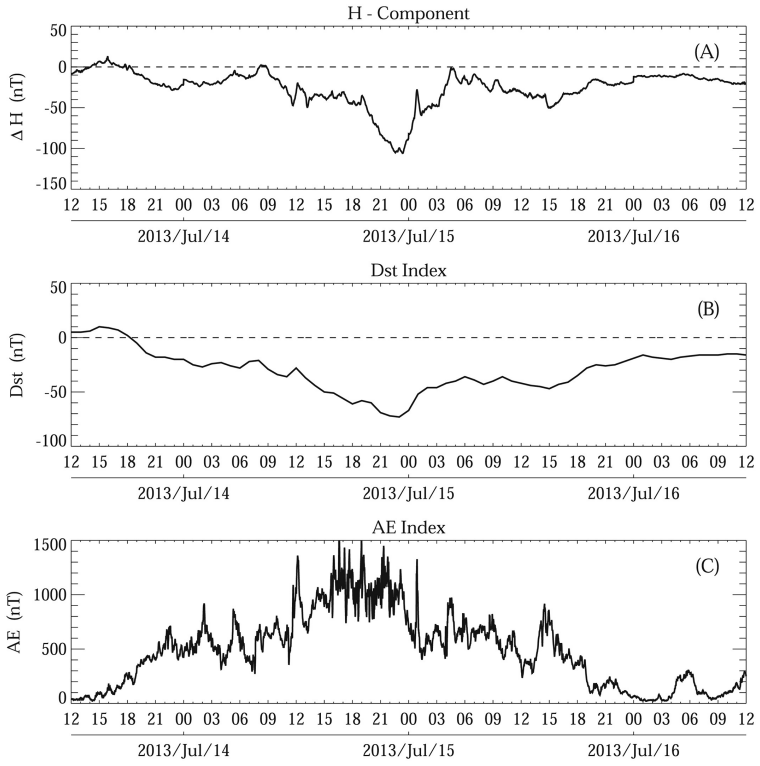

SOURCE: Takahashi et al. (2016).

Figure 3.20 - Color-shaded TEC maps over South America on (a) 13, (b) 14, and (c) 15 of July 2013, at 23:50 UT during the geomagnetic storm period.

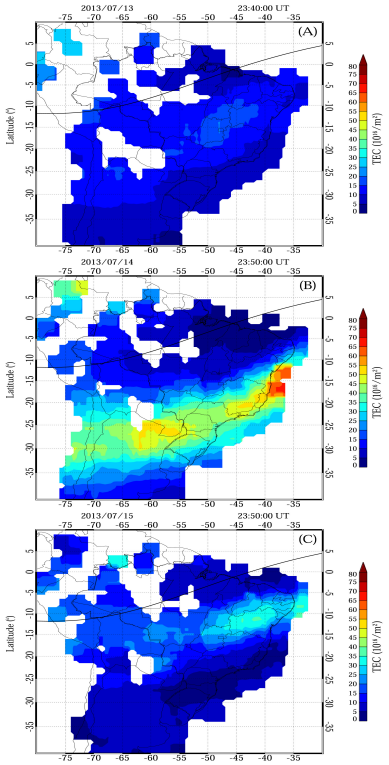

SOURCE: Takahashi et al. (2016).

In contrast to the enhancement of the EIA due to the PPEF, the disturbance dynamo electric field can inhibit the formation of the ionization anomaly (SHARMA et al., 2011; OYEDOKUN et al., 2022). This is because during daytime the DDEF is westward and thus suppresses the $E \times B$ drift. This was demonstrated by Sharma et al. (2011). Figure 3.21 (Left) shows the variation in IMF and solar parameters as well as geomagnetic indices during the geomagnetic storm of 24 August 2005. The main phase of the storm began at 09:10 UT and an hour later commenced the recovery phase.

Figure 3.21 (Right) shows contour plots of the TEC using the stations; Udaipur, HYDE, IISC, MALD (Maldives) and DGAR, stations which are within the longitude belt of $75E \pm 3°$ E. A quiet day was also plotted for comparison with the disturbed days. On 24 August there was a clear enhancement of TEC and the anomaly region grew towards the poles. The EIA was greatly reduced during the recovery phase. The crests shrunk back toward the equator and the TEC values were reduced. This was

Figure 3.21 - Left: The solar wind and IMF parameters, geomagnetic indices, and ΔH variations on 24 August 2005. Right: Contour map of VTEC with respect to time and magnetic latitude within the longitude belt of $75E \pm 3°$ E for 19 August, a reference quiet day, and 24–26 August.

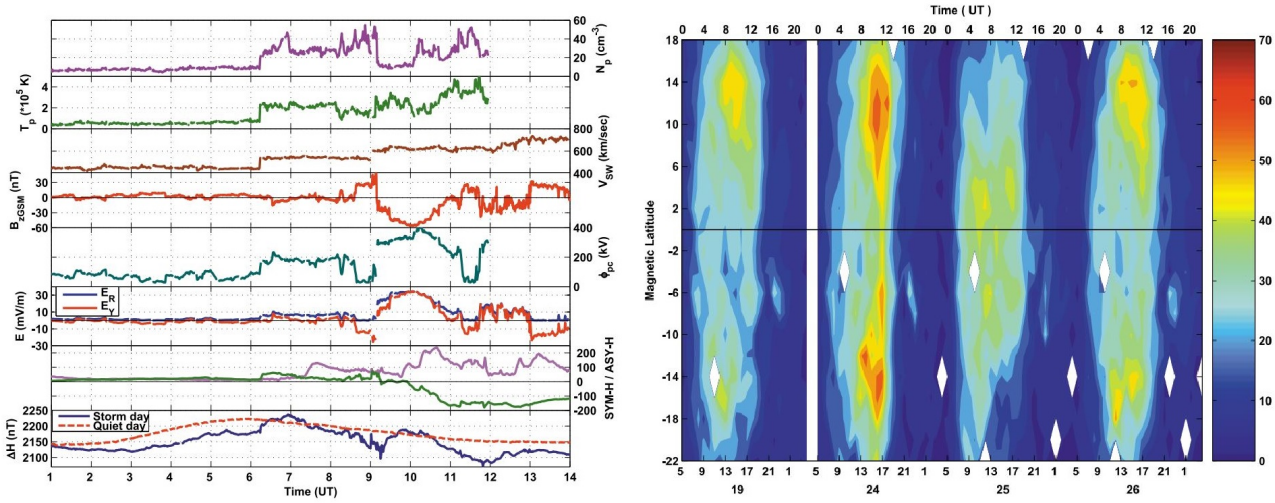

SOURCE: Sharma et al. (2011).

attributed to the presence of a Disturbance Dynamo Electric Field which inhibited the formation of the EIA (SHARMA et al., 2011).

3.6.1 Effect of geomagnetic storms on ionospheric irregularities

Apart from ionospheric storms and thermospheric composition geomagnetic storms also influence the occurrence of irregularities. DDEF together with the Prompt Penetration Electric Field (PPEF) has been observed to affect the formation and development of ionospheric irregularities by drastically modifying low-latitude electrodynamics by several authors using the TEC such as (BALAN et al., 1998; VENKATESH et al., 2017; ABREU et al., 2010; PAULA et al., 2019a; REZENDE et al., 2007). The effect of storms on the ionosphere depends on the local time and polarity of the PPEF (undershielding/overshielding) (ABDU et al., 2003; MARTINIS et al., 2005; REZENDE et al., 2007; PAULA et al., 2007; SRIPATHI et al., 2018). During magnetic the penetration of magnetospheric to low-latitude an eastward disturbance electric field on the dayside and westward electric field disturbance on the nightside which enhances/suppresses the evening prereversal enhancement (ABDU, 2001).

The increased vertical drift v_p at the PRE results in the rapid uplift of the F layer to higher altitudes where collision frequency increasing the RT instability favoring the development of irregularities (ABREU et al., 2011; SRIPATHI et al., 2018; DUGASSA et al., 2019; AA et al., 2020; OYEDOKUN et al., 2022). In particular, Sobral et al. (2002) found that the larger values of Kp index were correlated to the occurrence of plasma bubbles over Brazil. In contrast, suppression is caused by a westward penetration of electric fields and DDEF (MARTINIS et al., 2005; OLADIPO; SCHÜLER, 2013; FAGUNDES et al., 2016; PAULA et al., 2019a). At post-sunset, disturbance dynamo effects tend to inhibit the occurrence of equatorial Spread-F, (MARTINIS et al., 2005), irregularities and scintillation (PAULA et al., 2019a) although the effects of DDEF are more delayed in contrast to prompt penetration electric fields (BLANC; RICHMOND, 1980; FEJER, 2011).

Figure 3.22 illustrates the triggering followed by suppression of ionospheric irregularities during a two-step magnetic storm that occurred on September 6–10, 2017 as reported by Paula et al. (2019a). It can be observed that scintillation was present on the night 07/08 ($S4 > 0.15$) at all stations during the main phase of the first part of the storm. The amplitude is larger for stations over the EIA due to the larger background ionization (de Paula et al. 2003). On this day there was an increased vertical drift and rapid uplift of the F layer associated with an undershielding Eastward PPEF marked by a southward incursion of B_z.

However, on the night of 8 November during the second part of the storm, irregularities were suppressed. A large CEJ caused by westward electric field (DDEF) on 8 November during the day was observed. As DDEF is westward during the daytime, the combination of the DDEF from the first storm with the short-term DDEF from the second storm could have caused the CEJ and the downward movement of the F region thereby suppressing irregularities as shown in the amplitude of the S4 index (PAULA et al., 2019a).

Figure 3.22 - Left: S4 parameters from LISN GPS receivers from day 07 (12 UT) up to day 09 (12:00 UT). The green line is the threshold for ionospheric scintillation when $S4 > 0.15$. The vertical dashed red line represents the SSC at 23:00 UT on day 07. Right: Solar wind speed Vsw, north-south IMF component Bz, interplanetary east–west electric field Ey (positive to east), magnetic indices Kp, AE and Sym-H for the period of 06–10, September 2017. The vertical dashed red lines represent the 2 SSCs. The LT axis for the geographic longitude of 45°W is plotted at the upper panel (LT = UT-03).

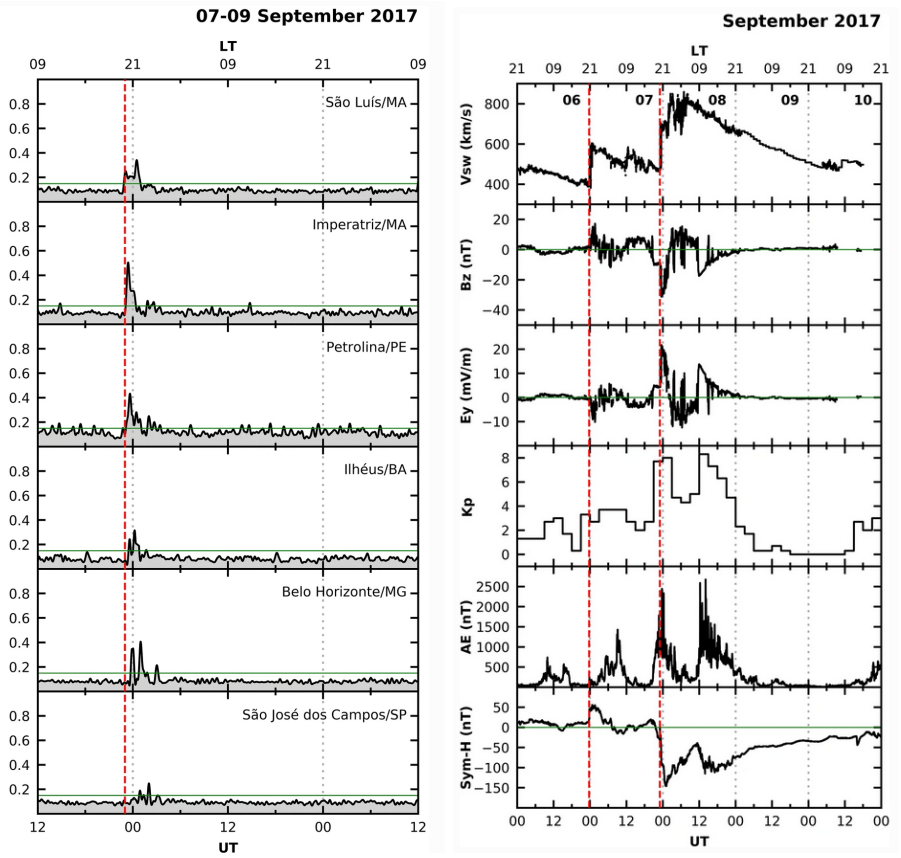

SOURCE: Paula et al. (2019a).

Another example of storm-enhanced irregularities due to PPEF is shown in Figure 3.23. The figure shows Geomagnetic indices as well as TEC variation for São Luís and São José dos Campos during a geomagnetic storm that occurred on October 28-31, 2003. The storm had 2 main phases on 30 October also shown. The S4 index is also shown for São Luís (an equatorial station), Cachoeira Paulista which is located near the anomaly region, and São Martinho da Serra.

Figure 3.23 - Total Electron Content (TEC), scintillation index (S4) and the magnetic indices Dst, Kp, and AE for the period of October 28-31, 2003.

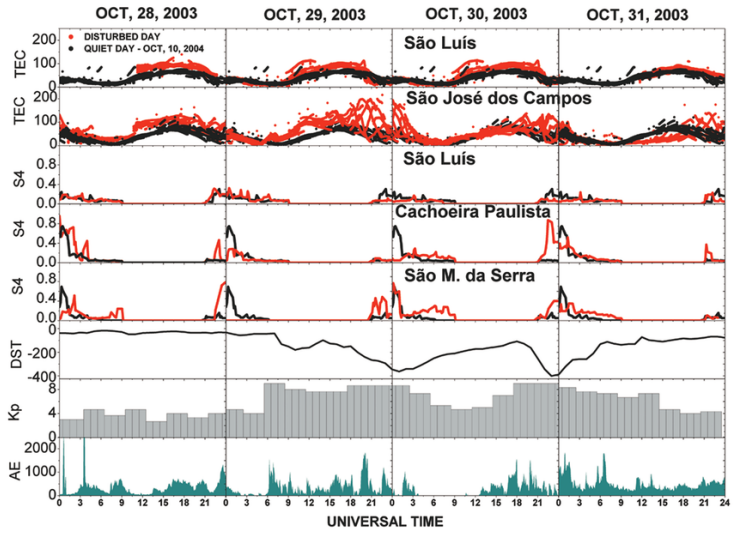

SOURCE: Rezende et al. (2007).

It can be observed that the scintillation was less intense during the disturbed period at São Luís while at Cachoeira Paulista and São Martinho da Serra there was intensification. This points to the presence of a PPEF that reduced plasma density at the equator and strengthened the anomaly. The scintillation also lasted longer than quiet time and even occurred after midnight which is caused by geomagnetic storms (PAULA et al., 2007).

An example of DDEF effect is shown in Figure 3.24 which shows the Geomagnetic indices and TEC variation similar to 3.23 but for the geomagnetic storm period 7–11 November 2004. The Kp index reached a peak of 8 while there was sustained auroral activity during the storm. The S4 index increased at São Luís on the 9th as compared to quiet time while at São José dos Campos it was weakened throughout the disturbed period. This is evidence of a Disturbance Dynamo Electric field which creates conditions that are not favorable for the development of the EIA, hence the extent of the irregularities could not lower latitude (REZENDE et al., 2007).

Figure 3.24 - Total Electron Content (TEC), scintillation index (S4) and the magnetic indices Dst, Kp, and AE for the period November 7-11, 2004.

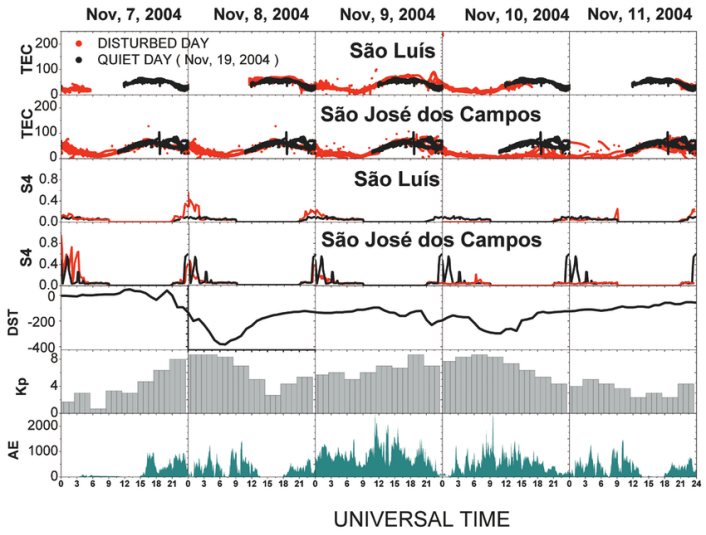

SOURCE: Rezende et al. (2007).

In this section, the variability of the equatorial and low latitude ionosphere was discussed as well as the unique phenomena over South America. The influence of solar wind and geomagnetic storms on the neutral composition, circulation, and electrodynamics on the plasma density and irregularities were also presented. In the next chapter, the methods used in this study are presented.

4 INSTRUMENTATION

Multiple ground and space-based instruments used to investigate the whole heliospace in particular the equatorial and low-latitude ionosphere behavior are described in this section. The various sensors probe the ionosphere at different spatial and temporal resolutions giving a comprehensive picture of the electrodynamic processes in the TI. The main instrument used was the widely available network ground-based GNSS. In addition, an Ionosonde digisonde, All-sky Imager, and ground magnetometer data were also used. Space-based measurements obtained from the GOLD FUV imager, SWARM satellite constellation, and TIMED/GUVI are also discussed.

4.1 Global Navigation Satellite Systems

Figure 4.1 - Illustration of the GPS satellite constellation.

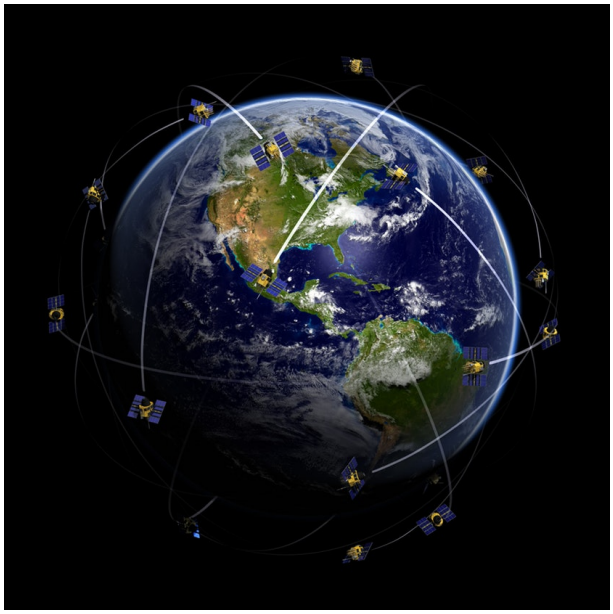

SOURCE: BlackJack3D (2020).

The Global Navigation Satellite System (GNSS) refers to all satellite-based terrestrial navigation systems, in general, (MISRA; ENGE, 2006). These include, among others, the Global Positioning System (GPS), Globalnaya Navigatsionnaya Sputnikovaya Sistema, (GLONASS) and BeiDou. GPS in particular is a constellation of 24 operational satellites in addition to an additional 8 for reserve. The GPS satellites orbit the Earth at an altitude of about 20 000 km above the surface in such

a way that there are at least four satellites in the field of view of the receiver. We used dual frequency receivers operating in the L1, L2 and L5 over Brazil. The receivers are part of the Brazilian Continuous Monitoring Network (RBMC) network of ground-based GPS receivers. Since GNSS has become an integral part of modern-day life, having its applications in navigation, communication, accurate positioning and agriculture, among others, it is important to understand how the ionosphere impacts performance through range errors, phase advance, and scintillation caused by irregularities, in addition to potentially catastrophic effects of space weather.

Monitoring space weather from the ground is to date the most reliable source of space weather monitoring. This typically means smaller latency in the data retrieval and more robust reliability, especially for space-based instruments that might be vulnerable to the same space weather conditions they are monitoring. However, while a single space-based instrument may be able to monitor the Sun-Earth environment continuously, ground-based instruments suffer from having a limited view of the Sun due to the nighttime and the local weather conditions, or they are limited by the Earth's magnetosphere, requiring instrumentation at different latitudes.

4.1.1 Ground-based augmentation system

The Ground-based augmentation system (GBAS) is a type of differential GPS whose purpose is to mitigate ionospheric errors by broadcasting corrections to aircraft to improve the accuracy of the positioning. Figure 4.2 shows the components typical of a GBAS setup.

Figure 4.2 - The GBAS Architecture.

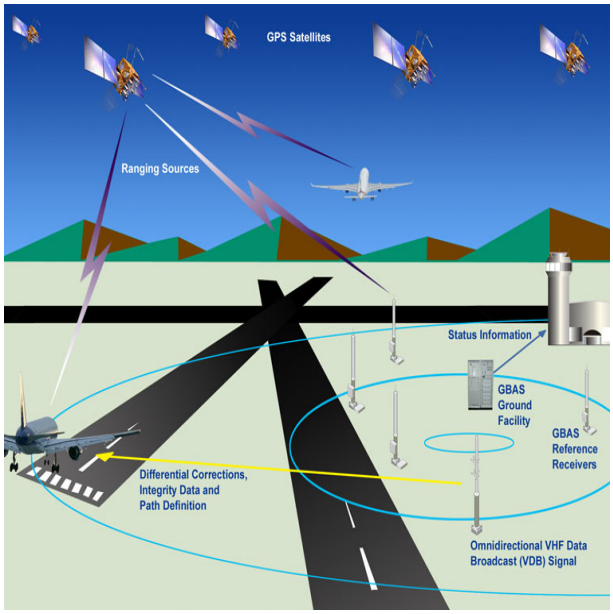

SOURCE: FAA (2021).

The Ground-based Augmentation System (GBAS) ground facility uses the Very High Frequency (VHF) radio link to provide GPS error corrections and integrity. One of the main applications is to provide guided approach to aircraft near airports. The GBAS system receives signals from GPS satellites. The reference receivers measure the time of flight between the GPS satellite and the reference antennas to estimate the distance the signal traveled. The GBAS ground facility then compares this distance with the actual, known GPS reference receiver position to determine the error in the measurement. The average error measured by all operational reference receivers represents the correction term that the GBAS avionics needs to apply. The GBAS ground facility also monitors general GPS satellite performance to ensure reliability of all satellites within its field of view. The GBAS avionics only use GPS satellites for which it receives valid ground corrections. When the ground facility determines there is a potential problem with a GPS satellite it stops broadcasting corrections from that particular satellite minimizing errors. Despite this, ionospheric gradients caused by irregularities pose threats to the safe operation of GBAS by introducing errors in transmission of the error corrections from the ground stations (WALTER et al., 2001).

4.2 The ionosonde

The ionosonde is a specialized radar used to sound the ionosphere. Advanced digital sounders (Digisondes) have been developed for ground-based observations that provide detailed information about the structure and dynamics of the bottomside ionosphere (REINISCH, 2015). The sounders also provide information about the direction and drift velocity of the echoes by measuring the arrival angle, wave polarization, and Doppler frequency. Digisondes operate in the High Frequency(HF) 1-20 MHz band which corresponds to the plasma frequencies of the ionosphere and operates at a peak power on the order of 10 kW and average power around 500 W (REINISCH, 2015). It sounds the ionosphere up to a maximum altitude of $\sim$ 1400 km, at a resolution of $\sim$10 km (CANDIDO et al., 2019). When an incident impulse is generated by the ionosonde it is reflected by the ionosphere, a two-dimensional profile of the ionosphere as a function of height and frequency is constructed called an ionogram (REINISCH, 1996). This is possible because the relative refractive index of the plasma is dependent on the density of the free electrons along the signal path. One limitation of this sounding technique is that it can only sound up to the F layer peak height due to shielding by the topside (REINISCH, 2015).

Figure 4.3 - The Digital Portable Sounder (DPS4D) with a computer system running the Digisonde software.

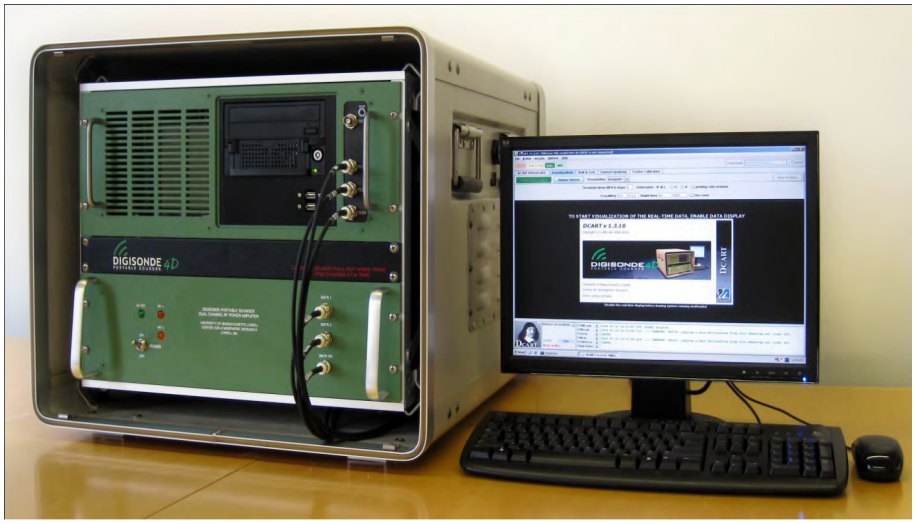

SOURCE: Reinisch (1978).

The Ionosonde is commonly operated in vertical sounding mode but in some cases, oblique sounding is necessary in cases where the region of study is located further away from the station. It provides ionospheric parameters such as critical frequency of the F layer f_0F_2, which is the highest frequency at which the layer reflects and transmits equally, F layer peak height h_mF_2, virtual height $h'F$ and electron density N_e (ABDU et al., 1983). The f_0F_2 is very important in VHF communications as it gives a reference to the maximum frequency that can be used. F-layer parameters are important in ascertaining the background electrodynamics conditions of the ionosphere that control the occurrence of irregularities.

The “Digisonde-Portable-Sounder-4D" (DPS-4) model, in particular, is made up of 4 components. The transmitter sends short pulses, sweeping through the HF frequency band. Each layer of the ionosphere reflects at a certain frequency and height. The reflected signal is received by an antenna on the ground. The resulting image is displayed in the form of an ionogram which is a plot of the virtual height determined by the full round trip time of the signal from the transmitter back to the receiver. The range measurements only give the virtual height due to ionospheric delay. The characteristics of the DPS-4 Digisonde are shown in Table 4.1. Ionosondes have been used to observe Equatorial SpreadF (ESF) due to plasma instabilities in the equatorial and low latitude ionosphere (MCNAMARA et al., 2008; ABDU et al., 2009). They are diffused F-region echoes on ionograms observed in the nightime. The size of irregularities that cause ESF varies greatly from scale size of $\sim$ 1000 km to less than 10 cm (HAERENDEL et al., 1992; BHATTACHARYYA, 2022).

Table 4.1 - Characteristics of the LOWELL DPS-4 Digisonde.

Parameter	**Characteristics**
Frequency scan	0.5– $\sim$ 30MHz
Frequency synthesis	Fully digital
Pulse width	533μs(16 chips of 33μs)
Peak pulse power	2 channels @150 W each
Doppler range	$\pm$3 Hz $\sim$ $\pm$50 Hz
Doppler resolution	0.0125 $\sim$ 12.5 Hz
TX antenna type	Turnstile Delta or Rhombic
RX antenna type	Active crossed loop

SOURCE: Reinisch (2015).

The electron density profile is calculated from the NRI model of the ionosphere to in-

vestigate F layer dynamics and structure in further detail. 10-minute Digisonde measurements for São Luís (dip latitude 3.7°S), an equatorial station, was obtained from the UML Digital Ionogram Database obtained from http://ulcar.uml.edu/DIDBa. Each ionogram was manually scaled using the *SAO Explorer* © software was used to visualize and process the ionogram so that accurate F layer parameters, virtual height, h'F, F layer peak height, h_mF_2, and critical frequency, f_0F_2 were extracted. Ionospheric true heights at fixed frequencies (isolines) are calculated by an inversion method implemented by the *ARTIST* software (REINISCH, 2004). The electromagnetic wave is polarized in the presence of the magnetic field this is shown by the two traces in the ionogram. These represent the splitting of the linearly polarized wave into an ordinary and extraordinary wave, each of which has a distinct wave velocity. Figure 4.4 shows an example of the software interface showing a daytime trace of the ionosphere over the equator during solar minimum.

Figure 4.4 - Ionogram obtained from DS4-D Ionosonde at São Luís for 6 October 2018 at 17:20 UT shown by the SAO Explorer software.

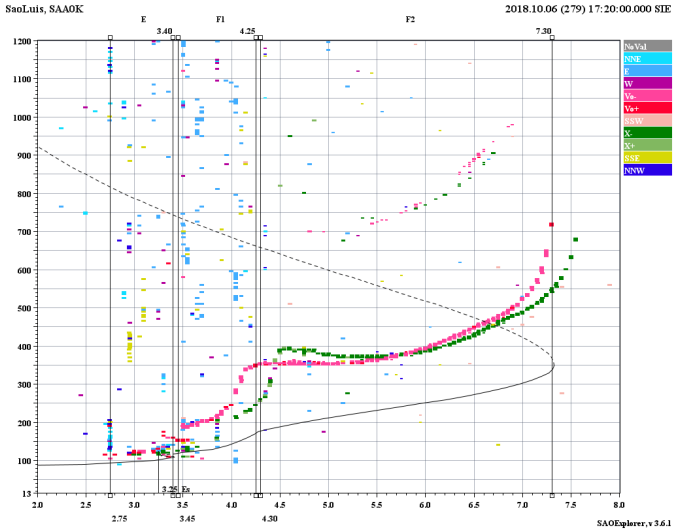

The figure shows the typical layers of the ionosphere and a fitted profile. The magenta and green traces indicate the ordinary and extra-ordinary waves respectively.

However, there are challenges in observing the F layer bottomside at the equatorial and low Latitude sectors due to two main processes. Strong Sporadic E layer sometimes leads to the complete disappearance of the F1 layer trace as it is shielded at the bottomside (*Blanketing Es*). During the Spread F season, strong range and

frequency Spread F also makes the trace invisible due to multiple reflections of the signal as it passes through ionospheric irregularities such as plasma bubbles (ABDU et al., 2009).

4.3 All sky imager observation of plasma bubbles

The All-Sky Imager captures images of airglow emissions produced by the recombination of ion species in the upper atmosphere. It has been used to detect equatorial plasma bubbles and gravity waves in the mesosphere (TAKAHASHI et al., 2014; VALLAT et al., 2005; PIMENTA et al., 2001; PIMENTA et al., 2004; SOBRAL et al., 2002). An example of an All-sky imager that was used in this study is shown in Figure 4.5. The imager has a "fish-eye" lens with a 180° field of view (FOV) hence the term “all-sky”. It provides monochromatic images of airglow emissions at different wavelengths for each emission line such as the OH red line Meinel band, OI 630 nm, OI 557.7 nm OI 777.4 nm filters. This is achieved through a filter wheel that switches between the different filters automatically using an actuator. After the light is collected by the lens, it passes through the telecentric lens combination through the filter and then onto the lens. The collimated beam falls normally on a Charge-coupled Device (CCD) sensor, which produces an electrical signal. The CCD sensor in São João do Cariri, for example, consists of a large area (6.45 cm^2), high-resolution, 1024×1024 pixel back-illuminated array (PIMENTA et al., 2003). The camera uses a fast telecentric lens system ($f/4$) to obtain a high signal-to-noise image, with an integration time of typically 15 s for the near-infrared OH emission (715–930 nm passband) and 90 s for the OI 630.0 nm emission. The atomic oxygen emission in particular is centered at $250-300$ km altitude in the F layer (CANDIDO et al., 2019; PIMENTA et al., 2001). The OI 630.0 nm is a forbidden emission and hence long-lived after sunset and is important in the study of post-sunset ionosphere dynamics in particular plasma bubbles. We used an optical All-sky imager located at São João do Cariri(7.4° S, 36.5° W; dip 12.0°S) in the equatorial region available from the *Estudo e Monitoramento BRAsileiro de Clima Espacial*, EMBRACE network obtained from EMBRACE.

Figure 4.5 - All-sky Imager assembly.

SOURCE: Keoscientific (2017).

4.4 Global-Scale Observations of the Limb and Disk mission

The National Aeronautics and Space Administration (NASA) Global Observations of Limb and Disk (GOLD) Far ultra-violet, FUV, imager, on board the SES-14 (Société Européenne des Satellites-14) communications satellite, was launched in 2018 into geostationary orbit at a central longitude of 47.5°W above South America (EASTES et al., 2017). GOLD brought new insights into the structures of the nighttime ionosphere (EASTES et al., 2019). Its altitude allows observations of airglow emissions that are otherwise not possible due to absorption in the lower atmosphere. One of the main objectives of the mission is to study the effect of geomagnetic storms on the thermosphere and to investigate the influence of the ionosphere on the formation and evolution of EPBs (EASTES et al., 2017; MCCLINTOCK et al., 2020). GOLD performs day and nighttime limb and disk scans, covering $\sim$ 120°W–20°E longitude sector and 70°S–70°N latitude. Figure 4.6 (Left) shows the GOLD instrument's substationary position above South America while Figure 4.6 (Right) shows the night scan low-resolution slit measurements (NI1) of the nighttime airglow showing a slit movement from East to West. Figure 4.6 (bottom) shows the disk spectrum measured by the GOLD imager with a peak centered around 135.6 nm. GOLD performs nighttime disk scans from (20:00 UT) 17:00 LT beginning 15° east of the terminator and extending eastward. The nighttime disk scans have an angular spacing (E-W, N-S) of 0.15° $\times$ 0.15° and spectral resolution of 0.02 nm (MCCLINTOCK et al., 2020; EASTES et al., 2017) which corresponds to 50 km $\times$ 100 km (latitude $\times$ longitude) spatial resolution or $\sim$93 km scale size (AA et al., 2020). A single nightside sequence consists of a pair of 15-minute duration, alternate scans of the Northern and Southern hemispheres by each Channel at 2010–22:45 UT. From 23:10 to 00:10 UT, simultaneous scans of the Northern and Southern Hemispheres are provided.

Figure 4.6 - (a). Location of the GOLD FUV Imager positioned over South America and its field of view. (b). Nighttime disk scan-Low Resolution slit. (c). The typical first light spectrum shows a peak centered at the 135.6 nm Atomic Oxygen emission.

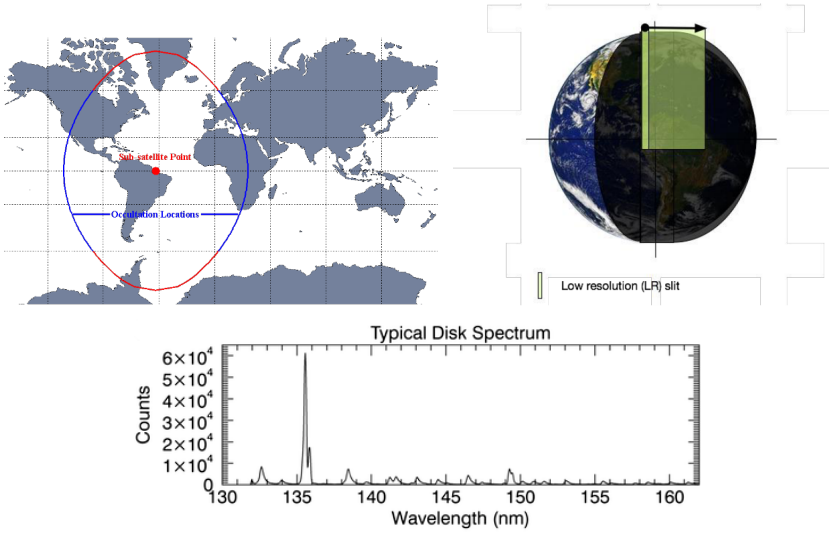

SOURCE: McClintock et al. (2020).

During the nighttime, the GOLD FUV imager disk measures airglow emissions from 132 to 162 nm including the OI 135.6nm produced by the recombination of atomic Oxygen, O^+ ions. This is an important emission as it is the dominant ion at an altitude of ∼300 km (EASTES et al., 2020) which represents the spatial and temporal variations of the ionosphere. The airglow emission is due to radiative recombination processes whose intensity is proportional to the square of the electron density at the F layer peak(CAI et al., 2020a).

$$O^+ + e = O + h\nu_{135.6} \tag{4.1}$$

A secondary source is ion-ion mutual neutralization, which involves the interaction of an O^+ ion with an O^- ion which produces two O atoms, one or both of which may be in an excited state, which can result in the emission of a photon at 135.6 nm. The O^- ion is emitted by the attachment of an electron to a neutral O atom, and it can also interact with a neutral O atom to produce an O_2 molecule and an electron.

Figure 4.7 - Illustration of GOLD Imaging of the dayside on-board the SES-14 satellite.

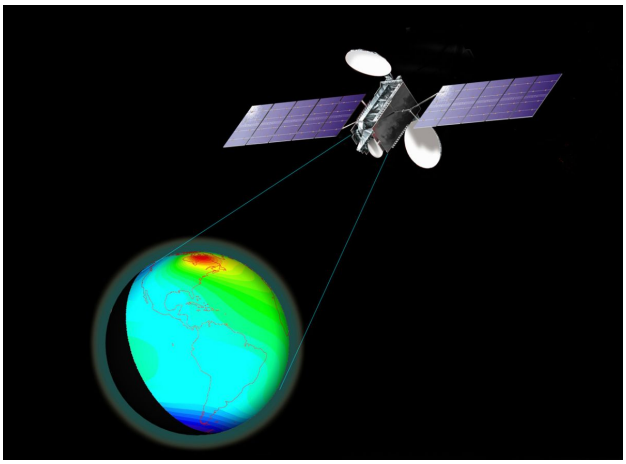

SOURCE: NASA (2021a).

During the day, GOLD measures the sunlit disk from 140.0 to 150.0 nm at a resolution of $0.2° \times 0.2°$ and 0.04 nm spectral sampling at a 30-minute cadence providing thermospheric temperature and composition. This spectrum includes Lyman-Birge-Hopfield (LBH) 132–162 nm emission bands from which the thermospheric O and N2 column density ratio (ΣO/N2) is derived (EASTES et al., 2017). Since the disk measurements are retrieved from near-nadir observations, the information retrieved is weighted by the line-of-sight corresponding to peak emissions at an altitude of 160 km (EASTES et al., 2020). Figure 4.7 is an illustration of GOLD imaging the daytime ionosphere. GOLD FUV imager allows for an unobstructed large-scale view with consistent daily observations as opposed to other ground instruments which are prone to weather conditions while Low Earth Orbit (LEO) satellites provide high-resolution in-situ measurements but lack spatial and temporal coverage (AA et al., 2020). GOLD is an indispensable tool for investigating the day-to-day variability of the nighttime ionosphere, particularly in remote areas such as Northern Brazil and over oceans where ground measurements are not available. To the best of our knowledge, this is the first time GOLD data is used to investigate the response of the ionosphere over Brazil. We used the GOLD O/N2 column-integrated density ratio derived from daytime disk imaging and the N2 Lyman-Birge-Hopfield (LBH) emission measurements (EASTES et al., 2017). An example of EPBs detected using GOLD 135.6nm airglow emission during the deep solar minimum of solar cycle 24 is shown in Figure 4.8. The nighttime EIA is represented by the two bright bands par-

allel to the magnetic equator. Multiple bite-outs in the radiance show EPBs within the EIA.

Figure 4.8 - Images of GOLD OI 135.6 nm airglow emission at 22:10—23:25 UT on 11 December 2019, showing the structure of the equatorial ionization anomaly. The dark emissions represent plasma bubbles.

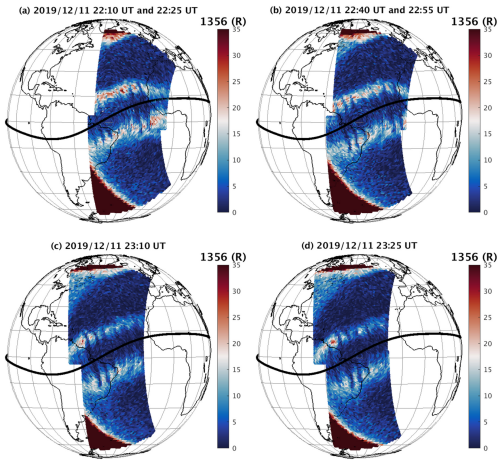

SOURCE: Chou et al. (2020).

Several ground- and space-borne instruments that differ in temporal and spatial resolution have been used to observe an aspect of EPB structure (AA et al., 2020). For example, all-sky imagers detect bubbles in the airglow (KELLEY et al., 2003; NAKATA et al., 2018) using the Global Ultraviolet Imager (GUVI) satellite on the TIMED satellite (KIL et al., 2004) and by an OI 630nm airglow imager on the International Space Station (ISS) (NAKATA et al., 2018) while EPBs appear as plumes in incoherent scatter radar measurements (AJITH et al., 2020), SpreadF in ionosonde (ABDU et al., 2009), scintillation in L-band GPS signals together with depletion in the line-of-site TEC from GNSS (KINTNER et al., 2007; AA et al., 2020) and more recently by the GOLD far ultraviolet imager (EASTES et al., 2019; CAI et al., 2020a). AA et al. (2020) observed EPBs simultaneously over South America using the GOLD FUV imager, SWARM in-situ electron density, and GPS receivers. This multi-instrument approach provides high certainty in the detection of EPBs which can be easily distinguished from other ionospheric structures. Similar to the TEC Maps, 2D maps of GOLD were utilized to calculate the horizontal drift velocity, inter-bubble distance as well as bubble width.

Chou et al. (2020) investigated the occurrence of plasma bubbles using GOLD during the deep solar minimum of 2019. Though recently launched, GOLD maps of irradiance have been used to observe the nighttime EIA as well as equatorial plasma bubbles as was shown by Eastes et al. (2019) and Cai et al. (2020a). The coverage of the observations is very useful in studying climatology as well as day-to-day variability of the nighttime ionosphere, especially in regions where there are sparse ground-based GPS stations, particularly in the Northern and Amazon region in Brazil. Cai et al. (2020a) showed a good correlation between GOLD irradiance measurements and TEC. GOLD has a wide spatial coverage because of its location in geostationary orbit, allowing consistent and continuous observations of the ionosphere (CAI et al., 2020a). However, its temporal resolution is limited to 15 min (EASTES et al., 2017), whereas the cadence of ground Based GPS receivers is much better, though the spatial coverage is also limited to certain areas. Eastes et al. (2019) found significant changes in the post-sunset EIA during quiet conditions. The authors alluded to possible PPEF of interplanetary origin, however, this was not investigated in detail. In addition, the behavior of the EIA during geomagnetically disturbed conditions using GOLD is still yet to be explored in further detail.

The inadequacy of consistent multi-scale 3D measurements and associated smaller structures in particular variability with altitude remains a challenge in understanding the formation, development, and evolution of EPBs (KLENZING et al., 2023). LEO satellites are limited by a narrow swat area, precessing orbits and a limited number of passes per night. In addition, the post-sunset plasma depletions have been studied also showing high variability in morphology and structure which was not previously expected before the mission (CAI et al., 2020a)

4.5 SWARM in-situ electron density measurements

SWARM constellation has been used to investigate the occurrence of irregularities such as plasma bubbles and plasma blobs at high spatial resolution. The constellation was launched in 2013 and comprises three satellites in near-polar low orbits. Swarm A and C have 1.4° separation at 462 km and 87.35° inclination, while Swarm B orbits at a higher altitude of 511 km. The satellites measure in-situ electron density at a much higher spatial resolution, which is ideal for observing small-scale irregularities and GPS signal loss. The data was accessed from https://swarm-diss.eo.esa.int/. Figure 4.9 shows a typical pass by the constellation during the post-sunset sector over South America in 2018. Although SWARM provides high-resolution measurements of the ionosphere, the number of passes is fairly limited hence the spatial coverage is quite

small. Hence, SWARM data was utilized in combination with other sources such as GNSS and GOLD satellite to better improve the coverage.

Figure 4.9 - Typical passes of SWARM Constellation from 21:00-06:00 UT over South America on the night of 8–9 October 2018. Each color represents each satellite pass. The black line indicates the dip equator.

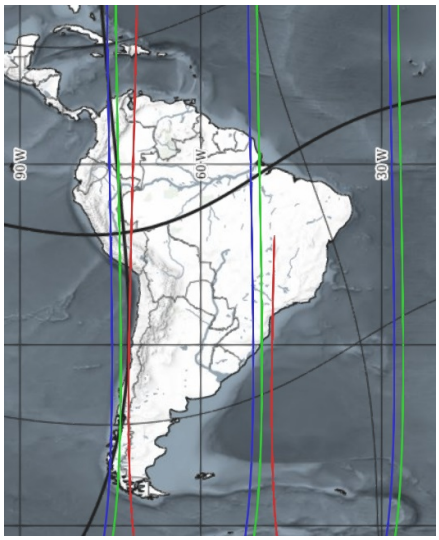

SOURCE: ESA (2021).

Often observations from GOLD 2D Maps, GNSS TEC Maps, and SWARM in-situ electron density have been combined to investigate in more detail the features of EPB in a technique used by (AA et al., 2019; CAI et al., 2020a). An example of the signature of EPBs observed in both GOLD and Swarm in-situ electron density over South America on 24 October 2018 is shown in 4.10. The SWARM A and C passes show a considerable difference in the small-scale structures within EPB whereas GOLD images show larger-scale structures.

4.6 Global Ultraviolet Imager

The Global Ultraviolet Imager, GUVI, is an imaging spectrograph, measuring the upper atmospheric airglow in 115–180 nm using limb and disk measurements. GUVI was installed on the Thermosphere Ionosphere Mesosphere Energy and Dynamics (TIMED) satellite at an altitude of 630 km orbit and an orbital inclination of 74.1° (CHRISTENSEN et al., 2003). GUVI data covers several airglow emission bands

Figure 4.10 - Combined global map of GNSS TEC and OI 135.6-nm radiance of GOLD/UV imaging at 22:10 UT with three consecutive satellite paths of Swarm A. (b) Variation of in-situ electron density as a function of latitudes along these paths. (c, d) The same as Figures 4.10 (a) and (b), respectively, but at 23:40 UT and for Swarm C satellite paths. The shaded areas represent certain plasma depletions. The magnetic equator is marked by the solid line in the left panels and the dotted line in the right panels.

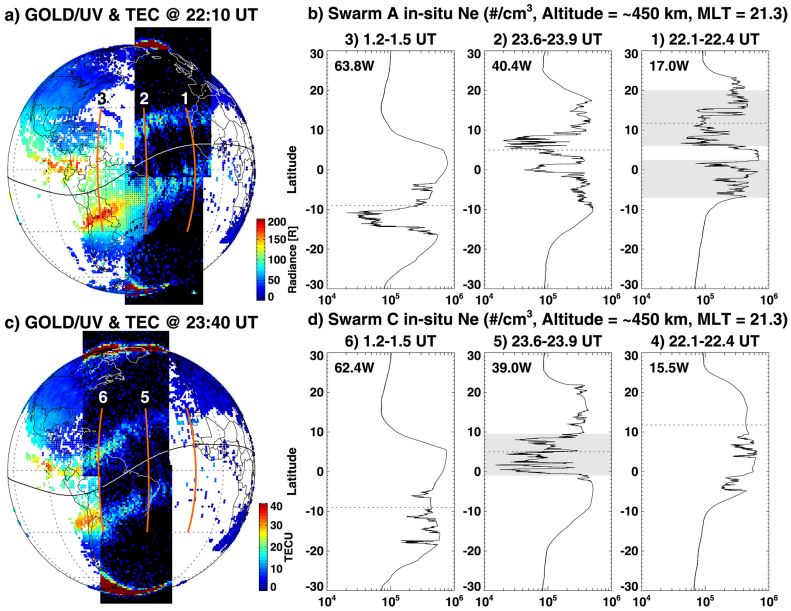

SOURCE: AA et al. (2020).

including OI 130.4 nm and 135.6 nm and the two N2 Lyman-Birge-Hopfield (LBH) bands. The OI 135.6 nm and LBH dayglow intensities from the limb scan are inverted to produce altitude profiles of atmospheric neutral concentration (O, N2, O2). The altitude range of profiles is from 110 km to 667 km. The variation of the column integrated O/N2 ratio is obtained from sunlit disk observations (CHRISTENSEN et al., 2003) which were obtained from the JHU/ APL website jhuapl.edu. GUVI data was used to investigate the storm-related changes in thermospheric composition ratio which also influences the plasma density in the ionosphere (TITHERIDGE, 1974).

4.7 Magnetometer measurements

The PRE in the ΔH (zonal electric field) is important in the development of post-sunset irregularities (KELLEY et al., 2003; SOUZA et al., 2000). The vertical $E \times B$ drift velocity can be directly measured by an Incoherent Scatter radar, however, measurements are often scarce. Other techniques have been used to infer the vertical

$E \times B$ drift from ionosonde measurements and magnetometers. The ΔH component was computed by using two magnetometers located in the Brazilian region namely; São Luís (dip latitude 3.7°S) which is a near-equatorial station obtained from the EMBRACE network available at EMBRACE. Another station was also selected which is located outside the electrojet was Vassouraas (Geomagnetic 13.87°S, 27.53°E, dip: 20°S), obtained from the International Real-time Magnetic Observatory Network website, INTERMAGNET. These stations were chosen because data from Petrolina and Belém stations which are typically used for the estimation of the $\mathbf{E} \times \mathbf{B}$ were not available during the period of interest.

5 METHODOLOGY

In this chapter, the methods, data, and techniques employed to characterize the impact of the solar minimum geomagnetic storms on the Brazilian low-latitude ionosphere are presented. Solar wind, interplanetary, geomagnetic, neutral and ionized parameters and indices, provided by space and ground-based instruments were analyzed. Multiple ionospheric indices and parameters from GNSS TEC, the most available data for diagnosis of the ionosphere, were used to calculate the magnitude of ionospheric storms and the intensity of plasma irregularities. Using these techniques we aim to examine the conditions that precede the development of plasma irregularities and their evolution during disturbed intervals, at various temporal and spatial scales.

5.1 Coronal holes, solar wind, IMF parameters and geomagnetic indices

To quantify the influence of geomagnetic storms on the low latitude ionosphere during deep minimum, we analyzed the source of high-speed streams i.e., coronal holes, as well as the solar wind and interplanetary magnetic field parameters and geomagnetic indices. This data was measured by the Advanced Composition Explorer (ACE) satellite located at Langragian point, L1 (1**au**) was obtained from the Omniweb platform (https://omniweb.gsfc.nasa.gov). The coronal hole and high-speed stream preliminary data were obtained from solen.info and solarmonitor.org. The Auroral Electrojet, AE index was obtained from the World Data Center for Geomagnetism (WDC), Kyoto website available from wdc.kugi.kyoto-u.ac.jp. The magnitude of the geomagnetic storms was determined by using the 1-min Sym–H (PROLSS, 1995) and classified into weak, moderate, and intense according to the criteria by Loewe (1997).

5.2 TEC and derived indices as a tool for diagnosing the ionosphere: a multi-parameter approach

In this work, a cut-off elevation angle of 30° was used for all GNSS observations to reduce multi-path errors and receiver noise. The receivers cover equatorial to low-latitude regions, including the North and South Crests of the EIA and beyond. We classified the equatorial region as dip latitude $\leq 5°$, the EIA region as $5° <$ dip latitude $< 15°$, and the low-latitude outside the EIA as dip latitude$\geq 15°$. Figure 5.1 shows a map with the location of ground-based GPS/GNSS receivers, which constitute the Rede Brasileira de Monitoramento Continuo (RBMC) network, obtained from https://www.ibge.gov.br/. The variation of TEC along similar longitude

sectors was used to investigate effects on the EIA and the latitudinal variation in irregularities over low-latitude (dip $> 9.0°$). To study the field-aligned structures, GPS receivers located along the magnetic field lines were selected using the International Geomagnetic Reference Field (IGRF-13) model for dip latitudes to show the latitudinal variation of irregularities.

Figure 5.1 - Location of GPS/GNSS receivers on the RBMC network in 2018. The dip equator is shown by the black line in the middle with the $\pm 10°$ dip latitude lines north and south of the equator. The locations of the two magnetometers at Vassouras (VASS, dip: 20°S) and São Luís (SALU, dip: 3.7°S) and the Digisonde are also indicated.

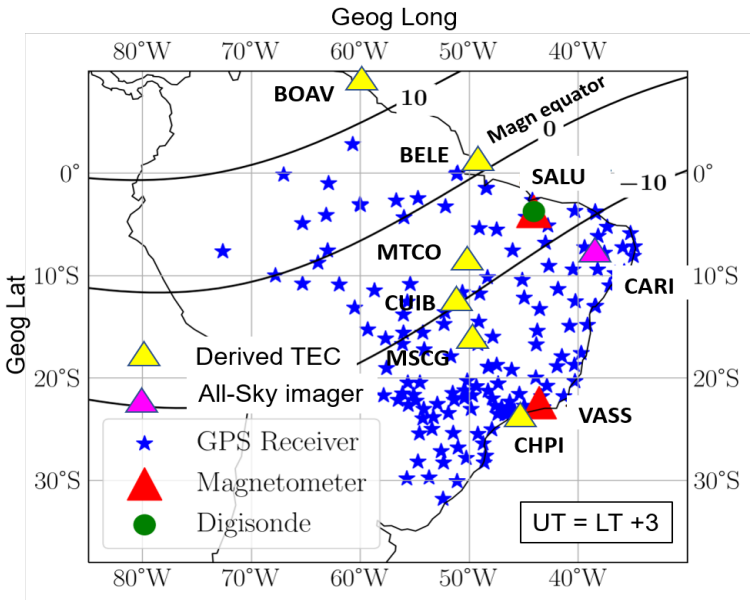

SOURCE: Chingarandi et al. (2023).

These stations were used to construct TEC maps and TEC-derived indices; the rate of TEC index, ROTI, ΔTEC, ∇TEC). However, to study the effect of storms in detail seven representative stations were selected as shown in 5.1. The details of their locations and the data types are in Table 5.1. GNSS Total Electron Content at locations in latitude range $\sim$ 2°N – 38°S geographic covering the North and South Crests of the EIA was used.

Table 5.1 - Geographic location of ground-based GNSS receivers used and data type observed.

NAME	LATITUDE	LONGITUDE	Magnetic Latitude	Dip Lat	Data
BOAV	2.83° N	60.69° W	12.09° N	9.2° N	GPS-TEC/S_4
BELE	1.40° S	48.4°W	7.26° N	0.3° S	GPS-TEC
SALU	2.59° S	44.12° W	6.03° S	3.7° S	GPS-TEC/S_4
MTCO	10.8°S	48.3° W	1.63°S	4.9° S	GPS-TEC/S_4
CUIB	15.55° S	56.10° W	6.51° S	7.6° S	GPS-TEC
MSCG	20.50° S	54.70° W	11.29° S	13.5° S	GPS-TEC
CHPI	22.70° S	45.01° W	14.07° S	17.4° S	GPS-TEC

5.3 Calculation of the TEC using GNSS receivers

Ground-based GNSS observations located in the Brazilian longitude sector 45° W –61° W, equatorial and low latitude 2.83° N–23° S covering the North and South Crests of the EIA; Boa Vista (2.8° N, 60.69° W, dip latitude 9.2° N; BOAV) and Campo Grande (20.5° S, 54.7° W, dip latitude 11.8° S; MSCG) and São Luis (2.59° S 44.21° W, dip latitude 4.67° S; SALU) located near the magnetic equator as shown in Figure 5.1. MTCO was chosen as it is closer to the middle of the country but still along the field line connecting BOAV.

The GPS Gopi software version 2.9.5 was used to obtain the absolute TEC using a technique by Seemala and Valladares (2011) utilizing the pseudorange and code phase observations in the L1 and L2 band frequencies to minimize errors such as tropospheric delay and clock offsets. The relative TEC is then adjusted to the level of the absolute TEC in a process of leveling technique. The pseudorange measurement is absolute but noisy whereas the code-phase observation is less noisy but ambiguous. The Vertical TEC (VTEC) was calculated from the slant TEC (STEC) using a mean ionospheric height of 350 km of altitude (MISRA; ENGE, 2011). The software requires Rinex observation and navigation files in order to compute the TEC. The Vertical TEC was calculated from the slant TEC using a mean ionospheric height of 350 km altitude (MISRA; ENGE, 2011). As mentioned above, in this work a cut-off elevation angle of 30° was used for all GNSS observations in order to minimize multi-path errors and receiver noise. It is essential to perform this filtering during the data preparation because multi-path errors have a similar effect on the signal as scintillation (KINTNER et al., 2007).

The atmosphere interacts with electromagnetic radiation emitted from the satellite to the ground receiver and causes a delay in the signal arrival time (CHAO, 1996).

The major part of the delay occurs in the Ionosphere and is called the *Ionospheric delay* (LIU et al., 2016). The TEC can be derived from the Ionospheric delay by utilizing the refractive index of a dispersive medium (DAVIES, 1990). An electromagnetic wave can be circularly polarised into two waves of opposite rotation by a magnetized plasma (HUNSUCKER, 1991). Considering an electromagnetic plane wave travelling at an angle Θ to a uniform magnetic field as shown in Figure 5.2.

Figure 5.2 - Propagation of an electromagnetic wave in a magnetic field.

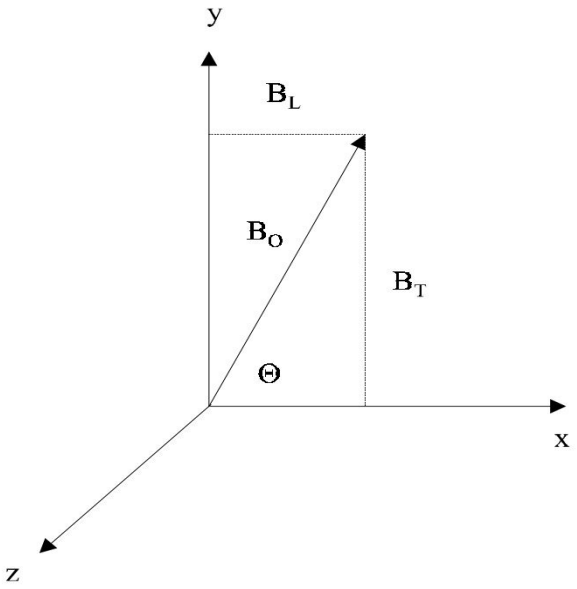

B_L and B_T are the longitudinal and transverse components of the magnetic field.
SOURCE: Davies (1990).

Applying the Appleton-Hartree formula for the refractive index of plasma; Davies (1965), Hunsucker (1991), Komjathy (1997) is given by;

$$n^2 = 1 - \frac{X}{(1 - iZ) - \left[\frac{Y_T^2}{2(1-X-iZ)}\right] \pm \left[\frac{Y_T^4}{4(1-X-iZ)^2} + Y_L^2\right]^{1/2}}, \tag{5.1}$$

Where;

$$X = \frac{\omega_N^2}{\omega^2} = \frac{f_N^2}{f^2}, \tag{5.2}$$

The angular plasma frequency (HARGREAVES, 1992) is given by;

$$\omega_N^2 = \frac{Ne^2}{\epsilon_0 m_e}, \tag{5.3}$$

Where;
N is the electron density;
e is the electric charge ($1.6 \times 10^{-19} C$);
ϵ is the permittivity of free space ($8.85 \times 10^{-12} F/m$);
m_e is the electron mass ($9.101 \times 10^{-31} kg$);
and;

$$Y = \frac{\omega_H}{\omega}, \tag{5.4}$$

$$Y_L = \frac{\omega_L}{\omega}, \tag{5.5}$$

$$Y_T = \frac{\omega_T}{\omega}, \tag{5.6}$$

$$Z = \frac{\omega_c}{\omega}, \tag{5.7}$$

Where ω_H is the angular gyrofrequency,
ω_L is the longitudinal angular gyrofrequency,
ω_T is the transversal angular gyrofrequency,
ω_c is the collision frequency between electrons and ions/neutrals;

Applying this refractive index to the upper atmosphere where the collision frequency is low and the magnetic field has an influence on the plasma yields $\omega_c = 0, \rightarrow Z = 0$.
Substituting $Z = 0$ into 5.1 and performing a series expansion of the resulting expression (BASSIRI; HAJJ, 1993; KOMJATHY, 1997) ;

$$n \approx 1 - \frac{X}{2} \pm \frac{1}{2} XY|Cos\theta| - \frac{1}{8} X^2 + ... \tag{5.8}$$

By analyzing the magnitude of each of the terms above using typical values of electron density, $N = 10^{12}/m^3$, magnetic field strength, $B = 5 \times 10^{-5} T$ and the L band frequency to approximate X and Y. Taking $\Theta = 0$, the contribution of the terms after the first two in the above series is negligible under typical F layer peak conditions (KOMJATHY, 1997). Therefore, by taking only the first two terms of the series the refractive index simplifies to;

$$n = 1 - \frac{X}{2} \tag{5.9}$$

The phase velocity is given by;

$$v_p = \frac{\omega}{k}, \tag{5.10}$$

where k is the wave number. The velocity of an electromagnetic wave in a medium of refractive index n is given by,

$$v = \frac{c}{n} \tag{5.11}$$

Substituting 5.10 into 5.11 the phase velocity is obtained as (MISRA; ENGE, 2011);

$$n_p = 1 - \frac{X}{2} \tag{5.12}$$

The delay causes the path traveled by the wave ds to be longer than the actual distance along the path ds_0 in the absence of any delay (NEGRETI, 2012). Therefore, the total distance traveled is given

$$\int n ds = \int n_0 ds_0 + \Delta^{iono}; \tag{5.13}$$

where Δ^{iono} is the ionospheric delay and $n_0 = 1$ in free space, for higher frequencies $ds_0 \approx ds$. Substituting for 5.12 and simplifying;

$$\Delta^{iono} = \int -\frac{X}{2} ds_0, \tag{5.14}$$

Taking;

$$\omega = 2\pi f, \tag{5.15}$$

and 5.3 into 5.14 and evaluating the constants $\frac{e^2}{8\pi^2 \epsilon_0 m_e} = 40.3$ (KOMJATHY, 1997),

The ionospheric delay reduces to ;

$$\Delta^{iono} = -\int \frac{40.3}{f^2} N ds_0, \tag{5.16}$$

Combining 5.3 and 5.16 the ionospheric delay is given by ;

$$\Delta^{iono} = -\int \frac{40.3}{f^2} TEC, \tag{5.17}$$

From the above equations, it is clear that a higher electron density will cause more delay of the signal (BRUNINI et al., 2004).

5.3.1 Calculation of total electron content from code delay

The pseudo-range is calculated by the taking round-trip distance of the signal from the satellite to the receiver. The roundtrip time is calculated by taking the difference between the time of transmission of the signal by the satellite and when the ground receiver receives it. This transmission time is encoded onto the signal that is sent by the satellite. However, there are several errors in this measurement and hence the *pseudo*-range is obtained instead (MISRA; ENGE, 2011). Figure 5.3 illustrates the sources of error in GPS range measurements.

Figure 5.3 - Components of GPS range measurement.

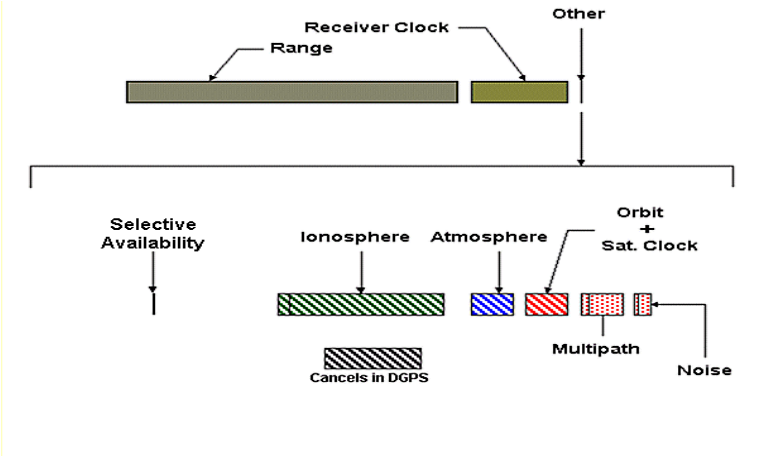

SOURCE: Clynch (2001).

One such source of error which was mentioned above is the error due to the tropospheric delay. The clock offset between the satellite and the receiver also introduces additional errors to the measurement. This error is as a result of the satellite and receiver clocks not being synchronized. Figure 5.4 shows the schematic of a typical satellite configuration being used to estimate the position by a ground receiver. A minimum of four satellites are required, three for each of the position co-ordinates and a fourth satellite for the time dimension. The pseudo-range in the L1 and L2

bands respectively is given by (KOMJATHY, 1997);

$$\rho_1 = L + c(DT - dt) + \Delta^{iono}_{\rho 1} + \Delta^{trop} + b^s_{\rho 1} + b^r_{\rho 1} + m_{\rho 1} + \epsilon_{\rho 1} \tag{5.18}$$

$$\rho_2 = L + c(DT - dt) + \Delta^{iono}_{\rho 2} + \Delta^{trop} + b^s_{\rho 2} + b^r_{\rho 2} + m_{\rho 2} + \epsilon_{\rho 2}, \tag{5.19}$$

Where;
ρ_1 and ρ_2 is the pseudorange in L1 and L2 band frequency respectively;
L is the geometric distance between the satellite and the receiver;
dT and dt are the satellite and receiver clock errors;
Δ^{iono}_{ρ} is the ionospheric delay;
Δ^{trop} is the delay in the troposphere;
$b^s_{\rho 1,2}$ and $b^r_{\rho 1,2}$ are the respective satellite and receiver biases ;
$m_{\rho 1,2}$ are the respective multi-path errors;
and $\epsilon_{\rho 1,2}$ is the respective instrument noise; To improve the accuracy of the measurement a dual-frequency system or a receiver pair is utilized (BIDAINE; WARNANT, 2009). By subtracting the pseudoranges from the L1 and L2 carrier bands, terms that are constant with frequency such as the geometric distance, clock errors, and the tropospheric delay are eliminated (MISRA; ENGE, 2011). The TEC from the code delay is given by subtracting the equation 5.18 from 5.19;

$$\rho_2 - \rho_1 = \frac{1}{A} TEC_\rho + b^r_\rho + b^s_\rho + m_\rho + \epsilon_\rho, \tag{5.20}$$

Where $b^r_\rho = b^r_{\rho 2} - b^r_{\rho 1}$ and $b^s_\rho = b^s_{\rho 2} - b^s_{\rho 1}$, Similarly $\epsilon_\rho = \epsilon_{\rho 2} - \epsilon_{\rho 1}$, $m_\rho = m_{\rho 2} - m_{\rho 1}$

A is the factor of conversion from distance to TEC Units obtained from the equation 5.17 and is given by;

$$A = \frac{1}{40.3} \frac{f_2^2 f_1^2}{f_2^2 - f_1^2}, \tag{5.21}$$

and is equivalent to $9.52 \times 10^{16} electrons/m^3$. From the above equation 5.20 we can write the TEC as ;

$$TEC_\rho = A(\rho_2 - \rho_1) - b_\rho - m_\rho + \epsilon_\rho, \tag{5.22}$$

where the differential bias due to the satellite and receiver b_ρ is given by $b^r_\rho + b^s_\rho$.
The TEC value obtained by this method is absolute and unambiguous however it still contains a lot of noise and hence the need to utilize the carrier-phase together with the code-delay in the code-leveling technique (BIDAINE; WARNANT, 2009).

Figure 5.4 - Estimation of pseudorange from range delay.

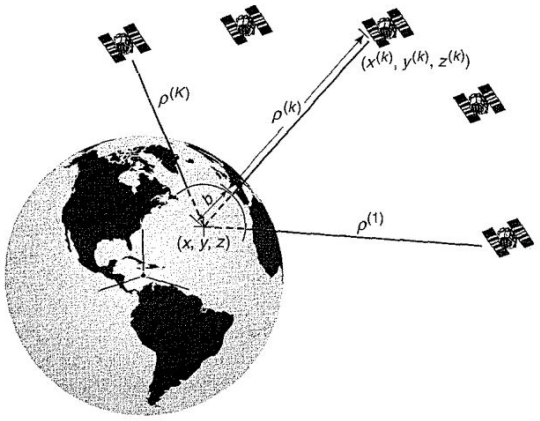

SOURCE: Misra and Enge (2011).

5.3.2 Calculation of total electron content from the carrier phase

Total Electron content can also be calculated using the *carrier phase*. The receiver generates a constant frequency which is used as a reference for measurements. The carrier phase is then the difference between the carrier of the received signal and that of the reference. The carrier phase, plus the number of complete cycles the signal has made between the satellite and the receiver, gives the actual range (MISRA; ENGE, 2011). Figure 5.5 demonstrates the difference between the carrier and code delay. The carrier phase has much less noise and is not affected by noise as compared to the code-delay however it is ambiguous since the actual number of integer cycles traveled is unknown as illustrated in the Figure (MISRA; ENGE, 2006).

$$\Phi_1 = \lambda_1\phi_1 = L + c(DT - dt) - \Delta^{iono}_{\phi_1} + \Delta^{trop} + b^s_{\phi_1} + b^r_{\phi_1} + m_{\phi_1} + \epsilon_{\phi_1} + \lambda_1 N_1 \quad (5.23)$$

$$\Phi_2 = \lambda_2\phi_2 = L + c(DT - dt) - \Delta^{iono}_{\phi_2} + \Delta^{trop} + b^s_{\phi_2} + b^r_{\phi_2} + m_{\phi_2} + \epsilon_{\phi_2} + \lambda_2 N_2 \quad (5.24)$$

where;
Φ_1 and Φ_2, are the respective carrier phase observations for L1 and L2 Band respectively in distance units;
ϕ_1 and ϕ_2, are the respective carrier phase observations for L1 and L2 Bands;

Figure 5.5 - Simplified schematic of carrier phase and code measurements.

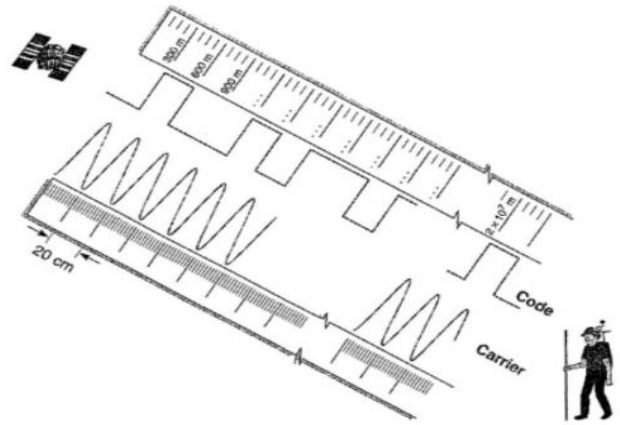

SOURCE: Misra and Enge (2006).

L is the geometric distance between the satellite and the receiver;
c is the velocity of light in a vacuum;
dT and dt are the satellite and receiver clock errors respectively;
Δ_{ϕ}^{iono} is the ionospheric delay on the carrier phase;
Δ^{trop} is the delay in the troposphere;
$b_{\phi 1,2}^{s}$ and $b_{\phi 1,2}^{r}$ are the satellite and receiver biases respectively ;
m_{ϕ} is the multi-path error;
ϵ_{ϕ} is the instrument noise;
λ_1, λ_2 is the respective wavelength for each corresponding carrier frequency;
N_1, N_2 are the integer carrier phase ambiguities for L1 and L2 band respectively.
The ionospheric delay in the carrier phase can be written in a similar manner to that of the pseudorange measurements as;

$$\Delta_{\phi}^{iono} = \int \frac{40.3}{f^2} TEC, \tag{5.25}$$

Subtracting the 5.24 from 5.23 and substituting for the ionospheric delay ;

$$\Phi_1 - \Phi_2 = \frac{1}{A} TEC_{\phi} + b_{\phi}^{r} + b_{\phi}^{s} + m_{\phi} + \epsilon_{\phi} + \lambda_1 N_1 - \lambda_2 N_2, \tag{5.26}$$

Where $b_{\phi}^{r} = b_{\phi 2}^{r} - b_{\phi 1}^{r}$ and $b_{\phi}^{s} = b_{\phi 2}^{s} - b_{\phi 1}^{s}$.
Similarly $\epsilon_{\phi} = \epsilon_{\phi 2} - \epsilon_{\phi 1}$, $m_{\phi} = m_{\phi 2} - m_{\phi 1}$ and A is the conversion factor from the

Equation 5.21. From the equation 5.22, TEC can be written as ;

$$TEC_\phi = A(\phi_1 - \phi_2) - (\lambda_1 N_1 - \lambda_2 N_2) - b_\phi - m_\phi - \epsilon_\phi, \tag{5.27}$$

where the differential biases due to the satellite and receiver b_ϕ is given by $b_\phi^r + b_\phi^s$. Subtracting the two in a method called carrier-to-code levelling (MISRA; ENGE, 2011);

Considering a case where the two are equal according to (KOMJATHY, 1997)

$$\langle TEC_\phi - TEC_\rho \rangle = 0 \tag{5.28}$$

The absolute TEC is obtained after removing the instrument errors and the satellite and receiver biases (COCO et al., 1991).

5.3.3 Vertical Total Electron Content

The Vertical Total Electron Content (VTEC) is a more useful parameter for studying the dynamics of TEC at a particular station. VTEC can be calculated from the slant TEC by use of a thin shell model (MISRA; ENGE, 2006). The model assumes that the ionosphere is made of a single layer which is at an altitude of about 300 km that coincides with the peak of the ionosphere. The mean height is approximately 3350 km in altitude (MISRA; ENGE, 2011). Hence, TEC is calculated at a point called the Ionospheric Piercing Point (IPP) which is the point where the signal path crosses the thin shell mean height, h_m (MISRA; ENGE, 2011) as shown in Figure 5.6.

Figure 5.6 - Ionosphere thin shell model showing signal path from satellite to receiver.

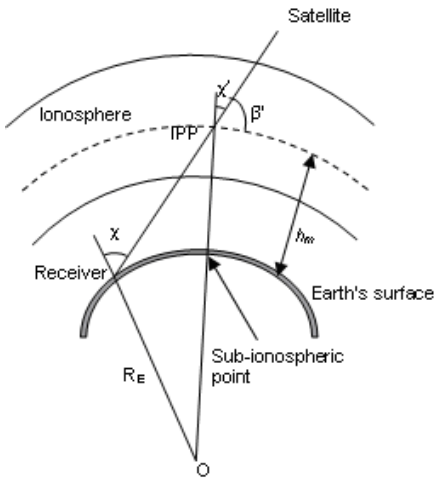

SOURCE: Norsuzila et al. (2008).

The Slant TEC is related to the Vertical TEC by ;

$$Cos\chi' = \frac{STEC}{VTEC} \tag{5.29}$$

By applying the law of sines in terms of the receiver elevation χ and satellite elevation, χ' ;

$$\frac{Sin(180-\chi)}{R_e + h_m} = \frac{Sin(\chi')}{R_e} \tag{5.30}$$

where R_e is the Earth radius ;
Since $Sin(180-\chi) = Sin(\chi)$ and $Sin^2(\chi') + Cos^2(\chi') = 1$. The obliquity factor (MISRA; ENGE, 2011) is given as;

$$M(\chi) = \left(1 - \left[\frac{R_e Sin(\chi)}{R_e + h_m}\right]^2\right)^{1/2} \tag{5.31}$$

where ;

$$STEC = M(\chi) \times VTEC \tag{5.32}$$

5.4 Ionospheric TEC maps

Two-dimensional maps of absolute VTEC are derived with a time resolution of $15-30$ minutes and spatial resolution of $0.5^\circ \times 0.5^\circ$ in latitude and longitude. TEC

Maps are a useful tool that may be applied for visualizing the spatial variation of the TEC (TAKAHASHI et al., 2016), especially during geomagnetic storms where there is high temporal and spatial variability of TEC under local time, presence of electric fields, and winds which vary with latitude. Ionosphere TEC Maps have been used to observe the initiation, growth, and development of plasma irregularities as was shown by Takahashi et al. (2016), Cai et al. (2020a), Barros et al. (2018). The maps are plotted using the latitude and longitude of the sub-ionospheric pierce point calculated from the satellite navigation data. In addition to TEC Maps, maps of $ROTI$ and ∇TEC were also developed to establish a relationship between the location of small-scale irregularities and the enhancement of TEC during storms.

5.5 Use of mapping to investigate EPBs and EIA

Two-dimensional, 2D, 135.6nm radiance maps measured by GOLD were used to determine the diurnal behavior of the EIA such as the latitudinal extent, intensity, and onset time during quiet and geomagnetic disturbances. GOLD measures emissions at approximately 300 km height which corresponds to the F-layer peak density where the highest contribution is located. In addition, the maps were used to estimate the drift velocity, inter-bubble distance, and with of EPBs over South America. The occurrence of plasma bubbles often exhibits a periodic longitudinal distribution suggesting a periodic seeding mechanism responsible for modulating the amplitude of intensity depletions (TAKAHASHI et al., 2009; HINES, 1960; ABDU et al., 2009; TSURUTANI et al., 2006). Recently, observations of periodic bubbles with distances between 100 and 500 km have been reported using images of the OI 630.0 nm emission (TAKAHASHI et al., 2009; AGYEI-YEBOAH et al., 2019). The EPB width was estimated by taking the coordinates of the edges of the bubble along the dip equator. The edges were identified by the bright bands between the EPBs.

5.6 Ionospheric indices: a multi-parameter approach

Ionospheric indices are very useful in understanding complex behavior in the ionosphere and can be used to disseminate information to end users and customers on potential negative effects on satellite navigation and positioning systems. However, because the ionosphere is highly dynamic, mitigation of errors requires the analysis of various indices derived from GNSS. The widespread availability of GNSS receivers allows for global monitoring of ionospheric variability, and response to space weather events.

5.6.1 Percentage deviation in TEC from quiet time

Multiple ionospheric parameters and indices were derived from the GNSS TEC to study the TEC variability and plasma irregularities. The first parameter used to quantify the magnitude of the ionospheric storms was the percentage deviation in TEC δTEC. A comparison of TEC during the disturbed period with the average of the five most geomagnetically quiet days (5QD) in that particular month as a reference is also a common technique for ionospheric studies. The difference between the TEC and the 5QD average is given by,

$$\Delta TEC = \text{VTEC} - \overline{VTEC}_{5qd} \tag{5.33}$$

The ΔTEC is also important because it gives a broader view of how the storm affected the TEC at that location during that month. It can also be expressed as a percentage change in TEC compared to quiet time,

$$\delta\text{VTEC}(\%) = \frac{\text{VTEC} - \overline{VTEC}_{5qd}}{\overline{VTEC}_{5qd}} \times 100\% \tag{5.34}$$

A similar technique was used to compute the percentage deviation of ionosonde parameters;

$$\delta\text{x}(\%) = \frac{\text{x} - \overline{x}_{5qd}}{\overline{x}_{5qd}} \times 100\%, \tag{5.35}$$

where x represents each ionosonde parameter; h_mF_2, $h'F$ and f_0F_2.

The 5QD are obtained from the GFZ German Research Centre for Geosciences Postdam International Quietest Days list derived from the Kp index available at http://wdc.kugi.kyoto-u.ac.jp/qddays. The percentage deviation has been used by several authors including Yao et al. (2016), Candido et al. (2018), Moro et al. (2021). A comparison was made with a geomagnetically quiet period as a reference to the disturbed period. The ionosphere has high diurnal variability even during quiet time due to several factors such as forcing from below including tidal activity, winds, and gravity waves. Therefore, the average of the 5 most quiet days was calculated to minimize this error.

5.6.2 Ionospheric irregularity indices

Several indices have been derived from the TEC. For instance, I_{ROT} (Wanninger 1993) derived from the Rate of TEC (ROT), f_{P} which is the median ROT and the

f_P irregularity index, which is the median value of the absolute ROT, among others.

These indices provide information about the state of the ionosphere at different spatial and temporal scales (BORRIES et al., 2020). The use of multiple indices has been utilized by (OLADIPO; SCHÜLER, 2013; WILKEN et al., 2018; BORRIES et al., 2020). Pereira et al. (2017) showed that ground-based GNSS can be utilized for real-time monitoring of irregularities over Brazil by using maps of ROTI, f_P irregularity index, F_P, I_{ROT}, among others while Oladipo and Schüler (2013) applied a similar technique over Africa. Furthermore, the multi-instrument approach has been employed by Astafyeva et al. (2015) and Paula et al. (2019b) to investigate the effect of geomagnetic storms on the occurrence of irregularities using observations from ground-based receivers and satellites. However, the use of the percentage deviation in TEC together with the irregularity indices that measure phase fluctuations, ROT and ROTI, as well as spatial gradients in TEC combined with the S_4 has not yet been applied to the low latitude ionosphere, in particular during solar minimum. Mendillo et al. (2000) found that the use of median spikes that might influence I_{Rot} and ROTI. In addition, maps were constructed for each of the calculated parameters or indices which are useful in understanding the spatial and temporal behavior of the ionosphere.

5.6.3 Estimation of phase fluctuations in TEC

ROTI is an ionospheric index that characterizes the phase fluctuations due to irregularities (LIU et al., 2009). ROTI is useful in investigating the spatial and temporal evolution of plasma irregularities (PI et al., 1997), particularly those associated with EPBs which are common at equatorial and low latitudes (ABDU, 2001; LI et al., 2011). At equatorial and low latitudes, ROTI detects small-scale irregularities of ∼km scale size. The scale size depends on the horizontal plasma drift velocity of the plasma in relation to the horizontal drift velocity relative to the IPP (PI et al., 1997). Several techniques have been used to calculate ROTI, however, the technique developed by Pi et al. (1997) is the most commonly used Pereira et al. (2017), Oladipo and Schüler (2013), AA et al. (2019), Lei et al. (2008), Liu and Radicella (2019).

In order to derive ROTI, the rate of change of TEC (ROT) was first derived. The amplitude of ROT is a measure of large-scale phase fluctuations due to plasma bubbles (PI et al., 1997; MENDILLO et al., 2000; CHANDRA et al., 2009; OLADIPO; SCHÜLER, 2013). The TEC data used to calculate ROTI was obtained from GPS receivers with a resolution of 30s. The ROT (PI et al., 1997) is defined as;

$$ROT = \frac{\Delta TEC}{\Delta t} \tag{5.36}$$

The ROT was calculated from 30s GPS line of sight TEC (slant TEC, or sTEC) for each satellite PRN and then converted to 1-minute resolution. ROTI is defined as the standard deviation of the ROT assuming a thin layer model of the ionosphere over a time interval (PI et al., 1997).

$$ROTI = \sqrt{\langle ROT^2 \rangle - \langle ROT \rangle^2} \tag{5.37}$$

Figure 5.7 shows an example of GPS phase fluctuations observed over South America at Arequipa, Peru (16.5°S, 288.5°E, dip latitude 3.35°) on 17 September 1995. It can be shown that the ROTI and ROT detected phase fluctuations associated with plasma depletions in the post-sunset hours. ROTI was computed over a moving window of 5 min from the 1-min ROT data for each satellite PRN separately. In this technique, the irregularity is"frozen-in" so that the ionosphere state remains constant over the time of flight of the signal from the satellite to the receiver. The sampling rate of the GNSS data and the time interval over which ROTI is computed impact the magnitude of its sensitivity to ionosphere perturbations (BORRIES et al., 2020). ROTI maps can be applied to monitor and study the instantaneous global activity of ionospheric irregularities. Although the climatology of plasma bubbles has been widely studied using all-sky imagers during high solar activity and low solar activity (SOBRAL et al., 2002; PAULA et al., 2007; BARROS et al., 2018), few studies have utilised ROTI during solar minimum. The intensity of irregularities is classified according to Pereira and Camargo (2014) as shown in Table 5.2.

Table 5.2 - Classification of irregularities according to ROTI.

ROTI	**Irregularity Level**
$ROTI \leq 0.05$	Low
$0.05 < ROTI \leq 0.2$	Moderate
$ROTI > 0.2$	Strong

SOURCE: Pereira and Camargo (2014).

The ROTI for all available PRNS was averaged every 10 minutes to obtain the averaged ROTI to investigate the diurnal and climatological behavior of irregularities. To determine the effect of irregularities on scintillation the ROTI was compared with the S_4. Recently, ROTI and the averaged ROTI, $ROTI_{ave}$, have been applied

Figure 5.7 - ROT and ROTI calculated from a GPS receiver located at Arequipa, Peru on 17 September 1995. The top panel shows the projected geographic locations of radio trajectories at 400 km altitude along receiver-satellite Line-of-Sight, LOS, for seven GPS satellites. Corresponding elevation and relative LOS TEC obtained from the differential phase (L1-L2) measurements are shown in panels 2 and 3 (from the top), labelled by PRN. The thicker lines in the top panel highlight the locations of observed GPS phase fluctuations seen in the ROT and ROTI.

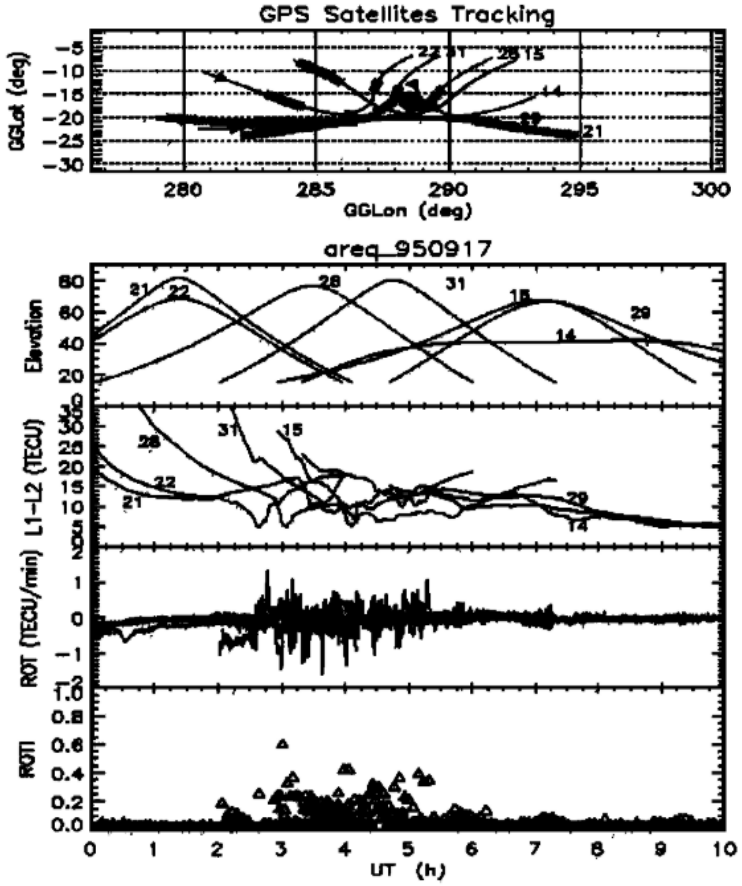

SOURCE: Pi et al. (1997).

to demonstrate and explain the level of ionospheric irregularities over the equatorial and low-latitude regions over South America by Pereira et al. (2017). $ROTI_{ave}$ eliminates the noise spikes or extreme value usually present in ROTI (OLADIPO; SCHÜLER, 2013) and represents well the ionospheric irregularity over equatorial station latitudes (DUGASSA et al., 2019). According to Mendillo et al. (2000),

$ROTI_{ave}$ is defined as;

$$ROTI_{ave}(0.5h) = \frac{1}{N}\sum_{n=1}^{N}\sum_{i=1}^{k}\frac{ROTI(n, 0.5h, i)}{k}; \tag{5.38}$$

where n is the satellite number, $0.5\sim$ h is half an hour $(0, 0.5,\ 1, \ldots 23.5, 24\sim \text{h}), i$ is the 5-minute section within half an hour $(i = 1, 2, 3, 4, 5, 6), N$ is the number of satellites observed within half an hour and k is the number of ROTI values available within half an hour for a particular satellite. The value of $ROTI_{ave} < 0.4$, $0.4 < ROTI_{ave} < 0.8$ and $ROTI_{ave} > 0.8$, respectively represent the background, phase fluctuations, and severe phase fluctuations (OLADIPO; SCHÜLER, 2013). These threshold values were used to observe the relation between the occurrence of ionospheric irregularities and the spatial gradient of TEC. Dugassa et al. (2019), Oladipo and Schüler (2013) showed that the $ROTI_{ave}$ is good for characterizing the climatology of EPB and irregularities over the equator. Damaceno et al. (2020) found a very good correlation between ROTI and the occurrence of loss of lock of GNSS over the Brazilian sector during solar cycle 24 showing that ROTI can be used as a proxy for scintillation. Pi et al. (1997), Damaceno et al. (2020) also showed that ROTI maps can be used to monitor irregularities on a global scale. This is particularly useful in Space Weather applications. Strong phase fluctuations measured in TEC over Brazil are associated with large dips in the line of sight TEC (EPBs) after sunset (KINTNER et al., 2004). Since the phase fluctuations are due to irregularities, ROTI has a strong correlation with the S_4 scintillation index (BASU et al., 1999; OLWENDO et al., 2018; LIU et al., 2016; LIU; RADICELLA, 2019). Hence there is a co-relation between the phase fluctuations given by the ROTI and the amplitude scintillation S_4 in the presence of ionospheric irregularities as plasma bubbles. Therefore, ROTI can be used as a proxy for the S_4 index (BASU et al., 1999; DAMACENO et al., 2020). In addition, ROTI has several benefits over S_4 and σ_ϕ because there is a large, readily available, data-set of GNSS receivers already deployed around the globe compared to scintillation receivers which have less coverage. ROTI also has a strong correlation with the magnitude of spatial gradients associated with post-sunset irregularities (DUGASSA et al., 2019). This facilitates better comparison between the multiple indices ROTI, S_4 index, and TEC gradients (∇TEC).

5.6.4 Estimation of ionospheric gradients from TEC

GPS signals encounter steep density gradients in the presence of ionospheric irregularities /plasma bubbles at equatorial and low latitudes (PI et al., 1997; KINTNER

et al., 2001; KINTNER et al., 2007). Pi et al. (1997) suggested that the rate of TEC changes could be converted to spatial gradients in TEC. There are two main sources of TEC gradients associated with EPB/irregularities after sunset. First, the side walls of the equatorial plasma bubbles give rise to steeper plasma density irregularities as the density abruptly changes from the background (PIMENTA et al., 2001; PRADIPTA; DOHERTY, 2016). Secondly, irregularities within the bubbles lead to weaker gradients with longer duration than the edge gradients. (PRADIPTA; DOHERTY, 2016) found severe TEC gradients of up to ±3 TECU/km over the South Crest of EIA in Brazil during solar maximum in the presence of EPBs. These gradients, therefore, introduce significant errors in GNSS positioning (CORREIA et al., 2018). In addition, if these gradients are over a certain ground station then it also the transmission of GBAS and SBAS error corrections (WALTER et al., 2001). It is necessary to detect and characterize these gradients to mitigate the effects on the ionosphere in the implementation of GBAS /SBAS. The occurrence pattern of steep gradients due to EPB has been characterized for GBAS and GNSS applications (PRADIPTA; DOHERTY, 2016). Three main methods that have been used to estimate gradients in the TEC from GNSS were presented by (LEE et al., 2006), and these are the station-pair method, the mixed pair (LEE et al., 2006) and the time-step (DATTA-BARUA et al., 2002) method shown in Figure 5.8. In this work, the spatial gradients in TEC were estimated using the time-step and station-pair methods. In this section, the three different techniques, their advantages, and disadvantages are discussed.

5.6.5 Station pair method

The Station-Pair method considers a pair of closely spaced GPS receivers in lock with the same satellite (PRN). The spatial gradient is given by the difference in TEC values between the two neighboring IPPs in a thin shell model (MISRA; ENGE, 2011) and fixed longitudinal separation between the two stations (LEE et al., 2006). This method gives an instantaneous estimate of the TEC gradient along the line segment chosen between the two stations. Ideally, the separation should not exceed the plasma bubble width, which varies between $300 - 750$ km. The spatial gradient between two locations A and B at epoch "i" (LEE et al., 2006), is given as,

$$\nabla TEC_{\perp} = \frac{VTEC_A(t_i) - VTEC_B(t_i)}{\Delta Long} \tag{5.39}$$

where i = 1 to 1440, and $\Delta Long$ represents the longitudinal separation between the two stations. The station pair method has been used to show a correlation

Figure 5.8 - The different methods for estimating TEC gradients.

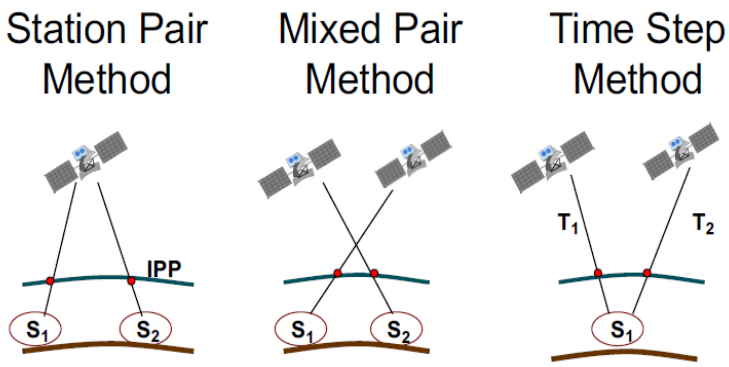

Satellite and Receiver Configuration for Station-Pair Method, Mixed-Pair Method, and Time-Step Method. The position of the IPP is shown at the two consecutive epochs T1 and T2.

SOURCE: Lee et al. (2006).

between the occurrence of irregularities (ROTI) and the spatial gradient in TEC in the equatorial region (DUGASSA et al., 2019). One advantage of the station pair method is that it gives unambiguous TEC gradients because it does not include temporal variation. Further, since only one satellite PRN is used, Inter-Frequency Bias (IFB) calibration error is minimized by taking the difference in TEC between the two receivers. However, the receiver IFB calibration error may still remain (LEE et al., 2006).

5.6.6 Mixed pair method

The Mixed-Pair method uses all possible combinations namely; two receivers paired with one satellite PRN, one receiver paired with two satellites, and two receivers paired with two different satellites (LEE et al., 2006). This method allows estimating the ionosphere gradients at both short and long baselines (DATTA-BARUA et al., 2002). The major disadvantage of this method is that satellite and receiver biases are compounded which increases uncertainty compared to the Station-pair and Time-step methods.

5.6.7 Time-step method

In this work, the time-step method was used. The method utilizes a single receiver-PRN pair as shown in Figure 5.8. The gradient along the path of the IPP ($\nabla TEC_{\parallel}$)

is the difference in the vertical TEC between the epochs T_1 and T_2 divided by the distance traveled by the IPP between the two epochs (DATTA-BARUA et al., 2002),

$$\nabla TEC_{\parallel} = \frac{VTEC_n(T_i) - VTEC_n(T_{i-1})}{\delta s_{ipp}}, \tag{5.40}$$

where $n(i = 1, 2, ..32)$ is the satellite PRN number. The distance traveled by the IPP δs_{ipp} was estimated by calculating the great circle distance using the displacement in geographic coordinates $\delta s(Lat, Lon)$,

$$\delta s_{ipp} = \sqrt{\delta Lon(T_i, T_{i-1})^2 + \delta Lat(T_i, T_{i-1})^2} \times 111km \tag{5.41}$$

In contrast to the station pair, the single-station method gives us an estimate of the TEC gradient along the direction parallel to the IPP trajectory. Of the three methods, it is the most reliable as it minimizes satellite and receiver biases. It is more accurate than the station pair method in Wide Area Augmentation System (WAAS) applications (DATTA-BARUA et al., 2002). One limitation of the time-step includes the temporal variation in TEC along the IPP path giving ambiguous gradients. This means it does not explicitly distinguish between spatial variations in TEC. This is mitigated by the "frozen in" assumption where changes due to ion production or recombination are negligibly small over the time-step interval of $30s$ for GPS (PRADIPTA; DOHERTY, 2016). In the case of the two-station method is advantageous in that it gives strictly unambiguous gradients.

5.7 Amplitude scintillation index

The amplitude scintillation index S_4 (BRIGGS, 1975), a statistical index that measures scintillation of the signal amplitude, which is frequent over the equatorial and low-latitudes (KINTNER et al., 2004). Scintillation occurs when GPS signals encounter plasma bubbles producing rapid amplitude fluctuations (diffractive scintillations) Kintner et al. (2007), and if the irregularities are intense enough cause loss of lock (KINTNER et al., 2001; KINTNER et al., 2007). This index is derived from special high-frequency GNSS receivers called scintillation monitors. The phase scintillation index, σ_ϕ, measures phase variation and is defined as the standard deviation of the detrended phase (YEH; LIU, 1982) σ_ϕ in radians (KINTNER et al., 2007). The amplitude scintillation index, which is defined as the normalized standard deviation of the received signal intensity according to Kintner et al. (2001) is

expressed as;

$$S_4 = \frac{\sqrt{\langle I^2 \rangle - \langle I \rangle^2}}{\langle I \rangle} \tag{5.42}$$

Table 5.3 - Classification of amplitude scintillation index.

Level	Scintillation Intensity
$0.1 < S_4 < 0.25$	Weak
$0.25 < S_4 < 0.7$	Moderate
$S_4 > 0.7$	Strong

The intensity of amplitude scintillation derived from high frequency (50Hz) GNSS receivers showing how the classification according to severity.
SOURCE: Correia et al. (2018).

S_4 is obtained from high-frequency 50 Hz scintillation operating in the GPS L1 Band(1575.42 MHz) (RASTOGI; KLOBUCHAR, 1990). In the L1 Band amplitude scintillation is due to irregularities of the order of ∼400m, which corresponds to the first Fresnel zone of the radio wave close to the ionospheric F layer peak height (PAULA et al., 2007; BHATTACHARYYA, 2022; KINTNER et al., 2001). Only $S_4 \geq 0.2$ was considered to minimize noise in the signal. The S_4 data used was accessed from the Low-Latitude Ionospheric network (LISN) as well as for the CIGALA /CALIBRA network. To obtain a wider coverage of data over the Brazilian region, the two networks were integrated. LISN has more receivers in the South-Eastern and North-Eastern region of South America while CIGALA/CALIBRA has a wider continental coverage as shown in the map 5.9.

It can be observed on the map that the two networks complement each other in data coverage. The individual stations were selected according to magnetic inclination and hence data from the IGRF−13 model was used to determine the inclination.

5.8 Estimation of vertical drifts from ground-based magnetometers

Near the magnetic equator, there is a large enhancement in the H-Component due to a rise in the Cowling conductivity. It leads to an intense Eastward current system located at around 100 km in altitude in the E region called the *Equatorial Electrojet* (KELLEY, 2009). This current is a measure of the equatorial electric field and can be detected as an enhancement in the H-component of the magnetometer. This EEJ is responsible for the vertical $E \times B$ drift near the magnetic equator. There is a strong linear relationship between the magnitude of ΔH and the $E \times B$ drift (ANDERSON et al., 2002). The quiet-

Figure 5.9 - Location of Scintillation Monitors over South America on the LISN & CIGALA /CALIBRA network.

time electrojet is driven by thermospheric winds in the neutral atmosphere. However, during geomagnetic disturbances, the electrodynamics of the low-latitude ionosphere can be severely altered. The ΔH is, therefore, an effective method to infer the presence of penetration electric fields that may enhance or suppress the $E \times B$ drift which is critical to the formation of irregularities. By computing the difference between the H-component at an equatorial site and another location outside the EEJ ($\sim 6-9°$ geomagnetic latitude), the magnitude of the EEJ can be estimated (ANDERSON et al., 2002). This subtracts the contribution of the ring current and global solar quiet component (ANDERSON et al., 2002). In order to avoid different offset values of different magnetometers, the nighttime baseline values in the H component are first obtained for each day and subtracted from the corresponding magnetometer data sets. The baseline value was defined as the average of the H-component nighttime (23:00–02:00 LT) value of the Earth's magnetic field (ANDERSON et al., 2002) as,

$$H_0 = \frac{H_{23} + H_{24} + H_{01} + H_{02}}{4} \tag{5.43}$$

The hourly departure for each magnetometer is obtained from;

$$\delta H(t) = H(t) - H_0 \tag{5.44}$$

where t is the time in hours ranging from 01:00 to 24:00 LT. The δH is obtained as,

$$\Delta H = \delta H_A - \delta H_B, \tag{5.45}$$

where A is the magnetometer located at the equator while B is the off-equator site.

6 CHARACTERISTICS OF THE DEEP SOLAR MINIMUM OF 2018 AND THE EQUATORIAL-LOW LATITUDE IONOSPHERE OVER BRAZIL

In this chapter, the results of the solar minimum of 2018 are presented, starting with the variation of solar flux, coronal holes, solar wind, and the subsequent geomagnetic storms mainly driven by HSS/CIRs. Thereafter, the diurnal, monthly and seasonal variability in TEC, strength of irregularities (ROTI), spatial gradients (∇TEC) and percentage deviation of TEC from quiet time δTEC obtained from GNSS receivers in Brazil is presented in Chapter 7. Finally, in Chapter 8 selected case studies of geomagnetic storms and how they impacted the equatorial and low-latitude ionosphere over Brazil are discussed. Lastly, the statistics of ionospheric storms in TEC during 2018 are presented.

6.1 Solar flux, Coronal Holes, Solar Wind and Geomagnetic Storms during the deep solar minimum of 2018

As mentioned in Chapter 1, solar cycles 23 and 24 were characterized by low solar activity. It ranks as the deepest solar Minimum in the century (RUSSELL et al., 2010; JIANG et al., 2015). Figure 6.1 shows the variation of the solar flux index, F10.7, in SFU. On average, F10.7 was around 69 SFU. Such levels of solar activity have been likened to the Maunder minimum of 1645–1710 when few sunspots were observed while temperatures dropped, leading to the freezing of ice glaciers. During SC23, the daily mean solar flux increased by 200% from 85 SFU during solar minimum to 235 SFU at solar maximum (JONAH et al., 2015). This was associated with a corresponding increase in TEC of 400% (JONAH et al., 2015). It is well known that the high daily solar flux variability (FUV) leads to high diurnal variability of the ionosphere plasma density(JONAH et al., 2015).

Low latitude coronal holes are the source of high-speed streams, HSSs which interact with forward slow streams forming co-rotating interaction regions, CIRs (KRIEGER et al., 1973). HSSs are the main drivers of geomagnetic storms during the declining phase and solar minimum (TSURUTANI et al., 2006; ABRAMENKO et al., 2010). Unlike storms caused by CMEs, CIR/HSS-driven storms are less intense and have a longer duration, $\sim$5 days on average, compared to CME storms (TSURUTANI et al., 1995; VERKHOGLYADOVA et al., 2011).

The geomagnetic storms which occurred during 2018 were characterized as follows; first, the source of the geomagnetic storm (solar flare/CME/coronal hole) was identified using observations from https://www.solen.info/solar/. The solar wind, IMF parameters, and geomagnetic indices were then analyzed thereafter to assess the influence of solar wind on the magnetosphere and consequently geomagnetic storms.

Figure 6.1 - Daily and monthly-averaged solar flux from 2018–2021 covering the minimum of solar cycle 24 and the ascending phase of cycle 25.

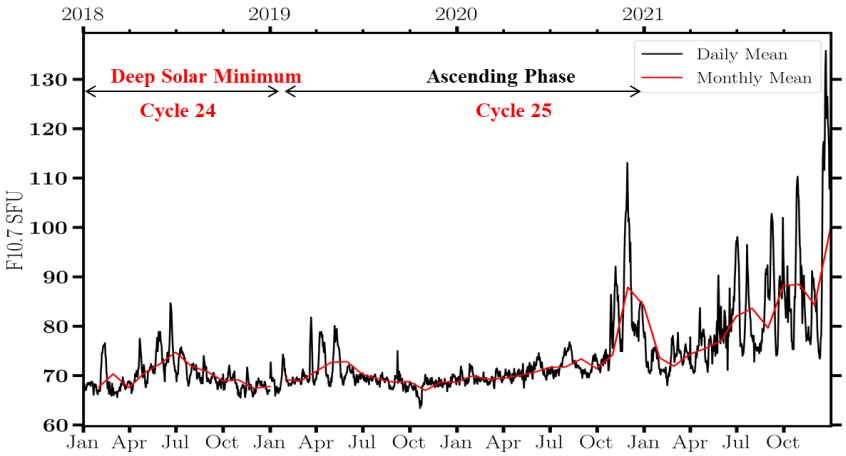

6.2 Features of Coronal Holes during 2018

There is a constant flux of particles which constitute the ambient solar wind, at a speed of less than $400 km/s$. However, from time to time HSSs from coronal holes which exceed this speed can reach $800 km/s$. Figure 6.2 illustrates the features of selected coronal holes observed during 2018. The figure shows images of 171, 193 and 211 Å emissions, taken from NASA SDO imager, for (a)-(b) 14 & 29 May (c) 24 August and (d)-(e) 7–10 October; and (f) 03 Nov 2018 identified using the multi-thermal emission recognition algorithm (CHIMERA). The details of the algorithm are outlined in (GARTON et al., 2018). The CH (dark blue) are outlined/segmented by white lines. A total of 43 CHs were detected in 2018 (Carrington rotations 845–901) according to (SOLEN, 2020).

The characteristics of coronal holes such as location, fragmentation, shape, and size are shown.The CHs observed on 14 May, (a) and 29 May(b), on 10 October (e) are located in the Southern Hemisphere while the CH on 24 August (c) was located in the Northern Hemisphere. The rest of the CHs are trans-equatorial. Another feature is the presence of weak prominences near the CHs, particularly in August and October, as seen in (a), (b) and (c). It can be noted that in each of the weaker storms in (a) and (b), there was a prominence close to the CH. These were much brighter than the solar flare /CME in (c). This supports the idea that the effectiveness of a CME may be weakened by the existence of CH since they are known to interact with CMEs and, in some cases, deflect CMEs away from the Sun-Earth line rendering them ineffective (GOPALSWAMY et al., 2009). This effect is likely prevalent during the descending phase of the solar cycle where there is an abundance of low-latitude CHs close to the disk center and will be the subject of future work (TSURUTANI et al., 2006; ABRAMENKO et al., 2010). The statistics of

Figure 6.2 - 171, 193 and 211 Angstrom (Å) emissions images from NASA SDO on 14 May & 29 May; 24 August; 7,10 October and 3 November 2018 showing CHs from CHIMERA segmentation tool. The minimum Sym–H for the associated geomagnetic storm is indicated in each panel. Small prominences can be seen in the images.

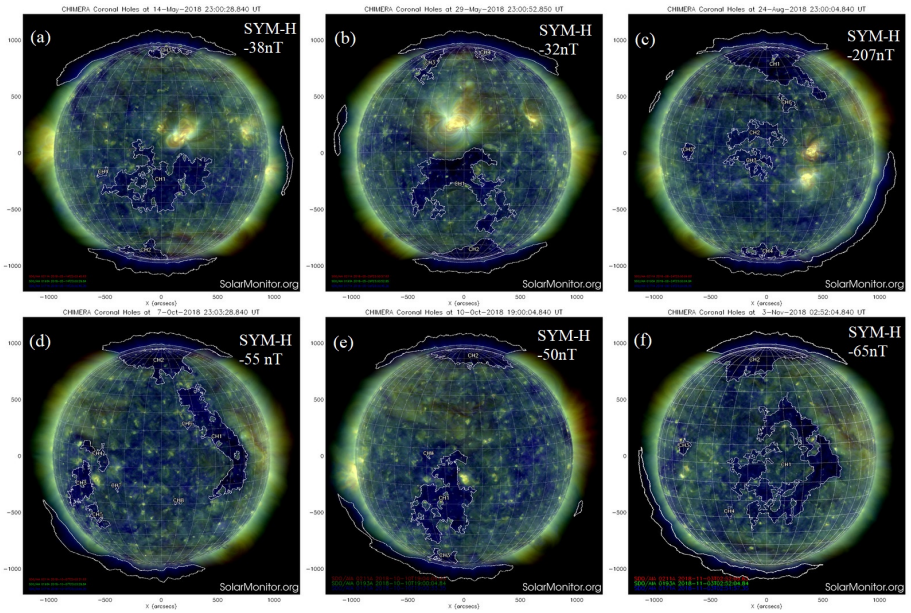

the ionospheric storms caused by these CH during the year 2018 are presented in later chapters.

6.3 Characteristics of Solar wind, Interplanetary Magnetic Field and Geomagnetic activity

In this session, we discuss the general features of the solar wind, IMF and geomagnetic indices associated with the geomagnetic storms caused by CIRs/HSS in 2018. Figure 6.3 shows, from top to bottom panel, the variation of solar wind speed, $v_{sw}(km/s)$; Proton temperature, $T_p(K)$; proton density, $N_p(cm^{-3})$; magnetic field magnitude, $|B|$, and its respective components, B_x, B_y and B_z in the GSM coordinate system; the interplanetary electric field, IEF E_y(mV/m); the 5-min ring current index, $Sym-H(nT)$; auroral electrojet index, $AE(nT)$; the planetary index, K_p; and finally, the solar flux index, F10.7(SFU). The solar wind speed, V_{sw}, varied between $267km/s$ and $\sim 720km/s$. The average speed was 548 km/s while the mean proton temperature was $7.4 \times 10^5 K$ and the mean plasma density was $7/cm^3$. The average Kp was 1.5 while the mean of the IMF magnitude, $|B|$, was $\sim 5nT$. IMF B_z had a minimum of –$17nT$ and maximum of $12nT$. This variability in the solar wind and IMF parameters is typical of HSS/CIR-driven geomagnetic activity which is generally weaker than the activity driven by CME-driven storms which can

Figure 6.3 - Solar wind, interplanetary parameters and geomagnetic indices for the year 2018. Vertical red boxes and arrows indicate the selected representative case studies for CIR/HSS geomagnetic storms.

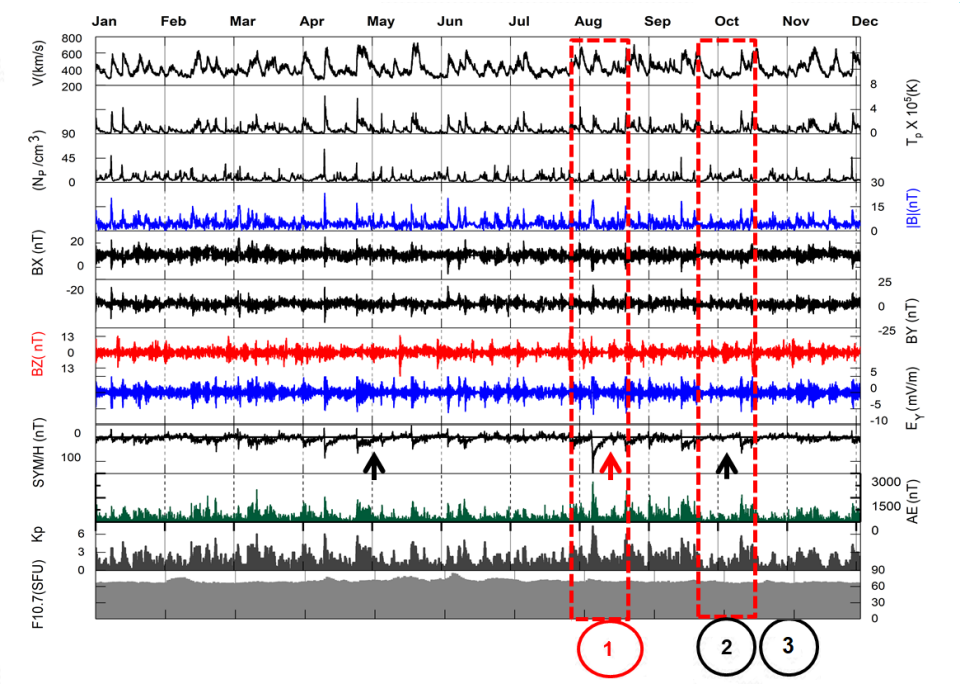

reach minimum $B_z \sim -30nT$, $|B| > 30nT$ and $E_y \sim 40mV/m$ (CANDIDO et al., 2018). Several HSSs were detected in the year 2018. It can be observed that the V_{sw} exceeded 400 km/s for several occasions followed by increases in $T_p(K);=$, $n_p(cm^{-3})$ and $|B|$. The longest duration of the HSS that caused a storm was ∼10 days during May and September whose sources were CH863 and CH886 respectively, while the shortest stream lasted 3.5 days during February from CH854. The average duration of the HSSs in 2018 was 6.2 days which indicates lengthened geomagnetic disturbances during solar minimum as was described by (ABRAMENKO et al., 2010; GIBSON et al., 2011).

6.3.1 Periodicity of Solar Wind

To investigate the periodicity of HSSs from CHs which drive geomagnetic activity, the Continuous Wavelet Transform (CWT) was used. Figure 6.4 shows on the top panel: the solar wind speed, and at the bottom panel: the Morlet wavelet spectral analysis for the year 2018. The solar wind speed shows 4,7, 9, 13.5 and 27-day periodicity throughout the year. From April to June and January–December the 13.5-day sub-harmonic coincides with peaks in v_{sw} (Figure 6.4 (top)). These occurred during the interval for CIR-driven geomagnetic storms shown in Figure 6.3. Weaker 4-7 and 9-day periodicities are also present which are sub-harmonics of the 27-day solar rotation period (VERKHOGLYADOVA et

Figure 6.4 - Spectral analysis of the solar wind speed. Top: Solar wind speed measured by the ACE satellite for 2018. Bottom: Continuous wavelet transform (CWT) power spectrum distribution of the solar wind speed. Strong 13.5 and 27 days periodicity is clearly shown.

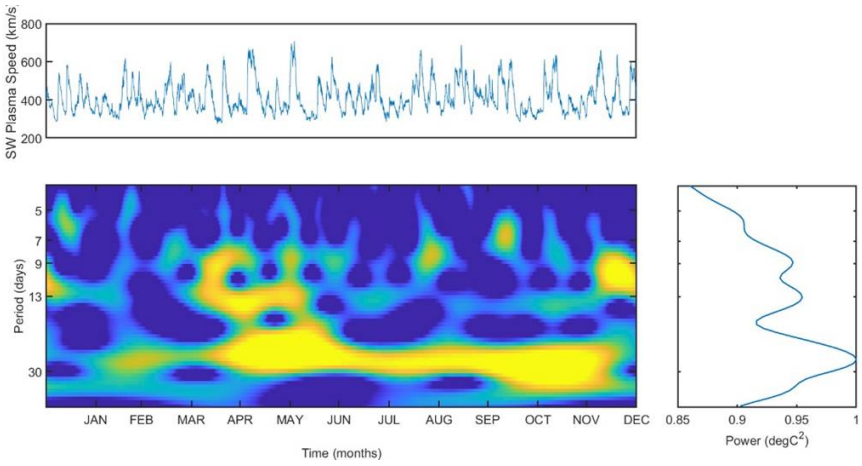

al., 2011; JONAH et al., 2015; CANDIDO et al., 2018). Further, Emery et al. (2011) also reported that the periodicity in v_{sw} among other solar wind, IMF parameters and F10.7 cm solar flux during SC23 minimum was dominated by HSS. The 13.5-day periodicity in solar, heliospheric, and geomagnetic indices has been attributed to the occurrence of two high-speed streams which emerge simultaneously from CHs in both the Northern and Southern hemispheres during each solar rotation (MURSULA; ZIEGER, 1996; EMERY et al., 2011). This is highly plausible considering the presence of several large and co-latitude CH during deep solar minimum as was presented in the previous section.

Oscillations in the B_z and IEF E_y were also prevalent during the long recovery phases of CIR-driven storms. The solar flux F10.7 was fairly constant with an average of 72 SFU, a minimum of 65 SFU, and a maximum of 85 SFU. This is considered very low solar flux conditions even for solar minimum (DERGHAZARIAN et al., 2021) and is consistent with findings by Abreu et al. (2017), Candido et al. (2018) who reported topside ionospheric response under similar levels of solar activity (F10.7 69 SFU) during SC23. F10.7 index was fairly constant which clearly shows that no such events were observed consistent with previous findings on deep minimum by Verkhoglyadova et al. (2011), Basu (2013), Hady (2013), Jiang et al. (2015). The AE index variation shows significant continuous auroral activity, although the intensity was mostly below 2000nT. These variations are indicators of continued injection of energy from the magnetosphere (TSURUTANI et al., 2006).

During 2018, the geomagnetic activity storms were mainly weak-moderate i.e., with minimum Sym–H > -50 nT. The majority of these storms had a maximum $Kp < 6$ except

for the intense CME-driven storm in August. These results of solar wind and IMF is in agreement with Candido et al. (2018) who investigated the variability of solar wind and IMF parameters during HSS/CIRs storms in the SC23 minimum of 2008-09.

A total of 28 geomagnetic storms occurred in 2018 according to the Sym–H, 27 of these were moderate, caused by HSS/CIRs. This result is in agreement with Grandin et al. (2019) compiled a catalog for HSS/CIRs from 2009–2019 using an automated event detection algorithm (see http://www.geodin.ro/varsiti/. A unique, intense storm, Sym–H $\sim -205nT$, occurred in August 2018, driven by the interaction between a CME and a HSS/CIR. This storm was 3 times more intense than the average minimum other Sym–H of the rest of the storms. Figure 6.3 shows the geomagnetic activity during the year 2018. The marked storms were chosen for detailed case studies to be presented.

No significant disturbance according to Sym–H was observed in the months of January, July, and December (min Sym–H$> -20nT$) which also coincides with the absence of HSSs. Considering the magnitude of the Sym–H, it is evident that the geomagnetic activity had a semi-annual variability, as more storms were observed during the equinox compared to the solstices (MATAMBA; HABARULEMA, 2018). This is attributed to the Russell-McPherron effect, in which the IMF Bz has a statistical probability of 50% of having southward polarity each year (RUSSELL; MCPHERRON, 1973). The first half of 2018 was characterized by low solar wind speed and weak magnetic field in the solar wind compared to previous minima which is in agreement with previous observations of deep solar minimum by Gibson et al. (2011). In the next chapter, the hourly, diurnal and seasonal variability of the equatorial and low-latitude ionospheric ionosphere using multiple parameters and indices derived from GNSS TEC during this period of solar minimum is discussed.

7 CLIMATOLOGY OF THE BRAZILIAN EQUATORIAL & LOW LATITUDE IONOSPHERE DURING DEEP MINIMUM 2018

In this chapter, the climatology of TEC and the ionospheric indices derived from GNSS receivers located in the Brazilian equatorial and low-latitude ionosphere in the year 2018, during the solar minimum of Solar Cycle 24 is presented. The local seasons are grouped as follows; March Equinox (March–May), June/Winter Solstice (June–August), November Equinox (September–November) and December/Summer Solstice (December–February). The following representative stations were used: Boa Vista (BOAV: 2.83° N, 60.69° W; dip Latitude 9.2° N) within the northern crest of the EIA; Cuiabá (CUIB: 15.55°S, 56.10°; dip latitude 7.6° S) and Campo Grande (MSCG: 20.50° S, 54.70° W; dip latitude 11.8° S) located around the southern crest of the EIA. These two last stations are used interchangeably in case there is no data for one of them. BOAV and MSCG are considered conjugate points as they are roughly on the same geomagnetic field line. A station at the dip equator Belém (BELE 1.40° S, 48.4° W; dip latitude 0.3°), and two near-equatorial stations; São Luís (SALU: 2.59° S, 44.12° W; dip latitude 3.7°S) located and Monte Carmelo (MTCO: 10.8°S, 48.3°W; dip latitude 4.9° S), west of São Luís, were selected.

7.1 Diurnal, monthly and seasonal variability of TEC

Figure 7.1 presents the VTEC variation for (a) left top and bottom panel: BOAV and MSCG (north and south crests of EIA); (b) right top and bottom panel: SALU and MTCO (stations close to the magnetic equator) as a function of universal and local time, UT (left) and LT (right), respectively and month (horizontal axis) for the year 2018. It can be observed that VTEC over Brazilian low-latitude shows a high hourly, diurnal, seasonal and semi-annual variation. The diurnal variations of GPS-TEC are evident from the plots. In general, the minimum is observed in the pre-dawn at ∼08:00 UT (05:00 LT) and the maximum is observed in the afternoon at ∼16:00 LT (19:00 UT).

The maximum values in VTEC occur during the March and September Equinoxes (∼ 40–45 TECU) followed by the December solstice (∼ 20–30 TECU) while minimum TEC is seen during the June solstice. During the equinoxes, TEC starts peaking earlier at 11:00 LT (14:00 UT) compared to the solstice ∼13:00 LT (16:00 UT). Semi-annual variation is also present since TEC during equinoxes is generally greater than during solstices (JONAH et al., 2015; ROMERO-HERNANDEZ et al., 2018). Semi-annual variability in TEC over Latin America has also been reported by Romero-Hernandez et al. (2020), Wu et al. (2004), Dias et al. (2020). TEC also shows a latitudinal variability, with peaks at around ±15° dip latitude, regions referred to as the crests of EIA located at Boa Vista and Campo Grande while lower values are seen at São Luis, a near-equatorial station. As previously mentioned, EIA is formed when the $E \times B$ vertical drifts due to the zonal electric field, drives plasma up to higher altitudes where it subsequently diffuses along the field lines to form peaks in

Figure 7.1 - Contour plots of VTEC as a function of universal (left) and local time (right)and month (horizontal axis) during 2018, at Boa Vista & Campo Grande (left panel); São Luís and Monte Carmelo (right panel). Where LT = UT–3. The dip latitude is indicated for each station. The white bands indicate gaps in data.

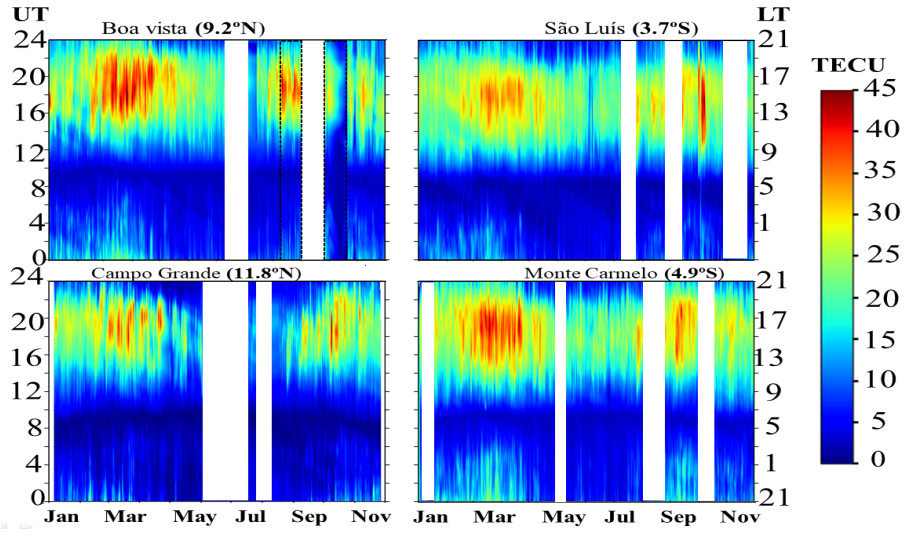

plasma density located at ±15° dip latitude (DIAS et al., 2020; KELLEY, 2009). Since Monte Carmelo is closer to the EIA, TEC presents larger values than in São Luís. It can be seen that the EIA also exhibits seasonal and semi-annual variation as well, with peaks during March and September Equinoxes. Abreu et al. (2017), Verkhoglyadova et al. (2011), Jonah et al. (2015), Candido et al. (2018) investigated the variability of TEC during SC23 minimum over the equatorial and low-latitude sector and found low levels of VTEC 0–30 TECU compared to 0–45 TECU which we found during SC24 minimum. Jonah et al. (2015), Abreu et al. (2017), Romero-Hernandez et al. (2018) reported similar seasonal and semi-annual variations in TEC over South America. Jonah et al. (2015) showed that the variability in TEC over, Brazil occurs in the afternoon and post-sunset sector compared to the pre-dawn minimum. This clearly shows the influence of thermospheric winds and electric fields which are driven by solar heating has an important role in the dynamics of the low-latitude ionosphere. The level of TEC is modulated by the neutral composition ratio [O]/[N2] given that the seasonal and semi-annual variation in TEC is mainly determined by the [O]/[N2] (TITHERIDGE, 1974). The [O]/[N2] is higher in summer and lowest during the winter solstice because of a larger scale height of N2 which increases the rate of recombination, leading to lower ionization(TITHERIDGE, 1974). Lower winter TEC values during the winter solstice (June-July) have been attributed to the minimum in solar flux EUV (ROMERO-HERNANDEZ et al., 2020) which is responsible for the production of ionization (RISHBETH; GARRIOTT, 1969).

7.2 Variability of the Equatorial Ionization Anomaly

To illustrate more clearly the variation in TEC over the EIA in Brazil during the equinoxes, Figure 7.2 shows the TEC variation during the months of March and September equinoxes, for the two representative crests of EIA: BOAV and MSCG (left top and bottom panel, respectively) which are also conjugate points, near-equatorial locations AMCO–MTCO, MGMT/MSCG/PPTE located at ±15–20° latitude near the South crest and lastly CHPI is located outside the crest of the EIA.

Figure 7.2 - VTEC hourly, diurnal (doy), and monthly variation for eight representative Brazilian stations during Autumn equinox (March) (left) and Spring equinox (November) (right) illustrating the equinoctial and hemispheric asymmetry in the EIA.

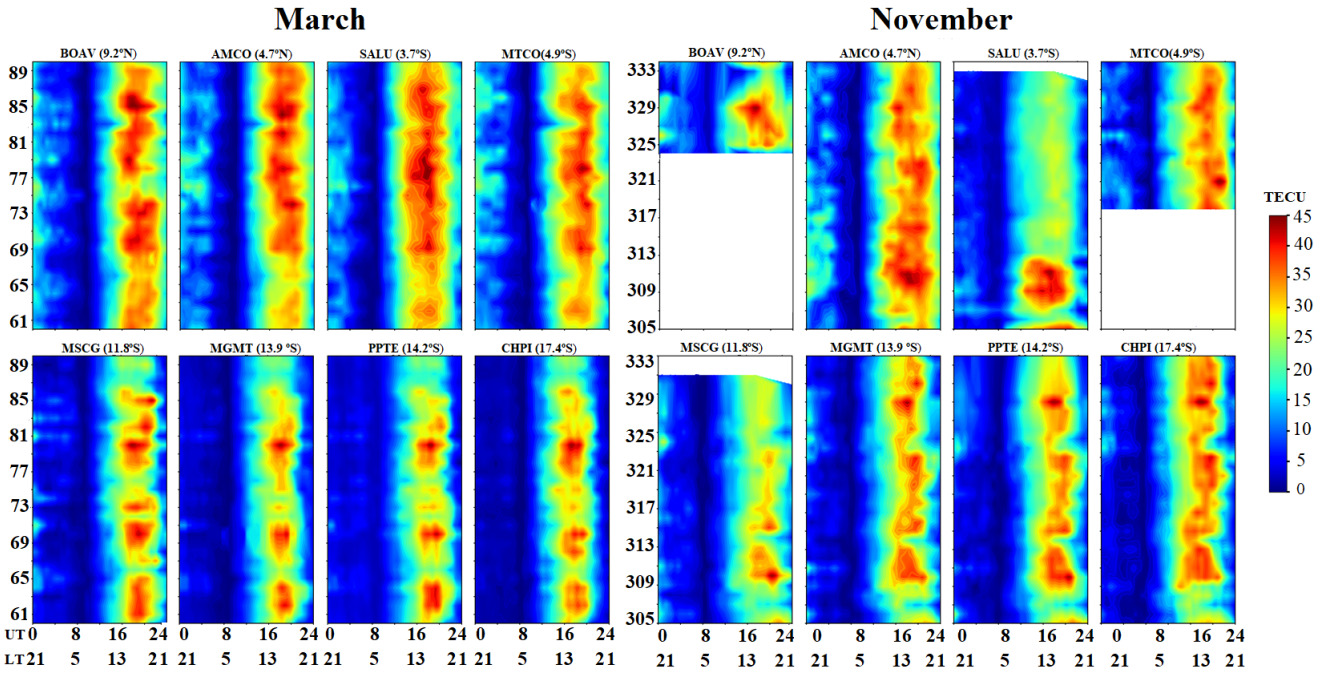

As shown in Figure 7.1, TEC is maximum over the EIA and decreases with dip latitude. Equinoctial asymmetry is evident, in most cases, the Autumn equinox (March) is stronger than the Spring equinox (November). Considering that the stations are arranged in decreasing latitude some significant differences can be observed between the top and bottom panels. The TEC amplitude is generally higher over the dip latitude sector, 9.0°N–5.0°S (top panel) compared to the 11.0° S–18.0°S sector (bottom panel). To summarize, the variability of TEC, Figure 7.3 presents the distribution of the maximum TEC (TECmax)

and average TEC, for each of the 4 seasons considering the four most representative stations from Figure 7.2. Similar seasonal and semi-annual variability is shown for both. As expected, higher values are observed during equinox and over the EIA (BOAV, PPTE) compared to the equator.

Figure 7.3 - Seasonal TEC distribution: (a) top panel: maximum VTEC and (b) averaged VTEC obtained over 4 Brazilian representative stations. The dip latitude is indicated in brackets.

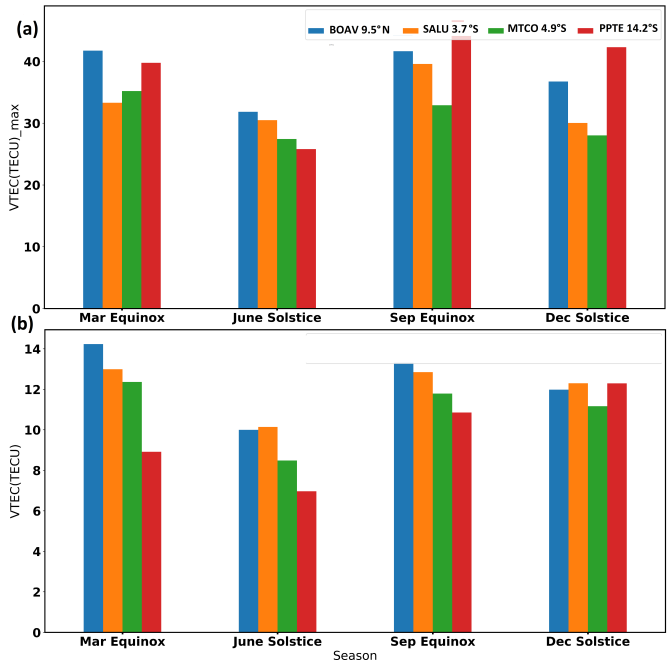

Dias et al. (2020) investigated the daily and monthly variations of the EIA using TEC over Brazil during the descending phase of Cycle 23. They found that the magnitude of the TEC at the EIA crests ranged up to 50 TECU from September to November. They also showed that the EIA is stronger during the equinox than solstice. Our results for solar minimum seem to be in agreement with this. Equinoctial asymmetry has been explained in terms of the differences in meridional winds leading to changes in thermospheric [O]/[N2] density ratio during the equinoxes as mentioned earlier. While changes in the solar zenith angle and the magnetic field geometry are responsible for the semi-annual variation in the EIA (WU et al., 2004; JONAH et al., 2015). During the equinox months, the subsolar point is above the equator which drives a larger equatorial electrojet electric field responsible for the fountain effect (ROMERO-HERNANDEZ et al., 2018). This also results in more production of ionization leading to a much stronger fountain effect (WU et al., 2004) while in the solstice, the subsolar point is over higher latitudes hence the fountain effect

is weaker. In addition, during the equinoxes, meridional winds flow from the equator toward the poles, by increasing the neutral composition ratio over latitude [O]/[N2] which increases the magnitude of the EIA crests (FULLER-ROWELL et al., 1996; WU et al., 2004). Thus, transequatorial winds are more effective in blowing plasma poleward whereas, during the summer solstice, the neutral wind can inhibit the strength of the EIA pushing plasma in an opposite direction as it diffuses downward from the magnetic equator (WU et al., 2004). The observed asymmetry between the equinoxes has been explained in terms of the differences in meridional wind circulation, which lead to changes in neutral gas composition (DANILOV et al., 1994). The North-South hemispheric asymmetry is attributed to meridional winds, which drive the stronger EIA crest toward the Northern Hemisphere during the March equinox. Additionally, these factors change during geomagnetic storms, where the TEC usually peaks much earlier than during quiet time (WU et al., 2004; FAGUNDES et al., 2016). The winter solstice had the lowest magnitude in all derived parameters VTEC, deviation in VTEC, ROT, ROTI and S4.

7.3 Climatology of TEC gradients and plasma irregularities over the Brazilian region

In this session, we present the GNSS TEC variation and derived indices to provide a detailed description of the equatorial and low latitude ionosphere during deep solar minimum 2018. Figure 7.4 shows the variability of the hourly averaged TEC, hourly averaged δTEC, and 10-minute averaged ROTI over an equatorial station, São Luís (SALU).

Figure 7.4 - TEC, δTEC, and ROTI variation in 2018 over São Luís. The maximum value for each parameter is indicated at the top of each panel.

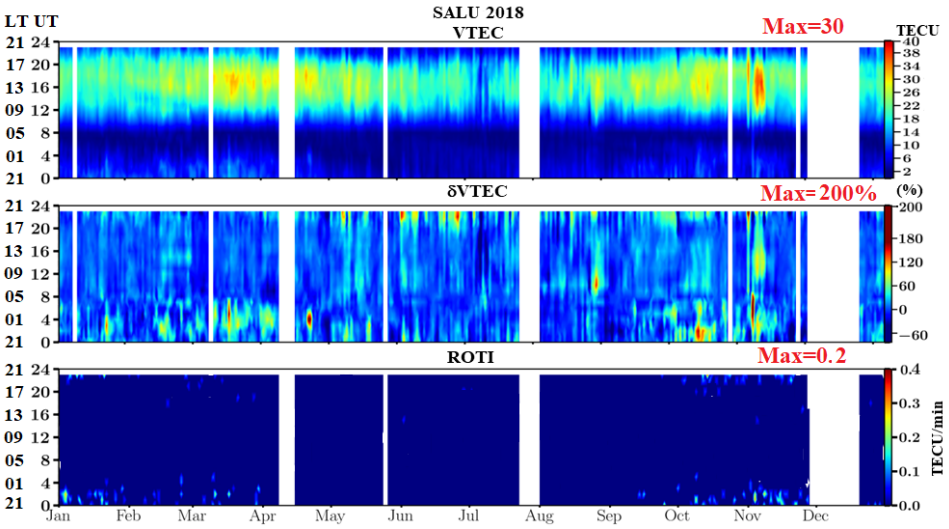

Large day-to-day TEC variability, as well as the peaks during equinoxes up to 30 TECU can be clearly seen in Figure 7.4. On the other hand, the $\delta VTEC$ (middle panel), which is the difference of the current day with the five quietest days in each month, presents a larger and more sporadic variation compared to the TEC and the 10-minute ROTI. The magnitude of $\delta VTEC$ is predominantly it is higher at nighttime during equinoxes. The maximum $\delta VTEC$ was around 200% at 6–18 UT (09:00–18:00LT) during a geomagnetic storm that occurred during November. The observations from ROTI show the occurrence of plasma irregularities between 21:00–06:00 UT (20:00–03:00 LT) during the local post-sunset to the post-midnight sector. The maximum amplitude of 0.2 TECU/min occurred between 21:00–01:00 LT. This level of ROTI is classified as moderate to strong irregularities according to criteria by (PEREIRA; CAMARGO, 2014) although larger amplitudes (ROTI=0.5) during solar minimum have been reported over South America by Pi et al. (1997). No significant irregularities were observed during daytime 09:00–21:00 UT (06:00–18:00 LT). Figure 7.5 shows the climatology of TEC, $\delta VTEC$, and 10-minute averaged ROTI at the north and south crests of EIA, Boa Vista, BOAV and Campo Grande, MSCG, respectively. The vertical axis is the Local and Universal time (LT = UT–3) (left) and the horizontal axis is each day of the year.

The variation over the crests of the EIA is shown in Figure 7.5. TEC exhibits seasonal and semi-annual variation, with peaks during equinoxes, as the maximum is seen during the March equinox at BOAV having a maximum of ∼45 TECU compared to 40 TECU at MSCG (latitudinal asymmetry). As it is expected, TEC values are higher than those observed in the equatorial region. $\delta VTEC$ is highly variable, revealing that geomagnetic storm effects vary between daytime and nighttime. The magnitude of ionospheric storms (positive and negative) is more significant during equinoxes compared to solstice. The percentage deviation, $\delta VTEC$, observed at MSCG, was $\sim 180\%$ during another geomagnetic storm in November. In addition, the magnitude of TEC was greater over Boa Vista than Campo Grande, indicating hemispheric asymmetry. Comparing the equator and EIA, a clear correlation between enhanced daytime electron density and strength of post-sunset irregularities is observed. Figure 7.6 shows the hourly, diurnal and seasonal variation of ROTI over 3 stations located in Brazil. It can be seen that irregularities occur during the equinox between 21:00 and 03:00 LT. Considering the magnitude of irregularities, our results show that ROTI is higher from September to April, which is the expected seasonal variation of EPBs and scintillation (PAULA et al., 2007; CORREIA et al., 2018; JESUS et al., 2020). The climatology of EPB/irregularities is controlled by the magnitude of the peak vertical $E \times B$ drift at the PRE (ABDU et al., 1981; KELLEY, 2009). In addition, the strength of irregularities is clearly larger over the EIA crests compared to the equator, consistent with Sobral et al. (2002). The difference has been attributed to higher background density, which causes larger gradients compared to the large depletions within the EPBs (ABDU et al., 2009). To summarize the behavior of irregularities, Figure

Figure 7.5 - Climatology of TEC, $\delta VTEC$, and ROTI at the north and south crests of EIA, Boa Vista, BOAV and Campo Grande, MSCG, respectively. The maximum values for each parameter are indicated above.

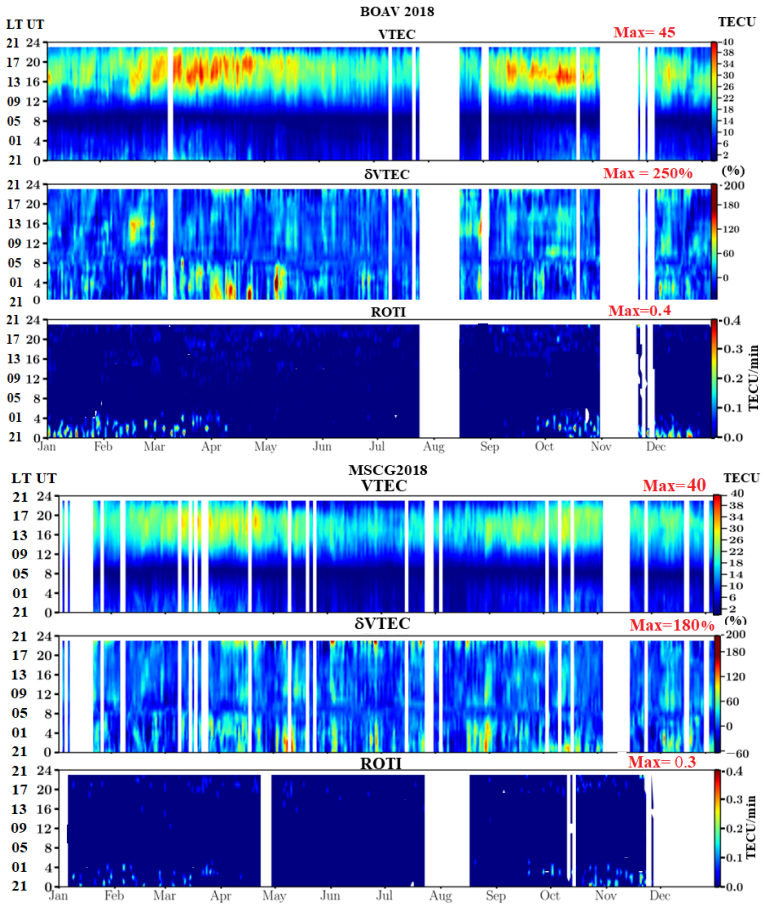

7.7 (top) shows the seasonal and semiannual variation of ROTI at 4 stations, while the bottom shows the monthly frequency of strong irregularities. The frequency was obtained by taking the nights which had maximum ROTI >0.2 and dividing by the total observed nights.

$$\text{Occurrence Rate} = \left(\frac{\text{Number of nights with maximum ROTI } >0\ .2}{\text{Total number of nights observed}}\right) \times 100\% \qquad (7.1)$$

Figure 7.6 - Climatology of 10-minute ROTI at the north and south crests of EIA, Boa Vista, BOAV and Campo Grande, MSCG, respectively and at the equator (SALU).

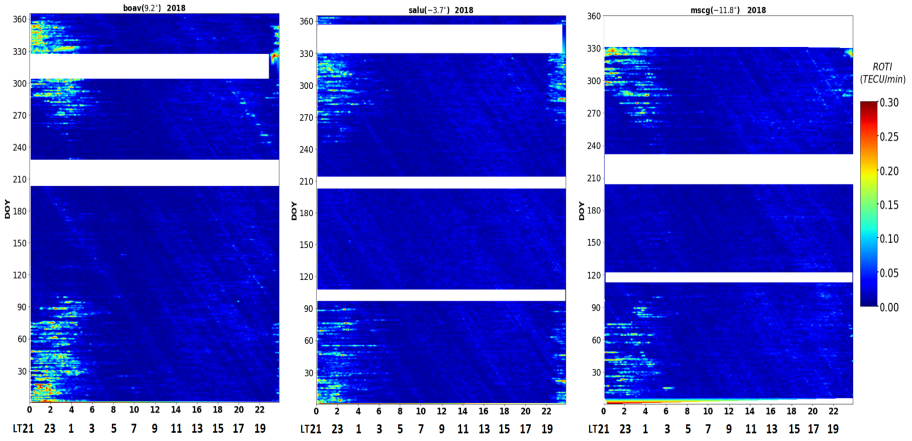

Figure 7.7 - Top: Climatology of 10-minute ROTI at 4 locations over Brazil during solar minimum. The blue and red lines mark the threshold for moderate and strong irregularities respectively. Bottom: The monthly frequency of strong irregularities during 2018.

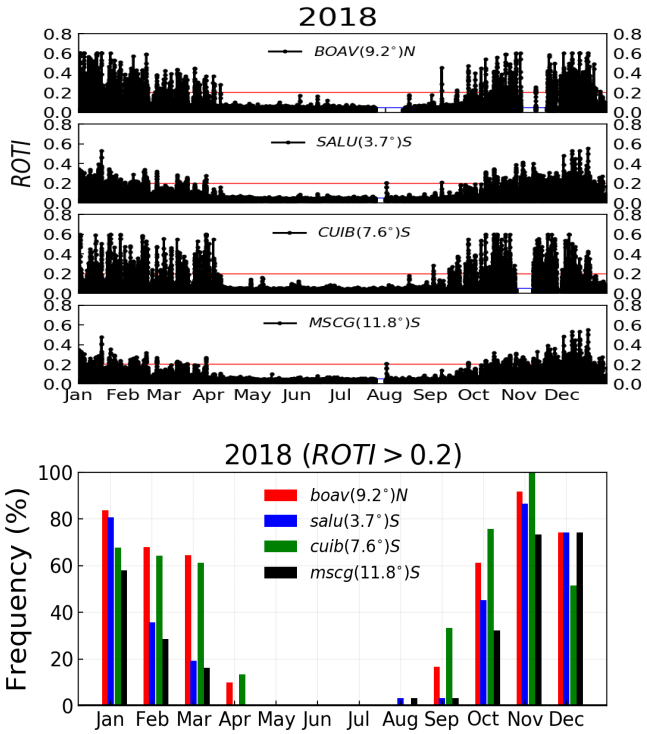

A total of 328 nights were analyzed at BOAV, 358 at SALU, 358 at MSCG days, and 320 at CUIB. It can be observed that the magnitude of ROTI is higher during the equinox over the EIA crests, although the magnitude is lower over MSCG. This could be because it is located at the edge of the south crest and hence the plasma density decreases leading to weaker irregularities. The frequency of strong irregularities exhibits similar behavior however the frequency was clearly higher during the transition from the spring equinox to summer solstice with a maximum of 100% during the month of November compared to 65% during the March equinox. In the next chapter, special case studies of geomagnetic storms of different magnitudes and their effect on the magnetosphere and ionosphere over the Brazilian equatorial and low latitudes are presented.

8 THE IMPACT OF GEOMAGNETIC STORMS ON THE EQUATORIAL & LOW LATITUDE IONOSPHERE: CASE STUDIES

In this chapter three representative case studies of CIR/HSS-driven geomagnetic storms and their impact on the low-latitude ionosphere 2018 are discussed namely: (1) An **intense** storm driven by CME/HSS which occurred on **25 August 2018** during the winter solstice in the South Hemisphere; (2) a **moderate** CIR/HSS storm **7-12 October 2018**, during equinox and finally (3) a **minor** CIR/HSS-storm on **13–14 October 2018** also during the equinox.

First, the solar event is characterized using images of coronal holes, solar wind, IMF and geomagnetic indices. Multiple ground- and space-based measurements and techniques described in Chapter 5 were used to provide a comprehensive analysis of the low latitude ionosphere behavior during disturbed periods. The ionospheric response was investigated using TEC and its derived indices, namely the TEC, ΔTEC, percentage deviation, ROTI, and spatial gradients in TEC. GOLD 2D radiance maps and OI 630 nm airglow emissions were used to observe and characterize the occurrence of EPBs. We also present the variation of ionospheric parameters such as F-layer virtual height, $h'F$ (km) F-layer peak height, h_mF_2 (km) and plasma frequency, f_oF_2 (MHz) extracted from Digisondes measurements at the equatorial region, São Luis. $E \times B$ vertical drifts were inferred from ground-based magnetometer observations to investigate the possible role of prompt penetration of electric fields, PPEF, at low latitudes.

8.1 Case study 1: the intense CME geomagnetic storm on 25 August 2018

An intense geomagnetic storm with minimum Sym–H of –205nT classified as (G3) by NOAA occurred on 25 August 2018. A weak filament eruption associated with a minor CME was detected on the solar disk on 21 August 2018. The CME also had an unusually low speed of 221 km/s at storm onset according to the NASA CME list. Due to the small size of the eruption, the arrival of the CME and the large magnitude came as a surprise and its effects were expected to be minor as was reported by Astafyeva et al. (2020). Figure 8.1 also shows a large trans-equatorial CH (CH881) on the solar disk image captured by the Solar Dynamics Observatory (SDO) at wavelength 195 Å on 22 August 2018, ∼ 3 days before the storm according to solen.info. An active region is seen adjacent to the CH as discussed in section 6.2. This brightening was associated with a weak solar flare eruption on 22 August 2018.

Figure 8.2 shows the variation of solar, interplanetary, and geomagnetic parameters from 24 to 31 August 2018. The quiet day before the storm, 24 August, was included for comparison. The figure shows from top to bottom: the solar wind speed, V_{sw} (km/s); the

Figure 8.1 - Trans-equatorial CH captured by the Solar Dynamics Observatory (SDO) at wavelength 193 Å on 22 August 2018 at 03:00UT. The bright emission represents an active region.

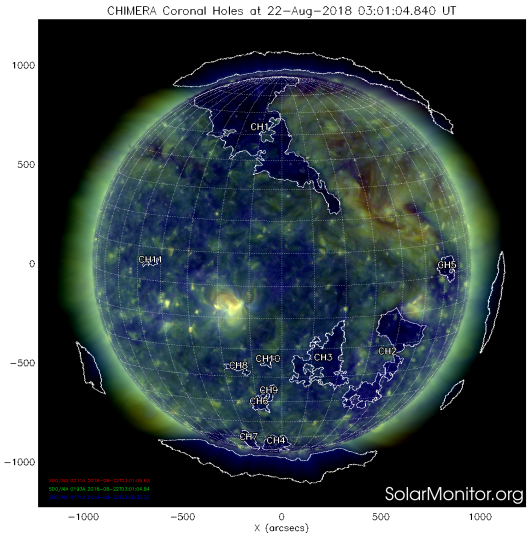

plasma temperature, Tp (K); the proton density, (n/cm^{-3}); the Interplanetary Magnetic Field (IMF) magnitude, |B|; and its components B_x, B_y, and B_z in (nT), GSM coordinate system; the east-west component of the Interplanetary Electric Field, IEF Ey (mV/m); the longitudinally symmetric index, Sym–H (nT); the auroral electrojet index AE (nT); the Kp index, and finally, the solar flux index, F10.7 (in SFU), where (1 SFU = 10^{-22}Wm^{-2}Hz^{-1}). The GSM coordinate system has its X-axis pointed away from Earth to the Sun, and the Y-axis is perpendicular to Earth's magnetic dipole so that the X-Z plane contains the dipole axis.

The initial shock began at 02:45 UT although there was no sudden impulse (SI). At ∼07:00UT there was a small increase in proton density which marked the initial phase (IP) of the storm. IMF B_z turned southward at 17:00 UT and remained so up to 12:00 UT on 26 August. The Sym–H became negative soon after B_z characterizing the beginning of the main phase (MP) of the storm. Sym–H decreased to a minimum of –205 nT at 07:00 UT while minimum B_z was –18nT. IEF Ey turned positive (eastward) during the MP at ∼16:00 UT and reached a maximum of 7.5mV/m while $|B|$ maximum was 18nT and n_p was $33/cm^{-3}$. However, during the recovery phase, the solar wind speed increased from $\sim$ $400km/s$ to a maximum of $\sim$ $630km/s$ on 27 August at 18:00UT. The proton temperature and proton density also increased gradually, typical of CIR/HSSs which do not have a sudden impulse (TSURUTANI et al., 2006). During the RP, there were large amplitude fluctuations in B_z and Ey (16 nT peak) from 10:00–21:00UT. Intensification of AE began during the MP on 25 August at 06:00UT. It reached a maximum of 2300 nT

Figure 8.2 - Variation of solar wind parameters, IMF and geomagnetic and indices on 24–31 August 2018. From top to bottom panel: the solar wind speed, V_{sw} (km/s), plasma temperature; Tp (K), proton density, n/cm^{-3}, the IMF, |B| (nT) and its components; Bx, By, Bz, IEF, Ey (mV/m), Sym–H (nT), AE index (nT), Kp index and the F10.7(S.F.U) solar flux. The red lines indicate the beginning of the initial, main, and recovery phases.

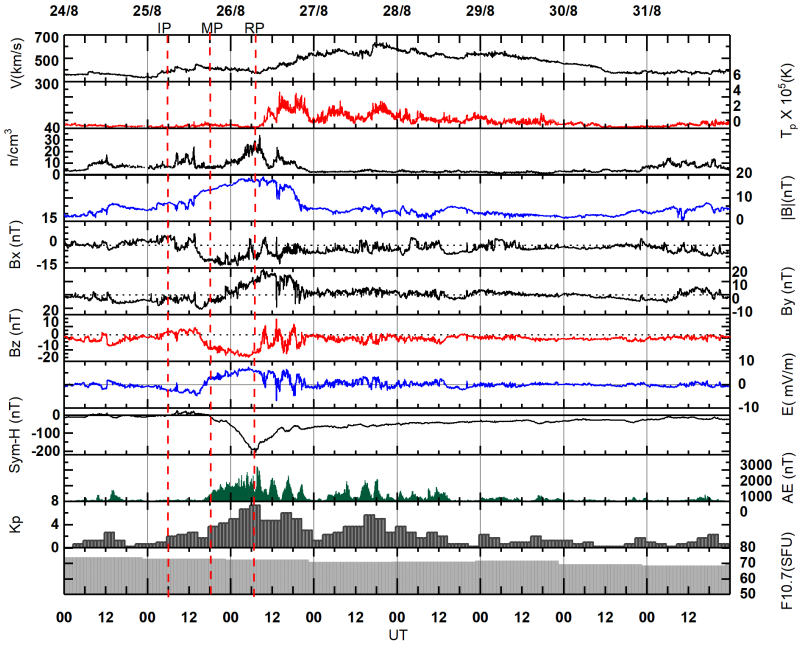

at 22:00 UT while the maximum Kp was 7.4. Weaker AE and Kp were observed on 27 August during the interval of the HSS. The F10.7 EUV flux remained fairly constant at $\sim$ 70 SFU throughout the storm. Enhanced auroral activity is generally attributed to the precipitation of energetic particles, responsible for Joule heating of the thermosphere at high latitudes (FEJER, 2011). The recovery phase began at 08:00 UT on 26 August when Sym–H increased smoothly and reached pre-storm levels by 06:00 UT on 31 August. It lasted for 5 days which is unusually long for a storm caused by an ICME which only lasts up to a few days from the SSC. The extended RP can be explained by the arrival of the HSS which emanated from a coronal hole a few days before the CME.

8.1.1 Low latitude ionosphere TEC response

To investigate the response of the thermosphere-ionosphere (TI) to the HSS/CIR-driven storm, we analyzed the variability of TEC over the Brazilian sector, followed by the thermospheric [O]/[N2] ratio. Figure 8.3 shows the temporal variation of VTEC observed at 7 representative stations during the storm.

Figure 8.3 - Variation of VTEC on 24–31 August, at 7 representative latitudinal stations in Brazil, arranged by decreasing geographic latitude. The dip latitude for each station is in brackets. The average of the 5 quietest days is represented in black. The vertical dashed lines indicate the beginning of the initial, main, and recovery phases respectively.

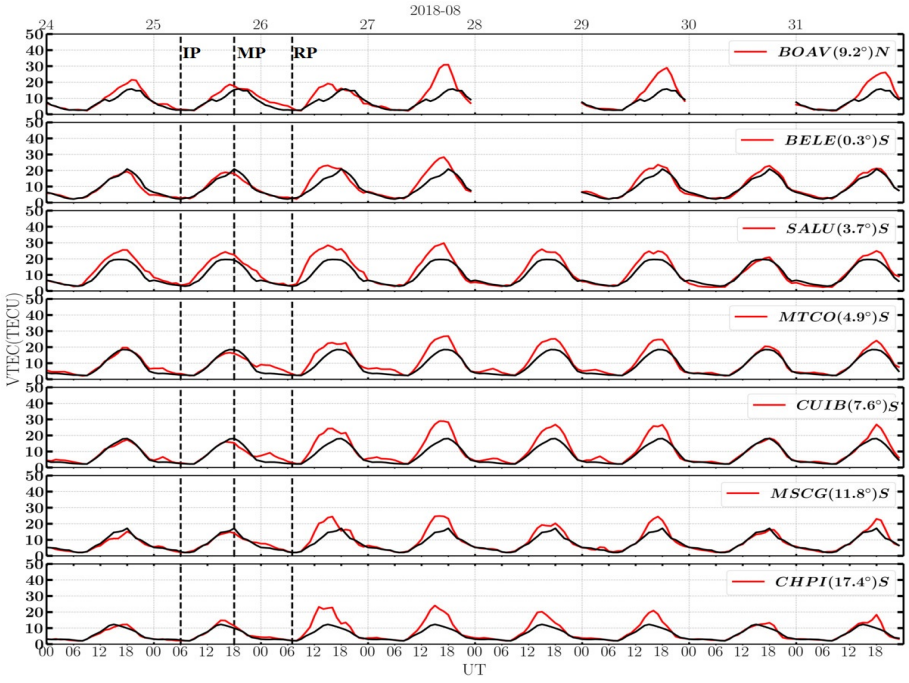

The receivers are located within the 45°W – 61°W longitude sector arranged in decreasing latitude as follows;

- The North crest of the EIA, Boa Vista (BOAV: 2.83° N, 60.69°W dip Latitude 9.2° N);
- The dip equator Belém (BELE: 1.40°S, 48.4° W; dip latitude 0.3°);
- Near-equatorial region stations: São Luís (SALU:2.59° S, 44.12° W; dip latitude 3.7°S) and Monte Carmelo (MTCO: 10.8°S, 48.3°W; dip latitude 4.9°S);
- The South crest of EIA; Cuiabá (CUIB: 15.55°S, 56.10°; dip latitude 7.6° S) and Campo Grande (MSCG: 20.50°S, 54.70° W; dip latitude 13.5°S). BOAV and MSCG are considered conjugate points as they are roughly on the same geomagnetic field line. CUIB and MSCG were used interchangeably in case of data unavailability;
- Cachoeira Paulista (CHPI: 22.70°S, 45.01° W; dip latitude 17.4° S) located around the southern boundary of the EIA.

The red curves represent the TEC variation during the disturbed interval while the black line represents the 5 quietest days average, 5QD TEC, based on Kp, for each station. The vertical dashed lines represent the initial phase, IP, the main phase, MP, and the recovery phase, RP, respectively. The main phase of the storm occurred at 18:00–0600 UT (15:00–03:00 LT) on 26 August. During quiet time, TEC was around 15–20 TECU with a daily maximum at ∼16:00–18:00 UT.

On 25 August, a small positive storm (PS) is seen at locations BOAV to SALU in the IP with a slightly lower bump over the equator at BELE. During the MP (0–6 UT), there was a clear enhancement at all stations with the highest increases at MTCO and CUIB (10 TECU). The TEC reached maximum (30 TECU) at the crests of EIA (BOAV and CUIB) during the RP on 27 and 30 August. An earlier peak in TEC is also observed compared to quiet time. The PS lasted for 4 consecutive days during the RP (26–30). However, a small PS (50%) was detected at night over the equator on 30 and 31 August.

Figure 8.4 - Similar to Figure 8.3 showing the TEC percentage deviation in TEC (δTEC) at the 7 representative stations. A strong PS was detected during the main phase.

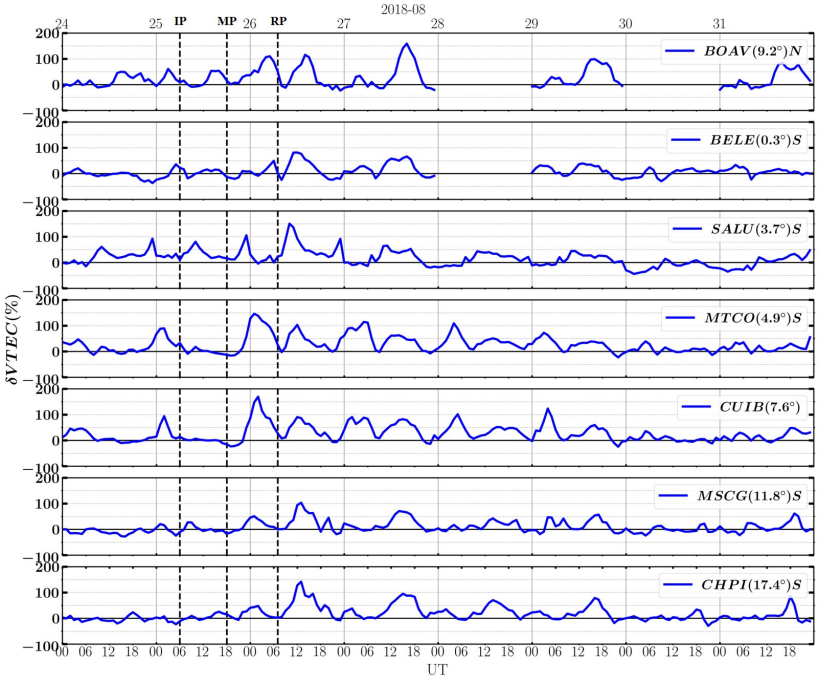

In order to demonstrate more clearly the magnitude of these ionospheric storms in TEC, we calculated the TEC percentage deviation, as shown in Figure 8.4 As seen from the TEC variation in Figure 8.4, the $\delta VTEC$ was predominantly positive (PS) at all locations

throughout the storm. The maximum PS was 180% observed at the south crest of EIA, CUIB, between 21:00–03:00 LT (00:00–06:00 UT) on the night of the main phase while the maximum deviation at the North crest of EIA, BOAV, was only 105%, indicating hemispheric asymmetry in response. The PS at the equator (BELE) was only around 5% during the MP. Throughout the RP, the PS continued to be higher over the south crest and weaker over the equator except for 27 August where there was a peak at BOAV at 12:00–18:00 UT. On 30 August the maximum PS declined to 50 % as the Sym–H recovered to quiet time levels.

Figure 8.5 presents the TEC variation in South America, in a sequence of TEC maps from 25 August to 31 August 2018, at the peak of the EIA ∼14:00 LT (17:00 UT). The quiet day before the storm, 24 August ($Kp < 3$) is also included in the first panel “(a)" for comparison. It can be seen that there are fewer GNSS receivers in the Northern Hemisphere (NH) compared to the Southern Hemisphere. During quiet time, the EIA can be observed over 45–70°W longitude sector with an amplitude of ∼ 20 TECU as shown in Figure 8.3. The crests are located around 10°S dip latitude. The intensification of the EIA began on 25 August (a) and continued for 4 days in the RP (b-h) as was seen in the TEC (amplitude of 30 TECU). The location of the EIA shifted poleward to 15°S dip latitude beyond the

Figure 8.5 - A sequence of TEC maps over South America taken at 17:00 UT (14:00LT) from the quiet day of 24 (a) to 31 August 2018 (b-h). The red line represents the geomagnetic equator. The locations of the 7 stations are marked by the green stars.

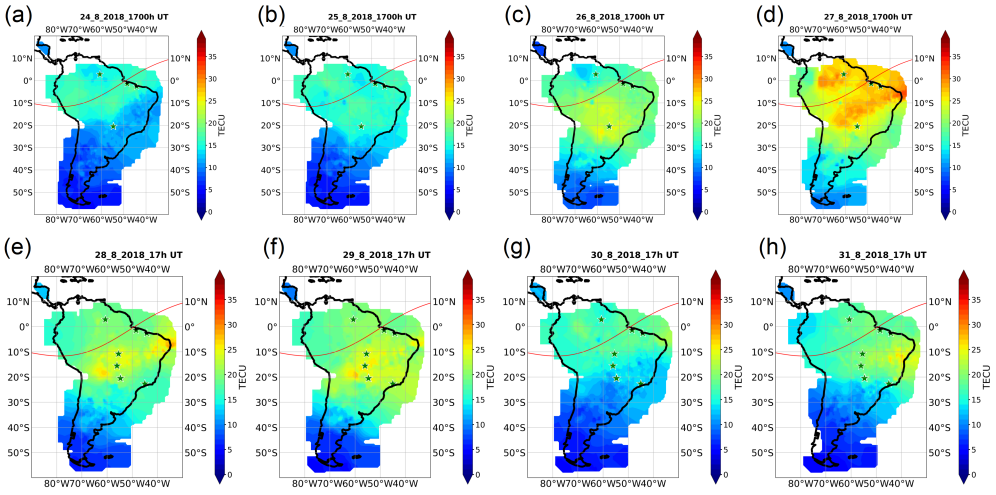

quiet time extent. It reached its maximum amplitude and latitudinal extent on 27 August at around 17:00 UT (14:00 LT). The increase occurred simultaneously with the large PS

during the RP (from 27 August). On this day it North-South asymmetry is also seen in the EIA. The EIA intensity decreased from 28 August to 31 August 2018, although it was still slightly higher than the quiet day before the storm. An increase in TEC over low latitude with a simultaneous decrease at the magnetic equator indicates an enhancement in the fountain effect as a result of an over-shielding PPEF which is westward in the nightside as was also reported by Astafyeva et al. (2020), Moro et al. (2021). One of the mechanisms for PS is the enhancements in the thermospheric neutral composition ratio, [O]/[N2] (PROLSS, 1995; BUONSANTO, 1999; CAI et al., 2020b).

Figure 8.6 - Sequence of thermospheric neutral composition ratio [O]/[N2] from the TIMED/GUVI satellite on (a) 24 August, a quiet day reference (b) 26, main phase and 27–29 August (d-f), recovery phase.

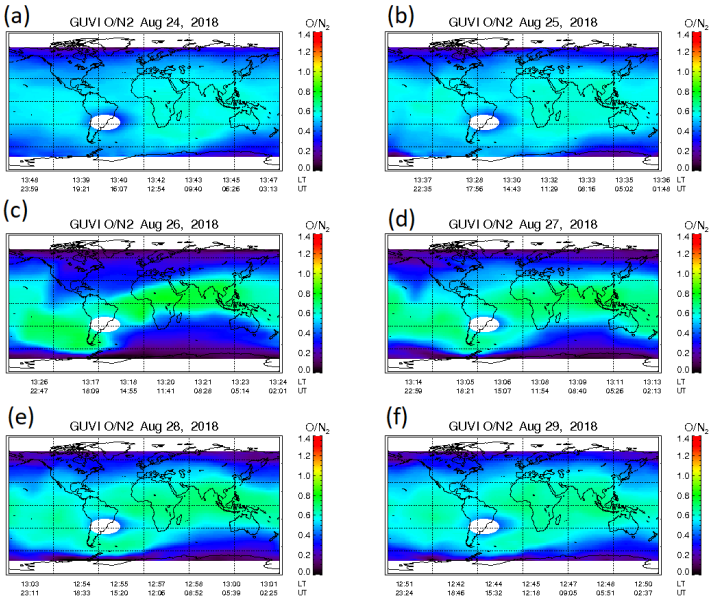

Figure 8.6 shows a sequence of global [O]/[N2] maps from 24 to 29 August 2018. It is observed that on the storm day, there was a slight enhancement over the African sector and the Indian Ocean. It reached a maximum on 26 and 27 August (0.9). Overall, there was a global enhancement in South American, Asian and African sectors. The [O]/[N2] enhancement clearly coincided with the PS in TEC shown in Figure 8.4. The peak in TEC occurred on the same day as a maximum of [O]/[N2] (Figure 8.5). The magnitude began to decrease on 29 August. The changes in thermospheric density were therefore partially responsible for the ionospheric storms observed over South America from the main and recovery phases of the storm. Astafyeva et al. (2020), Moro et al. (2021) also found TEC enhancements of 100% at low latitudes while we observed small PS of $\delta VTEC \sim 50\%$

over Brazil.

While Astafyeva et al. (2020) reported a weak PS (5TECU) in TEC over the American sector, Lissa et al. (2020) found a large PS in TEC (100%) in the dayside during the MP and RP over the Asian sectors. This indicates that the effect of the storm enhancement is dependent on the local time and longitude (LEKSHMI et al., 2011; DUGASSA et al., 2019). We also observe a hemispheric asymmetry in TEC response during the ICME storm, which is in agreement with previous findings by Astafyeva et al. (2020) and Moro et al. (2021). Hemispheric asymmetry in TEC was linked to seasonal differences in thermospheric composition and winds (DANILOV et al., 1994). The disturbed thermospheric winds drive plasma equatorward along field lines, causing PS in TEC (BALAN et al., 2010). Another factor responsible for ionospheric storms at low latitudes is prompt penetration of electric fields and disturbance winds (BLANC; RICHMOND, 1980; LIU et al., 1999; FEJER, 2011).

8.1.2 F layer response and equatorial electrojet strength

A positive ionospheric storm of maximum amplitude 180% was observed over the crests of the EIA over South America in the MP (0–6 UT). We investigate the electrodynamics of the F layer ($E \times B$ drift) that are responsible for low-latitude ionosphere (KELLEY, 2009). Figure 8.7 shows the variation of the F-layer virtual height, $h'F$, critical frequency, f_oF_2 and peak height, h_mF_2 on 24–31 August 2018, obtained from Digisonde observations over the equatorial region, São Luís. The ΔH (Equatorial electrojet strength) was calculated from the horizontal component of the magnetic field measured by a pair of ground-based magnetometers, one located at the dip equator, Jicamarca, Peru (76.8 °W; 11.9 ° S, dip Latitude: –0.34°) and an off-equator station, Piura (80.6 °W; 5.2°S, dip Latitude: –6 °) both located in Peru. The data was used due to the unavailability of data over the Brazilian sector during the storm period.

Figure 8.7 - Variation in (a) *Sym-H*, (b) B_z, (c) Ey, (d) $\Delta H(JIC - PIU)$ (magenta during the storm days with the quiet reference variation on 23 August in black), (e) the F-layer virtual height, $h'F$, (f) peak height, h_mF_2 and (g) critical frequency f_oF_2 at São Luís from 24 to 31 August 2018. The black curves represent the average of the 5 quietest geomagnetic days, 5QD, for each parameter. The initial (IP), main (MP), and recovery phases (RP) of the storm are indicated on the top of vertical red dashed lines. Spread F (SF) occurrence interval is shown by the horizontal bars in ("f").

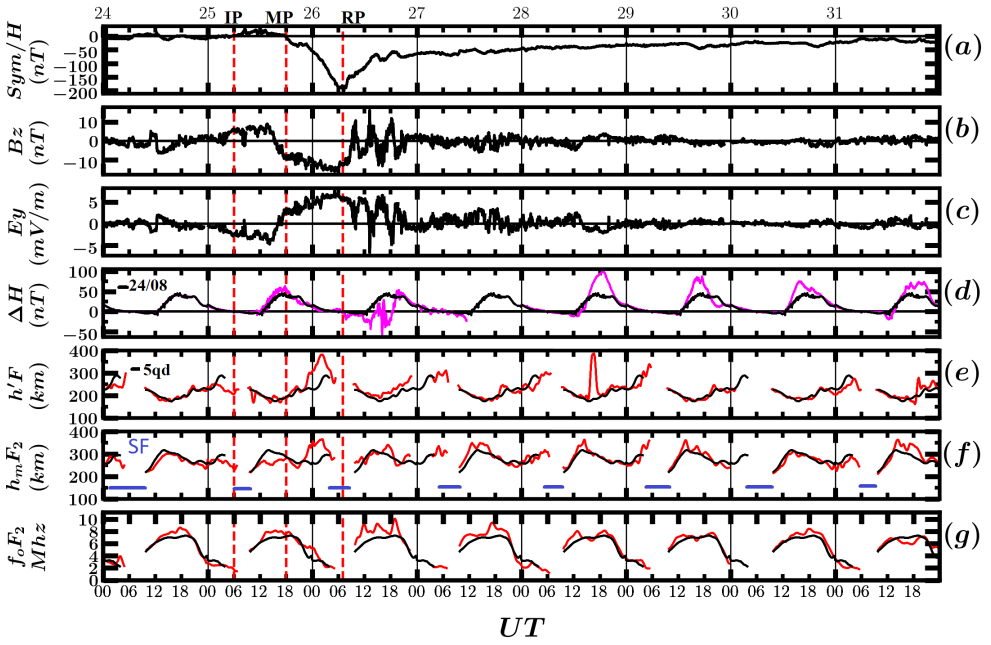

During the IP between 12–18 UT, there were no significant changes in the $h'F$ over the equator. However, there was a small PS in f_oF_2 as the h_mF_2 decreased. A similar PS in TEC over SALU is shown in Figure 8.4 and Figure 8.3. In the main phase, on 26 August, the $h'F$ rose sharply from 275 km to a storm time maximum of 390 km from 18:00–01:00 LT (2100–0400UT). This peak coincided with peak positive IEF Ey in ("c"). Likewise, a large increase in h_mF_2 from 280–375 km is seen, indicating an uplift on the F layer peak, was accompanied by a small PS in f_oF_2. The largest increase in TEC was observed in that interval over the EIA crests. Nevertheless, the ΔH was hardly unchanged during the MP. The enhancement in $h'F$, f_oF_2, and h_mF_2 persisted throughout the recovery phase, although the amplitude decreased after the MP. The variability of the F layer parameters during the RP was fairly consistent. There was a very abrupt, strong uplift in $h'F$ and ΔH after an increase in the h_mF_2.

The ΔH is a measure of the vertical ($E \times B$) drift at the equator (ANDERSON et al.,

2002). On 26 August, the ΔH was largely negative from 9–18 UT. Negative ΔH is a result of a strong counter-electrojet (CEJ). Despite this, there was a PS in f_oF_2 and TEC at all the stations on this day together with an uplift of the F layer. The sharp fluctuations in Ey at this time indicate the condition for prompt penetration of electric fields (KELLEY et al., 1979). Candido et al. (2018) reported that PS are caused by positive IEF Ey during solar minimum. As such, the increase in the neutral composition ratio we observed in the GUVI images on 26 August had a more dominant effect on the PS than the electric field.

Thereafter, there was an enhancement in ΔH from 28–31 August, 2 days into the RP. The PS reached maximum intensity on day 27 accompanied by oscillating B_z and positive Ey at 12-21 UT (9–18 LT). Our findings are in agreement with Moro et al. (2021) who found a maximum PS in f_oF_2 on day 27 over Brazil. Despite this PS, there was no significant increase in $h'F$ indicating that the neutral composition changes played a greater role than electric fields. The enhancement of the EIA during the RP was associated with the strengthening of $E \times B$ vertical drift under the influence of several episodes of PPEF (LISSA et al., 2020; MORO et al., 2021). Fagundes et al. (2016) observed a positive storm during the main phase of a CME-storm which was attributed to an eastward PPEF which enhances the fountain effect. In addition, a super fountain effect was also reported by Astafyeva et al. (2020) attributed to the increase in [O]/[N2] ratio, as observed by the TIMED GUVI instrument on day 26 and 27 (ASTAFYEVA et al., 2020; LISSA et al., 2020; MORO et al., 2021). The observed enhancement in TEC seems to be associated with a combination of PPEF and thermospheric composition changes during disturbed periods, which is in agreement with Titheridge (1974), Balan et al. (2010), Cai et al. (2020b).

8.1.3 Equatorial plasma irregularities

Our results show that during the long-duration CME/CIR storm there was a prolonged PS for several days during the recovery phase. It is well known that during the winter solstice, the magnitude of TEC and the PRE is low, especially during solar minimum (JONAH et al., 2015). This section investigates whether the intense storm caused by ICME/HSS had sufficient impact on the development of plasma irregularities/EPBs during August 2018. For this purpose, the variation of ROTI during the disturbed interval is analyzed.

Figure 8.8 - Variation of ROTI over Brazilian low latitude stations during the geomagnetic storm on 24–31 August 2018. The blue line marks the threshold for moderate irregularities ($0.05 \leq ROTI \leq 0.2$). The bottom panel shows the variation of B_z showing sharp oscillations on 26 August.

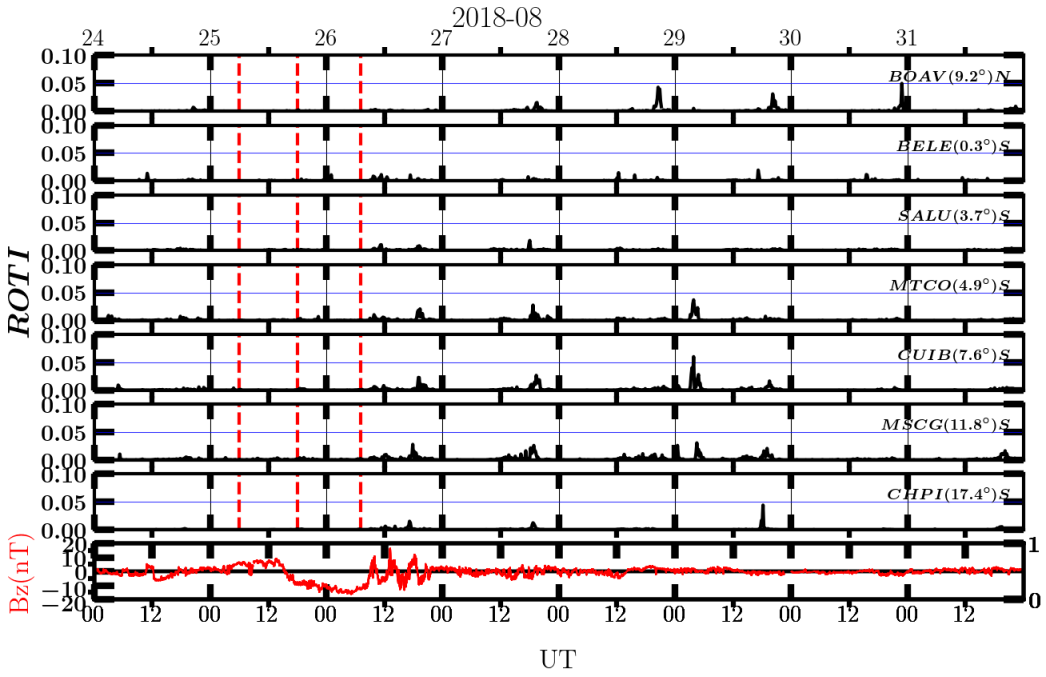

Figure 8.8 shows the variation of 10-minute averaged ROTI during the storm. In general, no irregularities were detected ($ROTI < 0.05$), particularly during the main phase of the storm. However, weak irregularities were observed on 29 October. On this day the TEC increased significantly and there was a large peak in the $E \times B$ drift. This was followed by an increase in ROTI after sunset. Overall, the amplitude of plasma irregularities was low. The ICME storm occurred during the winter solstice when EPBs have a low rate of occurrence over the Brazilian sector owing to unfavorable conditions for the development of the RT instability, in particular, weaker $E \times B$ drifts (ABDU et al., 1981; SOBRAL et al., 2002). The low level of TEC may also be another major contributor to the occurrence of strong irregularities. This is discussed further in section 8.2.4.

8.1.4 Discussion

The 25 August 2018 geomagnetic storm, the third-largest geomagnetic event of solar cycle 24 was quite peculiar since storms of such magnitude are uncommon during solar minimum. It was driven by a CME associated with a weak filament eruption on 20 August. The dynamics were complex due to interaction between a CME and a HSS which led to significant ionospheric perturbations during a recovery phase that lasted for 5 days.

Despite the intense magnitude, the effect of PPEF as measured by the ΔH during the MP was weak (ASTAFYEVA et al., 2020). As such, it was insufficient to trigger strong ionospheric irregularities.

It is worth noting however that the reason the ΔH was unchanged despite a sharp increase in $h'F$ could be due to longitudinal differences in the magnetic declination between the magnetometers in Peru (LT=UTC–5) and the local time over Brazil (LT=UTC–3). The largest increases in TEC were observed during the RP over South America during the HSS interval. In this time large amplitude B_z oscillations are linked to Alfvénic fluctuations during substorms which play an important role in causing PS during the recovery phase (LIU et al., 2012; MORO et al., 2021). However, under unusual conditions due to geomagnetic activity, irregularities can still occur outside the Spread F season as was reported by Candido et al. (2019) who observed SpreadF during the June solstice of solar minimum. During the storm, weak Spread F (not shown) was observed in the pre- to post-midnight sector, i.e., between 0000 to 0900UT (21:00 LT to 06:00 LT). However, the magnitude of irregularities was weak as expected during winter. The lower solar flux which results in reduced ionization levels (max 30 TECU) in the winter solstice of 2018 is likely another necessary factor for the formation of SpreadF/EPBs.

8.1.5 Summary

a) A large positive storm occurred during the main and recovery phase of the ICME STORM in the South crest of the EIA (maximum = 180%) credited to the combination of [O]/[N2] increases and a weak Eastward PPEF;
b) A negative storm of smaller magnitude (–50%) compared to the PS was observed at the equator during the RP;
c) Despite the intense storm, there were no significant changes to the zonal electric field during the MP. In addition, there was a weak influence on the development of ionospheric irregularities, as seen in ROTI amplitude;
d) The most significant ionospheric disturbances on the plasma density, EIA and irregularities that occurred during the recovery phase were driven by the high-speed stream.

8.2 Case study 2: a moderate CIR/HSS geomagnetic storm on 7 October 2018

In this section, a detailed study of a moderate, long-duration, CIR/HSS geomagnetic storm influence on the Brazilian low-latitude ionosphere on 7–13 October 2018 is discussed. The storm is classified as moderate (minimum Sym–H = –50nT) according to criteria by Loewe (1997). This case study forms the basis of the characterization of solar wind high-speed stream impact on the low-latitude ionosphere during the deep minimum. The 7–13

October storm was associated with a large transequatorial coronal hole (CH888) on 04 October 2018. It was located at the center of the solar disk and extended from the poles to low latitudes as shown in Figure 8.9. An active region is seen adjacent to the CH. This observation shows that a high-speed stream can emanate from a polar coronal hole that extends to low latitude as reported by Tsurutani et al. (2006).

Figure 8.9 - NASA SDO 193 Å image showing a Trans-equatorial Coronal Hole (CH888) on 4 October 2018 at 19:00 UT.

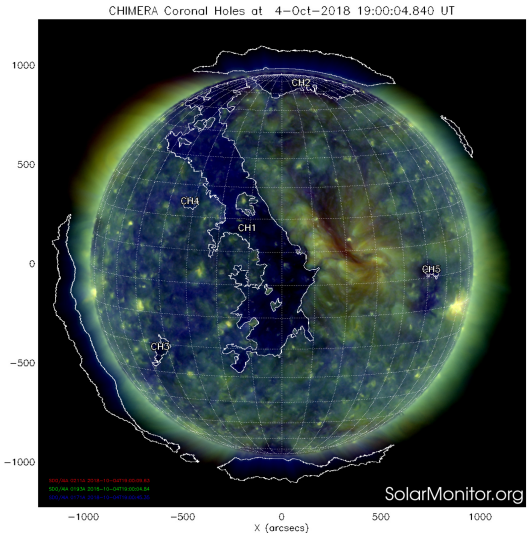

Figure 8.10 shows the same as Figure 8.2 but for the CIR/HSS-driven storm interval on 5–13 October 2018. On 7 October 2018 at ∼06:00UT, the solar wind speed V_{sw} increased from $400km/s$ to $600km/s$ associated with a proton temperature, T_p, and proton density, n_p enhancement. Sym–H shows the onset of the initial phase at 06:00UT.

Figure 8.10 - Variation of solar wind, interplanetary magnetic field, and geomagnetic parameters on 5–13 October 2018. From top to bottom: the solar wind speed, V_{sw} (km/s);, plasma temperature; Tp (K), proton density, $n_p(n/cm^{-3})$, Interplanetary Magnetic Field, magnitude |B| (nT);, and the Bx, By and Bz components; the east-west component of the IEF, Ey (mV/m), Sym–H (nT), the AE index (nT), the Kp index, and the F10.7 (SFU) solar flux. The red lines indicate the beginning of the initial (IP), main (MP) and recovery (RP) phases.

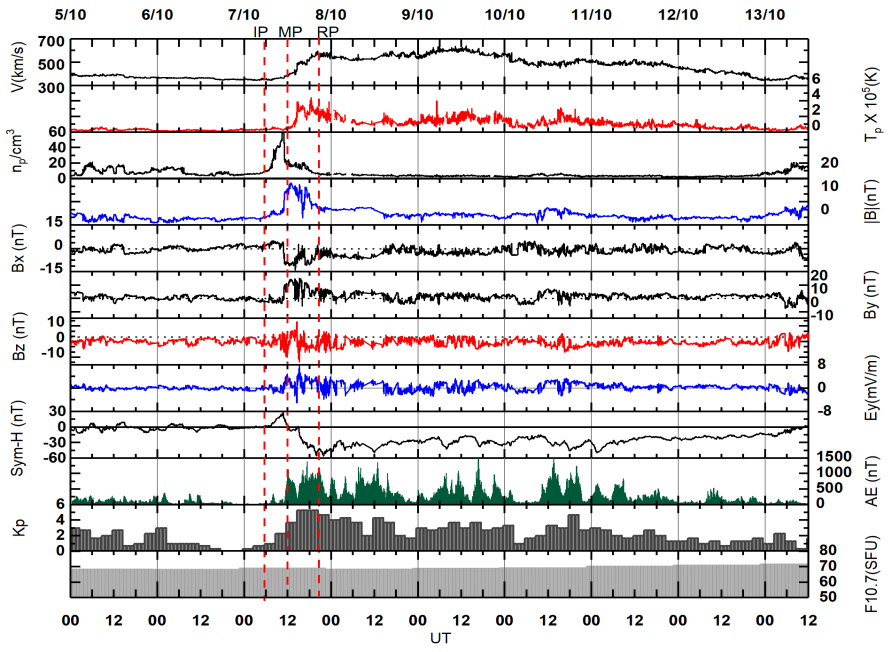

On 7 October 2018, there was an increase in the magnitude of the magnetic field, $|B|$ which represents the compression of the Earth's magnetosphere, typical of a CIR. The IMF Bx component (positive northward) and By (negative westward) were anti-correlated throughout the storm. At ∼10:00UT, B_z turned southward and reached a minimum of $-12nT$. Afterwards, the Sym–H became negative, marking the main phase of the storm in which Sym–H had a double-step decrease, one at 12:00 UT and another at 15:00 UT. It reached a minimum of –56 nT at 21:00UT while B_z and Ey showed oscillations throughout the main phase with Ey amplitude of $6mV/m$. AE and Kp increased to a maximum of 1300 nT and 5 respectively. From 21:00UT on 7 October, the Sym–H increased, while the amplitude of B_z and Ey decreased. IMF B_z was mostly southward which is a favorable condition for PPEF. There was an overall decrease in all the IMF and solar wind parameters during the RP, however, there were several negative incursions in Sym–H ranging between $-50nT$ and $-20nT$ associated with the persistence in solar wind speed. This was accompanied by

intermittent peaks in the AE index of $1000nT$. The storm had a long recovery phase of 6 days which ended on 13 October. The levels of solar flux F10.7 which remained constant throughout the storm are typical of low solar activity.

8.2.1 Ionospheric storms in TEC and changes in thermospheric composition ratio

Figure 8.11 - TEC variability on 6–13 October 2018 from North crest (BOAV) to South crest (CHPI) of EIA. The black lines represent the average of the 5 quietest days. The vertical dashed lines mark the IP, the MP & the RP of the storm.

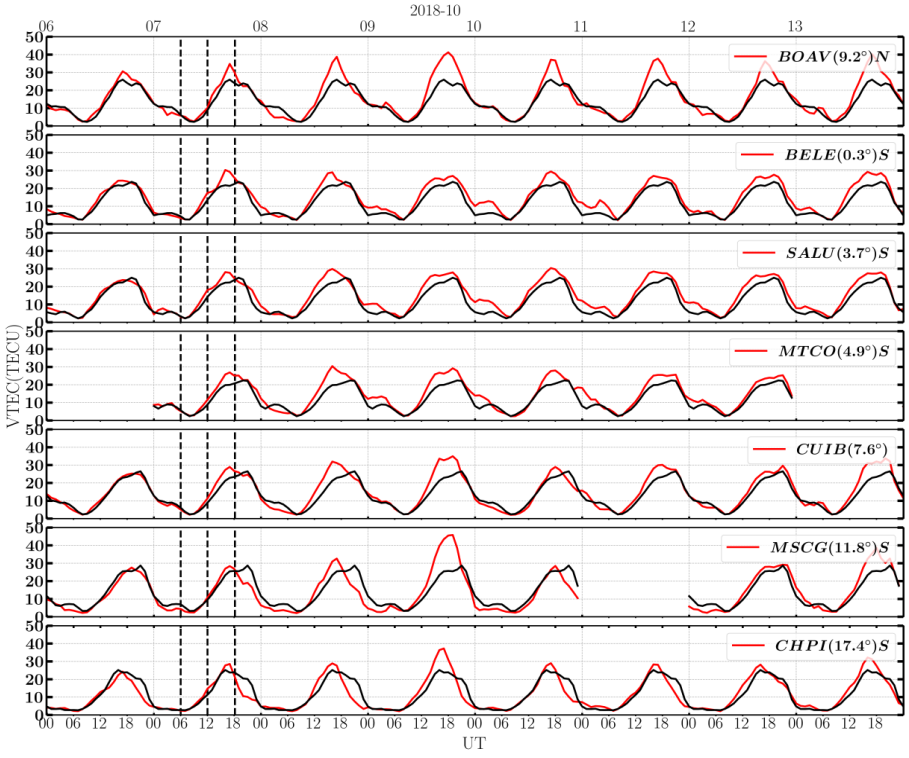

To investigate the response of the ionosphere to the moderate CIR/HSS-driven storm we present the TEC variability over the Brazilian sector. Figure 8.11 (same as Figure 8.3) shows the variation of VTEC on 6–13 October CIR-driven storm at 7 representative stations. It can be observed that the TEC increased instantaneously at all stations from ∼20 TECU to ∼35 TECU from 12–18 UT (9:00 –15:00 LT) during the main phase. In contrast, there was a NS over MSCG-CHPI during the recovery phase at 18–24UT (15–21 LT). On 8 October at 0–6 UT there was a strong and persistent negative ionospheric storm simultaneously at all latitudes in the nighttime. The largest PS occurred on the next day, 09 October, at the crests of EIA (BOAV, CUIB). It had a magnitude of 15 TECU at BOAV

(north crest of the EIA) and 20 TECU at MSCG (south crest of EIA) where the maximum TEC was observed (48 TECU). The larger PS at the North crest indicates a hemispheric asymmetry in TEC response. The NS observed on 7–12 October lasted the longest over the Southern low latitudes (MSCG, CHPI). In order to highlight the magnitude of the ionospheric storms in TEC, Figure 8.12 shows the percentage TEC deviation for the 7 stations during the storm. As discussed in Figure 8.11 there was a small PS ($\delta TEC \sim 50\%$)

Figure 8.12 - The percentage deviation in TEC from the 5QD TEC average on 6–13 October 2018 at the 7 locations.

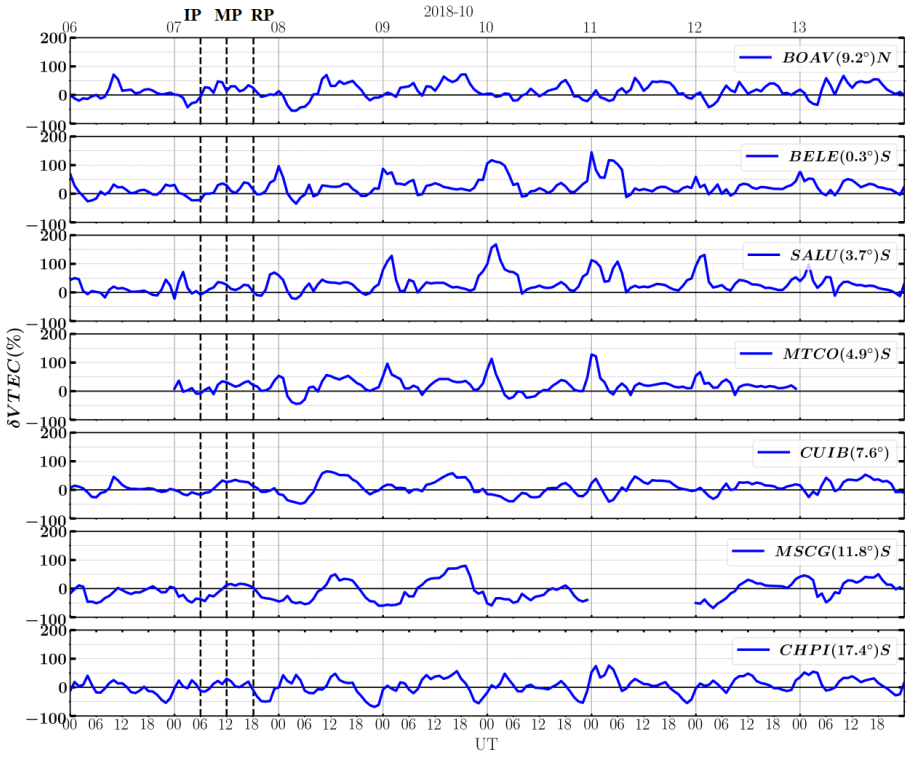

during the MP over the north and south crest of EIA. Thereafter, a simultaneous NS of 50% occurred at all stations on 7 October between 0:00–09:00UT (21:00–06:00LT). Over CUIB–CHPI, the NS began earlier and increased in magnitude to $\sim$ 80% at CHPI from 7 October between 1800 and 0900 UT, and it lasted for approximately 15 hours. The result shows that the depletion in plasma density was larger at MSCG compared to CUIB and CHPI. There was a strong and persistent positive ionospheric storm simultaneously at all latitudes during the whole recovery phase.

The PS was larger over the equator than the crests of the EIA, reaching a maximum of $\sim$170 % at SALU on 10 October between 00:00–03:00 UT. δTEC however was higher over

the crests of EIA. The reason for this is that the lower average quiet TEC at the equator results in a larger percentage increase in the nighttime during storm time compared to low latitude. On 11 October the amplitude of the PS began to decrease, although the NS remained over the southern stations.

Figure 8.13 shows enhancement on 7 October (280) compared to the quiet day before. The maximum TEC was ∼40 TECU over the crests of the EIA, with a trough at the equator (30 TECU). It can be observed that the PS was more sustained over Boa Vista than Campo Grande. The EIA occurred much earlier than during quiet time (1600 UT). The δTEC also shows the PS which was larger during nighttime (0–6 UT) particularly over SALU whilst over the crest it is seen during the daytime. We observed a decrease in TEC over the equator accompanied by an increase over the crests. There was a small PS in TEC which later intensified throughout the RP.

Figure 8.13 - Diurnal and Hourly variation of TEC and δTEC at the crests of the EIA (BOAV, MSCG) and over the equator (SALU) on 6–13 October 2018 showing higher TEC over the Northern crest and large PS over SALU. The maximum percentage deviation is indicated on the top.

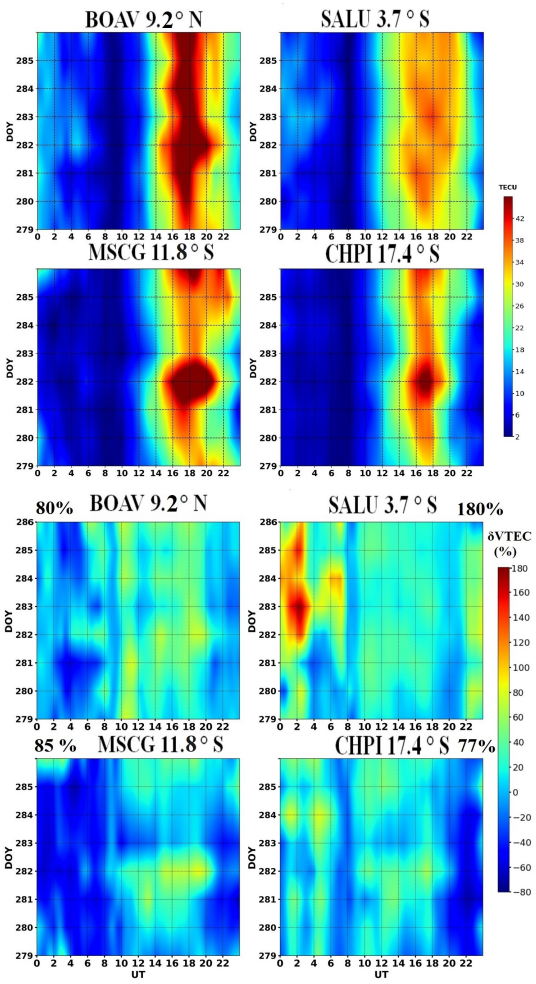

To analyze the EIA variability at a larger scale, Figure 8.14 shows a sequence of TEC maps over South America taken on 7–9 October 2018 at the time of the peak of EIA 17:00 UT (14:00 LT). The first day of the recovery phase (second panel) and the variation on 9 October (282) which had the highest magnitude of TEC (48TECU) are shown.

Figure 8.14 - Evolution of the EIA (IONEX TEC MAP) over South America on 7-9 October 2018.

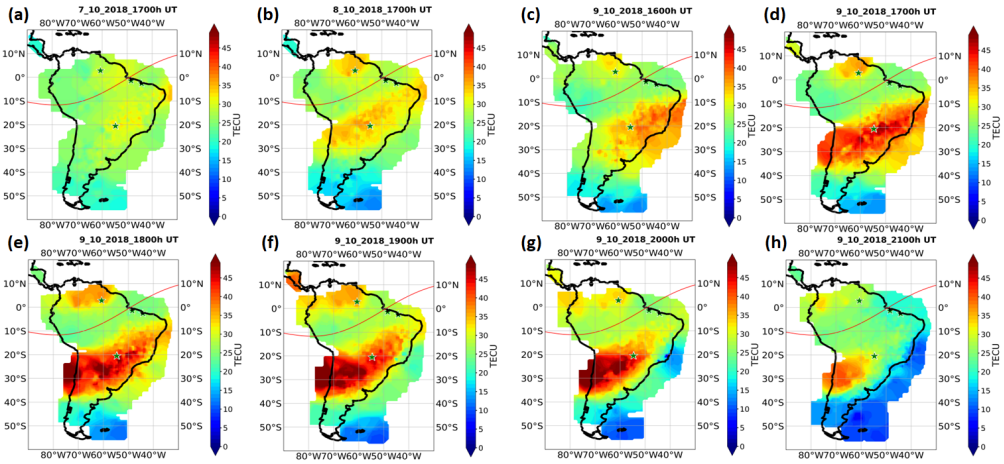

As shown in Figure 8.14 (a), initially, there was a weak development of the EIA crests which increased in amplitude from 30 TECU on 7 October (Figure 8.14(a)) to 45 TECU at its peak on 9 October (d). The peak in the EIA on 9 October "(d–h)" coincides with the highest TEC magnitude during the storm period. As shown in the map, the EIA grew poleward beyond the 20°S dip latitude. A possible mechanism for the PS in TEC is the thermospheric neutral composition changes (FULLER-ROWELL et al., 1996).

Figure 8.15 shows the global [O]/[N2] ratio maps obtained from GUVI/TIMED satellite from 06 (quiet reference day) to 9 October. On 7 October, there was a slight enhancement of [O]/[N2] ratio in comparison to the quiet day "(a)" over the South American, Pacific and African sectors. On 8 October 2018, the neutral composition ratio increased significantly, reaching its maximum on day 9. This enhancement is in agreement with the TEC maps in Figure 8.14. This could explain, at least partially, the positive ionospheric storm at the Brazilian low latitude in Figure 8.11 as well as the enhanced fountain effect shown in Figure 8.14. Positive (negative) ionospheric storms also arise from an increase (decrease) in the storm time thermospheric composition [O]/[N2] due to auroral heating which increases (decreases) the rate of recombination (DANILOV et al., 1994; PROLSS, 1995; FULLER-ROWELL et al., 1996).

Figure 8.15 - Thermospheric neutral composition ratio, [O]/[N2], from TIMED/GUVI from 6–0 October 2018 on; (a) A quiet reference day 6 October 2018, (b) Main phase of the storm-7 October; and (c)-(d) Recovery phase of the storm 8-9 October 2018. Satellite passes at 02:50–06:40 UT and 16:10 and 16:30 UT. A clear enhancement can be observed from day 7 October.

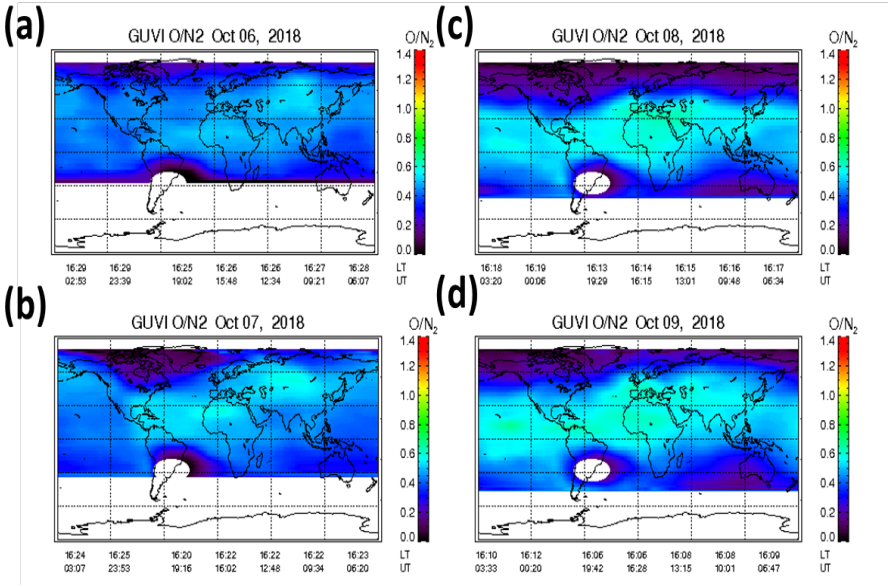

In addition, the combined effect of equatorward neutral winds and Eastward electric field also contribute to positive storms, particularly at equatorial and low latitudes (BALAN et al., 2010).

8.2.2 Equatorial plasma bubbles and post-sunset equatorial ionization anomaly

During the RP of the storm, there was a remarkable intensification in TEC (+180%), over the equator after sunset. We pose the following question: Does the large and persistent PS in TEC affect the magnitude of post-sunset plasma gradients and irregularities? To answer this the features of EPBs, gradients and irregularities were analyzed in a multiple instrument approach, using GOLD FUV imager, TEC MAPS, spatial TEC gradient, and the Rate of TEC index, ROTI. Figure 8.16 shows GOLD 2D maps of FUV 135.6 nm emissions on the night before the storm, 6 October, during the MP, on 7 October and in the recovery phase; 09, 10, 12 and 13 October.

Figure 8.16 - GOLD FUV 135.6 nm irradiance at 23:55 UT (20:55) LT on the nights of 6–13 October 2018. The locations of the 7 stations are marked. EPBs are represented by dark emissions (depletions) on 6 and 13 October. The red triangle shows the location of the São Luís Digisonde.

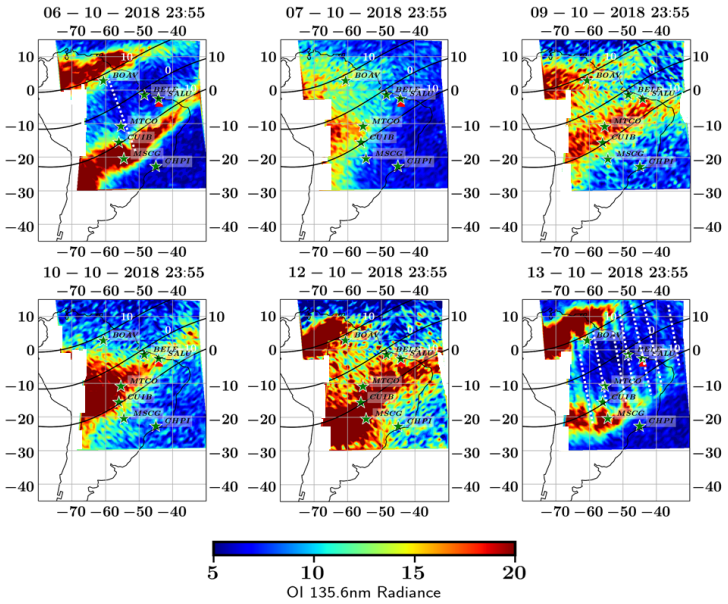

A clearly-developed post-sunset EIA can be observed on 6 October 2018 at 23:55 UT(20:55 LT), represented by bright emissions in the GOLD 135.6 nm, over South America (30–75°W longitude sector) extending to $\sim$ 15° dip latitude. On 7 October, the EIA shrank equatorward compared to the quiet day, signifying inhibition of the fountain effect. In addition, no structured depletions were observed. On 9 and 12 October the EIA was strengthened showing well-defined crests while on 10 October it was only visible in the Southern Hemisphere (SH) at this time. However, weaker depletions, located near 60°W can be present on 9 and 12 October. The maps thus show a large day-to-day variability in the EIA and plasma bubbles.

Since the post-sunset EIA that is formed by the fountain effect (PROLSS, 1995; ABDU, 2001; KELLEY, 2009; EASTES et al., 2019) it follows that $E \times B$ drifts were stronger on days 6, 12, 13 and weaker on days 7 and 9. Significant changes in the post-sunset EIA indicate that the possible mechanism may be prompt penetration fields (PPEF) of interplanetary origin (EASTES et al., 2019). Large diurnal variability in the structure, depth, onset time and duration of EIA is therefore expected during geomagnetic storms. Figure 8.17 shows OI 630 nm airglow emissions from an all-sky imager located at São Joao do Cariri (dip:12° S) on the nights of 5–12 October. On the nights of 7 and 10 October, no observations were made due to cloud cover.

Figure 8.17 - OI 630 nm emissions images taken from 23:00–04:00UT (20:00–01:00 LT) on the nights of 5–13 October 2018. Equatorial Plasma bubbles are marked by the dotted lines.

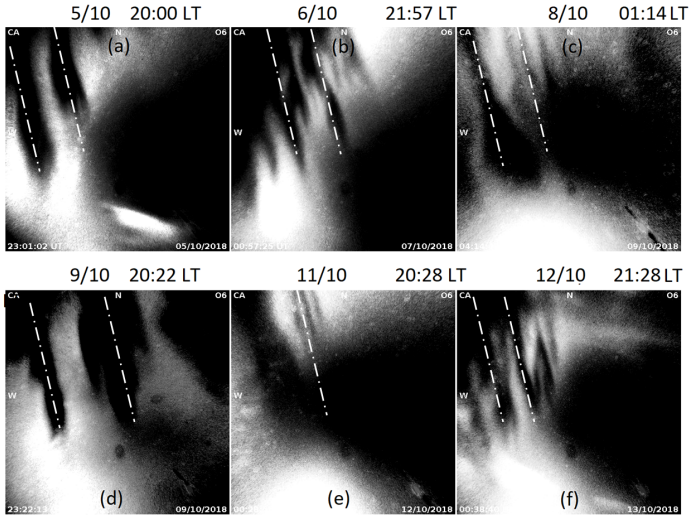

EPB structures are clearly shown on most nights which is typical of the SpreadF season (ABDU et al., 1981). On the nights of 9 and 12 October EPBs are clearly shown in the all-sky imager but were barely visible in GOLD maps. The development of EPBs was clearly suppressed during the main phase of the storm, on 07 October. Although there is some agreement between the GOLD and the all-sky images, there are still some differences. First, the field of view of the imager of $\sim 1000 \times 1000$ km (PIMENTA et al., 2001) is much smaller than GOLD but has a better resolution. The height of the peak emission of the ASI OI 630nm is at ∼200–300 km (PIMENTA et al., 2001) compared to 300 km for GOLD (EASTES et al., 2019). These differences contribute to the observed discrepancies. This particular scenario on 5–13 October highlights the advantage of the ASI over the GOLD imager in providing high-resolution observations of plasma bubbles (TAKAHASHI et al., 2009) despite being prone to bad weather, unlike the GOLD instrument. Nevertheless, the combined observations from both instruments provide valuable information about the structure and variability of plasma bubbles.

It is well known that the ionosphere presents a day-to-day variability in the plasma vertical drifts and consequently on the development of EIA and EPBs. This is observed both in GOLD emission images and airglow. However, the storm-time electric fields can have a role in the development of the EIA and EPBs.

8.2.3 Response of plasma irregularities, ionospheric gradients and scintillation

Figure 8.18 shows the hourly and latitudinal variations of 10-minute averaged ROTI during the storm. The amplitude of irregularities was detected on 09 October 2018. Therefore, a more detailed analysis for this day is presented to demonstrate the correlations between TEC, the amplitude of irregularities, and spatial gradients in TEC. On the night of 5 October at 21:00–03:00 LT (0–6 UT), strong irregularities (ROTI > 0.2) were detected. The ROTI reached a maximum of 0.5 around local midnight (03:00 UT) over the crests of EIA (BOAV, CUIB and MSCG). At the equator, the irregularities were weak ($ROTI \leq 0.05$). On the night of 6 October, before the MP, the amplitude decreased significantly. However, during the initial and main phases of the storm, ROTI decreased drastically to 0.05, indicating suppression of plasma irregularities. This lasted up to the first day of the RP on 8 October. The peak ROTI occurred around local midnight (03:00 UT). The amplitude of the irregularities was larger over the EIA compared to the equator which decreased during the rest of the recovery phase.

On 10 October, there was a large peak in ROTI at MTCO. It is likely the irregularities extended only up to CUIB while on 12 October the magnitude and latitudinal extent reached CUIB, although it was still lower compared to 6, 9 and 13 October. On these same nights, plasma bubbles were observed in the ASI (Figure 8.17). On the other hand, the weak amplitude on the nights of 7, 8, and 12 October shows weak/no irregularities were observed, consistent with GOLD and an all-sky imager in Figure 8.16. The observations show large latitudinal and day-to-day variability in the strength of the irregularities during the storm. This case study demonstrates the multiple-instrument approach of simultaneously observing plasma bubbles and irregularities at various scales for the first time over South America during solar minimum.

Figure 8.18 - Top: Hourly and latitudinal variation of ROTI, IMF B_z and IEF Ey on 6–13 October 2018. The blue dots indicate coincident observation of EPBs by GOLD and/or All-sky imager, while the magenta bar indicates SpreadF. The vertical blue dashed lines indicate, the beginning of the initial, the main, and the recovery phase, respectively. Bottom: The location of the GNSS receivers and scintillation monitors over Brazil. Peak ROTI is indicated by the green star.

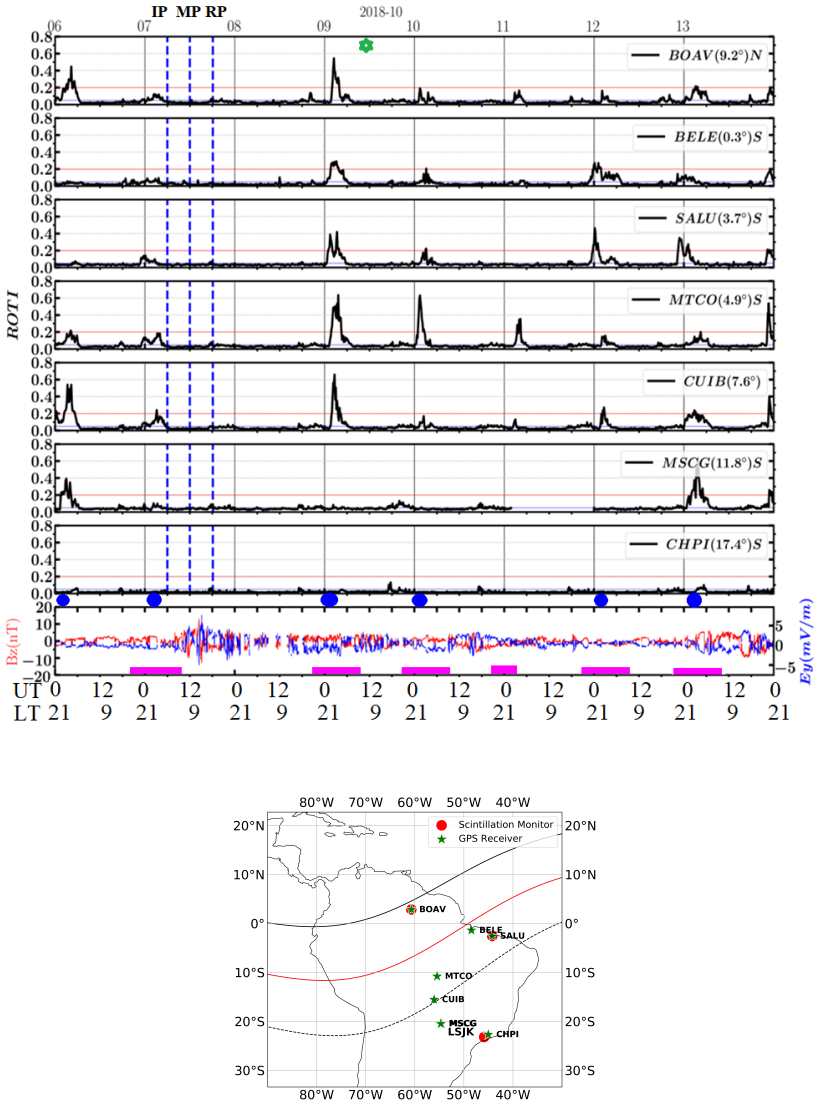

8.19 shows the hourly and latitudinal variation of the spatial gradients in TEC for the storm period. ∇TEC follows the behavior of the ROTI. Gradients occurred from the post-sunset to the post-midnight sector ∼22:00–05:00UT (19:00–02:00 LT). Similar to ROTI, peak gradients occurred on 09 October, around local midnight (03:00UT). On this day

Figure 8.19 - Same as Figure 8.18 but for Spatial gradients showing stronger amplitude gradients during the RP.

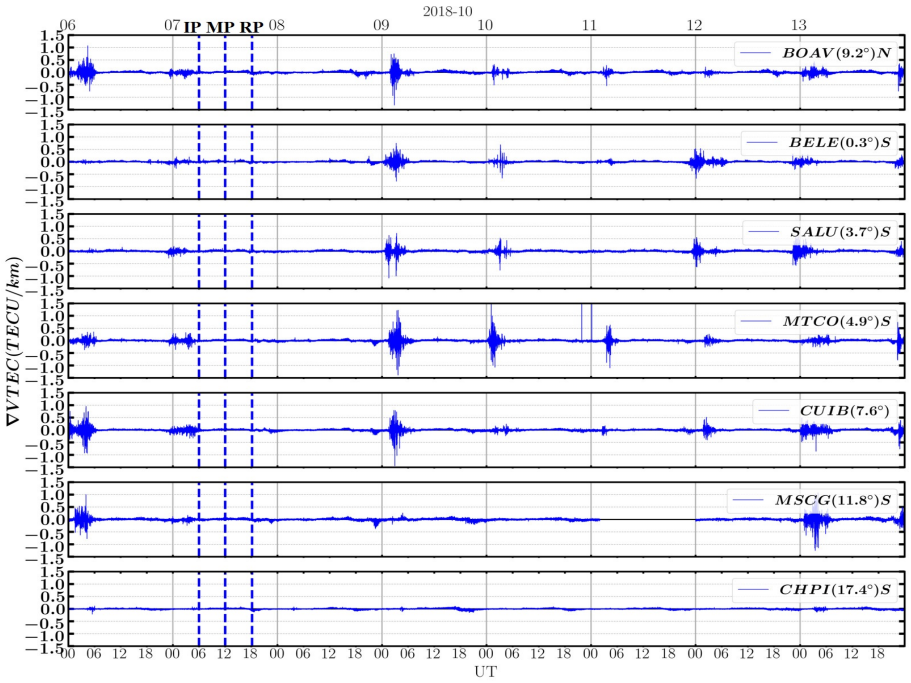

stronger gradients are also seen over the EIA crests, however, they were limited to CUIB. One key difference between the ∇TEC and ROTI is that spatial gradients show the two main sources of gradients while ROTI only shows the amplitude of irregularities. The sharper gradients are due to larger gradients at the side wall while the smaller gradients are due to the inside of the EPBs (PIMENTA et al., 2001; PRADIPTA et al., 2015). As mentioned previously, special attention is given to 9 October 2018 when the irregularities and gradients reached maximum.

To corroborate the observations from GNSS TEC, the amplitude scintillation index calculated from scintillation monitors located in Brazil was obtained from the LISN network namely: (BOAV, SALU, LSJK: São José dos Campos) and the CIGALA/CALIBRA network (STSN: Sinop). The locations of these monitors are shown in Figure 8.18. S4 < 0.2 was considered as noise while the white gaps indicate the absence of data. Figure 8.20 shows the S4 index during the storm. It can be observed that during the MP and early RP the scintillation was weak–moderate ($S_4 < 0.4$) however from 9 October the amplitude of scintillation increased, from weak to strong. The maximum was 0.9 detected at Boa Vista at the north crest. The magnitude also shows a decrease with dip latitude. This variability shows very good agreement with the ROTI and spatial gradients in TEC indicating that small-scale ionospheric irregularities are responsible for scintillation as was reported by (KINTNER et al., 2004; PAULA et al., 2007). The result indeed shows that the 10-minute

ROTI can be used to supplement the S4 index in the absence of observations which often is the case as shown in the figure.

Figure 8.20 - Variation of the S4 Amplitude scintillation index at 4 Brazilian locations on 7–13 October 2018. The dip latitude for each is also indicated. The vertical lines represent the onset of the main (MP) and the recovery phase (RP).

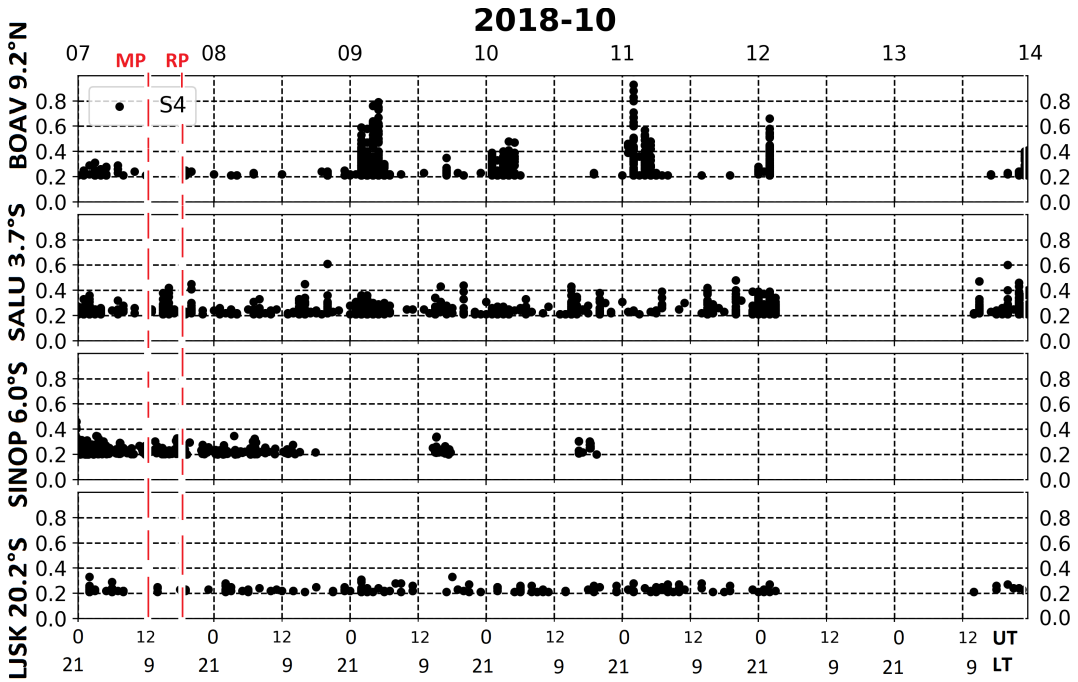

Strong scintillation can be observed outside the main phase ($S_4 > 0.7$).

Figure 8.21 shows unwarped (linearized) images of the OI 630 nm emission which correspond to a mapped area of 1024 km× 1024 km at a peak emission altitude of 250 km. The EPBs are shown as depletions (black regions). The relative airglow intensity in Figure 8.21 was extracted along the dotted line to obtain a one-dimensional profile of the plasma bubbles. It shows sharp fluctuations in the plasma density at the edges of the bubbles, while inside the bubble there is smoother variation. This effect of EPBs was reported for the solar maximum of SC24 using TEC by Pradipta and Doherty (2016), however, this is the first result of this kind during deep solar minimum.

To further demonstrate the robustness of GNSS TEC in observing irregularities, Figure 8.22 shows the variation of ionospheric indices on the night of October 2018 an hour after observations from the all-sky imager and the GOLD FUV spectrograph. It can be observed that the magnitude of the gradients and ROTI is the proportional depth of the depletions

Figure 8.21 - Top: OI 630.0 nm emission all-sky images observed at Cariri on 9 October 2018 at 10:22 LT showing plasma bubbles. The red dot in the center of the image shows the location of the imager while the bottom plot shows the airglow intensity profile along the white dotted line.

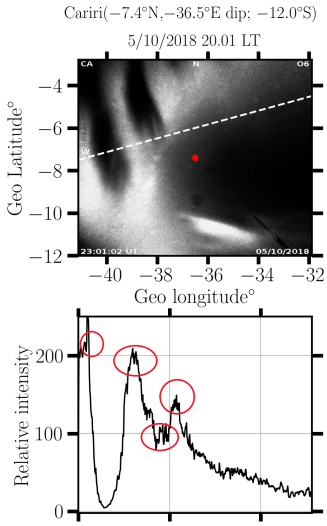

in TEC. The ∇TEC and ROT are negative at the edges as the IPP enters the EPBs and increases together with the background TEC.

Figure 8.22 - Use-case of a multi-parameter approach. Top: The projected geographic locations of the IPPs along receiver-satellite line-of-sight for PRN 32 at 01:00-05:00UT (22:00-02:00 LT) showing (a) the satellite elevation, (b) line-of-sight TEC, (c) spatial gradients (∇TEC), (d) the rate of TEC (ROT) and (e) the rate of TEC Index (ROTI).

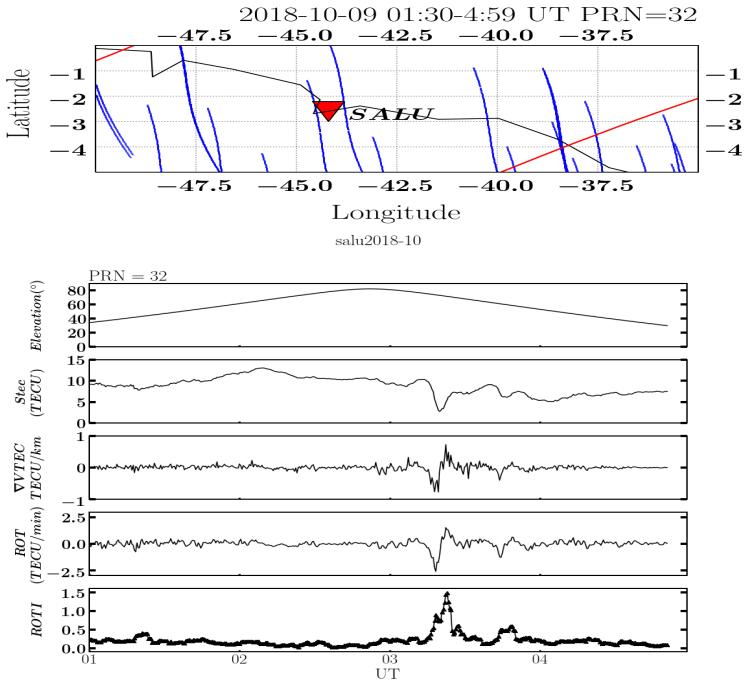

Signatures of plasma depletions over São Luis on 9 October 2018 are observed.

The presence of EPBs is represented by the strong phase fluctuations in the ROT. The advantage of ∇TEC is that it provides information on the structure of the EPBs, unlike ROTI which only shows the magnitude of the irregularities. This case study demonstrates the effectiveness of the Time-step method in deriving spatial gradients for the monitoring of EPBs/irregularities.

To investigate the latitudinal variability in the gradients over the equator and EIA crests, Figure 8.23 (Right) shows the spatial variation of ∇TEC for PRN 32 on 9 October 2018 between 22:30–02:00LT (1:30–05:00 UT). The scale has been adjusted to show stronger gradients localized within the EIA amplitude. Beyond the EIA crests (dip latitude $> 10°$), the magnitude was very low (CHPI). As mentioned previously, our results show the highest amplitude of ROTI and gradients were detected over the crest of the EIA, where plasma density is higher. Several irregularity indices were analyzed to establish some correlation between plasma depletions and irregularities as well as to infer the relationship between the different ionospheric parameters in a technique that was used by Pi et al. (1997), Kintner et al. (2007).

Figure 8.23 - Left Top: TEC maps and ROTI maps (Left bottom) on 9–10 October 2018 at 23:10 – 02:10 LT (02:10–05:10 UT). Right: ∇TEC map from PRN 32 from 22:30–23:59 LT (01:30–04:59 UT). The maps show ionospheric irregularities and gradients located within 10° dip latitude.

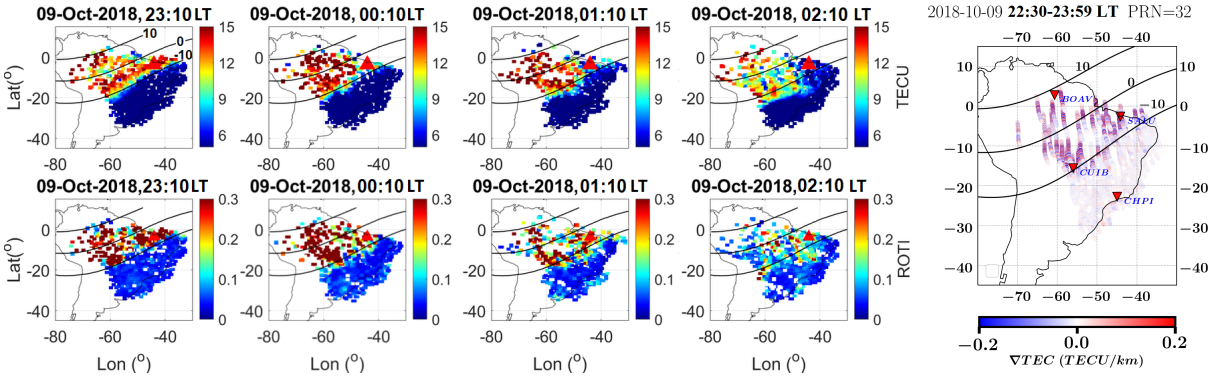

8.2.4 The influence of plasma density on the amplitude of ionospheric gradients

To demonstrate the correlation between TEC magnitude and irregularities rather qualitatively, Figure 8.23 shows the spatial and temporal variability of TEC and ROTI on 09 October 2018 at 23:10–02:10 LT when maximum ROTI was observed. It can be seen that the irregularities have similar temporal and spatial variability to the TEC. The ROTI is highest near 10° dip latitude when TEC was also maximum. From 01:00 LT, ROTI decreased as the magnitude of TEC dropped. Our results show that the strength of irregularities and spatial gradients is dependent on the plasma density. This demonstrates the effectiveness of using spatial gradients for real-time monitoring of errors in GNSS (PI et al., 1997; PRADIPTA; DOHERTY, 2016). During solar minimum, irregularities occur between local sunset and midnight (21:00–0300UT) over South America, however, this may extend to post-midnight during disturbed periods (PAULA et al., 2007). It is important to note that moderate irregularities were observed at 23:00 UT (20:00 LT) followed by a stronger peak at 24:00 LT (03:00UT).

Pereira et al. (2017) observed strong irregularities at Brazilian low latitudes during equinox ($ROTI > 0.2$). However, this was observed during solar maximum, when levels of ionization are much higher than during solar minimum. It has been shown that the intensity of the irregularities is determined by the plasma density and is considerably higher over the EIA (ABDU et al., 2009; SOBRAL et al., 2002; SAHITHI et al., 2019). Since at L-band, amplitude scintillation is due to smaller-scale irregularities (KINTNER et al., 2007), it fol-

lows that the plasma density has a strong correlation with the intensity of irregularities.

8.2.5 F-layer response and equatorial electrojet strength

In this section, the role of penetration electric fields in the occurrence of ionospheric storms, formation of the EIA and plasma irregularities is discussed using ionosonde and magnetometer data. Figure 8.24 shows, from the top panel, the temporal variation of Sym–H, IMF B_z, interplanetary electric field E_y, equatorial electrojet strength, ΔH, in comparison with the quiet day, 6 October 2018 (black curve) and F layer parameters on 6–13 October 2018. The gaps in the "(f)" and "(g)" are due to the presence o strong range and frequency Spread F indicated by the horizontal bars which typically begins after the local sunset (22:00UT) to local sunrise (09:00UT). No Spread F was observed on 8 and 11 October. During the main phase (12:00–21:00UT) the $h'F$ had similar variability to quiet time. There was a large decrease in the h_mF_2 during the MP. On 8 October, the $h'F$ and h_mF_2 increased abruptly during the post-sunset hours 01:00–04:00 UT (23:00–0100 LT). At the onset of the RP, it decreased from 275–250 km. On 8 October there was an enhancement in $h'F$ at 01:00–04:00UT (23:00–01:00 LT) followed by a downward movement on the following night. A strong CEJ is clearly observed in the ΔH during the MP and on 8–9 October.

Figure 8.24 - Variations of (a) *Sym-H*, (b) Bz, (c) Ey, (d) $\Delta H(SLZ - VSS)$ during the storm days with a quiet reference day on 6 October 2018 in black, (e) the F-layer virtual height, $h'F$, (f) peak height h_mF_2, and (g) critical frequency f_oF_2 for São Luís. The black curves represent the average of the 5 quietest geomagnetic days in the (5QD) for each parameter. The dotted lines indicate onset of the initial, main, and recovery phases. The SpreadF interval is also shown by the horizontal bars.

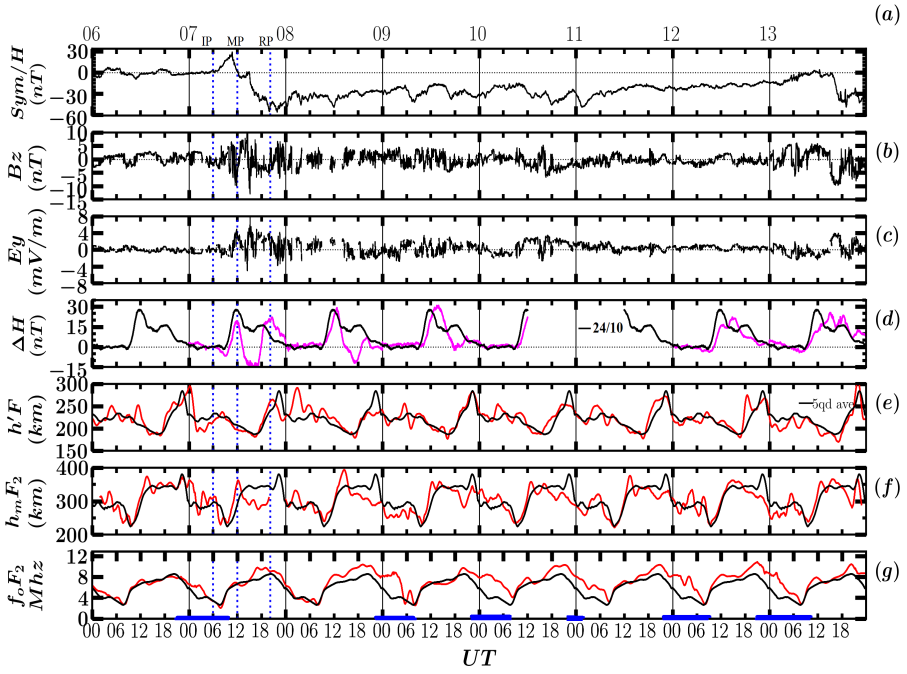

On 8 October, there was a peak in h_mF_2 at 12:00–15:00 UT indicating the upward movement in the F layer peak. This was immediately followed by a strong downward movement which lasted up to sunrise (09:00 UT) on the next day (9 October). This behavior was similar for most of the recovery phase, although the amplitude decreased. The strong downward movement in h_mF_2 on 7 and 8 October was accompanied by the absence of Spread F in the ionograms. ROTI, ∇TEC also show the absence of irregularities while no EPBs were observed by GOLD and ASI.

During the MP, there was a positive storm phase in the f_oF_2. It had a maximum of 10MHz at 1700UT. Meanwhile, the h_mF_2 decreased significantly in the same interval. During the MP at 12–18UT (9–15 LT) there was a large decrease in the ΔH (EEJ). The increase in the f_oF_2 at the equator and together with a decrease in h_mF_2 indicates suppression of the $E \times B$ drift. In addition, the absence of irregularities and SpreadF on the nights of 7 and 8 October was also associated with the CEJ. The CEJ was associated with large Northward, B_z which is known to be a condition for a Westward PPEF. The Westward

PPEF inhibits $E \times B$ drift responsible for the development of EIA, weakening amplitude of scintillation and irregularities, and usually occurs during the main phase (KELLEY et al., 1979; FEJER, 2011; PAULA et al., 2019a). This is in agreement with who Shreedevi and Choudhary (2017) reported a downward movement in $h_m F_2$ during the afternoon, due to a counter-electrojet (CEJ). The suppression of equatorial irregularities is also caused by the disturbance dynamo electric field (MARTINIS et al., 2005; OLADIPO; SCHÜLER, 2013; FAGUNDES et al., 2016; PAULA et al., 2019a). Rastogi and Klobuchar (1990) showed that the strength of ΔH controls the development of the EIA and when it was reversed there is inhibition of the EIA.

However, the effects of disturbance winds are delayed by several hours and even days into the storm (BLANC; RICHMOND, 1980; FEJER, 2011), which explains the suppression of irregularities during the recovery phase. Our findings are in agreement with Paula et al. (2019a) who reported an intensification in the vertical plasma drifts under a strong Eastward PPEF while on the following night, there was the suppression of irregularities under an overshielding PPEF and DDEF. Trans-equatorial winds caused asymmetry in the F layer irregularities at the conjugate points. These winds are generally more effective during equinox compared to winter solstice (DANILOV et al., 1994). The horizontal wind component which is in the direction of the magnetic fields drives plasma in the upward hemisphere up along the field lines to higher altitudes where the rate of recombination is lower, while in the downward hemisphere, the plasma is driven to lower altitudes which suppresses the formation of irregularities (BITTENCOURT; SAHAI, 1978).

8.2.6 Summary of the HSS/CIR storm of 7–13 October 2018

a) There was a PS in TEC (50 %) in the MP and 180 % during the RP. This was followed by a long-lasting NS (80 %) over the South crest;
b) The suppression of EPBs over the south crest was initially caused by an overshielding PPEF and later by a DDEF;
c) Large-scale plasma bubbles in GOLD 135.6 nm, TEC and All-sky imager airglow emission were associated with strong irregularities and gradients;
d) The hemispheric asymmetry in the amplitude of irregularities was likely driven by transequatorial winds. The magnitude of the plasma density magnitude has a strong correlation with irregularities;
e) Sharp fluctuations in the airglow were observed at the walls of the EPBs.

8.3 Discussion: comparison of the CME- and CIR-driven storm

Two peculiar case studies of geomagnetic storms are presented namely; an intense storm with minimum Sym–H of –205 nT classified as (G3) that was caused by an interaction between a CME and a HSS (LISSA et al., 2020). Two months later, a moderate geomagnetic

storm which had a minimum Sym–H of –55 nT occurred on 7 October during the local equinox, driven by a HSS/CIR emanating from a CH. In this section comparison of the conditions of Geospace, IMF and geomagnetic indices is made. Thereafter, the ionospheric response to the two storms and their implications is discussed.

Considering the magnitude of the storms, the CME-driven storm was 3 times more intense according to the minimum Sym–H compared to the CIR-driven storm, but its effects on the ionosphere were less significant. A CH was observed adjacent to the CME days before the storm on 24 August. CHs have been reported to deflect Earth-directed CMEs away from the Sun-Earth line (TSURUTANI et al., 2006; GOPALSWAMY et al., 2011) thereby weakening the impact of the CME. The August CME-driven storm had a maximum Kp of 7 and AE index 2500nT, while the CIR storm was minor with maxima of 5.5 and 1200 nT respectively. The CIR storm was characterized by a long recovery phase with high auroral activity due to substorms indicated by multiple negative incursions of Sym–H while the CME storm had a smoother recovery phase with low auroral activity. The main features of the two storms and their impact on the ionosphere are summarized in Table 8.1.

Table 8.1 - Summary of CME- and CIR -driven storms.

Feature	**24 August CME**	**7 October CIR**
Min Sym–H (nT)	–205	–55
Duration of RP (Days)	~ 5	~ 6
Kp max	~ 7	~ 5.5
Electric Field Amplitude mV/m	8	5
B_z (nT) min	–8	–8
ΔH (nT) max	100	25
Auroral activity(nT) max	2500	1200
Solar Flux F10.7 (SFU)	~ 69	~ 69
PPEF (MP)	Weak U/shielding	Strong O/shielding
PS [MP|RP] (%)	50|180	180|150
Max ROTI	0.06	0.6
EPBs	None	Strong

Despite having a similar magnitude in IMF B_z and IEF E_y, B_z was highly oscillatory during the CIR storm. The polarity was also Northward for a longer duration compared to the CME storm. Northward B_z is a condition for overshielding PPEF which has opposite polarity to the under-shielding Eastward PPEF caused by sudden Southward turning of the IMF B_z (KELLEY et al., 1979; TSURUTANI et al., 2003). Positive (PS) and negative (NS) ionospheric storms were observed during both storms over most latitudes in addition to enhancement in the EIA. A larger PS magnitude, during the CME storm MP, was caused by an undershielding PPEF. In contrast, an overshielding PPEF observed during

the MP of the moderate CIR led to a smaller magnitude PS. In addition, a long-lasting NS was observed over the south crest during the recovery phases. The NS magnitude was 30% larger during the moderate CIR-driven storm compared to the CME storm.

One mechanism for such long-lasting NS could be transequatorial winds which can drive plasma down, along the field lines to lower altitudes where the rate of recombination is higher (ABDU et al., 2009), causing negative ionospheric storms (PROLSS, 1995; BUONSANTO, 1999). Neutral winds can transport nitrogen-rich air over much of the high-latitude region and part of the mid-latitude region, causing a decrease in thermospheric composition (DANILOV et al., 1994; PROLSS, 1995). Our observations show that the prolonged recovery phase of the CIR storm led to the continuous injection of energy into the magnetosphere/ionosphere system during a longer RP (VERKHOGLYADOVA et al., 2011), unlike CME-driven storms which have shorter recovery phase (TSURUTANI et al., 2006). The RP of the CIR was also characterized by a HILDCAA indicated by the heightened auroral activity which occurs during long-lasting recovery phases. However, the duration of the CME storm was peculiar since it had an unusually long RP. This is attributed to the influence of a HSS which was preceded by the CME. Silva et al. (2017) found evidence of PPEF during HILDCAA events which had a significant impact on the F-layer. The long-lasting PS during the RP of the CIR storm that was 30% larger than the CME. Verkhoglyadova et al. (2011), Liu et al. (2012), Candido et al. (2018) studied the effects of high-speed streams on the equatorial and low-latitude ionosphere during deep solar minimum and showed that the storm effects are most significant during the recovery phase despite having only moderate magnitude. Consequently, RP of the CIR-storm led to significant PS compared to CME storms (LIU et al., 2012).

Apart from differences in magnitude and source, the local time of the storm main phases is also known to determine ionospheric response. The main phase of the CIR storm occurred during the daytime over Brazil while the CME storm's main phase was during the nighttime. It has been shown that the occurrence of a positive or negative ionospheric storm depends on the local time at which B_z reaches minimum (BALAN; RAO, 1990; DUGASSA et al., 2019; OYEDOKUN et al., 2022) although during solar minimum there is a preference for nighttime (LEKSHMI et al., 2011). The southward or northward turning of B_z determines the polarity of the PPEF (KELLEY et al., 2003). The dynamics of the F layer peak height and density during the main phases were quite contrasted. The CEJ during the CIR storm main phase was not observed during the CME storm. As opposed to the downward movement of the h_mF_2 and $h'F$ during the CIR MP, there was a sudden uplift during the CME storm. This caused a smaller magnitude PS and suppression of irregularities during the MP. This contrasting behavior is attributed to the inverse polarity of undershielding and overshielding PPEF. Sudden southward turning of IMF B_z causes an Eastward (dawn-to-dusk) electric field which enhances the $E \times B$ drift, leading to uplift

(KELLEY et al., 1979). On the other hand, sudden northward turning of IMF B_z causes a Westward electric field that reverses the direction of the $E \times B$, suppressing the F layer height (KELLEY et al., 1979; TSURUTANI et al., 2008).

Considering the differences in the post-sunset ionosphere, stronger irregularities and sharper gradients were observed during the CIR storm. This is because the occurrence of EPBs is mainly determined by the magnitude of the PRE which is much larger during equinoxes. The effectiveness of the PPEF also depends on the conductivity of the ionosphere, which depends on the season. Therefore, the conditions during the CIR storm favored a larger ionospheric response. It is evident that the magnitude of a geomagnetic storm is not the main factor that influences ionospheric response, particularly in the nighttime. Therefore, the season of occurrence of the storm, and the time of the main phase are all factors that influence the response of the ionosphere (DUGASSA et al., 2019; OYEDOKUN et al., 2022). However, comparing geomagnetic storms is a challenging undertaking because every storm is unique in terms of the features of the solar wind, interplanetary magnetic field and magnetospheric drivers (BURNS et al., 2014). To further complicate matters the background conditions of the thermosphere-ionosphere are very dynamic for each period.

8.4 Case study 3: assessing the effects of a minor CIR-HSS geomagnetic storm on the Brazilian low-latitude ionosphere

This section presents a case study of a minor CIR/HSS-driven geomagnetic storm (min *Sym-H* =– 50nT) which occurred on 13-14 October 2018 titled: *"Assessing the effects of a Minor CIR-HSS Geomagnetic Storm on the Brazilian Low-Latitude Ionosphere: Ground and Space-Based Observations"* (CHINGARANDI et al., 2023) published in the AGU Space Weather Journal. Understanding the effects of minor storms on the thermosphere-ionosphere has become of great interest, particularly following the loss of 38 SpaceX satellites due to ion drag after a geomagnetic storm in February 2022 (FANG et al., 2022). In light of this, the first investigation into the effects of a minor storm specifically over Brazilian low latitudes is presented.

The CIR/HSS-driven geomagnetic storm on 13-14 October is related to the appearance of a HSS/CIR from a coronal hole. Figure 8.25 shows a trans-equatorial CH (CH889) on the solar disk on 10 October 2018, ∼3 days before the storm. The CH is mostly located in the Southern Hemisphere. Small active regions and bright prominences are visible beside it.

Figure 8.25 - Trans-equatorial CH captured by the (SDO) at wavelength 193 Å on 10 October 2018. Weak prominences surround the coronal hole.

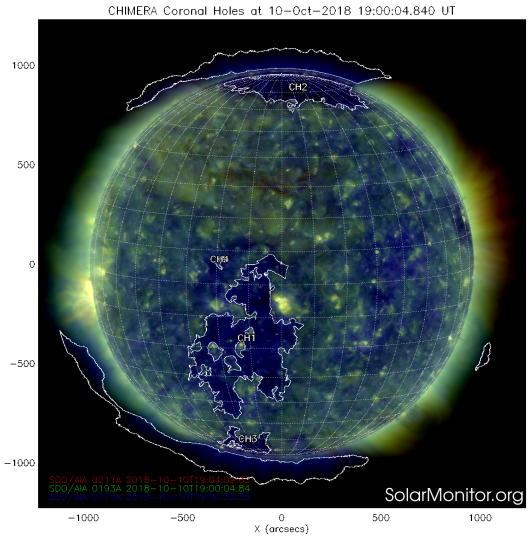

SOURCE: Chingarandi et al. (2023).

We first characterize the space weather event using observations of the IMF, solar wind, and geomagnetic indices. Ionospheric and thermospheric responses were investigated using thermospheric column density ratio, [O]/[N2]; TEC and its derived indices as well as the GOLD 135.6 nm radiance. SWARM in-situ electron density measurements and Digisonde located within the equatorial region are also presented.

8.4.1 Solar, interplanetary, and geomagnetic parameters and indices-CIR/HSS-driven storm on 13-14 October 2018

Figure 8.26 shows the variation of solar wind, interplanetary, and geomagnetic parameters and indices on 13–14 October. From top: the solar wind speed, V_{sw} (km/s), the plasma temperature, Tp (K), the proton density, N_p/cm^{-3}, the Interplanetary Magnetic Field (IMF)m magnitude, |B|, and its components Bx, By, and B_z (nT), in GSM coordinate system; the east-west component of the Interplanetary Electric Field, IEF, Ey (mV/m), the 5-min ring current symmetric index, Sym–H (nT), the auroral electrojet index, AE (nT), the planetary index Kp , and the solar flux index, F10.7 (in SFU) where (1 SFU = 10^{-22}W m^{-2} Hz^{-1}).

Figure 8.26 - Variation of the solar wind, interplanetary magnetic field, and geomagnetic parameters and indices from 13 to 14 October 2018. From top to bottom: the solar wind speed, V_{sw} (km/s);, the plasma temperature; Tp (K), the proton density, $n_p(/cm^{-3})$, the Interplanetary Magnetic Field, |B| (nT);, and its components Bx, By, B_z, the east-west component of the IEF, Ey (mV/m), the longitudinally symmetric index, Sym–H (nT), AE index (nT), Kp index, and the F10.7 (SFU) solar flux. The red lines indicate the beginning of the main and recovery phases.

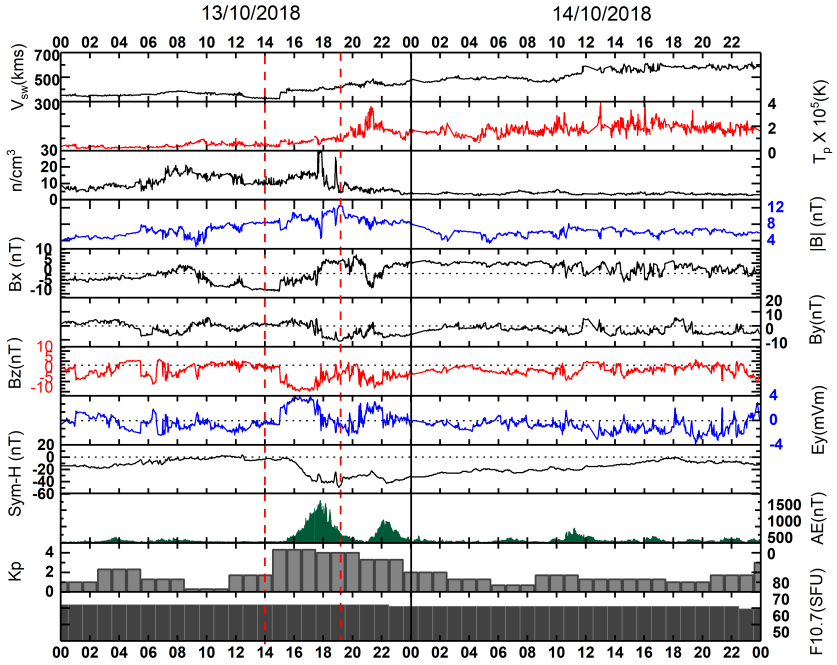

SOURCE: Chingarandi et al. (2023).

On 13 October, a small abrupt increase in the solar wind speed was observed at 15:00 UT (noon LT) accompanied by an increase in n_p and Tp, which is typical of a CIR/HSS (TSURUTANI et al., 2006). The B_z abruptly turned from northward to southward within a few minutes and remained southward for more than 3 hours. There was no clear Sudden Storm Commencement, SSC. The main phase (MP) of the storm occurred from 14:00 UT to 19:00 UT (11:00 LT to 16:00 LT) on 13 October 2018, when Sym–H reached its minimum of –50nT. The Kp maximum during the MP was 4 while AE increased from $<$ 100 nT to a peak of ∼1300 nT. The increase in AE together with southward B_z indicates the injection of energy through substorms and particle precipitation (TSURUTANI et al., 1995). The storm had a shorter recovery phase (RP) which began on 13 October at 19:00 UT (16:00 LT) to 18:00 UT (15:00 LT) on 14 October, a duration of ∼23 hours. At the end of the main phase, the IMF components Bx and By reached – 6 nT and – 10 nT, respectively.

B_z had southward polarity with oscillations from 15:00 to 21:00 UT (12:00 to 18:00 LT). There was a second southward turning of B_z after 20:00UT. During the disturbed interval, the solar flux F10.7 remained at around 70 SFU, indicating very low solar activity (AA et al., 2021; DERGHAZARIAN et al., 2021). On 14 October, the v_{sw} reached a maximum of ∼600 km/s. Following the NOAA classification, this event is considered as a minor storm, G1. It should be noted that the negative SymH before the storm onset is related to the end of the recovery phase of a previous moderate storm, which was discussed in Section 8.2.

8.4.2 Low-latitude ionospheric and thermospheric response - TEC and [O]/[N2] variation

To investigate the response of the ionosphere to the 13 October 2018 minor HSS/CIR-driven storm the variation of TEC over the Brazilian low latitude ionosphere sector is analyzed.

Figure 8.27 shows from the top panel: hourly TEC maps obtained from ground-based GNSS receivers on October 13, from 14:00–23:40 UT (11:00–20:40 LT). The beginning of the main phase and the recovery phases are indicated on the maps as MP and RP, respectively. (b) The bottom panel shows the variation of TEC, ΔTEC, which is the difference in magnitude of the TEC between the disturbed day, 13 October (Kp > 4), and the reference quiet day, 6 October ($Kp \leq 3$). The criteria for the quiet day were determined based on the auroral activity (AE < 250 nT) and the daily maximum planetary index (Kp < 3) (KLENZING et al., 2013; CAI et al., 2020b; CAI et al., 2021). The TEC and the ΔTEC maps were generated every 15 min. However, for the post-sunset hours, we only show the observations that coincide with the GOLD irradiance maps from 22:00–23:40 UT (19:00–20:40 LT). Figure 8.27 (a) shows large temporal and spatial variability in TEC during the main phase of the storm (MP) with strong development in the southern crest of EIA (data over the northern region are scarce), prolonged at least to 22:00 UT. The EIA over the western sector of Brazil (longitude > 50°W) was stronger than the eastern sector around 21:00 UT (18:00 LT). The TEC had a maximum of ∼40 TECU, occurred at∼17:00 UT (14:00 LT) around the southern crest of the EIA (dip lat ∼15°S). The EIA expanded poleward up to dip latitude ∼20°S from 16:00 –19:00 UT (13:00 – 16:00 LT), an expansion of ∼5° latitude compared to the quiet time EIA on 06 October when it extended to 15°S dip latitude. The enhancement of the EIA during the disturbed interval indicates the strengthening of $E \times B$ vertical drift under the influence of an enhanced zonal electric field, PPEF (LIU et al., 1999; KELLEY et al., 2003). At 22:20 UT (19:20 LT in this longitude), the local sunset, depletions in TEC, aligned from north-southeast (dark blue structures) can be observed at ∼45 °W longitude. These structured depletions are signatures of Equatorial Plasma Bubbles, EPBs (CHU et al., 2005; TAKAHASHI et al.,

Figure 8.27 - (a) TEC maps and (b) ΔTEC maps over Brazil on 13 October 2018 (LT = UT-3). The black lines represent the magnetic equator in the middle, and the outer lines represent ±10° dip latitude. The evolution of the EIA is shown in the TEC while the dotted black lines indicate EPBs. ΔTEC maps show a large positive ionospheric storm followed by a negative ionospheric storm.

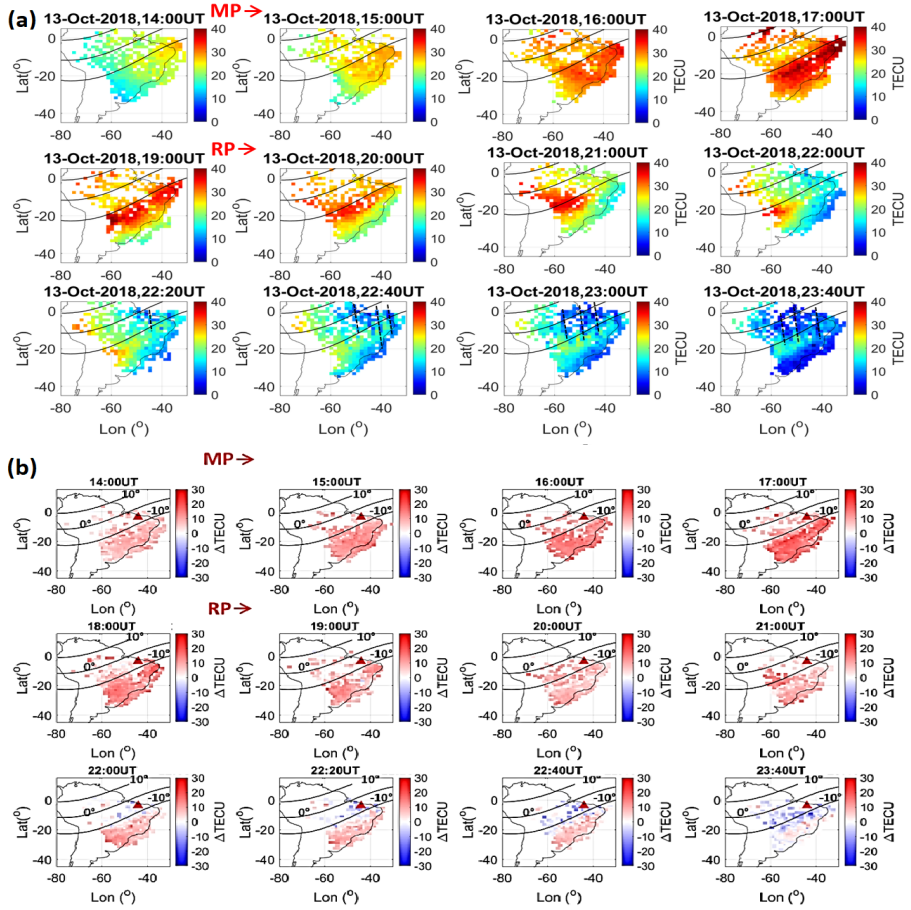

SOURCE: Chingarandi et al. (2023).

2016; BARROS et al., 2018; AA et al., 2019; CAI et al., 2020a) that were observed from sunset up to 23:40 UT (20:40 LT). Figure 8.27 (b) shows an increase in TEC, ($\Delta TEC > 0$), in comparison to the quiet day. A positive ionospheric storm began soon after the main phase and reached a maximum of ∼23 TECU at 17:00 UT (14:00 LT) around the crests of EIA. The PS lasted until local the postsunset hours. However, after sunset, it transitioned into a negative storm (NS) after 22:00 UT (19:00 LT) during the occurrence of EBPs (Figures 8.27 (a) and (b)). The magnitude of the PS is in agreement with Liu et al. (2012) who found PS of 15 TECU over low latitudes during a CIR/HSS-driven storm with similar magnitude (minimum Sym–H ∼– 50 nT and B_z∼ –18 nT).

To assess the possible mechanisms responsible for the daytime ionospheric storm, the influence of the neutral thermospheric composition changes and prompt penetration of the electric fields is considered. The ΣO/N2 variation plays an important role in modulating the daytime TEC (TITHERIDGE, 1974; CAI et al., 2020b) and during geomagnetic storms (DANILOV et al., 1994). Figure 8.28 shows the variation of the column density ratio (ΣO/N2) from GOLD over the South American sector from 20:45–22:45 UT (17:45 – 19:45 LT) on the quiet reference day of 06 October (top row) and on 13 October (bottom panel). The ΣO/N2 is available only up to an hour after sunset, which is around 22:00 UT (19:00 LT). At 20:45 UT (17:45 LT), there was a 20%–30% patch-like enhancement in [O]/[N2] over equatorial and low latitudes (0–40°, geographic latitude) compared to the quiet reference day. Although there was a lack of data coverage over the eastern part of the continent, it is possible to infer that the Σ O/N2 column density ratio increased over quiet time. As seen in Figure 8.27 (b), a prolonged positive ionospheric storm of amplitude ∼23 TECU began during the main phase lasting up to ∼ 22:40 UT (20:40 LT) although it decreased after 19:00 UT (16:00 LT). During this interval, the EIA was well pronounced (Figure 8.27 (a). This increase also coincided with enhancement in ΣO/N2.

Figure 8.28 - GOLD ΣO/N2 variation over South America from 20:45 to 22:45 UT (17:45 to 19:45 LT) on the quiet day of 6 October 2018 (top row) and the disturbed day 13 October 2018 (bottom row) showing a large enhancement in the thermospheric composition ratio.

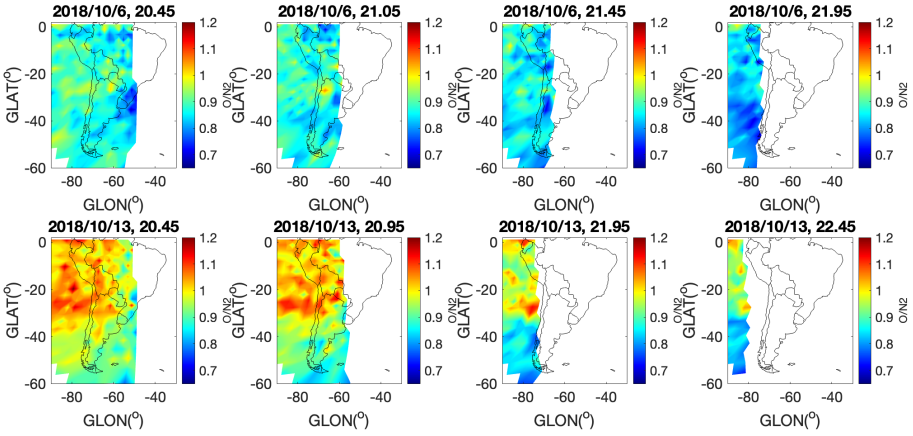

SOURCE: Chingarandi et al. (2023).

The quiet day closest to the storm (day 6) was selected as the reference instead of the five quietest days (18, 19, 20, 23, and 29) since the 5QD are much further from the storm and thus could include seasonal changes which would have compounded the analysis of

the thermospheric composition. Thus, the storm occurred during the period of transition into the local equinox (BHATTACHARYYA, 1992) in which there are seasonal changes in the thermospheric composition (TITHERIDGE, 1974). The quiet background conditions in the thermosphere before a geomagnetic storm are determined by solar EUV and thus seasonal variations are very important in understanding the TI response (LIU, 2016). Thermospheric composition increases during the storm time are associated with thermospheric expansion due to Joule heating (PROLSS, 1995; FULLER-ROWELL et al., 1996; CAI et al., 2021). This causes upwelling of the thermosphere, decreasing the neutral composition ratio and causing a PS over low latitudes (ASTAFYEVA et al., 2015). This may explain the sustained positive storm effect in VTEC.

8.4.3 Equatorial plasma bubbles

Apart from the remarkable intensification in TEC, large-scale plasma irregularities were observed in TEC maps after 22:00 UT (19:00LT), as shown in Figure 8.27 (a). Plasma irregularities are responsible for ionospheric scintillation which in turn disrupts the operation of GNSS navigation positioning, and communications systems (KINTNER et al., 2004). This poses the question: Can a minor storm cause significant impact on the ionosphere during deep solar minimum? We assess whether the enhancement in TEC and the EIA plays a significant role in the development of plasma irregularities. For a broader view of the EPBs over the South Americansector, GOLD 135.6 nm irradiance maps are presented.

Figure 8.29 - GOLD night-time observations of 135.6nm irradiance maps showing Six scans on 6 October 2018. The first two are a combination of scans at 22:10& 22:25 and 22:40 & 22:55 UT respectively. Weaker plasma bubbles can be seen from 23:10 UT.

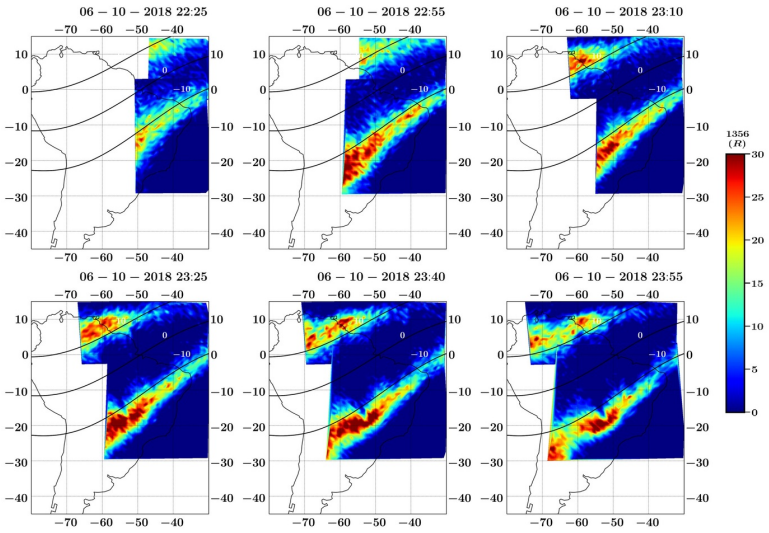

For perspective, Figure 8.29 shows a sequence of GOLD OI 135.6 nm on a quiet day, 6 October 2018. Weaker plasma bubbles and EIA during the same interval although the post-sunset EIA is present. The 135.6 nm radiance represents the F-layer peak electron density, N_mF_2, in the nighttime ionosphere although most of the contribution is localized at the F-layer peak height (CAI et al., 2020a).

Figure 8.30 - Top: GOLD OI 135.6-nm airglow emission on 13 October 2018 from 21:55 to 23:40 UT (18:55 to 20:40 LT) showing the post-sunset EIA and plasma depletions over the Brazilian sector. Bottom: Fluctuations in the electron density, N_e, over $\sim$ 39°W longitude measured by the SWARM satellite during a pass between 00:38 to 00:54 UT (21:38 to 21:54 LT) at an altitude of $\sim$500 km.

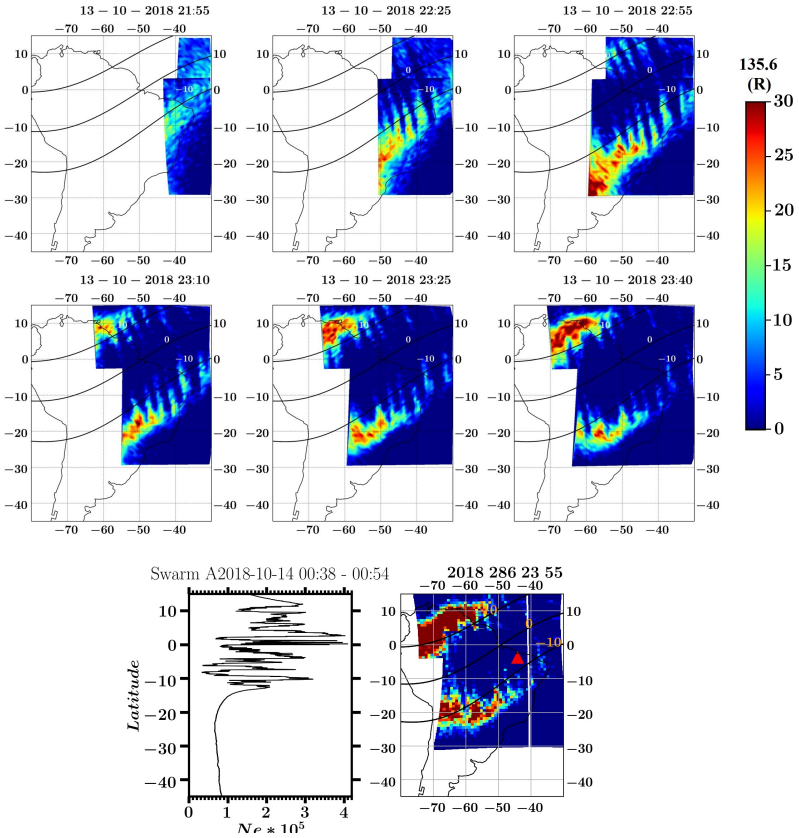

SOURCE: Chingarandi et al. (2023).

Figure 8.30 (top) shows a sequence of GOLD OI 135.6 nm emissions on 13 October 2018 from 21:55 UT (18:55 LT) to 23:55 UT (20:55 LT) while Figure 8.30 (bottom) shows the electron density (N_e) variation with latitude from a single pass of the satellite SWARM over $\sim$ 39° W longitude at 00:38 to 00:54 UT (21:38 to 21:54 LT) (bottom left panel),

around 50 minutes after the last GOLD map. The images show the post-sunset equatorial ionization anomaly (EIA) which extends up to$\sim \pm 15°$ off the equator as regions of brighter irradiance with crests North and South of the geomagnetic equator. In addition, structured depletions, elongated in the northwest-southeast direction, representing equatorial plasma bubbles which extend to the crests of the EIA. These depletions coincide with the TEC maps shown in Figure 8.27 (a) but at a higher resolution. The westward inclination of the depletions is likely due to gradients in the zonal drift velocity, which decreases with increasing latitude (BARROS et al., 2018; AA et al., 2020). The largest depletions in SWARM electron density had magnitude $\sim 4\times10^5/\text{cm}^3$ near the geographic equator. Sharp variations are found within $\pm 15°$ geographic latitude along the 39°W longitude. geographic latitudes over the TEC depletions which were detected in the GOLD image 50 minutes earlier. These are signatures of small-scale irregularities associated with EPBs (AA et al., 2020).

To obtain a more detailed analysis of the EPB characteristics from distinct techniques, we compare simultaneous observations using a GOLD OI 135-nm image and a TEC map at 23:55 UT (20:55 LT) on 13 October 2018. The scales have been adjusted to highlight the plasma depletions and the EIA. Figure 8.31 shows clear signatures of plasma depletions observed by the GOLD radiance image and in the Madrigal TEC obtained from ground-based receivers over South America. The GOLD 135.6 nm scan began at 23:55 UT. Plasma depletions are marked by dashed lines.

Figure 8.31 - GOLD 135.6 nm radiance showing scans at 23:55 UT on 13 October 2018 and TEC map on the right-hand panel. Large-scale plasma depletions are shown over South America indicated by dashed lines. The magnetic equator is in the middle with $\pm 10°$ dip latitudes.

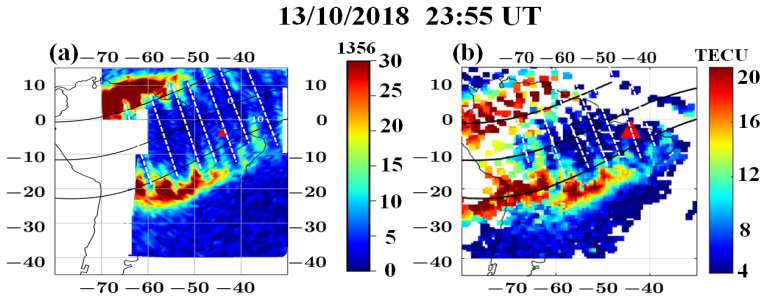

SOURCE: Chingarandi et al. (2023).

The structure of the EIA and the depletions observed by GOLD images and TEC maps

show a good correlation although there are some differences. Cai et al. (2020a) showed that observations of GOLD OI 135.6 radiance and GPS TEC have a good agreement in the magnitude and morphology of the EIA and depletions. However, there are some differences between the two observations. First, GOLD images have higher resolution in comparison with TEC maps. One reason is the sparse distribution of GNSS receivers in the northern region of Brazil). Secondly, TEC represents the integral of the electron density map to a mean shell height of 350 km (MISRA; ENGE, 2011) while the OI 135.6 nm represents the F layer peak electron density in the nighttime ionosphere (CAI et al., 2020a). A significant portion of the airglow emission is absorbed in the thermosphere before it reaches ground-based imagers. As such GOLD measurements are more sensitive to the weak airglow emissions in the nightside allowing the detection of fainter structures (CAI et al., 2020a).

The EPB depletions have a periodic longitudinal separation, as previously reported by Eastes et al. (2019); especially in the 35–60°W sectors. The estimated distance between the EPBs ranged from 300–500 km, and varies with latitude, while the plasma bubble width was ∼200 km. The amplitude of the difference in irradiance between the bubble walls and surrounding plasma was around 10 Rayleighs (15 at the walls and 5 within the bubble) while for TEC it was around 15 TECU. On the quiet night (06 October), the depletions/EPBs had a magnitude of ∼8 TECU against a background of 16 TECU. The depletions measured by GOLD, therefore, seem to be deeper than those detected in the TEC. One advantage of GNSS is that it offers continuous monitoring of the ionosphere while GOLD is limited to the local pre-midnight sector at 20:10–24:25 UT (17:10–21:25 LT) (EASTES et al., 2019). However, during solar minimum EPBs usually occur from the local sunset to local midnight (SOBRAL et al., 2002) hence GOLD satellite window of observation is within the time interval where the evolution of the EPBs can be shown. On the other hand, GOLD provides new insights into the finer morphology of EPBs over the eastern coast and northern part of South America which was previously not well known. The EPBs extend beyond ∼ 45° W and are therefore not only a threat to inland navigation and positioning systems but also over the Atlantic Ocean.

Figure 8.32 shows the maximum radiance for each disk scan on the night of 13 October 2018 from 21:40 –23:55UT. GOLD alternates between the Northern and Southern Hemisphere from 21:40 to 22:55 UT hence each scan only shows one hemisphere. The location of the EIA can be shown by the position of maximum radiance for each hemisphere. As shown in the figure, the EIA was located between 15–20° S dip latitude consistent with the GOLD 135.6 nm maps. It also shows hemispheric asymmetry in terms of the location of the crests. Similar symmetry is shown in the TEC map in Figure 8.31.

Figure 8.32 - The bar plot shows the approximate location of the crests of the EIA with respect to dip latitude. The red dots represent the maximum irradiance observed at that time. The scan numbers "(0–5)" indicate alternate hemispheres and "(6-13)" show simultaneous North-South hemisphere scans. Symmetry in the crest position can be observed from 23:10 UT.

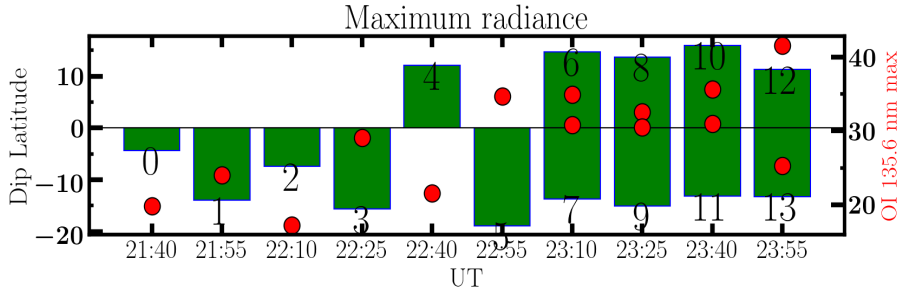

8.4.4 Response of small-scale ionospheric irregularities and spatial gradients in TEC

In this section, the response of ionospheric irregularities measured by ROTI and spatial gradients is presented. ROTI is used to describe small-scale ionospheric irregularities that can disrupt the operation of satellite navigation and communication. Figure 8.33 shows

Figure 8.33 - Maps of ROTI calculated from GNSS receivers in Brazil on 13 October; (first three panels) and 6 October 2018 (last panel) showing the presence of strong, periodic irregularities (ROTI > 0.2) highlighted by the black dashed lines.

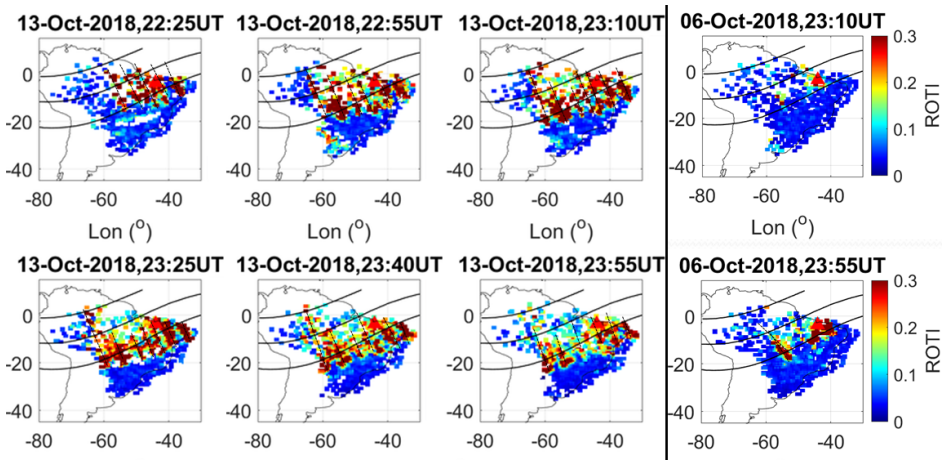

SOURCE: Chingarandi et al. (2023).

a sequence of maps showing the temporal variation in post-sunset ROTI obtained from ground-based GNSS receivers in Brazil. Strong, irregularities (ROTI $>$ 0.2) began at 22:25 UT (19:25 LT) over the eastern sector of Brazil while weaker on the quiet day, the irregularities were weaker. The structures extend beyond 15°S dip latitude, while on 6 October they were only limited to 10°S dip latitude. The amplitude of the irregularities was located over low latitudes where plasma density gradients are generally larger (PAULA et al., 2003; ABDU et al., 2009). At 22:55 UT (19:55 LT) ROTI increased as the irregularities expanded poleward. Thereafter, the amplitude decreased at 23:25 UT (20:25 LT) over the equatorial region while some irregularities remained over the EIA. Small-scale irregularities were also detected by the SWARM N_e, although the ROTI maps indicate irregularities lasted until 05:00 UT (02:00 LT) the next day. Furthermore, the irregularities show similar temporal and spatial distribution as the EPB depletions observed in GOLD and GNSS TEC maps, however, were smaller and have a shorter longitudinal separation. The periodic structures were unique to the 13 October case and were not observed during the 7 October CIR storm period. Although regular spacing in large-scale plasma bubbles has previously been detected using GOLD and all-sky imagers (TAKAHASHI et al., 2018; EASTES et al., 2019), this is the first time that periodic spacing of smaller-scale irregularities is shown in such fine detail consistent with the large-scale bubbles detected by GOLD OI 135.6 nm. The behavior of the spatial TEC gradients due to plasma bubbles is also analyzed. Figure 8.34 shows ∇TEC variation on 06 (quiet reference) and 13 October 2018, during the first 2 hours of the recovery phase of the storm. The map on the right shows depletions/EPBs in the GOLD FUV OI 135.6 nm.

Figure 8.34 - Left and middle panels show the variation of the temporal gradients in the TEC (time-step method) on the nights of 06-07 (quiet day) and 13–14 October. The dip latitude indicated in brackets (b) Right: GOLD 135.6 nm emission image at 23:55 (20:55 LT) showing plasma depletions and the nighttime EIA. The locations of the stations are also shown on the map.

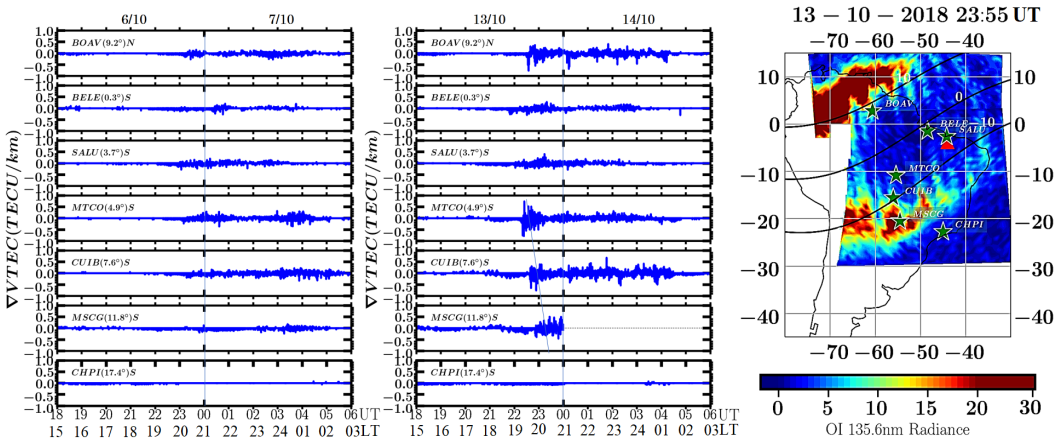

SOURCE: Chingarandi et al. (2023).

The representative stations are also indicated on the map. Plasma irregularities were detected on both days in agreement with GOLD and TEC observations. There was an increase in the magnitude of ∇TEC on the disturbed day which also peaked earlier than quiet time. Gradients occurred from the post-sunset to the post-midnight sector (∼22:00–05:00UT, 19:00–02:00 LT) on the next day. On the disturbed day, peak gradients in TEC can be observed from 22:30–05:00UT at all latitudes indicating a greater latitudinal extent in the EPBs than during quiet time. Sharper edge gradients can be observed at the side walls of the EPBs compared to those observed inside the bubbles (PIMENTA et al., 2003; PRADIPTA; DOHERTY, 2016). On 13 October, the gradients were maximum at MTCO, a near-equatorial station. Near the dip equator (BELE, SALU) the TEC gradients were much weaker compared to the crests of EIA (BOAV and CUIB). There is no evidence of TEC gradients at around CHPI, indicating that this station was outside the latitudinal extent of the EPBs, as shown in the GOLD OI 135.6 nm map.

The performance of GNSS and GBAS is more severely affected over the EIA the strength of irregularities and gradients is largest (DATTA-BARUA et al., 2002; LEE et al., 2006; PRADIPTA; DOHERTY, 2016). These gradients can affect GNSS, and GBAS systems, causing navigation errors or critical system failure while changes in thermospheric composition enhance orbital drag, potentially leading to the loss of satellites. As expected, the strong TEC gradients coincide with the maxima in ROTI and TEC as discussed in sec-

tion 8.2.4. Although plasma density is lower during solar minimum, our observations show that the occurrence of a minor geomagnetic storm can create favorable conditions for the development of plasma bubbles occurrence such as enhancement in TEC and prolonged EIA.

8.4.5 F-layer dynamics and equatorial electrojet strength

A large positive ionospheric storm, of amplitude ∼23 TECU, was observed mainly at the crests of the EIA over South America. In addition, there was the development of EPBs early into the Spread-F season (October) together with the strengthening of plasma TEC irregularities, ROTI and TEC gradients.

Figure 8.35 - Variation in (a) *Sym-H*, (b) B_z, (c) Ey, (d) $\Delta H(SLZ - VSS)$ (magenta during the storm days with a quiet reference day on 6 October 2018 in black), (e) the F-layer virtual height, $h'F$, (f) peak height, h_mF_2 and (g) critical frequency, f_oF_2 for São Luís. The black curves represent the average of the 5 quietest geomagnetic days (5QD) for each parameter. The main and recovery phases are indicated as MP and RP, respectively. The horizontal bar represents Spread F interval.

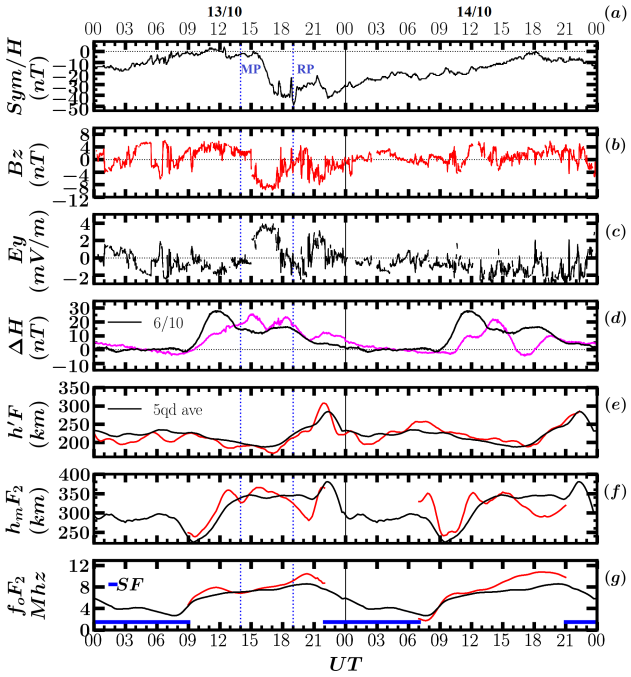

SOURCE: Chingarandi et al. (2023).

An increase in Σ O/N2 was partly responsible for the TEC enhancement during the daytime. Apart from thermospheric composition changes, penetration electric fields also play an important role in low-latitude electrodynamics that control the development of the EIA and plasma irregularities (FEJER, 2011). We investigate the behavior of the F layer parameters obtained from a Digisonde located at São Luís.

Figure 8.35 shows, from top to bottom; the temporal variation of (a) the Sym–H index, (b) the vertical component of the interplanetary magnetic field B_z,(c) the interplanetary electric field E_y; (d) the equatorial electrojet strength, ΔH, in comparison with the quiet day, 6 October 2018 (black curve); (e) the F-layer virtual height, $h'F$, peak height, h_mF_2, and the critical frequency, f_oF_2 on 13–14 October 2018.

During the main phase, h_mF_2 increased from 350 km to 375 km over 1.5 hours and peaked around 15:30 UT (12:30 LT). However, prior to that, there was a downward movement in the bottom side of the F layer ($h'F$) from 16:00 to 18:00 UT (13:00 to 15:00 LT) in the MP. This interval is when the PS in TEC was strongest (Figure 8.27). On 13 October the h_mF_2 decreased from 350 km (18:00UT, 15:00 LT) to 285 km (20:30 UT, 17:30 LT). Soon after there was a sharp increase in $h'F$ from 230 km to 310 km at 20:40–22:00 UT. The PRE peak in $h'F$ also occurred one hour earlier than the 5QD (black line) during which there was a sudden southward turning of B_z from 20:30 to 22:00 UT (17:30 to 19:00 LT). A positive storm seen in f_oF_2 occurred on 13 October during both the main (MP) and recovery (RP) phases after 14:00 UT (11:00 LT) and 14:00 UT (11:00 LT), respectively. In both cases, there was a significant decrease in the h_mF_2.

On 14 October the $h'F$ variation was similar to quiet time, with no noticeable increase at the PRE. An upward movement in the h_mF_2 occurred up to 15:00 UT (noon LT) when there was a downward reversal. On 14 October, at the end of the recovery phase, the h_mF_2 decreased from 350 to 280 km at 15:00-21:00 UT while f_oF_2 increased in the same interval. This PS over the equator together with a downward movement in the F-layer peak indicates suppression of the $E \times B$ drift. Figure 8.35 (d) shows an enhancement in the ΔH which began at 13:30 UT (10:30 LT) and peaked at 15:00 UT (noon LT) and 18:30 UT (15:30 LT) during the MP. The increase lasted up to 19:30 UT (16:30 LT). The large PS in ΔTEC and strengthening of the EIA around 17:00 UT (14:00 LT) coincided with the two peaks in the ΔH during the MP. This was accompanied by the negative excursion of the B_z and intensification of AE (Figure 8.35). An increase in ΔH indicates an enhancement in the equatorial electrojet, EEJ, which is responsible for the fountain effect and development of the EIA. A sudden southward turning of B_z is a condition for the undershielding prompt penetration electric field, PPEF, which enhances the $E \times B$ drift and leads to poleward expansion of the EIA crests in comparison with the quiet time, as was observed in TEC maps, This effect was also reported by (BLANC; RICHMOND, 1980; LIU et al., 1999; ABREU et al., 2010; ASTAFYEVA et al., 2015; FAGUNDES et al.,

2016). Fagundes et al. (2016) reported large PS in TEC and expansion in the EIA region over South America under eastward PPEF which is typical of geomagnetic disturbances effects over low latitudes (ABDU, 1997). After the sunset and near the PRE at 21:00 UT (18:00 LT), there was another increase in the ΔH which lasted up to 03:00 UT (00:00 LT) on 14 October. The enhanced PRE, in comparison to quiet reference day, is caused by the strengthening of $E \times B$ drift, which is responsible for the observed F layer uplift in $h'F$ after the sunset. On the other hand, at the beginning of the recovery phase, a PS at the magnetic equator accompanied by a decrease in $h_m F_2$ is caused by the counter-electrojet which suppresses the fountain effect (SHARMA et al., 2011). This usually occurs in the recovery phase of geomagnetic storms driven by a disturbance dynamo electric field (DDEF) of westward polarity during the day (BLANC; RICHMOND, 1980).

The estimated vertical $E \times B$ drift velocity from Digisonde measurements shows that during the quiet time, it reached a PRE maximum v_p, of 20 m/s at 23:00 UT (20:00 LT). In comparison, the average v_p for the month was $\sim$ 22 m/s and hence the quiet day is a fair representation of quiet time behavior. On 13 October, v_p reached a maximum of 39 m/s at 21:30 UT (18:30 LT) when the PRE occurred $\sim$1 hr 30 min earlier than the quiet day. The increase in ΔH implies an enhanced zonal eastward electric field by PPEF which caused a larger v_p at the PRE resulting in the rapid uplift of the F layer. Abreu et al. (2011), AA et al. (2020) found that peak vertical drifts can increase up to $\sim$30 m/s over São Luís during a minor geomagnetic disturbance period, consistent with our findings. The vertical drift at the PRE is a critical factor in the formation of RT instability (ABDU et al., 1981; PAULA et al., 2019a; AA et al., 2020). The maximum drift velocity determines the equatorial apex height of the EPBs after which they diffuse along the field lines. Thus, it controls the latitudinal extension of the EPBs (ABDU et al., 1983). Consequently, irregularities had a larger latitudinal extension in comparison with the quiet day as shown in the ROTI in addition to Spread-F in ionograms and depletions in OI 630 nm.

8.4.6 Gravity waves as a possible seeding mechanism for equatorial plasma bubbles

Apart from the PRE in the $E \times B$ drift gravity waves also play an important role in the development of the Rayleigh-Taylor instability by providing the initial seed perturbation at the F-layer bottomside. Traveling ionospheric disturbances, TIDs and Large-scale Wave Structures, LSWS have been considered as seeding mechanisms for EPBs (AJITH et al., 2020). Our observations using GOLD FAR UV 135.6 nm images and TEC maps revealed periodically spaced depletions, as also reported by Eastes et al. (2019). This has been attributed to the presence of gravity waves and TIDs which have been extensively studied by (ABDU et al., 2009; KELLEY, 2009; RETTERER; RODDY, 2014; TAKAHASHI et al., 2015) and the references therein. We examine the behavior of F-layer true heights provided

by an inversion algorithm using the *SAO Explorer software* (HUANG; REINISCH, 1996). The true heights at fixed frequencies (5-8 MHz) (isolines) were used for estimating the vertical drift (dhF/dt) and detecting oscillations due to GWs. This was done by applying a band-pass filter (20 min to 3 hours) to the true heights. More details of this technique are described elsewhere (ABDU et al., 2009). The same filter was applied to the TEC data. Figure 8.36 shows a sinusoidal oscillation at multiple frequencies with a periodicity

Figure 8.36 - (a) Left: Band-pass filtered (20 min-3 hours) of F layer true heights at 5–8 MHz, over São Luís.(b) Right: Latitudinal variation (keogram) of detrended TEC between 14:00 and 24:00 UT (11:00–21:00 LT), on 13 October, for 35–45 ° W longitude showing wave-like oscillations before the sunset.

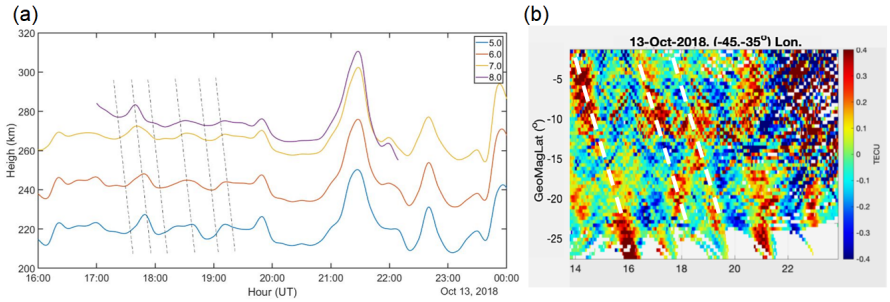

SOURCE: Chingarandi et al. (2023).

of∼ 50 min and amplitude of ∼30 km. A downward propagating phase at 18:00–03:00 UT (15:00–00:00 LT) can be observed. The same structures can be observed propagating in the TEC. This is the signature of propagating gravity wave structures in the F layer near sunset (ABDU et al., 2009; JONAH et al., 2016). In general, MSTIDs have a period of 15–60 min, horizontal wavelength of 100–1000 km, and a phase speed of 100–300m/s (JONAH et al., 2016). During the previous case study in Section 8.2, persistent oscillation in the $h'F$ and h_mF_2 were observed during the month of October as shown in Figure 8.24. It is plausible these TIDs were present throughout this period. Several studies had also reported that large-scale periodic wave structures precede EPBs (TAKAHASHI et al., 2009; TAKAHASHI et al., 2018; AA et al., 2019). Further, the horizontal wavelength of TIDs (not inferred here) is correlated to the separation between adjacent plasma bubbles (TAKAHASHI et al., 2009; TAKAHASHI et al., 2018). AA et al. (2020) estimated an inter-bubble distance of ∼500–800 km over South America in late October 2018 using GOLD OI 135.6 nm and TEC maps under geomagnetically quiet conditions consistent with previous studies (TAKAHASHI et al., 2018; BARROS et al., 2018; AA et al., 2019). We inferred a shorter inter-bubble distance of ∼250–700 km. The shortest separation was over the middle sector of South America (45 °– 55 ° W) which suggests that TIDs that

seeded EPBs on that day possibly had shorter horizontal wavelengths.

Gravity waves which seed EPBs have been known to originate from tropospheric sources (HINES, 1960; TAKAHASHI et al., 2016; AA et al., 2020). Figure 8.37 (a) shows the cloud top brightness temperature measured by the Geosynchronous Operational Environmental Satellites (GOES-16) meteorological satellite. Strong eastward convection is observed by the deep cloud brightness (T < –50° C), 2 hours prior to sunset. Colder regions are characterized by stronger convection (VADAS, 2007; JONAH et al., 2018). Figure 8.37 (b) shows the map of detrended TEC over South America at 21:00 UT on 13 October 2018 near sunset. TIDs can be observed with a wavefront propagating northeastward as indicated by the red arrow. The wavefront seems to be aligned with the convective region which was located between 54–75°W over South America. Tropospheric convection zones are sources of TIDs observed over equatorial and low latitudes (TAKAHASHI et al., 2018). The simultaneous presence of plasma bubbles and MSTIDs detected over the same sector has been reported as a case of MSTID seeding (TAKAHASHI et al., 2018; AJITH et al., 2020).

Figure 8.37 - (a) Cloud-top brightness temperature measured by GOES satellite showing several highly convective sources (T < –50° C) on 13 October 2018 at 19:00 UT (16:00LT). (b) Detrended TEC obtained from GNSS receivers at 21:00UT showing MSTIDs excited by tropospheric convection.

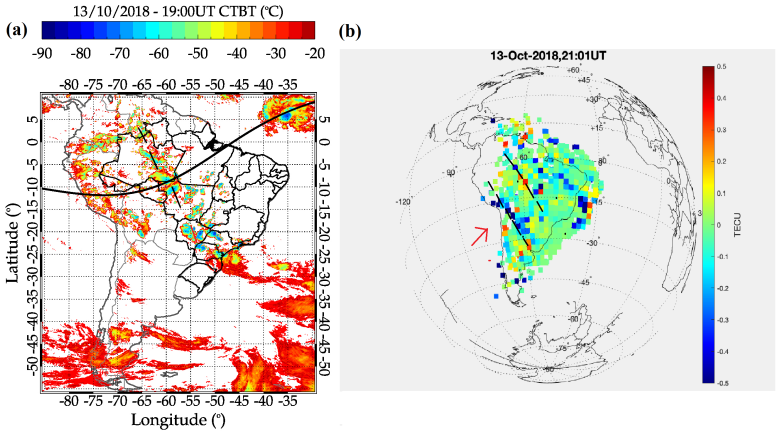

8.4.7 Discussion

The minor CIR/HSS storm on 13-14 October 2018 was characterized by a short recovery phase. In addition, the auroral activity was relatively low (AE< 300nT). Our results show a large positive ionospheric storm (∼23 TECU) during the main and recovery phases on 13–14 October, at 19:00 UT (16:00 LT). The main mechanisms responsible for the remarkable

changes in the ionosphere were; (a) the strengthening of the fountain effect indicated by the expansion of the EIA due to PPEF, and (b) thermospheric neutral composition changes in ΣO/N2 column which led to a large PS. The intensification of TEC and expansion of the EIA during the disturbed interval over the Brazilian equatorial and low latitudes have been previously reported (LIU et al., 2012; FAGUNDES et al., 2016; ABREU et al., 2017; MORO et al., 2021), however, this is the first time this is reported for a minor geomagnetic storm. In addition, we observed a long-lived, nighttime EIA. Eastes et al. (2019) observed large variability in the post-sunset EIA under very quiet conditions (1 < Kp <2) using GOLD OI 135.6 nm. They reported shifting of the EIA to higher latitudes during an interval of sporadic B_z negative which is an indicator of eastward PPEF. The effects of PPEF are usually short-lived, lasting from a few minutes to hours after the storm onset (KELLEY et al., 2003). However, the PS in TEC began in the MP and lasted up to the next day, well into the recovery phase (23:40 UT, 20:40 LT) indicating a different mechanism.

Changes in the ΣO/N2 density ratio driven by thermospheric winds are believed as main drivers low- and mid-latitude ionospheric effects during the recovery phase of the storms. Enhancements in the thermospheric composition over low latitudes during deep solar minimum can contribute significantly to the PS (CAI et al., 2020b). Global changes in ΣO/N2 during an intense (SymH –205 nT) CME-driven storm in the same year during August 2018 were reported by (KUMAR; KUMAR, 2019; ASTAFYEVA et al., 2020; MORO et al., 2021). Since the storm occurred under similar solar flux levels, we can compare the impact of this intense CME-driven storm with that of the minor CIR-driven storm. Astafyeva et al. (2020) observed a PS of ∼5 TECU at low latitudes and Moro et al. (2021) reported a PS in the f_0F_2 together with the poleward expansion of the EIA crests in the Brazilian sector attributed to a combination of ΣO/N2 enhancement and an eastward PPEF (LIU et al., 2012). They also observed that the largest PS in (f_0F_2) occurred during the recovery phase. Cai et al. (2021) reported 2 cases of ∼30% long-lasting increase in TEC related to ΣO/N2 over mid-latitude during weak geomagnetic disturbances ($K_p < 2$). The ΣO/N2 variations were generated at high latitudes and subsequently transported equatorward. Astafyeva et al. (2020) observed a small PS of ∼5 TECU associated with significant depletions in the [O]/[N2] ratio over low-to-high latitudes which were then displaced equatorward by disturbance thermospheric winds. Thermospheric changes and winds are associated with Joule heating at auroral latitudes (FULLER-ROWELL et al., 1996; CAI et al., 2020a). Although these effects originate from high latitudes, they can be advected equatorward from high latitudes to mid and low by neutral winds (LIU et al., 2012; ASTAFYEVA et al., 2020; CAI et al., 2020b).

Therefore, our observations indicate that the positive ionospheric storm, PS, was due to the combination of an increase in the thermosphere composition ΣO/N2 ratio and an

eastward PPEF. However, there are several competing processes over equatorial and low latitudes such as PPEF, disturbance dynamo electric fields, DDEFs, meridional winds (BALAN et al., 2010) as well as thermospheric composition changes. As such quantifying the individual contributions of each mechanism remains a challenge (MORO et al., 2021). Moreover, the effects of geomagnetic storms on changes in the neutral thermosphere are more significant during solar minimum compared to solar maximum as equatorward winds are more effective (BURNS et al., 2004). Burns et al. (2004) also found that the spatial extent of enhancements in storm-time [O]/[N2] ratio is much more restricted in winter than in summer likely due to seasonal differences in thermosphere circulation patterns (FULLER-ROWELL et al., 1996) which could also explain the larger PS in the CIR storm compared to the winter CME storm. During the minor CIR-driven storm, the strengthening of the EEJ shown by an increase in ΔH, was responsible for the expansion of the EIA, whereas, during the intense storm, the magnetic field hardly deviated from the quiet time levels (ASTAFYEVA et al., 2020). This could explain the large PS in the MP of the CIR storm in contrast to a weaker enhancement in TEC during the CME. This is evidence that the PPEF was more effective during the minor storm causing an intense daytime ionospheric response and stronger post-sunset irregularities as opposed to the weaker response during the CME storm. Despite the small magnitude of the geomagnetic storm and the weak background conditions characterized by solar minimum, there was a very large increase in the TEC ($\sim$23 TECU) during the daytime and a prolonged EIA at night in comparison with the quiet geomagnetic day.

Although the storm occurred during the early Spring equinox, which is the onset of EPBs/Spread F season, such large enhancements are very rarely expected considering the magnitude of the CIR-driven storm and low solar flux, F10.7 $\sim$70 SFU (CAI et al., 2020a; CAI et al., 2021). Dugassa et al. (2019) also observed that a CIR-driven storm in the equinox greatly enhanced the EIA and irregularities over the American sector compared to a larger magnitude CME-driven storm during winter which is contrary to what is expected.

Our findings are also in agreement with these observations. It is also important to note that, besides the storm magnitude, other factors such as the storm onset time (DUGASSA et al., 2019) longitude and solar activity contribute to the background quiet time conditions that control ionospheric response (BURNS et al., 2004). The seasonality of geomagnetic activity (RUSSELL; MCPHERRON, 1973) also plays a major role in the ionospheric response. Finally, wave-like oscillations were simultaneously observed in F-layer true heights TEC over the same region, with a period of $\sim$45 min which is typical of GWs. Periodic depletions were detected in GOLD 135.6 nm and TEC maps. To the best of our knowledge, it is the first time that coincident ground- and space-based are used to investigate the development and evolution of EPBs in the Brazilian sector.

8.5 Similarities and differences between long and short-duration HSSWS/CIR driven Storms

In section 8.3 a comparison was made between an intense CME-driven storm during August 2018 and a CIR-driven storm in October. In this section, we compare and contrast the minor, short-duration CIR-driven storm of 13–14 October discussed in the previous section and the moderate, long-duration CIR of 7 October 2018 presented in Section 8.2 using the same criteria as in section 8.3.

8.5.1 Differences in the IMF and solar wind parameters

The two storms occurred within the equinox just a few days from one another under similar solar flux F10.7 $\sim 70SFU$. However, there were several differences in characteristics and ionospheric response. The main differences in the characteristics between the two storms are shown in Figure 8.38. The scales have been adjusted for easier comparison. The Sym–H and level of AE show that the first storm was fully recovered by 13 October, some hours before the commencement of the second storm. As was presented in section 8.2, a long-duration CIR/HSS geomagnetic storm occurred on 7–13 October classified as moderate (min $Dst = -53nT$) (LOEWE, 1997) but was considered minor (G1) according to the NOAA scale ($Kp < 5$). It reached a maximum solar wind speed of 796 km/s and maximum Kp of ~ 4 while the longer duration CIR had $Kp \sim 5$. One similarity between the two is that both main phases occurred during the daytime (09:00–21:00 UT) even though the 7 October storm extended to a few hours after sunset, producing remarkable effects in the post-sunset TEC, EIA and irregularities. Table 8.2 shows a comparison of the characteristics of solar wind, IMF and ionospheric response between the two storms. The 7 October storm had slightly lower min Sym–H (–$55nT$) than the 13 October case (–$50nT$). The peak solar wind speed ($\sim 600km/s$), proton density, plasma temperature and maximum AE were similar in magnitude. On 7 October the minimum B_z and Ey were $-10nT$ and $-5mv/m$ respectively. This was lower on 13 October where minimum B_z was $-8nT$ and Ey were $-4mV/m$. The 7 October storm had a much longer duration, over 6 days in total, 18 hours being the main phase and 5 days being the recovery phase whereas the 13 October storm had a total duration of only 27 hours, a short main phase of only 4 hours and a 24 hour long recovery phase. The 7 October had heightened AE compared to the main phase. In addition, during the RP, there was significant oscillation in the Sym–H while the second storm had a smoother recovery phase.

The TEC response during the long-duration CIR of 7 October 2018 is shown in Figures 8.12 while Figure 8.18 and 8.19 indicate the magnitude of irregularities during the storm. The PS was higher during the MP of the 13 October storm, 23 TECU against 10 TECU. In addition, the development of irregularities was suppressed (ROTI$\leq$ 0.05) as shown in Figure 8.18. This is in contrast to strong irregularities observed on 13 October 2018 and

Figure 8.38 - Variation of the solar wind, interplanetary, and geomagnetic parameters and indices during the moderate, long-duration (6-day) and minor, short-duration (1-day) CIR/HSS Geomagnetic storms.

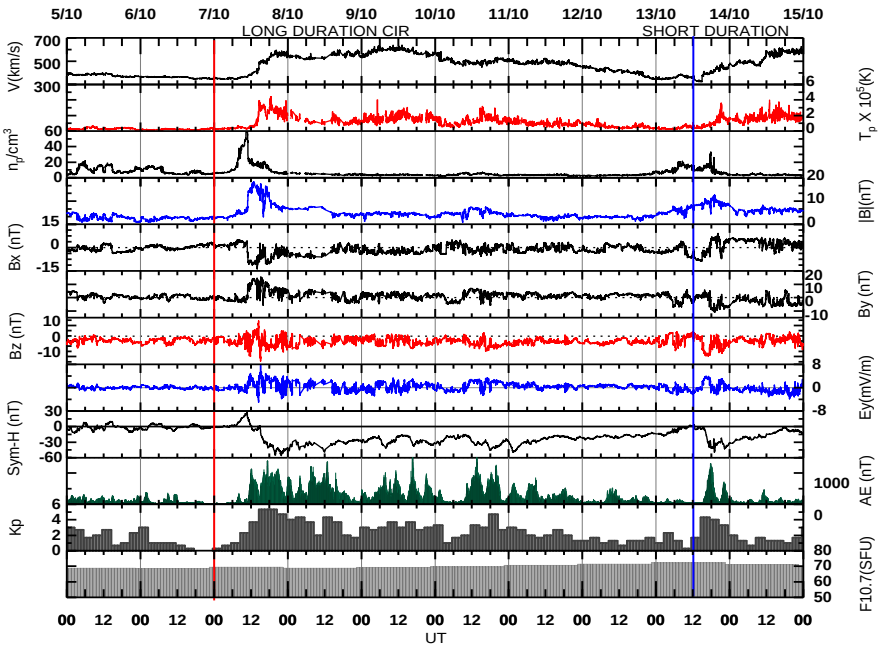

EPBs (Figure 8.30) which were associated with a sharp increase in the PRE of F layer virtual height (Figure 8.24) driven by a strong Eastward PPEF. GOLD 2D maps show a stronger fountain effect, EIA, on 13 October compared to the 7 October storm.

To compare the response of the post-sunset ionosphere during the storm recovery phases, Figure 8.39 shows 2D GOLD Maps obtained on 9 and 13 October 2018 showing the EIA. The intensity of emissions is higher on day 13. The EPB structure can be clearly seen in Figure 8.39 on day 13 compared to day 9. Smaller-scale irregularities indicated by the fragmentation of the EIA on 9 October may explain why the EPBs are not clearly visible in the GOLD maps although ROTI indicates the presence of strong irregularities. It can be seen that the EIA was more intense on 13 October. In addition, a large poleward expansion can be observed beyond $\geq 15°$ dip latitude compared to day 9. This is due to the larger magnitude of the $E \times B$ drift. the dark streaks (< 5 Rayleigh) cutting through the EIA band represent reduced emissions caused by low plasma density within the plasma bubbles. The magnitude of the emissions within the bubbles is ~ 6 orders of magnitude less than within the EIA (~ 30 Rayleigh). Stronger EPBs were observed on 13 October owing to a stronger PRE in the $E \times B$ drift and sharper F layer uplift. EPBs also occurred earlier as shown in ROTI and gradients (Figure 8.18 and 8.19). In contrast, the $h'F$ was lower for

Table 8.2 - Characteristics of short & long duration CIR storms.

Feature	**7-13 October**	**13–14 October**
Min Sym–H (nT)	–55	–50
Kp max	~ 4	~ 5.5
Electric Field Magnitude (mV/m)	5	4
Min B_z (nT)	10	8
Auroral activity AE (nT)	1200	1300
Duration of RP (Days)	Long-lasting (~ 6)	Short ($1 \sim$)
Prompt Penetration	Overshielding	Undershielding
PS (MP)	10 TECU	23 TECU
EPBs	Strong (Visible)	Strong
Max ROTI (MP, RP)	0.06|0.6	0.6

Figure 8.39 - Comparison of GOLD OI 135.6-nm radiance maps at 23:55 UT on 9 (left) during the RP of the first storm on and 13 October 2018 (right) RP of the second storm. The location of the 7 GPS receivers used in the study is also marked. Large-scale depletions in airglow emissions can be observed over South America on 13 October.

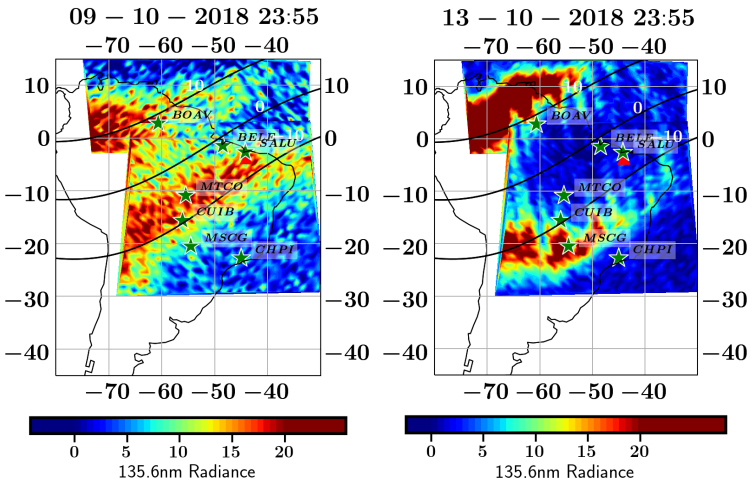

the 7 October 2018 storm during the MP due to a CEJ event. In this next section, the variability of the ionosphere during this disturbed month is presented.

8.6 Plasma irregularities and TEC Gradients during a geomagnetically "active" month of October 2018

In this section, we present an analysis of the variability of the VTEC, $\delta VTEC$, the TEC gradients and ROTI during the whole of October 2018 which was characterized by geomagnetic disturbances. The notable cases were discussed in the previous sections. Another

minor storm occurred from 1–4 October, and it is not analyzed here. As mentioned previously, plasma bubbles /irregularities have high frequency during the month of October, however significant perturbations were shown during the aforementioned case studies. Figure 8.40 shows the variation of TEC, $\delta VTEC$, the spatial gradients in TEC (∇TEC) and ROTI as a function of the day of the year (DOY) and Universal (UT) and Local Time (LT) over the equatorial region (BELE, dip: –0.3 °) and at the north crest of EIA (BOAV, dip: 9.2°). The horizontal axis is DOY, from 276–304. The vertical dashed lines indicate the onset of each storm: 01 Oct (DOY 274); 07–12 (DOY: 280–285) and 13–14 Oct (286–287).

Figure 8.40 - The hourly, diurnal and seasonal variability of the TEC, $\delta VTEC$, ∇TEC and ROTI over Boa Vista (BOAV: dip lat: 9.2°) and Belém (BELE: dip lat: $-0.3°$) for the month of October 2018. The dashed lines indicate the onset of the three geomagnetic storms.

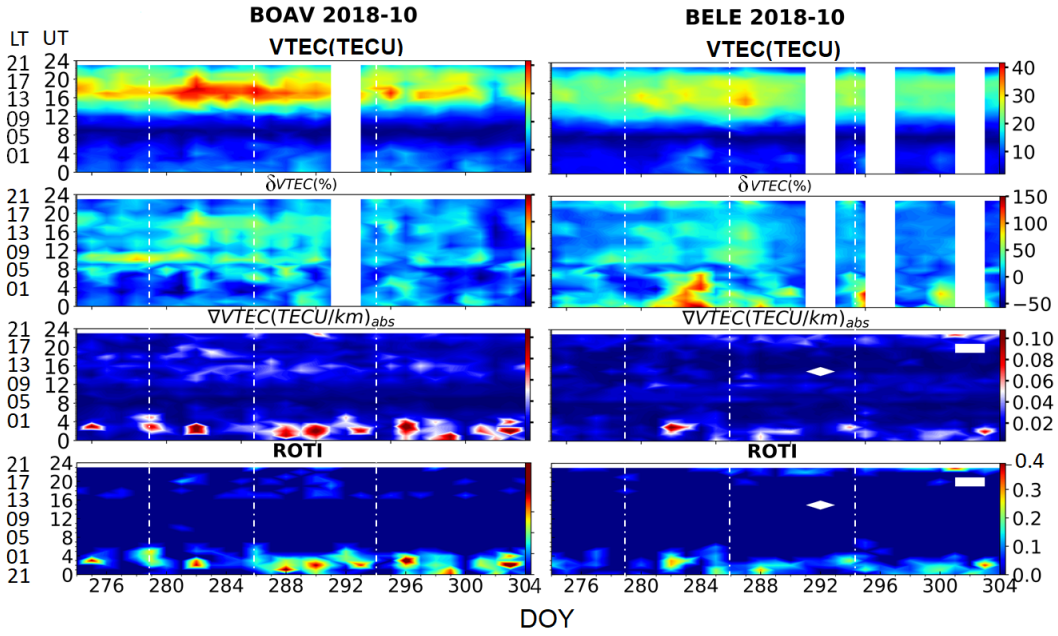

The geomagnetic storm effects are seen in the percentage deviation, $\delta VTEC$ variation, during daytime (10–20 UT) or (07–17 LT). However, the maximum PS $\delta VTEC$ at BELE on day of year 280–284 (07–11 October) between 00:00–07:00UT (21:00– 04:00 LT) after sunset. This was during the long-duration CIR which was discussed in Section 8.2 in which the peak PS was observed over the equator 8.13.

As expected, spatial gradients, ∇TEC are stronger at BOAV than in BELE, and are maximum at nighttime (21 to 04 LT). The ionospheric gradients are mainly associated with EPBs at equatorial region and low latitudes and maximizes at the side walls being weaker

inside the plasma bubbles (small scale irregularities) (DUGASSA et al., 2019; PRADIPTA; DOHERTY, 2016). ROTI magnitude is, as expected, higher at nighttime hours, and shows a good correlated day-to-day variability with the spatial gradients (∇TEC). The amplitude of spatial gradients in TEC over the equatorial sector has a strong, positive, linear correlation with ROTI and similar climatology to the occurrence of irregularities (DUGASSA et al., 2019). ROTI was simultaneously intensified during storm periods, although it was more pronounced at Boa Vista. Strong irregularities show high diurnal variation likely influenced by HSSs notwithstanding October is also the SpreadF season. The strength of irregularities is higher in the EIA region (7.5) because of higher background electron density (TEC) which causes sharper gradients associated with EPBs(ABDU et al., 2009). There appears to be a correlation between higher ROTI and intensification during the storm intervals at low latitudes compared to the equator.

The dominant process over low latitudes as well as winds may have a different effect to those over the equatorial sector, which may explain the differences in ionospheric response. This analysis shows the possible influence of weak-to-moderate geomagnetic storms on the electrodynamics of the ionosphere which can favor or suppress the occurrence of plasma irregularities like EPBs, as seen on 7 October (suppression) and 13 (occurrence) October that are responsible for the formation of plasma irregularities is clearly demonstrated. This is despite the very low levels of ionization due to extremely low levels of solar flux (SOLOMON et al., 2018; DERGHAZARIAN et al., 2021) hence the effects of storms can be more pronounced (BURNS et al., 2014; CAI et al., 2020a).

It is well known that EPBs present a strong seasonal occurrence rate, peaking from September to March (solar maximum) and from October to March (solar minimum) (AGYEI-YEBOAH et al., 2019; SOBRAL et al., 2002). This variation is controlled by the amplitude of the $E \times B$ drift at the PRE, v_p, which controls the growth rate of the RT instability (ABDU et al., 1981; SOBRAL et al., 2002; KELLEY, 2009). Vertical plasma drifts from an Incoherent scatter radar show that the v_p is higher during equinox and summer while during the winter solstice, the amplitude is not sufficient to cause the formation of plasma irregularities (ABDU et al., 1981; ABDU, 1997; KELLEY, 2009). The amplitude of the PRE is determined by the alignment between the solar terminator and magnetic meridian compared to winter (ABDU et al., 1981; SOBRAL et al., 2002). The large magnetic declination angle over Brazil explains the higher occurrence of EPBs compared to other lower-latitude sectors over South America. The irregularities had high diurnal variation likely to storm disturbances, notwithstanding, October is the season for SpreadF. The statistics of ionospheric storms in TEC measured by GNSS receivers in Brazil are presented in the next section.

8.7 Statistics of ionospheric storms over the Brazilian equatorial and low-latitude sector during 2018

In the previous sections, case studies of the ionospheric response to storms during 2018 were presented. In this section, we present the overall statistics of these HSS which drove geomagnetic storms as well as the resulting ionospheric storms over the Brazilian equatorial and low-latitude regions for the year 2018. Figure 8.41 illustrates the seasonal distribution of HSS/CIRs and subsequent geomagnetic storms during 2018. The maximum solar wind speed according to the catalog of HSS by (GRANDIN et al., 2019). As was presented before in Chapter 6, the majority of CIR-driven storms were observed during the first half of the year with few events during the winter solstice, consistent with previous literature (RUSSELL; MCPHERRON, 1973; TSURUTANI et al., 1995; MATAMBA et al., 2015). The weak geomagnetic activity is linked to low solar wind speed from January to February shown in Figure 8.41. The seasonal variation of the geomagnetic activity has been explained by the polarity of the Interplanetary Magnetic Field (IMF) B_z. During equinox the Earth's magnetic field is more likely to be Southward than during solstice (RUSSELL; MCPHERRON, 1973).

Figure 8.41 - Top: The bar plot shows the monthly frequency of the geomagnetic storms. The black line indicates the daily minimum Sym–H for the storm period. Bottom: The maximum solar wind speed of high-Speed Streams observed in 2018 according to (GRANDIN et al., 2019).

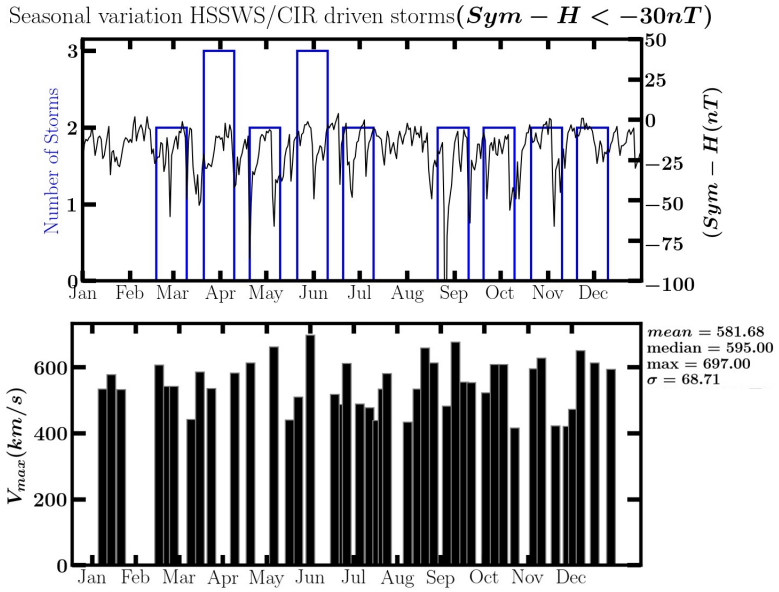

As mentioned in the previous sections, the majority of geomagnetic storms during the deep minimum of Cycle 24 were weak to moderate in magnitude according to the Sym–H index. Figure 8.42 shows the relationship between minimum Sym–H and B_z component for the year 2018. Only storms with minimum Sym–H > –100 nT were considered, thus the intense storm of August 2018 driven by a CME/CIR is not included in this analysis. The correlation coefficient obtained using a linear regression fit was 0.8 while the intercept was at –93.0 nT. A strong positive correlation between the two parameters. Previous studies by Gonzalez and Echer (2005) investigated the relationship between peak negative Dst and the southward component of B_z during moderate storms and showed that the average delay between the B_z and Dst is 2 hours.

Figure 8.42 - Monthly minimum Sym–H against the minimum B_z for the geomagnetic storms in 2018. The blue line shows the linear regression fit. A coefficient of r=0.8 shows a strong positive correlation between them.

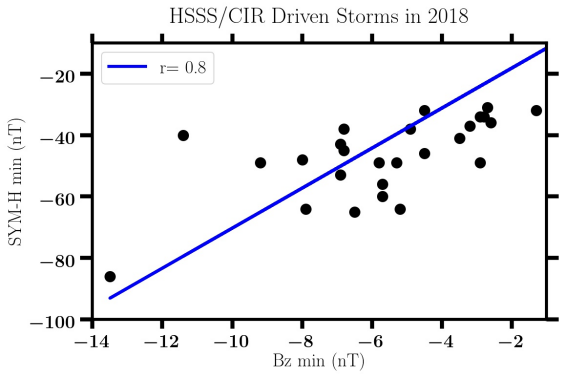

Analysis of the statistics of Positive (PS) and Negative (NS) ionospheric storms (TEC) in response to HSSWS/CIR and CME-driven storms is presented. Data from 4 GPS receivers located within equatorial and low latitudes during 2018 is presented.

Figure 8.43 - The annual distribution of maximum positive and negative δTEC over the North Crest (Boa vista) and the South Crest (Campo Grande) of the EIA. The maximum monthly Kp is also shown. An anomaly in Kp is observed in August.

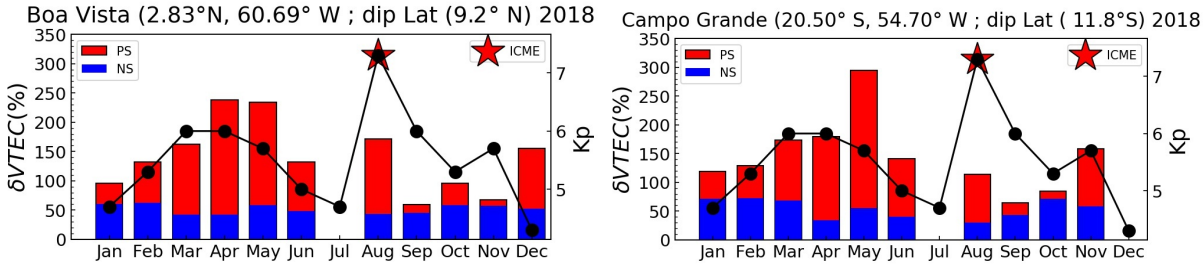

Figure 8.43 (a) and (b) illustrate the overall variation of PS and NS storm effects over the Northern and Southern crests of the EIA, Boa vista and Campo Grande respectively, mainly during CIR-driven storms together with the variation of the Kp index. The gaps indicate the unavailability of data. The monthly Kp shows a semiannual variation although the September equinox had slightly fewer disturbances. A spike in Kp is observed toward the end of August due to the only intense ICME-geomagnetic storm of 2018. The annual variability in the ionospheric storms between the two stations was similar. The magnitude of PS was generally higher over Boa Vista in comparison to its conjugate point.

Figure 8.44 - Same as 8.43 but for equatorial stations, Belém and São Luis. An anomaly in the PS is seen during the month of April.

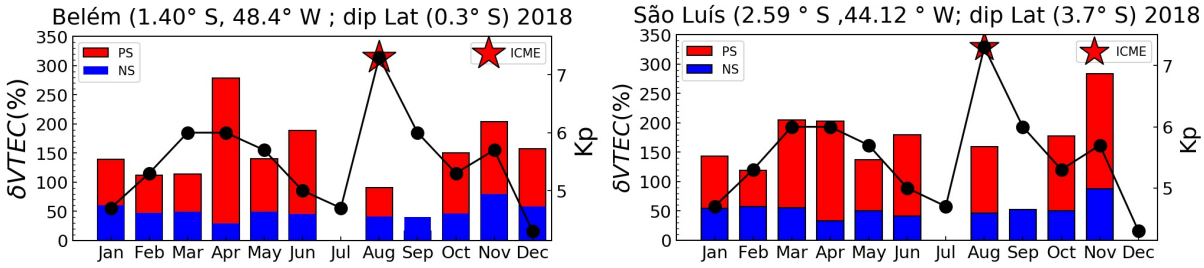

Figure 8.44 (a) and (b) illustrates the variation over the equator. The PS effect was much larger than the EIA crests, in particular over Belém where an unusually large PS occurred in April. This corresponds to several peaks in V_{sw} which led to HSS-driven storms in April

as shown in Figure 8.41.

8.7.1 Discussion

We found that ionospheric storms have seasonal dependence, which has been shown in various studies (LEKSHMI et al., 2011). Liu et al. (2012) studied the influence of HSS-driven storms on TEC during solar minimum 2008 over Brazil and showed that ionospheric storms in the f_oF_2 have a strong correlation with Kp. Furthermore, Chen and Wang (2015) investigated the response of the Global Electron Content (GEC) during SC23 deep minimum and found that the daily mean GEC has a strong positive correlation with geomagnetic activity (Ap index). Our results for the magnitude of positive and negative storms in TEC during SC24 minimum are consistent with this. This indicates the influence of planetary activity on the ionospheric plasma density. Our observations show a correlation between the Kp and TEC which is a new finding, particularly in South America. Figure 8.44 (a) and (b) illustrate the overall variation of ionospheric storm effects over the equator.

Using peak electron density data, N_{max}, Lekshmi et al. (2011) showed that ionospheric storms have a seasonal and solar cycle dependence. Matamba and Habarulema (2018) reported statistics of positive and negative ionospheric storms during Cycle 23 and found that CIR-driven storms are generally weak to moderate while CME-driven storms are intense (TSURUTANI et al., 2006). They observed both positive (PS) and negative (NS) ionospheric storms over equatorial and low latitudes, though PS was more prevalent which is in agreement with our result. The semi-annual variation in geomagnetic storms has been attributed to the Russell-McPheron IMF-effect (RUSSELL; MCPHERRON, 1973) in which more geomagnetic storms occur during the equinox as was observed in the year 2018 (Figure 6.3). This is because the polarity of IMF B_z has a 50% statistical probability of being Southward.

Consequently, there are larger positive storms during equinox compared to the solstices (MATAMBA; HABARULEMA, 2018). The nature of the ionospheric storm, whether positive or negative, also has a seasonal dependence (MANNUCCI et al., 2005; BUONSANTO, 1999; LEKSHMI et al., 2011). Negative and positive ionospheric storm effects occur mostly in winter and summer, respectively (DANILOV et al., 1994; PROLSS, 1995). This is because, during summer, poleward winds reinforce one another, which causes the composition disturbance zone to extend much further from high latitudes toward middle and low latitudes (PROLSS, 1995). During the winter solstice, the seasonal and disturbance winds are out of phase which inhibits the enhancement in thermospheric composition ratio (PROLSS, 1995).

A good correlation between the velocity of solar wind and ionospheric storms shows that HSS from CHs is the main driver of geomagnetic activity during solar minimum. It has been

demonstrated the HSS/CIRs drive large changes in the plasma density and perturbations in the electrodynamics of the equatorial and low-latitude ionosphere. Large changes in the intensity and time of occurrence of the EIA are a common feature while post-sunset irregularities can be greatly promoted or inhibited by the action of disturbed electric fields. As was discussed in section 8.6, large PS in TEC during the disturbed periods are associated with sharper gradients and stronger irregularities and consequently scintillation in GNSS signals. As such understanding of ionospheric response is critical in order to mitigate larger uncertainty that may arise in navigation systems as well as ground-based augmentation systems.

8.7.2 Summary

The statistics of ionospheric storm effects due to CIR- and CME-driven storms were analyzed using GNSS TEC over the stations located within 30°E–40°E geographic longitude in the Southern and Northern hemispheres (low and equatorial latitudes). Positive ionospheric storm effects were more prevalent during both CME- and CIR-driven storms, although the magnitude of the NS were larger during CIRs. In general, the largest positive ionospheric storm effects were observed over the south crests of the EIA while the highest nighttime PS were seen over the equator and the lowest were over the crests. This occurred during deep solar minimum in which the levels of solar activity were extremely low. There are however, a number of suggested mechanisms for positive ionospheric storms including TIDs (HINES, 1960), PPEF of magnetospheric origins (KELLEY et al., 2003), changes in neutral composition (MATSUSHITA, 1969; TITHERIDGE, 1974; DANILOV et al., 1994; PROLSS, 1995) and equatorward neutral winds (BALAN et al., 2010). The selected case studies showed that the PS were largely due to a combination of neutral composition changes and PPEF. One interesting phenomenon observed are long-lasting negative ionospheric storms that occurred mostly during the recovery phases of CIR-driven storms over the southern low latitude. These could be associated with the disturbance dynamo of westward polarity (BLANC; RICHMOND, 1980), however, further investigation is needed to better understand the mechanisms responsible.

9 CONCLUSIONS

In this work, the first detailed characterization of the features of heliospace and the low latitude ionosphere over South America during the deep solar minimum 2018 of Solar Cycle 24–25 was successfully conducted. For the first time, multiple ionospheric indices derived from GNSS were applied over South America. The main contributions are as follows;

- The features of the solar wind, interplanetary magnetic field, and geomagnetic activity during 2018 were presented in Chapter 6. The main contribution of this chapter is that HSSWS/CIR emanating from CHs are the main driver of recurrent geomagnetic storms which had similar features in IMF and solar wind and Sym–H. Despite the very low solar activity during the deep minimum, significant geomagnetic disturbances were recorded. The seasonal variation of the geomagnetic activity has been explained by the Russell-McPherron effect described by Russell and McPherron (1973). This knowledge is applicable to long-term space weather forecasts and satellite launch planning.

- The second part of the results in Chapter 7 provided a detailed picture of the equatorial and low-latitude ionosphere over Brazil using multiple instruments, parameters and indices derived from GNSS TEC namely; the ROT, ROTI, δTEC, and ∇TEC. Analysis shows that the magnitude of TEC was 50 % lower than during solar maximum, however, plasma bubbles were still detected by the GOLD FUV, TEC maps and All-sky imager. Associated with these are strong irregularities and sharp spatial gradients enough to disrupt the operation of GNSS. A good correlation between the amplitude scintillation index, S_4, and the GNSS ROTI demonstrates that it is a viable tool for detecting EPBs and radio wave scintillation in areas where high-cost scintillation monitors are otherwise scarce. The GOLD mission is a powerful tool for studies of the Brazilian low-latitude region in remote areas and over oceans.

- Detailed case studies of geomagnetic storms covered in Chapter 7 showed that moderate CIR-driven storms of weaker magnitude have a more significant impact on the thermosphere-ionosphere than intense CME-driven storms during solar minimum.

- During HSS/CIR storms, the magnitude of TEC enhancement was larger in the recovery phase compared to the main phase. Another peculiar feature was long-lasting negative ionospheric storms that occurred over the southern low latitude, also during the recovery phases. These were more prevalent during CIR-driven storms than CME storms. The amplitude of irregularities was also often higher in the RP than during the main phase due to PPEF and disturbance dynamo. This shows that increased auroral activity is an important factor in

the ionospheric response during solar minimum. The hemispheric asymmetry in the magnitude of the indices between the northern and southern crest of the EIA demonstrates the role of meridional wind in the F-layer electrodynamics.

- The third case study of a short-duration, minor storm was the first simultaneous observation of periodically-spaced both large-scale EPBs and smaller-scale irregularities by multiple instruments. GOLD 2D maps demonstrate the high diurnal variability of the ionosphere post-sunset EIA and EPBs especially during disturbed periods.

- Comparison of the two CIR-driven storms of October 2018 between the minor short-duration (NOAA G1) and the moderate-long duration storm (NOAA G2). The peak solar wind parameters and IMF Bz as well as AE were similar in magnitude however the key differences were the magnitude and duration. The magnitude of the positive ionospheric storms, the strength of the EIA and the amplitude of irregularities were higher during the MP of the minor storm compared to the moderate storm. An important finding is that under favorable conditions such as PPEF, minor storms can cause a more profound ionospheric response than moderate or even intense storms. The remarkable effects of geomagnetic activity on the thermosphere-ionosphere show that solar minimum is important and can therefore no longer be ignored.

  This demonstrates that weaker geomagnetic storms can cause large changes in thermospheric composition (up to 50 %), perturbations in the global circulation systems and electron density during solar minimum than in solar maximum. This is a result of weak background conditions (BURNS et al., 2014). Consequently, large variations in the TI during deep solar minimum have been recently reported (GAN et al., 2020; AA et al., 2021; CAI et al., 2020b; CAI et al., 2020a). The time of the main phase, longitude and season of occurrence are thus important factors in ionospheric response apart from the storm magnitude.

- The last part of the results in Chapter 8.7 showed that in general, the largest positive ionospheric storm effects were observed over the south crests of the EIA while the highest nighttime PS were seen over the equator and the minima occurred over the crests. This was during deep solar minimum in which the levels of solar activity were extremely low. A combination of mechanisms is responsible for the positive ionospheric storms including TIDs (HINES, 1960), PPEF (KELLEY et al., 2003), changes in neutral composition (ASTAFYEVA et al., 2015; TITHERIDGE, 1974) and equatorward neutral winds (BALAN et al., 2010).

In conclusion, the strengthening of ionospheric irregularities and TEC gradients during

solar minimum is of great interest to GNSS/GBAS operations while increases in the orbital drag due to geomagnetic storms impact satellite orbits. The mapping of ionospheric indices is essential in understanding the spatial and temporal evolution of post-sunset ionospheric irregularities.

REFERENCES

AA, E. et al. Salient midlatitude ionosphere thermosphere disturbances associated with saps during a minor but geo-effective storm at deep solar minimum. *Journal of Geophysical Research: Space Physics*, v. 126, 2021. ISSN 2169-9402. Available from: <https://onlinelibrary.wiley.com/doi/full/10.1029/2021JA029509>. 1, 2, 3, 5, 148, 176

AA, E. et al. Coordinated ground-based and space-based observations of equatorial plasma bubbles. *Journal of Geophysical Research: Space Physics*, v. 125, p. 1–13, 2020. ISSN 21699402. 2, 37, 50, 62, 64, 65, 68, 153, 160, 161, 162

AA, E. et al. Merging of storm time midlatitude traveling ionospheric disturbances and equatorial plasma bubbles. *Space Weather*, v. 17, n. 2, p. 285–298, 2019. Available from: <https://agupubs.onlinelibrary.wiley.com/doi/abs/10.1029/2018SW002101>. 67, 85, 148, 149, 161

ABDU, M.; BATISTA, I.; TAKAHASHI, H.; MACDOUGALL, J.; SOBRAL, J.; MEDEIROS, A.; TRIVEDI, N. Magnetospheric disturbance induced equatorial plasma bubble development and dynamics: a case study in brazilian sector. **Journal of Geophysical Research: Space Physics**, v. 108, p. 1–13, 2003. ISSN 21699402. 49

ABDU, M.; MEDEIROS, R. D.; SOBRAL, J.; BITTENCOURT, J. Spread f plasma bubble vertical rise velocities determined from spaced ionosonde observations. **Journal of Geophysical Research: Space Physics**, v. 88, n. A11, p. 9197–9204, 1983. 34, 38, 39, 40, 59, 160

ABDU, M. A. Major phenomena of the equatorial ionosphere-thermosphere system under disturbed conditions. **Journal of Atmospheric and Solar-Terrestrial Physics**, v. 59, p. 1505–1519, 1997. 25, 38, 44, 160, 169

_____. Outstanding problems in the equatorial ionosphere-thermosphere electrodynamics relevant to spread f. **Journal of Atmospheric and Solar-Terrestrial Physics**, v. 63, p. 869–884, 2001. ISSN 13646826. 2, 33, 34, 37, 38, 49, 85, 131

ABDU, M. A.; BATISTA, I. S.; REINISCH, B. W.; SOUZA, J. R. D.; SOBRAL, J. H. A.; PEDERSEN, T. R.; MEDEIROS, A. F.; SCHUCH, N. J.; PAULA, E. R. D.; GROVES, K. M.; SOUZA, J. R. D.; SOBRAL, J. H. A.; SOUZA, J. R. D.; SOBRAL, J. H. A.; PEDERSEN, T. R.; MEDEIROS, A. F.; SCHUCH, N. J.; PAULA, E. R. D.; GROVES, K. M. Conjugate point equatorial experiment (copex) campaign in Brazil: electrodynamics highlights on spread f development conditions and day-to-day variability. **Journal of Geophysical Research: Space Physics**, v. 114, 2009. ISSN 21699402. 24, 30, 31, 32, 36, 37, 39, 40, 44, 59, 61, 65, 83, 106, 139, 144, 156, 169

ABDU, M. A.; BITTENCOURT, J. A.; BATISTA, I. S. Magnetic declination control of the equatorial f region dynamo electric field development and spread f. **Journal of Geophysical Research**, v. 86, p. 11443, 1981. ISSN 0148-0227. 2, 31, 33, 34, 38, 42, 106, 121, 132, 160, 169

ABDU, M. A.; KHERANI, E. A.; BATISTA, I. S.; PAULA, E. R. D.; FRITTS, D. C.; SOBRAL, J. H. A.; KHERANI, E. A.; BATISTA, I. S.; PAULA, E. R. D.; FRITTS, D. C.; SOBRAL, J. H. A.; ESPACIAIS, N. D. P.; DIVISION, A.; KHERANI, E. A.; BATISTA, I. S.; PAULA, E. R. D.; FRITTS, D. C.; SOBRAL, J. H. A. Gravity wave

initiation of equatorial spread f/plasma bubble irregularities based on observational data from the spreadfex campaign. **Annales Geophysicae**, v. 27, p. 2607–2622, 2009. ISSN 09927689. 2, 37, 160, 161

ABRAMENKO, V.; YURCHYSHYN, V.; LINKER, J.; MIKIć, Z.; LUHMANN, J.; LEE, C. O. Low-latitude coronal holes at the minimum of the 23rd solar cycle. **Astrophysical Journal**, v. 712, p. 813–818, 2010. ISSN 15384357. 2, 5, 15, 16, 95, 96, 98

ABREU, A. J. D.; FAGUNDES, P. R.; SAHAI, Y.; JESUS, R. D.; BITTENCOURT, J. A.; BRUNINI, C.; GENDE, M.; PILLAT, V. G.; LIMA, W. L.; ABALDE, J. R.; PIMENTA, A. A. Hemispheric asymmetries in the ionospheric response observed in the american sector during an intense geomagnetic storm. **Journal of Geophysical Research: Space Physics**, v. 115, p. 1–10, 2010. ISSN 21699402. 2, 42, 44, 49, 159, 160

ABREU, A. J. D.; SAHAI, Y.; FAGUNDES, P. R.; JESUS, R. D.; BITTENCOURT, J. A.; PILLAT, V. G. An investigation of ionospheric f region response in the brazilian sector to the super geomagnetic storm of may 2005. **Advances in Space Research**, v. 48, p. 1211–1220, 2011. ISSN 02731177. Available from: <<http://dx.doi.org/10.1016/j.asr.2011.05.036>>. 44, 45, 46, 50, 160

ABREU, A. J. de; MARTIN, I. M.; FAGUNDES, P. R.; VENKATESH, K.; BATISTA, I. S.; JESUS, R. de; ROCKENBACK, M.; COSTER, A.; GENDE, M.; ALVES, M. A.; WILD, M. Ionospheric f-region observations over american sector during an intense space weather event using multi-instruments. **Journal of Atmospheric and Solar-Terrestrial Physics**, v. 156, p. 1–14, 2017. ISSN 13646826. 2, 4, 19, 99, 102, 163

ABREU, A. J. de; SAHAI, Y.; FAGUNDES, P. R.; BECKER-GUEDES, F.; JESUS, R. de; GUARNIERI, F. L.; PILLAT, V. G.; ABREU, A. J. D.; SAHAI, Y.; FAGUNDES, P. R.; JESUS, R. D.; GUARNIERI, F. L.; PILLAT, V. G.; ABREU, A. J. de; SAHAI, Y.; FAGUNDES, P. R.; BECKER-GUEDES, F.; JESUS, R. de; GUARNIERI, F. L.; PILLAT, V. G. Response of the ionospheric f-region in the brazilian sector during the super geomagnetic storm in april 2000 observed by gps. **Advances in Space Research**, v. 45, p. 1322–1329, 2010. ISSN 02731177. Available from: <<http://dx.doi.org/10.1016/j.asr.2010.02.003>>. 42, 45, 46

AGYEI-YEBOAH, E.; PAULINO, I.; MEDEIROS, A. F.; BURITI, R. A.; PAULINO, A. R.; ESSIEN, P.; LOMOTEY, S. O.; TAKAHASHI, H.; WRASSE, C. M. Seasonal variation of plasma bubbles during solar cycle 23–24 over the brazilian equatorial region. **Advances in Space Research**, v. 64, p. 1365–1374, 2019. ISSN 18791948. 33, 34, 83, 169

AJITH, K. K.; LI, G.; RAM, S. T.; YAMAMOTO, M.; HOZUMI, K.; ABADI, P.; XIE, H. On the seeding of periodic equatorial plasma bubbles by gravity waves associated with tropical cyclone: a case study. **Journal of Geophysical Research: Space Physics**, v. 125, n. 10, p. 1–15, oct 2020. ISSN 21699402. Available from: <<https://onlinelibrary.wiley.com/doi/10.1029/2020JA028003>>. 2, 37, 65, 160, 162

ANDERSON, D.; ANGHEL, A.; YUMOTO, K.; ISHITSUKA, M.; KUDEKI, E. Estimating daytime vertical exb drift velocities in the equatorial f-region using ground-based magnetometer observations. **Geophysical Research Letters**, v. 29, n. 12, p. 37–1–37–4, 2002. ISSN 00948276. 92, 93, 120

ASTAFYEVA, E.; BAGIYA, M. S.; FöRSTER, M.; NISHITANI, N. Unprecedented hemispheric asymmetries during a surprise ionospheric storm: a game of drivers. **Journal of Geophysical Research: Space Physics**, v. 125, p. 1–15, 2020. ISSN 21699402. 3, 18, 111, 117, 118, 120, 122, 163, 164

ASTAFYEVA, E.; ZAKHARENKOVA, I.; FöRSTER, M. Ionospheric response to the 2015 st. patrick's day storm: a global multi-instrumental overview. **Journal of Geophysical Research: Space Physics**, v. 120, p. 9023–9037, 10 2015. ISSN 21699380. Available from: <<http://doi.wiley.com/10.1002/2015JA021629>>. 3, 20, 42, 43, 85, 151, 159, 160, 176

BALAN, N.; BAILEY, G. J.; ABDU, M. A.; OYAMA, K. I.; RICHARDS, P. G.; MACDOUGALL, J.; BATISTA, I. S. Equatorial plasma fountain and its effects over three locations: evidence for an additional layer, the f3 layer. **Journal of Geophysical Research A: Space Physics**, v. 102, p. 2047–2056, 1997. ISSN 01480227. 24

BALAN, N.; BATISTA, I. S.; ABDU, M. A.; MACDOUGALL, J.; BAILEY, G. J. Physical mechanism and statistics of occurrence of an additional layer in the equatorial ionosphere. **Journal of Geophysical Research: Space Physics**, v. 103, p. 29169–29181, 1998. 49

BALAN, N.; OTSUKA, Y.; NISHIOKA, M.; LIU, J. Y.; BAILEY, G. J. Physical mechanisms of the ionospheric storms at equatorial and higher latitudes during the recovery phase of geomagnetic storms. **Journal of Geophysical Research: Space Physics**, v. 118, p. 2660–2669, 2013. ISSN 21699402. 33, 42, 43, 45

BALAN, N.; RAO, P. Dependence of ionospheric response on the local time of sudden commencement and the intensity of geomagnetic storms. **Journal of Atmospheric and Terrestrial Physics**, v. 52, n. 4, p. 269–275, apr 1990. ISSN 00219169. Available from: <<https://www.sciencedirect.com/science/article/abs/pii/0021916990900944https://linkinghub.elsevier.com/retrieve/pii/0021916990900944>>. 144

BALAN, N.; SHIOKAWA, K.; OTSUKA, Y.; KIKUCHI, T.; LEKSHMI, D. V.; KAWAMURA, S.; YAMAMOTO, M.; BAILEY, G. J. A physical mechanism of positive ionospheric storms at low latitudes and midlatitudes. **Journal of Geophysical Research: Space Physics**, v. 115, p. 1–12, 2010. ISSN 21699402. 40, 42, 43, 44, 118, 120, 130, 164, 174, 176

BALAN, N.; SOUZA, J.; BAILEY, G. J. Recent developments in the understanding of equatorial ionization anomaly: a review. **Journal of Atmospheric and Solar-Terrestrial Physics**, v. 171, p. 3–11, 2018. ISSN 13646826. Available from: <<https://doi.org/10.1016/j.jastp.2017.06.020>>. 35, 42

BANKS, P.; KOCKARTS, G. **Aeronomy**. [S.l.]: Academic, 1973. 175–186 p. 23, 24, 31, 39

BARROS, D.; TAKAHASHI, H.; WRASSE, C. M.; FIGUEIREDO, C. A. O. Characteristics of equatorial plasma bubbles observed by tec map based on ground-based gnss receivers over south america. **Annales Geophysicae**, v. 36, p. 91–100, 2018. ISSN 14320576. 83, 86, 148, 149, 153, 161

BASSIRI, S.; HAJJ, G. A. Higher-order ionospheric effects on the global positioning system observables and means of modeling them. **Manuscripta Geodaetica**, v. 18, n. 5, p. 280–280, 1993. 75

BASU, S. The peculiar solar cycle 24 – where do we stand? **Journal of Physics: Conference Series**, v. 440, p. 012001, jun 2013. Available from: <<https://doi.org/10.1088/1742-6596/440/1/012001>>. 1, 4, 5, 99

BASU, S.; GROVES, K. M.; QUINN, J. M.; DOHERTY, P. A comparison of tec fluctuations and scintillations at ascension island. **Journal of Atmospheric and Solar-Terrestrial Physics**, v. 61, p. 1219–1226, 1999. 38, 88

BECKER-GUEDES, F. et al. The ionospheric response in the brazilian sector during the super geomagnetic storm on 20 november 2003. **Annales Geophysicae**, v. 25, p. 863–873, 2007. ISSN 14320576. 42

BHATTACHARYYA, A. Deducing turbulence parameters from transionospheric scintillation measurements. **Japanese Society of Biofeedback Research**, v. 19, p. 709–715, 1992. 151

_____. Equatorial plasma bubbles: a review. **Atmosphere**, v. 13, n. 10, p. 1637, 2022. 59, 92

BIDAINE, B.; WARNANT, R. Measuring total electron content with gnss: investigation of two different techniques. **IET Conference Publications**, v. 2009, p. 201–206, 2009. 42, 78

BITTENCOURT, J. A.; SAHAI, Y. F-region neutral winds from ionosonde measurements of hmf2 at low latitude magnetic conjugate regions. **Journal of Atmospheric and Terrestrial Physics**, v. 40, p. 669–676, 1978. ISSN 00219169. 40, 142

BLACKJACK3D. **Photography**. 2020. Available from: <<https://www.istockphoto.com/br/portfolio/BlackJack3D?mediatype=photography>>. Access in: 25 Aug. 2020. 55

BLANC, M.; RICHMOND, A. D. The ionospheric disturbance dynamo. **Journal of Geophysical Research: Space Physics**, v. 85, p. 1669–1686, 1980. 20, 42, 43, 50, 118, 142, 159, 160, 174

BOROVSKY, J. E.; DENTON, M. H. Differences between cme-driven storms and cir-driven storms. **Journal of Geophysical Research: Space Physics**, v. 111, p. 1–17, 2006. ISSN 21699402. 12

BORRIES, C.; WILKEN, V.; JACOBSEN, K. S.; GARCÍA-RIGO, A.; DZIAK-JANKOWSKA, B.; KERVALISHVILI, G.; JAKOWSKI, N.; TSAGOURI, I.; HERNÁNDEZ-PAJARES, M.; FERREIRA, A. A.; HOQUE, M. M. Assessment of the capabilities and applicability of ionospheric perturbation indices provided in Europe. **Advances in Space Research**, v. 66, n. 3, p. 546–562, aug 2020. ISSN 18791948. 85, 86

BRIGGS, B. Ionospheric irregularities and radio scintillations. **Contemporary Physics**, v. 16, n. 5, p. 469–488, 1975. 91

BRUNINI, C.; MEZA, A.; AZPILICUETA, F.; ZELE, M. A. V.; GENDE, M.; DíAZ, A. A new ionosphere monitoring technology based on gps. **Astrophysics and Space Science**, v. 290, p. 415–429, 2004. ISSN 0004640X. 77

BUONSANTO, M. J. Ionospheric storms – a review. **Space Science Reviews**, p. 563–601, 1999. 44, 117, 144, 173

BURNS, A.; WANG, W.; SOLOMON, S.; QIAN, L. Energetics and composition in the thermosphere. **Modeling the Ionosphere–Thermosphere System**, p. 39–48, 2014. 3, 145, 169, 176

BURNS, A. G.; KILLEEN, T. L.; WANG, W.; ROBLE, R. G. The solar-cycle-dependent response of the thermosphere to geomagnetic storms. **Journal of Atmospheric and Solar-Terrestrial Physics**, v. 66, n. 1, p. 1–14, 2004. ISSN 13646826. 3, 164

CAI, X.; BURNS, A. G.; WANG, W.; COSTER, A.; QIAN, L.; LIU, J.; SOLOMON, S. C.; EASTES, R. W.; DANIELL, R. E.; MCCLINTOCK, W. E. Comparison of gold nighttime measurements with total electron content: preliminary results. **Journal of Geophysical Research: Space Physics**, v. 125, p. 1–18, 2020. ISSN 21699402. 3, 6, 63, 65, 66, 67, 83, 148, 149, 152, 154, 163, 164, 169, 176

CAI, X.; BURNS, A. G.; WANG, W.; QIAN, L.; SOLOMON, S. C.; EASTES, R. W.; PEDATELLA, N.; DANIELL, R. E.; MCCLINTOCK, W. E. The two-dimensional evolution of thermospheric σ o/n2 response to weak geomagnetic activity during solar-minimum observed by gold. **Geophysical Research Letters**, v. 47, n. 18, p. e2020GL088838, 2020. 2, 3, 117, 120, 148, 150, 163, 176

CAI, X.; BURNS, A. G.; WANG, W.; QIAN, L.; PEDATELLA, N.; COSTER, A.; ZHANG, S.; SOLOMON, S. C.; EASTES, R. W.; DANIELL, R. E.; MCCLINTOCK, W. E. Variations in thermosphere composition and ionosphere total electron content under "geomagnetically quiet" conditions at solar-minimum. **Geophysical Research Letters**, v. 48, n. 11, p. e2021GL093300, jun 2021. ISSN 1944-8007. Available from: <<https://onlinelibrary.wiley.com/doi/full/10.1029/2021GL093300>>. 2, 44, 148, 151, 163, 164

CANDIDO, C. M.; BATISTA, I. S.; BECKER-GUEDES, F.; ABDU, M. A.; SOBRAL, J. H.; TAKAHASHI, H. Spread f occurrence over a southern anomaly crest location in brazil during june solstice of solar minimum activity. **Journal of Geophysical Research: Space Physics**, v. 116, p. 1–10, 2011. ISSN 21699402. 42

CANDIDO, C. M.; BATISTA, I. S.; KLAUSNER, V.; NEGRETI, P. M. de S.; BECKER-GUEDES, F.; PAULA, E. R. de; SHI, J.; CORREIA, E. S. Response of the Total Electron Contentat brazilian low latitudes to corotating interaction region and high-speed streams during solar minimum 2008. **Earth, Planets and Space**, v. 70, 2018. ISSN 18805981. Available from: <<https://doi.org/10.1186/s40623-018-0875-8>>. 6, 7, 18, 19, 42, 84, 98, 99, 100, 102, 120, 144

CANDIDO, C. M.; SHI, J.; BATISTA, I. S.; BECKER-GUEDES, F.; CORREIA, E.; ABDU, M. A.; MAKELA, J.; BALAN, N.; CHAPAGAIN, N.; WANG, C.; LIU, Z. Postmidnight equatorial plasma irregularities on the june solstice during low solar activity - a case study. **Annales Geophysicae**, v. 37, p. 657–672, 2019. ISSN 14320576. 58, 61, 122

CANDIDO, C. M. N.; BECKER-GUEDES, F.; KLAUSNER, V.; MORAES-SANTOS, S. P.; CHINGARANDI, F. S.; ABAIDOO, S. Solar wind high-speed streams effects on the Brazilian low-latitude ionosphere during solar minima. In: SPACE WEATHER WORKSHOP 2022, 2022. **Proceedings...** [S.l.]: UCAR, 2022. v. 04. 1

CHANDRA, K. R.; SRINIVAS, V. S.; SARMA, A. D. Investigation of ionospheric gradients for gagan application. **Earth, Planets and Space**, v. 61, p. 633–635, 2009. ISSN 18805981. 85

CHAO, C. H. J. **Improved modelling of high precision wide area differential GPS**. PhD Thesis (PhD) — University of Nottingham, 1996. 73

CHEN, A.; WANG, J. Super-active regions in solar cycle 24. **International Astronomical Union**, v. 320, 2015. Available from: <<https://doi.org/10.1017/S1743921316000223>>. 1, 3, 4, 5, 6, 173

CHINGARANDI, F. S.; CANDIDO, C. M. N.; BECKER-GUEDES, F.; JONAH, O. F.; MORAES-SANTOS, S. P.; KLAUSNER, V. I.; TAIWO, O. O. Assessing the effects of a minor CIR-HSS geomagnetic storm on the brazilian low-latitude ionosphere : ground and space-based observations. **Space Weather**, 2023. 72, 145, 146, 147, 149, 150, 152, 153, 155, 157, 158, 161

CHOU, M. Y.; PEDATELLA, N. M.; WU, Q.; HUBA, J. D.; LIN, C. C.; SCHREINER, W. S.; BRAUN, J. J.; EASTES, R. W.; YUE, J. Observation and simulation of the development of equatorial plasma bubbles: Post-sunset rise or upwelling growth? **Journal of Geophysical Research: Space Physics**, v. 125, p. 1–14, 2020. ISSN 21699402. 65, 66

CHRISTENSEN, A. B.; PAXTON, L. J.; AVERY, S.; CRAVEN, J.; CROWLEY, G.; HUMM, D. C.; KIL, H.; MEIER, R. R.; MENG, C. I.; MORRISON, D.; OGORZALEK, B. S.; STRAUS, P.; STRICKLAND, D. J.; SWENSON, R. M.; WALTERSCHEID, R. L.; WOLVEN, B.; ZHANG, Y. Initial observations with the Global Ultraviolet Imager (GUVI) in the NASA TIMED satellite mission. **Journal of Geophysical Research: Space Physics**, v. 108, n. A12, p. 1–16, 2003. ISSN 21699402. 67, 68

CHU, F. D.; LIU, J. Y.; TAKAHASHI, H.; SOBRAL, J. H. A.; TAYLOR, M. J.; MEDEIROS, A. F. The climatology of ionospheric plasma bubbles and irregularities over brazil. **Annales Geophysicae**, v. 23, p. 379–384, 2005. ISSN 1432-0576. 148, 149

CLYNCH, J. **A short overview of differential GPS**. 2001. Available from: <<https://www.oc.nps.edu/oc2902w/gps/dgpsnote.html>>. 77

COCO, D. S.; COKER, C.; DAHLKE, S. R.; CLYNCH, J. R. Variability of gps satellite differential group delay biases. **IEEE Transactions on Aerospace and Electronic Systems**, v. 27, n. 6, p. 931–938, 1991. 81

CORREIA, E.; MUELLA, M.; ALFONSI, L.; PROL, F.; CAMARGO, P.; SANLI, D. U. Gps scintillations and Total Electron Content climatology in the southern american sector. **Accuracy of GNSS Methods**, 2018. 16, 39, 40, 89, 92, 106

DAMACENO, J. G.; BOLMGREN, K.; BRUNO, J.; FRANCESCHI, G. D.; MITCHELL, C.; CAFARO, M. Gps loss of lock statistics over Brazil during the 24th solar cycle. **Advances in Space Research**, v. 66, p. 219–225, 2020. ISSN 18791948. Available from: <<https://doi.org/10.1016/j.asr.2020.03.041>>. 88

DANILOV, A.; MOROZOVA, L. Ionospheric storms in the f2 region-morphology and physics. **Geomagnetism and Aeronomy**, v. 25, p. 705–721, 1985. 3, 42, 44

DANILOV, A. D.; MOROZOVA, L. D.; FULLER-ROWELL, T. J.; CODRESCU, M. V.; MOFFETT, R. J.; QUEGAN, S. Response of the thermosphere and ionosphere to geomagnetic storms. **Journal of Geophysical Research: Space Physics**, v. 99, p. 3893–3914, 1994. 44, 105, 118, 129, 142, 144, 150, 173, 174

DAS, T.; ROY, B.; PAUL, A. Effects of transionospheric signal decorrelation on global navigation satellite systems (gnss) performance studied from irregularity dynamics around the northern crest of the eia. **Radio Science**, v. 49, p. 851–860, 2014. 38

DATTA-BARUA, S.; WALTER, T.; PULLEN, S.; LUO, M.; BLANCH, J.; ENGE, P. Using WAAS ionospheric data to estimate laas short baseline gradients. In: . [s.n.], 2002. p. 523–530. Available from: <<http://urlib.net/ibi/8JMKD3MGP3W34R/43F627H>>. 89, 90, 91, 157

DAVIES, K. **Ionospheric radio propagation**. [S.l.]: US Dept. of Commerce, National Bureau of Standards, 1965. 74

_____. _____. [S.l.]: IET, 1990. 14, 74

DERGHAZARIAN, S.; HYSELL, D. L.; VARNEY, R. H. Topside measurements at jicamarca during the 2019–2020 deep solar minimum. **Journal of Geophysical Research: Space Physics**, v. 126, p. e2021JA029695, 12 2021. ISSN 2169-9380. Available from: <<https://onlinelibrary.wiley.com/doi/10.1029/2021JA029695>>. 1, 5, 99, 148, 169

DIAS, M. A.; FAGUNDES, P. R.; VENKATESH, K.; PILLAT, V. G.; RIBEIRO, B. A.; SEEMALA, G. K.; ARCANJO, M. O. Daily and monthly variations of the equatorial ionization anomaly (eia) over the brazilian sector during the descending phase of the solar cycle 24. **Journal of Geophysical Research: Space Physics**, v. 125, p. 1–17, 2020. ISSN 21699402. 101, 102, 104

DUGASSA, T.; HABARULEMA, J. B.; NIGUSSIE, M. Investigation of the relationship between the spatial gradient of total electron content (TEC) between two nearby stations and the occurrence of ionospheric irregularities. **Annales Geophysicae**, v. 37, n. 6, p. 1161–1180, dec 2019. ISSN 1432-0576. Available from: <<https://angeo.copernicus.org/articles/37/1161/2019/>>. 50, 87, 88, 90, 118, 144, 145, 164, 169

EASTES, R.; MCCLINTOCK, W. E.; BURNS, A.; ANDERSON, D.; ANDERSSON, L.; CODRESCU, M.; CORREIRA, J.; DANIELL, R.; ENGLAND, S. L.; EVANS, J. et al. The global-scale observations of the limb and disk (GOLD) mission. **Space Science Reviews**, v. 212, p. 383–408, 2017. 2, 3, 62, 64, 66

EASTES, R. W.; MCCLINTOCK, W. E.; BURNS, A. G.; ANDERSON, D. N.; ANDERSSON, L.; ARYAL, S.; BUDZIEN, S. A.; CAI, X.; CODRESCU, M. V.; CORREIRA, J. T.; DANIELL, R. E.; DYMOND, K. F.; ENGLAND, S. L.; EPARVIER, F. G.; EVANS, J. S.; FOROOSH, H.; GAN, Q.; GREER, K. R.; KARAN, D. K.; KRYWONOS, A.; LASKAR, F. I.; LUMPE, J. D.; MARTINIS, C. R.; MCPHATE, J. B.; OBERHEIDE, J.; SIEGMUND, O. H.; SOLOMON, S. C.; VEIBEL, V.; WOODS, T. N. Initial observations by the gold mission. **Journal of Geophysical Research: Space Physics**, v. 125, p. 1–11, 2020. ISSN 21699402. 63, 64

EASTES, R. W.; SOLOMON, S. C.; DANIELL, R. E.; ANDERSON, D. N.; BURNS, A. G.; ENGLAND, S. L.; MARTINIS, C. R.; MCCLINTOCK, W. E. Global-scale observations of the equatorial ionization anomaly. **Geophysical Research Letters**, v. 46, p. 9318–9326, 2019. ISSN 19448007. Available from: <<https://doi.org/10.1029/2019GL084199>>. 37, 62, 65, 66, 131, 132, 154, 156, 160, 163

ECHER, E.; TSURUTANI, B. T.; GONZALEZ, W. D. Extremely low geomagnetic activity during the recent deep solar cycle minimum. **International Astronomical Union**, n. 286, 2011. Available from: <<https://doi.org/10.1017/S174392131200484X>>. 1, 4

EMERY, B. A.; RICHARDSON, I. G.; EVANS, D. S.; RICH, F. J.; WILSON, G. R. Solar rotational periodicities and the semiannual variation in the solar wind, radiation belt, and aurora. **Solar Physics**, v. 274, n. 1-2, p. 399–425, 2011. ISSN 00380938. 1, 4, 16, 99

EMMERT, J.; RICHMOND, A.; DROB, D. A computationally compact representation of magnetic-apex and quasi-dipole coordinates with smooth base vectors. **Journal of Geophysical Research: Space Physics**, v. 115, n. A8, 2010. 4

ESA. **VirES for swarm web client**. 2021. Available from: <<https://earth.esa.int/eogateway/missions/swarm/data>>. 67

FAA. **Schematic of the ground-based augmentation system**. 2021. Available from: <<https://www.faa.gov/about/office_org/headquarters_offices/ato/service_units/techops/navservices/gnss/laas/howitworks>>. 57

FAGUNDES, P. R.; CARDOSO, F. A.; FEJER, B. G.; VENKATESH, K.; RIBEIRO, B. A. G.; PILLAT, V. G. Positive and negative gps-tec ionospheric storm effects during the extreme space weather event of march 2015 over the brazilian sector. **Journal of Geophysical Research: Space Physics**, v. 121, p. 1–13, 6 2016. ISSN 21699380. Available from: <<http://doi.wiley.com/10.1002/2015JA022214>>. 2, 42, 44, 50, 105, 120, 142, 159, 160, 163

FANG, T.-W.; KUBARYK, A.; GOLDSTEIN, D.; LI, Z.; FULLER-ROWELL, T.; MILLWARD, G.; SINGER, H. J.; STEENBURGH, R.; WESTERMAN, S.; BABCOCK, E. Space weather environment during the spacex starlink satellite loss in february 2022. **Space Weather**, p. e2022SW003193, 2022. 7, 145

FARLEY, D.; BONELLI, E.; FEJER, B. G.; LARSEN, M. The prereversal enhancement of the zonal electric field in the equatorial ionosphere. **Journal of Geophysical Research: Space Physics**, v. 91, n. A12, p. 13723–13728, 1986. 31

FEJER, B. G. Low latitude ionospheric electrodynamics. **Space Science Reviews**, v. 158, p. 145–166, 2011. ISSN 00386308. 2, 20, 37, 41, 42, 50, 113, 118, 142, 159

FIGUEIREDO, C. A.; TAKAHASHI, H.; WRASSE, C. M.; OTSUKA, Y.; SHIOKAWA, K.; BARROS, D. Medium-scale traveling ionospheric disturbances observed by detrended total electron content maps over brazil. **Journal of Geophysical Research: Space Physics**, v. 123, p. 2215–2227, 2018. ISSN 21699402. 2, 41

FORBES, J. M. The equatorial electrojet. **Reviews of Geophysics**, v. 19, n. 3, p. 469–504, 1981. 24

FULLER-ROWELL, T.; CODRESCU, M.; RISBETH, H.; MOFFETT, R.; QUEGAN, S. On the seasonal response of the thermosphere and ionosphere to geomagnetic storms. **Journal of Geophysical Research**, v. 101, p. 2343–2354, 02 1996. 41, 44, 105, 129, 151, 163, 164

GALVIN, A. B.; KOHL, J. L. Whole sun month at solar minimum: an introduction. **Journal of Geophysical Research: Space Physics**, v. 104, p. 9673–9678, 1999. 1

GAN, Q.; EASTES, R. W.; BURNS, A. G.; WANG, W.; QIAN, L.; SOLOMON, S. C.; CODRESCU, M. V.; MCINERNEY, J.; MCCLINTOCK, W. E. First synoptic observations of geomagnetic storm effects on the global-scale oi 135.6-nm dayglow in the thermosphere by the GOLD mission. **Geophysical Research Letters**, v. 47, n. 3, 2020. ISSN 19448007. 3, 176

GARTON, T. M.; GALLAGHER, P. T.; MURRAY, S. A. Automated coronal hole identification via multi-thermal intensity segmentation. **Journal of Space Weather and Space Climate**, v. 8, p. A02, 2018. 96

GIBSON, S. E.; TOMA, G. de; EMERY, B.; RILEY, P.; ZHAO, L.; ELSWORTH, Y.; LEAMON, R. J.; LEI, J.; MCINTOSH, S.; MEWALDT, R. A.; THOMPSON, B. J.; WEBB, D. The whole heliosphere interval in the context of a long and structured solar minimum: An overview from sun to earth. **Solar Physics**, v. 274, p. 5–27, 2011. ISSN 00380938. 1, 2, 4, 5, 7, 98, 100

GONZALEZ, W.; ECHER, E. A study on the peak dst and peak negative bz relationship during intense geomagnetic storms. **Geophysical Research Letters**, v. 32, n. 18, 2005. 171

GONZALEZ, W.; PARKER, E. **Magnetic reconnection: concepts and applications**. [S.l.: s.n.], 2016. ISBN 978-3-319-26430-1. 12, 41

GONZALEZ, W. D.; JOSELYN, J.-A. A.; KAMIDE, Y.; KROEHL, H. W.; ROSTOKER, G.; TSURUTANI, B. T.; VASYLIUNAS, V. M. What is a geomagnetic storm? **Journal of Geophysical Research: Space Physics**, v. 99, p. 5771–5792, 1994. ISSN 0148-0227. 12, 13, 17, 41

GOPALSWAMY, N.; MäKELä, P.; XIE, H.; AKIYAMA, S.; YASHIRO, S. Cme interactions with coronal holes and their interplanetary consequences. **Journal of Geophysical Research: Space Physics**, v. 114, p. 1–17, 2009. ISSN 21699402. 13, 96

GOPALSWAMY, N.; NITTA, N.; AKIYAMA, S.; MÄKELÄ, P.; YASHIRO, S. Coronal magnetic field measurement from euv images made by the solar dynamics observatory. **The Astrophysical Journal**, v. 744, n. 1, p. 72, 2011. 5, 143

GRANDIN, M.; AIKIO, A. T.; KOZLOVSKY, A. Properties and geoeffectiveness of solar wind high-speed streams and stream interaction regions during solar cycles 23 and 24. **Journal of Geophysical Research: Space Physics**, v. 124, p. 3871–3892, 2019. ISSN 21699402. xxvi, 4, 5, 6, 17, 18, 100, 170

HADY, A. A. Deep solar minimum and global climate changes. **Journal of Advanced Research**, v. 4, p. 209–214, 2013. ISSN 20901232. Available from: <<http://dx.doi.org/10.1016/j.jare.2012.11.001>>. 1, 2, 4, 99

HAERENDEL, G.; ECCLES, J. V.; CAKIR, S. Theory for modeling the equatorial evening ionosphere and the origin of the shear in the horizontal plasma flow. **Journal of Geophysical Research: Space Physics**, v. 97, p. 1209–1223, 1992. 37, 59

HAMILTON, C. J. **Solar structure**. 2020. Available from: <<https://solar.physics.montana.edu/ypop/Spotlight/SunInfo/Structure.html>>. 9

HANSON, W.; PATTERSON, T. The maintenance of the night-time f-layer. **Planetary and Space Science**, v. 12, n. 10, p. 979–997, 1964. 23, 24

HARGREAVES, J. K. **The solar-terrestrial environment: an introduction to geospace the science of the terrestrial upper atmosphere, ionosphere, and magnetosphere**. [S.l.]: Cambridge University Press, 1992. 9, 10, 11, 12, 14, 16, 41, 75

HATHAWAY, D. H. The solar cycle. **Living Reviews in Solar Physics**, v. 12, n. 1, p. 1–87, 2015. 1, 11, 12

HINES, C. O. Internal atmospheric gravity waves at ionospheric heights. **Canadian Journal of Physics**, v. 38, p. 1441–1481, 1960. 2, 41, 83, 162, 174, 176

HUANG, X.; REINISCH, B. W. Vertical electron density profiles from the digisonde network. **Advances in Space Research**, v. 18, n. 6, p. 121–129, 1996. ISSN 02731177. 161

HUBA, J. D.; JOYCE, G. Global modeling of equatorial plasma bubbles. **Geophysical Research Letters**, v. 37, p. 1–5, 2010. ISSN 00948276. 37

HUBA, J. D.; LIU, H. L. Global modeling of equatorial spread f with sami3/waccm-x. **Geophysical Research Letters**, v. 47, p. 1–17, 2020. ISSN 19448007. 37

HUNSUCKER, R. Radio techniques for probing the terrestrial ionosphere, phys. chem. **Space**, v. 22, p. 293, 1991. 74

HUNSUCKER, R. D.; HARGREAVES, J. K. **Radio techniques for probing the ionosphere**. [S.l.]: Cambridge University Press, 2002. 181–226 p. 41

IMTIAZ, N.; ALI, O. H.; RIZVI, H. Impact of the intense geomagnetic storm of august 2018 on the equatorial and low latitude ionosphere. **Astrophysics and Space Science**, v. 366, 2021. ISSN 1572946X. Available from: <<http://dx.doi.org/10.1007/s10509-021-04009-2>>. 6

JESUS, R. de; BATISTA, I. S.; TAKAHASHI, H.; PAULA, E. R. de; BARROS, D.; FIGUEIREDO, C. A.; ABREU, A. J. de; JONAH, O. F.; FAGUNDES, P. R.; VENKATESH, K. Morphological features of ionospheric scintillations during high solar activity using gps observations over the South American sector. **Journal of Geophysical Research: Space Physics**, v. 125, p. 1–20, 2020. ISSN 21699402. 106

JIANG, J.; CAMERON, R. H.; SCHüSSLER, M. The cause of the weak solar cycle 24. **Astrophysical Journal Letters**, v. 808, p. L28, 7 2015. ISSN 20418213. 1, 95, 99

JONAH, O.; PAULA, E. de; MUELLA, M.; DUTRA, S.; KHERANI, E.; NEGRETI, P.; OTSUKA, Y. Tec variation during high and low solar activities over South American. **Journal of Atmospheric and Solar-Terrestrial Physics**, v. 135, p. 22–35, dec 2015. ISSN 13646826. Available from: <<http://dx.doi.org/10.1016/j.jastp.2015.10.005https://linkinghub.elsevier.com/retrieve/pii/S1364682615300663>>. 2, 95, 99, 101, 102, 104, 120

JONAH, O. F.; COSTER, A.; ZHANG, S.; GONCHARENKO, L.; ERICKSON, P. J.; PAULA, E. R. de; KHERANI, E. A. Tid observations and source analysis during the 2017 memorial day weekend geomagnetic storm over north america. **Journal of Geophysical Research: Space Physics**, v. 123, p. 8749–8765, 2018. ISSN 21699402. 42, 162

JONAH, O. F.; KHERANI, E. A.; PAULA, E. R. D. Observation of tec perturbation associated with medium-scale traveling ionospheric disturbance and possible seeding mechanism of atmospheric gravity wave at a brazilian sector. **Journal of Geophysical Research: Space Physics**, v. 121, p. 2531–2546, 3 2016. ISSN 21699380. Available from: <<http://doi.wiley.com/10.1002/2015JA022273>>. 2, 20, 44, 161

JYOTI, N.; DEVASIA, C.; SRIDHARAN, R.; TIWARI, D. Threshold height for the meridional wind to play a deterministic role in the bottom side equatorial spread f and its dependence on solar activity. **Geophysical research letters**, v. 31, n. 12, 2004. 40

KELLEY, M.; FEJER, B. G.; GONZALES, C. A. An explanation for anomalous equatorial ionospheric electric fields associated with a northward turning of the interplanetary magnetic field. **Geophysical Research Letters**, v. 6, n. 4, p. 301–304, 1979. 41, 120, 142, 143, 145

KELLEY, M. C. **The Earth's ionosphere: plasma physics and electrodynamics**. [S.l.]: Academic Press, 2009. 2, 23, 24, 25, 26, 28, 29, 30, 31, 32, 34, 36, 42, 92, 102, 106, 118, 131, 160, 169

KELLEY, M. C.; MAKELA, J. J.; CHAU, J. L.; NICOLLS, M. J. Penetration of the solar wind electric field into the magnetosphere/ionosphere system. **Geophysical Research Letters**, v. 30, p. 23–25, 2003. ISSN 00948276. 6, 30, 41, 42, 65, 68, 144, 148, 163, 174, 176

KEOSCIENTIFIC. **Keo Scientific**. 2017. Available from: <<http://www.keoscientific.com/>>. 62

KIKUCHI, T.; LÜHR, H.; SCHLEGEL, K.; TACHIHARA, H.; SHINOHARA, M.; KITAMURA, T.-I. Penetration of auroral electric fields to the equator during a substorm. **Journal of Geophysical Research: Space Physics**, v. 105, p. 23251–23261, 2000. ISSN 2156-2202. 41

KIL, H.; SU, S.; PAXTON, L. J.; WOLVEN, B. C.; ZHANG, Y.; MORRISON, D.; YEH, H. C. Coincident equatorial bubble detection by timed/guvi and rocsat-1. **Geophysical Research Letters**, v. 31, p. 4–7, 2004. ISSN 00948276. 65

KINTNER, P. M.; KIL, H.; BEACH, T. L.; PAULA, E. R. de. Fading timescales associated with gps signals and potential consequences. **Radio Science**, v. 36, p. 731–743, 2001. 37, 88, 89, 91, 92

KINTNER, P. M.; LEDVINA, B. M.; PAULA, E. R. D. Gps and ionospheric scintillations. **Space Weather**, v. 5, p. 1–23, 2007. ISSN 15427390. 65, 73, 88, 89, 91, 138, 139

KINTNER, P. M.; LEDVINA, B. M.; PAULA, E. R. D.; KANTOR, I. J. Size, shape, orientation, speed, and duration of gps equatorial anomaly scintillations. **Radio Science**, v. 39, 2004. ISSN 00486604. 88, 91, 135, 151

KLENZING, J.; BURRELL, A. G.; HEELIS, R. A.; HUBA, J. D.; PFAFF, R.; SIMõES, F. Exploring the role of ionospheric drivers during the extreme solar minimum of 2008. **Annales Geophysicae**, v. 31, p. 2147–2156, 2013. ISSN 14320576. 148

KLENZING, J.; HALFORD, A. J.; LIU, G.; SMITH, J. M.; ZHANG, Y.; ZAWDIE, K.; MARUYAMA, N.; PFAFF, R.; BISHOP, R. L. A system science perspective of the drivers of equatorial plasma bubbles. **Frontiers in Astronomy and Space Sciences**, v. 9, p. 1064150, 2023. 66

KLOBUCHAR, J. Ionospheric issues for a sbas in the equatorial region. In: . [S.l.: s.n.], 2002. 38

KNEPP, D. L.; HAUSMAN, M. A. Ionospheric propagation effects on ground and space based radars. In: INTERNATIONAL CONFERENCE ON RADAR, 2007, Watham, USA. **Proceedings...** Watham, 2007. p. 916–921. 38

KOMJATHY, A. Global ionospheric total electron content mapping using the global positioning system. **Engineering**, p. 248, 1997. Available from: <<http://www2.unb.ca/gge/Pubs/TR188.pdf>>. 74, 75, 76, 78, 81

KRAINEV, M. B. On the solar activity cycles 23-24. **Bulletin of the Lebedev Physics Institute,**, v. 39, p. 3–12, 2012. 1

KRIEGER, A.; TIMOTHY, A.; ROELOF, E. A coronal hole and its identification as the source of a high velocity solar wind stream. **Solar Physics**, v. 29, n. 2, p. 505–525, 1973. 16, 95

KUMAR, S.; KUMAR, V. V. Ionospheric response to the st. patrick's day space weather events in march 2012, 2013, and 2015 at southern low and middle latitudes. **Journal of Geophysical Research: Space Physics**, v. 124, p. 584–602, 2019. ISSN 21699402. 163

LAPENTA, G. Space weather: variability in the sun-earth connection. In: MATERASSI, M.; FORTE, B.; COSTER, A. J.; SKONE, S. (Ed.). **The Dynamical Ionosphere**. Elsevier, 2020. p. 61–85. ISBN 978-0-12-814782-5. Available from: <<https://www.sciencedirect.com/science/article/pii/B978012814782500008X>>. 1

LEE, J.; PULLEN, S.; DATTA-BARUA, S.; ENGE, P. Assessment of nominal ionosphere spatial decorrelation for laas. **Record - IEEE PLANS, Position Location and Navigation Symposium**, v. 2006, p. 506–514, 2006. 89, 90, 157

LEI, J.; THAYER, J. P.; FORBES, J. M.; SUTTON, E. K.; NEREM, R. S. Rotating solar coronal holes and periodic modulation of the upper atmosphere. **Geophysical Research Letters**, v. 35, p. 23–26, 2008. ISSN 00948276. 19, 85

LEKSHMI, D. V.; BALAN, N.; RAM, S. T.; LIU, J. Y. Statistics of geomagnetic storms and ionospheric storms at low and mid latitudes in two solar cycles. **Journal of Geophysical Research: Space Physics**, v. 116, n. A11, p. n/a–n/a, nov 2011. ISSN 01480227. Available from: <<https://onlinelibrary.wiley.com/doi/full/10.1029/2011JA017042>>. 3, 118, 144, 173

LI, G.; NING, B.; ABDU, M. A.; YUE, X.; LIU, L.; WAN, W.; HU, L. On the occurrence of postmidnight equatorial F region irregularities during the June solstice. **Journal of Geophysical Research: Space Physics**, v. 116, n. 4, 2011. ISSN 21699402. 85

LISSA, D.; SRINIVASU, V. K. D.; PRASAD, D. S. V. V. D.; NIRANJAN, K. Ionospheric response to the 26 august 2018 geomagnetic storm using gps-tec observations along 80° e and 120° e longitudes in the asian sector. **Advances in Space Research**, v. 66, p. 1427–1440, 2020. ISSN 18791948. Available from: <<https://doi.org/10.1016/j.asr.2020.05.025>>. 118, 120, 142

LIU, H. L. Variability and predictability of the space environment as related to lower atmosphere forcing. **Space Weather**, v. 14, n. 9, p. 634–658, 2016. ISSN 15427390. 2, 3, 151

LIU, J.; LIU, L.; ZHAO, B.; WEI, Y.; HU, L.; XIONG, B. High-speed stream impacts on the equatorial ionization anomaly region during the deep solar minimum year 2008. **Journal of Geophysical Research: Space Physics**, v. 117, n. 10, p. 1–12, oct 2012. ISSN 21699402. Available from: <<http://doi.wiley.com/10.1029/2012JA018015>>. 2, 5, 6, 19, 43, 122, 144, 149, 163, 173

LIU, J.; ZHANG, D.; MO, X.; XIONG, C.; HAO, Y.; XIAO, Z. Morphological differences of the northern equatorial ionization anomaly between the eastern asian and american sectors. **Journal of Geophysical Research: Space Physics**, v. 125, 2020. ISSN 21699402. 3

LIU, J. Y.; TSAI, H. F.; WU, C. C.; TSENG, C. L.; TSAI, L. C.; TSAI, W. H.; LIOU, K.; CHAO, J. K. The effect of geomagnetic storm on ionospheric Total Electron Content at the equatorial anomaly region. **Advances in Space Research**, v. 24, p. 1491–1494, 1999. ISSN 02731177. 118, 148, 159, 160

LIU, L.; WAN, W.; NING, B.; ZHANG, M. L. Climatology of the mean Total Electron Contentderived from gps global ionospheric maps. **Journal of Geophysical Research: Space Physics**, v. 114, p. 1–13, 2009. ISSN 21699402. 85

LIU, Y.; RADICELLA, S. On the correlation between roti and s4. **Annales Geophysicae Discussions**, p. 1–14, 2019. ISSN 0992-7689. 85, 88

LIU, Z.; LI, Y.; GUO, J.; LI, F. Influence of higher-order ionospheric delay correction on gps precise orbit determination and precise positioning. **Geodesy and Geodynamics**, v. 7, n. 5, p. 369–376, 2016. 74, 88

LOEWE, C. A. Classification and mean behavior of magnetic storms. **Journal of Geophysical Research A: Space Physics**, v. 102, p. 14209–14213, 1997. ISSN 01480227. 41, 71, 122, 165

MANNUCCI, A. J.; TSURUTANI, B. T.; IIJIMA, B. A.; KOMJATHY, A.; SAITO, A.; GONZALEZ, W. D.; GUARNIERI, F. L.; KOZYRA, J. U.; SKOUG, R. Dayside global ionospheric response to the major interplanetary events of october 29-30, 2003 "halloween storms". **Geophysical Research Letters**, v. 32, p. 1–4, 2005. ISSN 00948276. 42, 173

MARTINIS, C. R.; MENDILLO, M. J.; AARONS, J. Toward a synthesis of equatorial spread f onset and suppression during geomagnetic storms. **Journal of Geophysical Research: Space Physics**, v. 110, p. 1–12, 2005. ISSN 21699402. 34, 49, 50, 142

MATAMBA, T. M. Long-term analysis of ionospheric response during geomagnetic storms in mid, low and equatorial latitudes. 2017. 10, 19

MATAMBA, T. M.; HABARULEMA, J. B. Ionospheric responses to cme- and cir-driven geomagnetic storms along 30 e–40 e over the african sector from 2001 to 2015. **Space Weather**, v. 16, n. 5, p. 538–556, 2018. ISSN 15427390. Available from: <<https://doi.org/10.1029/2017SW001754>>. 100, 173

MATAMBA, T. M.; HABARULEMA, J. B.; MCKINNELL, L. A. Statistical analysis of the ionospheric response during geomagnetic storm conditions over south africa using ionosonde and gps data. **Space Weather**, v. 13, p. 536–547, 2015. ISSN 15427390. 170

MATSUSHITA, S. Dynamo currents, winds, and electric fields. **Radio Science**, v. 4, p. 771–780, 1969. ISSN 1944799X. 26, 27, 28, 174

MCCLINTOCK, W. E. et al. Global-scale observations of the limb and disk mission implementation: 2. observations, data pipeline, and level 1 data products. **Journal of Geophysical Research: Space Physics**, v. 125, n. 5, p. e2020JA027809, 2020. 62, 63

MCDONALD, S. E.; DYMOND, K. F.; SUMMERS, M. E. Hemispheric asymmetries in the longitudinal structure of the low-latitude nighttime ionosphere. **Journal of Geophysical Research: Space Physics**, v. 113, p. 1–13, 2008. ISSN 21699402. 13

MCNAMARA, L. F.; RETTERER, J. M.; ABDU, M.; BATISTA, I. S.; REINISCH, B. W. F2 peak parameters, drifts and spread f derived from digisonde ionograms for the copex campaign in Brazil. **Journal of Atmospheric and Solar-Terrestrial Physics**, v. 70, p. 1144–1158, 2008. ISSN 13646826. 59

MENDILLO, M.; LIN, B.; AARONS, J. The application of gps observations to equatorial aeronomy. **Radio Science**, v. 35, n. 3, p. 885–904, 2000. 85, 87

MISRA, P.; ENGE, P. **Global Positioning System: signals, measurements and performance second editions**. [S.l.]: Ganja Jamuna Press, 2006. 55, 79, 80, 81

_____. **Global Positioning System: signals, measurements, and performance**. [S.l.]: Ganga-Jamuna Press, 2011. ISBN 9780970954428. 73, 76, 77, 78, 79, 81, 82, 89, 154

MORO, J.; XU, J.; DENARDINI, C. M.; RESENDE, L. C.; NETO, P. F.; SILVA, L. A. D.; SILVA, R. P.; CHEN, S. S.; PICANçO, G. A.; CARMO, C. S.; LIU, Z.; YAN, C.; WANG, C.; SCHUCH, N. J. First look at a geomagnetic storm with Santa Maria digisonde data: F region responses and comparisons over the american sector. **Journal of Geophysical Research: Space Physics**, v. 126, p. 1–18, 2021. ISSN 21699402. 2, 3, 6, 42, 44, 84, 117, 118, 120, 122, 163, 164

MUELLA, M. T. A. H.; PAULA, E. R. de; MONTEIRO, A. A. Ionospheric scintillation and dynamics of fresnel-scale irregularities in the inner region of the equatorial ionization anomaly. **Surveys in Geophysics**, v. 34, p. 233–251, 2013. ISSN 01693298. 38

MURSULA, K.; ZIEGER, B. The 13.5-day periodicity in the sun, solar wind, and geomagnetic activity: the last three solar cycles. **Journal of Geophysical Research: Space Physics**, v. 101, n. A12, p. 27077–27090, 1996. 99

NAKATA, H.; TAKAHASHI, A.; TAKANO, T.; SAITO, A.; SAKANOI, T. Observation of equatorial plasma bubbles by the airglow imager on iss-imap. **Progress in Earth and Planetary Science**, v. 5, 2018. ISSN 21974284. 65

NASA. **Schematic of NASA GOLD Imaging of the Nightime Ionosphere**. 2021. Available from: <<http://www.space.com/>>. 64

_____. **Terrestrial atmosphere ITM (Ionosphere, Thermosphere, Mesosphere) processes**. 2021. Available from: <<https://svs.gsfc.nasa.gov/4641>>. 20

NEGRETI, P. M. de S. **Estudo Do Conteúdo Eletrônico Total Na Região Brasileira Em Períodos Magneticamente Perturbados**. 1–121 p. Tese (Doutorado em Geofisica Espacial — Instituto Nacional de Pesquisas Espaciais (INPE), São José dos Campos, 2012. Available from: <<http://mtc-m16d.sid.inpe.br/col/sid.inpe.br/mtc-m19/2012/05.10.21.43/doc/publicacao.pdf>>. 76

NITTA, N. Observables indicating two major coronal mass ejections during the whi. **Solar Physics**, v. 274, n. 1, p. 219–232, 2011. 1, 4

NORSUZILA, Y.; ABDULLAH, M.; ISMAIL, M. Leveling process of total electron content(tec) using malaysian global positioning system(gps) data. **American Journal of Engineering and Applied Sciences**, v. 1, n. 3, 2008. 82

OLADIPO, O.; SCHÜLER, T. Equatorial ionospheric irregularities using gps tec derived index. **Journal of Atmospheric and Solar-Terrestrial Physics**, v. 92, p. 78–82, 2013. 50, 85, 87, 88, 142

OLWENDO, J. O.; CILLIERS, P.; WEIMIN, Z.; MING, O.; YU, X. Validation of roti for ionospheric amplitude scintillation measurements in a low-latitude region over Africa. **Radio Science**, v. 53, p. 876–887, 2018. ISSN 1944799X. 88

OYEDOKUN, O. J.; AMAECHI, P. O.; AKALA, A. O.; SIMI, K. G.; OGWALA, A.; OYEYEMI, E. O. Solar and interplanetary events that drove two cir-related geomagnetic storms of 1 june 2013 and 7 october 2015, and their ionospheric responses at the american and african equatorial ionization anomaly regions. **Advances in Space Research**, v. 69, p. 2168–2181, 2022. ISSN 18791948. Available from: <<https://doi.org/10.1016/j.asr.2021.12.027>>. 48, 50, 144, 145

PARK, J.; LüHR, H.; MIN, K. W. Characteristics of f-region dynamo currents deduced from champ magnetic field measurements. **Journal of Geophysical Research: Space Physics**, v. 115, p. 1–12, 2010. ISSN 21699402. 27

PAULA, E.; KHERANI, E.; ABDU, M.; BATISTA, I.; SOBRAL, J.; KANTOR, I.; TAKAHASHI, H.; REZENDE, L. F.; MUELLA, M.; RODRIGUES, F.; KINTNER, P.; LEDVINA, B.; MITCHELL, C.; GROVES, K. Characteristics of the ionospheric irregularities over brazilian longitudinal sector. **Indian Journal of Radio and Space Physics**, v. 36, p. 268–277, 08 2007. 39, 40, 49, 52, 86, 92, 106, 135, 139

PAULA, E. R. D.; RODRIGUES, F. S.; IYER, K. N.; KANTOR, I. J.; ABDU, M. A.; KINTNER, P. M.; LEDVINA, B. M.; KIL, H. Equatorial anomaly effects on gps scintillations in Brazil. **Advances in Space Research**, v. 31, p. 749–754, 2003. 38, 39, 156

PAULA, E. R. de; OLIVEIRA, C. B. de; CATON, R. G.; NEGRETI, P. M.; BATISTA, I. S.; MARTINON, A. R.; NETO, A. C.; ABDU, M. A.; MONICO, J. F.; SOUSASANTOS, J.; MORAES, A. O. Ionospheric irregularity behavior during the september 6–10, 2017 magnetic storm over brazilian equatorial–low latitudes. **Earth, Planets and Space**, v. 71, 2019. ISSN 18805981. Available from: <<https://doi.org/10.1186/s40623-019-1020-z>>. 21, 38, 49, 50, 51, 142, 160

PAULA, E. R. de et al. Ionospheric irregularity behavior during the september 6–10, 2017 magnetic storm over brazilian equatorial–low latitudes. **Earth, Planets and Space**, v. 71, p. 42, 2019. 85

PAZNUKHOV, V.; REINISCH, B.; SONG, P.; HUANG, X.; BULLETT, T.; VELIZ, O. Formation of an f3 layer in the equatorial ionosphere: a result from strong imf changes. **Journal of Atmospheric and Solar-Terrestrial Physics**, v. 69, n. 10-11, p. 1292–1304, 2007. 24

PEREIRA, V. A. S.; CAMARGO, P. de O. Padrões para classificação dos indices de irregularidades da ionosfera: I rot e roti. In: SIMPÓSIO BRASILEIRO DE CIÊNCIAS GEODÉSICAS E TECNOLOGIAS DA GEOINFORMAÇÃO, 2014, Recife, Pernambuco. **Anais...** UFPE: SIMGEO, 2014. p. 547–555. Available from: <<http://urlib.net/ibi/8JMKD3MGP3W34R/43F627H>>. 86, 106

PEREIRA, V. A. S.; CAMARGO, P. de O.; PEREIRA, V. A. S.; CAMARGO, P. de O. Brazilian active gnss networks as systems for monitoring the ionosphere. **GPS Solutions**, v. 21, p. 1013–1025, 2017. ISSN 15211886. 85, 87, 139

PESNELL, W. D. Predictions of solar cycle 24. **Solar Physics**, v. 252, n. 1, p. 209–220, 2008. 5

PI, X.; MANNUCCI, A. J.; LINDQWISTER, U. J.; HO, C. M. Monitoring of global ionospheric irregularities using the worldwide gps network. **Geophysical Research Letters**, v. 24, p. 2283–2286, 1997. 85, 86, 87, 88, 89, 106, 138, 139

PIMENTA, A. A.; BITTENCOURT, J. A.; FAGUNDES, P. R.; SAHAI, Y.; BURITI, R. A.; TAKAHASHI, H.; TAYLOR, M. J. Ionospheric plasma bubble zonal drifts over the tropical region: a study using oi 630 nm emission all-sky images. **Journal of Atmospheric and Solar-Terrestrial Physics**, v. 65, p. 1117–1126, 2003. ISSN 13646826. 61, 157

PIMENTA, A. A.; FAGUNDES, P. R.; BITTENCOURT, J. A.; SAHAI, Y. Relevant aspects fo equatorial plasma bubbles under different solar activity conditions. **Advances in Space Research**, v. 27, p. 1213–1218, 2001. ISSN 02731177. 32, 33, 61, 89, 132, 135

PIMENTA, A. A.; SAHAI, Y.; BITTENCOURT, J. A.; ABDU, M. A.; TAKAHASHI, H.; TAYLOR, M. J. Plasma blobs observed by ground-based optical and radio techniques in the brazilian tropical sector. **Geophysical Research Letters**, v. 31, p. n/a–n/a, 2004. ISSN 0094-8276. 61

PRADIPTA, R.; DOHERTY, P. H. Assessing the occurrence pattern of large ionospheric tec gradients over the brazilian airspace. **Navigation, Journal of the Institute of Navigation**, v. 63, p. 335–343, 2016. ISSN 00281522. 89, 91, 136, 139, 157, 169

PRADIPTA, R.; VALLADARES, C. E.; DOHERTY, P. H. An effective tec data detrending method for the study of equatorial plasma bubbles and traveling ionospheric disturbances. **Journal of Geophysical Research: Space Physics**, v. 120, p. 11048–11055, 2015. ISSN 21699402. 135

PROLSS, G. W. Ionospheric f-region storms. In: VOLLAND, H. (Ed.). **Handbook of Atmospheric Electrodynamics**. Boca Raton: CRC Press, 1995. v. 2, p. 195–248. 41, 42, 44, 45, 71, 117, 129, 131, 144, 151, 173, 174

RAGHAV, A. N.; CHORAGHE, K.; SHAIKH, Z. I. The cause of an extended recovery from an icme-induced extreme geomagnetic storm: A case study. **Monthly Notices of the Royal Astronomical Society**, v. 917, p. 910–917, 2019. ISSN 13652966. 6

RAO, S. S.; CHAKRABORTY, M.; KUMAR, S.; SINGH, A. K. Low-latitude ionospheric response from gps, iri and tie-gcm tec to solar cycle 24. **Astrophysics and Space Science**, v. 364, p. 1–14, 12 2019. ISSN 1572946X. Available from: <<https://link-springer-com.ez61.periodicos.capes.gov.br/article/10.1007/s10509-019-3701-2>>. 5

RASTOGI, R. G.; KLOBUCHAR, J. A. Ionospheric electron content within the equatorial f2 layer anomaly belt. **Journal of Geophysical Research**, v. 95, p. 19045–19052, 1990. ISSN 0148-0227. 43, 44, 92, 142

REINISCH, B. W. **An HF radar system for ionospheric Research and Monitoring technical manual operation and maintenance**. Lowell, MA, 1978. Available from: <<chrome-extension://efaidnbmnnnibpcajpcglclefindmkaj/https://digisonde.com/pdf/Digisonde4DManual_LDI-web.pdf.>>. 58

_____. Modern ionosondes. **Modern Ionospheric Science**, v. 37191, p. 440–458, 1996. 30, 58

_____. Automated collection and dissemination of ionospheric data from the digisonde network. **Advances in Radio Science**, v. 2, p. 241–247, 2004. ISSN 16849965. 60

_____. **Hf sounders for geospace plasma observations 1**. [S.l.], 2015. 2–5 p. 58, 59

RETTERER, J. M.; RODDY, P. Faith in a seed: on the origins of equatorial plasma bubbles. **Annales Geophysicae**, v. 32, n. 5, p. 485–498, 2014. ISSN 14320576. 37, 160

REZENDE, L. F. C. D.; PAULA, E. R. D.; BATISTA, I. S.; KANTOR, I. J.; MUELLA, M. T. D. A. H. Study of ionospheric irregularities during intense magnetic storms. **Revista Brasileira de Geofisica**, v. 25, p. 151–158, 2007. ISSN 0102261X. 32, 39, 49, 52, 53

RICHARDSON, I. G.; CLIVER, E. W.; CANE, H. V. Sources of geomagnetic activity over the solar cycle: relative importance of coronal mass ejections, high-speed streams, and slow solar wind. **Journal of Geophysical Research: Space Physics**, v. 105, n. A8, p. 18203–18213, 2000. ISSN 21699402. 17

RICHARDSON, I. G.; ROSENVINGE, T. T. von; CANE, H. V. 25 mev solar proton events in cycle 24 and previous cycles. **Advances in Space Research**, v. 60, p. 755–767, 8 2017. ISSN 0273-1177. 5

RICHMOND, A.; PEYMIRAT, C.; ROBLE, R. Long-lasting disturbances in the equatorial ionospheric electric field simulated with a coupled magnetosphere-ionosphere-thermosphere model. **Journal of Geophysical Research: Space Physics**, v. 108, n. A3, 2003. 42

RISHBETH, H. Polarization fields produced by winds in the equatorial f-region. **Planetary and Space Science**, v. 19, p. 357–369, 1971. ISSN 00320633. 23

RISHBETH, H.; EDWARDS, R. The isobaric F2-layer. **Journal of Atmospheric and Terrestrial physics**, v. 51, n. 4, p. 321–338, 1989. 24

RISHBETH, H.; GARRIOTT, O. K. Book. **Introduction to ionospheric physics**. New York: Academic Press, 1969. x, 331 p. p. 26, 38, 102

ROMERO-HERNANDEZ, E.; DENARDINI, C. M.; JONAH, O. F.; ESSIEN, P.; PICANçO, G. A.; NOGUEIRA, P. A.; RODRIGUEZ-MARTINEZ, M.; RESENDE, L. C.; LUZ, V. de la; AGULAR-RODRIGUEZ, E.; SERGEEVA, M.; GONZALEZ-ESPARZA, J. A.; TAKAHASHI, H.; PEREZ-TIJERINA, E. Nighttime ionospheric tec study over latin america during moderate and high solar activity. **Journal of Geophysical Research: Space Physics**, v. 125, p. 1–18, 2020. ISSN 21699402. 101, 102

ROMERO-HERNANDEZ, E.; DENARDINI, C. M.; TAKAHASHI, H.; GONZALEZ-ESPARZA, J. A.; NOGUEIRA, P. A. B.; PADUA, M. B. de; LOTTE, R. G.; NEGRETI, P. d. S.; JONAH, O. F.; RESENDE, L. C. A.; RODRIGUEZ-MARTINEZ, M.; SERGEEVA, M. A.; BARBOSA-NETO, P. F.; LUZ, V. De la; MONICO, J. F. G.; AGUILAR-RODRIGUEZ, E. Daytime ionospheric TEC weather study over Latin America. **Journal of Geophysical Research: Space Physics**, v. 123, n. 12, p. 2018JA025943, dec 2018. ISSN 2169-9380. Available from: <<https://onlinelibrary.wiley.com/doi/abs/10.1029/2018JA025943>>. 101, 102, 104

RUSSELL, C.; MCPHERRON, R. Semiannual variation of geomagnetic activity. **Journal of Geophysical Research**, v. 78, n. 1, p. 92–108, 1973. 100, 164, 170, 173, 175

RUSSELL, C. T.; LUHMANN, J. G.; JIAN, L. K. How unprecedented a solar minimum? **Reviews of Geophysics**, v. 48, n. 2, p. RG2004, 2010. Available from: <<http://doi.wiley.com/10.1029/2009RG000316>>. 1, 2, 4, 5, 7, 95

SAHITHI, K.; SRIDHAR, M.; KOTAMRAJU, S. K.; KAVYA, K. C. S.; SIVAVARAPRASAD, G.; RATNAM, D. V.; DEEPTHI, C. Characteristics of ionospheric scintillation climatology over indian low-latitude region during the 24th solar maximum period. **Geodesy and Geodynamics**, v. 10, p. 110–117, 2019. ISSN 16749847. Available from: <<https://doi.org/10.1016/j.geog.2018.11.006>>. 139

SARRIS, T. E. Understanding the ionosphere thermosphere response to solar and magnetospheric drivers: Status, challenges and open issues. **Philosophical Transactions of the Royal Society A: Mathematical, Physical and Engineering Sciences**, v. 377, 2019. ISSN 1364503X. 2

SEEMALA, G. K.; VALLADARES, C. E. Statistics of Total Electron Content depletions observed over the South American continent for the year 2008. **Radio Science**, v. 46, p. 1–14, 2011. ISSN 00486604. 73

SHARMA, S.; GALAV, P.; DASHORA, N.; ALEX, S.; DABAS, R. S.; PANDEY, R. Response of low - latitude ionospheric Total Electron Content to the geomagnetic storm of 24 august 2005. **Journal of Geophysical Research Space Physics**, v. 116, p. 1–12, 2011. Available from: <<https://agupubs.onlinelibrary.wiley.com/doi/abs/10.1029/2010JA016368>>. 27, 41, 43, 44, 48, 49, 160

SHREEDEVI, P. R.; CHOUDHARY, R. K. Impact of oscillating imf bz during 17 march 2013 storm on the distribution of plasma over indian low-latitude and mid-latitude ionospheric regions. **Journal of Geophysical Research: Space Physics**, v. 122, p. 11,607–11,623, 2017. ISSN 21699402. 142

SILVA, R. P.; HUMBERTO, J.; SOBRAL, A.; KOGA, D.; SOUZA, J. R.; SILVA, R. P.; SOBRAL, J. H. A.; KOGA, D.; SOUZA, J. R. Evidence of prompt penetration electric fields during hildcaa events. **Annales Geophysicae**, v. 35, p. 1165–1176, 2017. ISSN 14320576. 6, 144

SINGH, A. K.; NARAYAN, D.; SINGH, R. P. Weak-scattering theory for ionospheric scintillation. **Nuovo Cimento della Societa Italiana di Fisica C**, v. 20, p. 541–552, 1997. ISSN 18269885. 37

SOBRAL, J.; ABDU, M.; YAMASHITA, C. S.; GONZALEZ, W.; GONZALEZ, A. C. de; BATISTA, I. S.; ZAMLUTTI, C.; TSURUTANI, B. Responses of the low-latitude ionosphere to very intense geomagnetic storms. **Journal of Atmospheric and Solar-Terrestrial Physics**, v. 63, p. 965–974, 2001. ISSN 13646826. 17

SOBRAL, J. H. A.; ABDU, M. A.; TAKAHASHI, H.; TAYLOR, M. J.; PAULA, E. R. D.; ZAMLUTTI, C. J.; AQUINO, M. G. D.; BORBA, G. L. Ionospheric plasma bubble climatology over brazil based on 22 years (1977–1998) of 630nm airglow observations. **Journal of Atmospheric and Solar-Terrestrial Physics**, v. 64, p. 1517–1524, 2002. 32, 33, 39, 40, 42, 61, 86, 106, 121, 139, 154, 169

SOLEN. **Solar Terrestrial Activity Report**. 2020. Available from: <<https://www.solen.info/>>. 96

SOLOMON, S. C.; QIAN, L.; MANNUCCI, A. J. Ionospheric electron content during solar cycle 23. **Journal of Geophysical Research: Space Physics**, v. 123, p. 5223–5231, 6 2018. ISSN 2169-9380. Available from: <<https://onlinelibrary.wiley.com/doi/10.1029/2018JA025464>>. 5, 169

SOUZA, J. R.; ABDU, M. A.; BATISTA, I. S.; BAILEY, G. J. Determination of vertical plasma drift and meridional wind using the sheffield university plasmasphere ionosphere model and ionospheric data at equatorial and low latitudes in brazil: Summer solar minimum and maximum conditions. **Journal of Geophysical Research: Space Physics**, v. 105, p. 12813–12821, 2000. ISSN 21699402. 68

SRIPATHI, S.; ABDU, M. A.; PATRA, A. K.; GHODPAGE, R. N. Unusual generation of localized epb in the dawn sector triggered by a moderate geomagnetic storm. **Journal of Geophysical Research: Space Physics**, v. 123, p. 9697–9710, 2018. ISSN 21699402. 49, 50

TAKAHASHI, H.; COSTA, S.; OTSUKA, Y.; SHIOKAWA, K.; MONICO, J. F.; PAULA, E.; NOGUEIRA, P.; DENARDINI, C. M.; BECKER-GUEDES, F.; WRASSE, C. M.; IVO, A. S.; GOMES, V. C.; GARGARELA, W.; SANT'ANNA, N.; GATTO, R. Diagnostics of equatorial and low latitude ionosphere by tec mapping over brazil. **Advances in Space Research**, v. 54, p. 385–394, 2014. ISSN 18791948. Available from: <<http://dx.doi.org/10.1016/j.asr.2014.01.032>>. 61

TAKAHASHI, H. et al. Simultaneous observation of ionospheric plasma bubbles and mesospheric gravity waves during the spreadfex campaign. **Annales Geophysicae**, v. 27, p. 1477–1487, 2009. ISSN 09927689. 37, 41, 83, 132, 161

TAKAHASHI, H.; WRASSE, C. M.; DENARDINI, C. M.; PáDUA, M. B.; PAULA, E. R. de; COSTA, S. M.; OTSUKA, Y.; SHIOKAWA, K.; MONICO, J. F.; IVO, A.; SANT'ANNA, N. Ionospheric TEC weather map over south america. **Space Weather**, v. 14, p. 937–949, 2016. ISSN 15427390. 27, 37, 42, 46, 47, 48, 83, 148, 149, 162

TAKAHASHI, H.; WRASSE, C. M.; FIGUEIREDO, C. A. O. B.; BARROS, D.; ABDU, M. A.; OTSUKA, Y.; SHIOKAWA, K. Equatorial plasma bubble seeding by mstids in the ionosphere. **Progress in Earth and Planetary Science**, v. 5, 2018. ISSN 21974284. 37, 41, 156, 161, 162

TAKAHASHI, H.; WRASSE, C. M.; OTSUKA, Y.; IVO, A.; GOMES, V.; PAULINO, I.; MEDEIROS, A. F.; DENARDINI, C. M.; SANT'ANNA, N.; SHIOKAWA, K. Plasma

bubble monitoring by tec map and 630nm airglow image. **Journal of Atmospheric and Solar-Terrestrial Physics**, v. 130-131, p. 151–158, 2015. ISSN 13646826. 160

TITHERIDGE, J. Changes in atmospheric composition inferred from ionospheric production rates. **Journal of Atmospheric and Terrestrial Physics**, v. 36, n. 7, p. 1249–1257, 1974. 3, 68, 102, 120, 150, 151, 174, 176

TSURUTANI, B. T.; GONZALEZ, W. D.; GONZALEZ, A. L.; GUARNIERI, F. L.; GOPALSWAMY, N.; GRANDE, M.; KAMIDE, Y.; KASAHARA, Y.; LU, G.; MANN, I.; MCPHERRON, R.; SORAAS, F.; VASYLIUNAS, V. Corotating solar wind streams and recurrent geomagnetic activity: a review. **Journal of Geophysical Research: Space Physics**, v. 111, 2006. ISSN 21699402. 6, 12, 14, 16, 17, 18, 83, 95, 96, 99, 112, 123, 143, 144, 147, 173

TSURUTANI, B. T.; GONZALEZ, W. D.; GONZALEZ, A. L. C.; TANG, F.; ARBALLO, J. K.; OKADA, M. Interplanetary origin of geomagnetic activity in the declining phase of the solar cycle. **Journal of Geophysical Research: Space Physics**, v. 100, p. 21717–21733, 1995. 6, 17, 95, 147, 170

TSURUTANI, B. T.; GONZALEZ, W. D.; LAKHINA, G. S.; ALEX, S. The extreme magnetic storm of 1-2 september 1859. **Journal of Geophysical Research: Space Physics**, v. 108, p. 1–8, 2003. ISSN 21699402. 143

TSURUTANI, B. T.; VERKHOGLYADOVA, O. P.; MANNUCCI, A. J.; SAITO, A.; ARAKI, T.; YUMOTO, K.; TSUDA, T.; ABDU, M. A.; SOBRAL, J. H.; GONZALEZ, W. D.; MCCREADIE, H.; LAKHINA, G. S.; VASYLIUNAS, V. M. Prompt penetration electric fields (ppefs) and their ionospheric effects during the great magnetic storm of 30-31 october 2003. **Journal of Geophysical Research: Space Physics**, v. 113, 5 2008. ISSN 21699402. 145

VADAS, S. L. Horizontal and vertical propagation and dissipation of gravity waves in the thermosphere from lower atmospheric and thermospheric sources. **Journal of Geophysical Research: Space Physics**, v. 112, n. A6, 2007. 2, 41, 162

VALLAT, C.; DANDOURAS, I.; DUNLOP, M.; BALOGH, A.; LUCEK, E.; PARKS, G. K.; WILBER, M.; ROELOF, E. C.; CHANTEUR, G.; RÈME, H. First current density measurements in the ring current region using simultaneous multi-spacecraft cluster-fgm data. **Annales Geophysicae**, v. 23, n. 5, p. 1849–1865, 2005. Available from: <<https://angeo.copernicus.org/articles/23/1849/2005/>>. 61

VENKATESH, K.; RAM, S. T.; FAGUNDES, P. R.; SEEMALA, G. K.; BATISTA, I. S. Electrodynamic disturbances in the Brazilian equatorial and low-latitude ionosphere on st. patrick's day storm of 17 march 2015. **Journal of Geophysical Research: Space Physics**, v. 122, p. 4553–4570, 2017. ISSN 21699402. 42, 49

VERKHOGLYADOVA, O. P.; TSURUTANI, B. T.; MANNUCCI, A. J.; MLYNCZAK, M. G.; HUNT, L. A.; KOMJATHY, A.; RUNGE, T. Ionospheric vtec and thermospheric infrared emission dynamics during corotating interaction region and high-speed stream intervals at solar minimum: 25 march to 26 april 2008. **Journal of Geophysical Research: Space Physics**, v. 116, 2011. ISSN 21699402. 2, 6, 7, 18, 19, 42, 43, 95, 99, 102, 144

WALTER, T.; HANSEN, A.; BLANCH, J.; ENGE, P.; MANNUCCI, T.; PI, X.; SPARKS, L.; IIJIMA, B.; EL-ARINI, B.; LEJEUNE, R.; HAGEN, M.; ALTSHULER, E.; ROB, F.; CHU, A. Robust detection of ionospheric irregularities. **Navigation, Journal of the Institute of Navigation**, v. 48, p. 89–100, 2001. ISSN 00281522. 57, 89

WATARI, S. Geomagnetic storms of cycle 24 and their solar sources global data systems for the study of solar-terrestrial variability 3. space science. **Earth, Planets and Space**, v. 69, 2017. ISSN 18805981. 4, 5

WILKEN, V.; KRIEGEL, M.; JAKOWSKI, N.; BERDERMANN, J. An ionospheric index suitable for estimating the degree of ionospheric perturbations. **Journal of Space Weather and Space Climate**, v. 8, 2018. ISSN 21157251. 85

WU, C. C.; FRY, C. D.; LIU, J. Y.; LIOU, K.; TSENG, C. L. Annual tec variation in the equatorial anomaly region during the solar minimum: September 1996-august 1997. **Journal of Atmospheric and Solar-Terrestrial Physics**, v. 66, p. 199–207, 2004. ISSN 13646826. 101, 104, 105

YAO, Y.; LIU, L.; KONG, J.; ZHAI, C. Analysis of the global ionospheric disturbances of the March 2015 great storm. **Journal of Geophysical Research: Space Physics**, v. 121, p. 12,157–12,170, 2016. ISSN 21699402. 42, 84

YEH, K. C.; LIU, C.-H. Radio wave scintillations in the ionosphere. **Proceedings of the IEEE**, v. 70, p. 324–360, 1982. ISSN 15582256. 91